Fault Detection and Isolation in Attitude Control Subsystem of Spacecraft Formation Flying using Extended Kalman Filters

Sara Ghasemi

A Thesis

in

The Department

of

Electrical and Computer Engineering

Presented in Partial Fulfillment of the Requirements

for the Degree of

Master of Applied Science (Electrical and Computer Engineering) at

Concordia University

Montreal, Quebec, Canada

June 2013

CONCORDIA UNIVERSITY

School of Graduate Studies

This is to certify that the thesis prepared

By: SARA GHASEMI

Entitled: Fault Detection and Isolation in Attitude Control Subsystem of Spacecraft Formation Flying using Extended Kalman Filters

and submitted in partial fulfillment of the requirements for the degree of

Master of Applied Science (Electrical and Computer Engineering)

complies with the regulations of the University and meets the accepted standards with respect to originality and quality.

Signed by the final examining committee:

Rabin Raut Chair

George Vatistas Examiner

Yousef Shayan Examiner

Khashayar Khorasani Supervisor

Approved by

Chair of Department or Graduate Program Director

Dean of Faculty

Date

ABSTRACT

Fault Detection and Isolation in Attitude Control Subsystem of Spacecraft Formation Flying using Extended Kalman Filters

Sara Ghasemi

In this thesis, the problem of fault detection and isolation in the attitude control subsystem of spacecraft formation flying is considered. For this purpose, first the attitude dynamics of a single spacecraft is analyzed and a nonlinear model is defined for our problem. This is followed up by generating the model of the spacecraft formation flight using the attitude model and controlling the formation based on virtual structure control scheme. In order to design the fault detection method, an extended Kalman filter is utilized which is a nonlinear stochastic state estimation method. Three fault detection architectures, namely, centralized, decentralized, and semi-decentralized are designed based on extended Kalman filters. Moreover, the `residual generation and threshold selection techniques are proposed for these architectures. The capabilities of the architectures for fault detection are studied through extensive numerical simulations. Using a confusion matrix evaluation system, it is shown that the centralized architecture can achieve the most reliable results relative to the semi-decentralized and decentralized architectures. Furthermore, the results confirm that the fault detection in formations with angular velocity measurements achieve higher level of accuracy, true faulty, and precision, along with lower level of false healthy misclassification as compared to the formations with only attitude measurements.

In order to isolate the faults, structured residuals are designed for the

decentralized, semi-decentralized, and centralized architectures. By using the confusion matrix tables, the results from each isolation technique are presented for different fault scenarios. Finally, based on the comparisons made among the architectures, it is shown that the centralized architecture has the highest accuracy in isolating the faults in the formations. Furthermore, the results confirm that fault isolation in formations with angular velocity measurements achieve higher level of accuracy when compared to formations with only attitude measurements.

ACKNOWLEDGMENTS

Foremost, I would like to express my sincere appreciation and deep gratitude to my supervisor Dr. Khashayar Khorasani. I am thankful to him for giving me the opportunity to join his research group at Concordia University. I have been inspired by his consistent motivation, guidance, and support in all steps of my graduate study and research.

I am thankful to all my friends and colleagues in Control and Systems Laboratory of Concordia University who have been next to me in various situations and projects. They provide me a warm and friendly environment and made my time with full of memorable and wonderful moments.

I am particularly indebted to my family for all of their never ending love and continuous encouragement during this work. No words can express how I am grateful to them for preparing me the opportunity to do this job and make a big step to the goals of my life. This thesis is dedicated to them.

TABLE OF CONTENTS

ABSTRACT III

ACKNOWLEDGMENTS V

TABLE OF CONTENTS VI

LIST OF FIGURE X

LIST OF TABLES XIX

LIST OF ABBREVIATIONS XXVII

CHAPTER 1 : INTRODUCTION 1

1.1. MOTIVATION 1

1.2. LITERATURE REVIEW 3

1.2.1. Fault Detection and Isolation (FDI) 3

1.2.2. Spacecraft Formation Flying 7

1.2.3. Formation Control Architectures 8

1.2.4. Spacecraft Fault Diagnosis 10

1.3. OBJECTIVE OF THE THESIS 12

1.4. THESIS CONTRIBUTION 13

1.5. ORGANIZATION OF THE THESIS 15

CHAPTER 2 : BACKGROUND 17

2.1. SPACECRAFT ATTITUDE DYNAMICS 17

2.1.1. Reference Frames 18

2.1.2. Kinematics and Dynamics Equations of Angular Motion.....19
2.1.3. Modeling Environmental Disturbances 26
2.2. FORMATION CONTROL.....29
2.2.1. Formation Flying Using Virtual Structure Architecture.....29
2.3. FAULT DETECTION AND ISOLATION.....34
2.3.1. Fault Types 35
2.3.2. Modeling of Faults.....36
2.3.3. Fault Diagnosis 38
2.3.4. Fault Detection and Isolation (FDI) Approaches 39
2.3.5. Model-Based Approaches for Fault Detection and Isolation 40
2.3.6. Model-based Residual Generation.....42
2.3.7. Fault Detection and Isolation in Formation Flight of Spacecraft46
2.4. CONCLUSION.....47
CHAPTER 3 : FAULT DETECTION IN A FORMATION FLIGHT MISSON .. 48
3.1. GRAPH BASED FORMATION FLIGHT MODELLING.....48
3.1.1. Basic Concepts and Notations in Graph Theory.....48
3.2. MODELLING THE FORMATION FLIGHT OF SPACECRAFT.....50
3.3. ARCHITECTURES FOR FAULT DETECTION OF ACTUATOR FAULTS IN FORMATION FLIGHT OF SPACECRAFT.....52
3.3.1. Decentralized Architecture 53
3.3.2. Semi-Decentralized Architecture 54
3.3.3. Centralized Architecture 55
3.4. FAULT DETECTION IN FORMATION FLIGHT.....57
3.4.1. Extended Kalman Filter for Decentralized Architecture 58
3.4.2. Extended Kalman Filter for Semi-Decentralized Architecture .61
3.4.3. Extended Kalman Filter for Centralized Architecture 66

3.4.4. Stochastic Stability of the Architectures 70

3.5. SIMULATION FOR ATTITUDE CONTROL OF SPACECRAFT FORMATION FLYING BY USING THE VIRTUAL STRUCTURE 75

3.6. SIMULATION RESULTS FOR FAULT DETECTION 82

3.6.1. Decentralized Fault Detection Architecture 84

3.6.2. Semi-decentralized Fault Detection Architecture 103

3.6.3. Centralized Fault Detection Architecture 122

3.6.4. Performance Comparison of the Architectures Based on Confusion Matrix Results 143

3.6.5. Performance Comparison of the Attitude Measurement and the Angular Velocity Measurement 153

3.7. CONCLUSION 165

CHAPTER 4 : FAULT ISOLATION IN FORMATION FLIGHT OF SPACECRAFT 168

4.1. FAULT ISOLATION 168

4.2. FAULT ISOLATION BY USING THE STRUCTURED RESIDUAL SET 169

4.2.1. Fault Isolation in the Decentralized Architecture 171

4.2.2. Fault Isolation in the Semi-Decentralized Architecture 172

4.2.3. Fault Isolation in the Centralized Architecture 174

4.3. SIMULATION RESULTS 176

4.3.1. Decentralized Isolation Architecture 177

4.3.2. Semi-decentralized Isolation Architecture 189

4.3.3. Centralized Isolation Architecture 211

4.4. COMPARING AND DISCUSSING THE RESULTS 233

4.4.1. Comparing the Isolation Accuracy of the Decentralized, Centralized, and Semi-decentralized Architectures 233

4.4.2. Comparing the Isolation Accuracy of the Formation with Angular

Velocity Measurement and Attitude Measurement 237

4.5. CONCLUSION.....239

CHAPTER 5 : CONCLUSIONS AND FUTURE WORK 241

5.1. CONCLUSIONS 241

5.2. FUTURE WORKS.....243

BIBLIOGRAPHY 245

LIST OF FIGURE

Figure 2.1 Reference frames…….. 19

Figure 2.2 Effect of disturbance in different altitudes…… 26

Figure 2.3 Coordinate frame geometry [110].…….....…… 31

Figure 2.4 Ring topology…… 32

Figure 2.5 Closed loop system for virtual structure control of spacecraft formation flying..…… 34

Figure 2.6 Block diagram for the input and output signals of the actuator and system.. 37

Figure 2.7 Structure for model-based fault diagnosis...…..……. 41

Figure 2.8 Classification of the model-based residual generation methods. ……. 42

Figure 3.1 Graph G with nodes $V=\{1,2,3,4\}$ and edges $E=\{(1,2),(1,3),(1,4),(2,3),(2,4)\}$ ……. 78

Figure 3.2 Decentralized FD architecture…….. 53

Figure 3.3 Semi-decentralized FD architecture……. 55

Figure 3.4 Centralized FD architecture.…….. 57

Figure 3.5 Four spacecraft formation flying topology…… 76

Figure 3.6 Attitude parameters q_1, q_2, q_3 for the formation flight of spacecraft controlled by the virtual structure.……. 78

Figure 3.7 Angular velocity parameters $\omega_1, \omega_2, \omega_3$ for formation flight of spacecraft controlled by the virtual structure..... 79

Figure 3.8 Attitude error for the formation flight of spacecraft controlled by the virtual structure..... 80

Figure 3.9 Residual d_{11} in the decentralized fault detection architecture with angular velocity measurement for 5% reduction in the torque effectiveness of actuator x of spacecraft #1.. 87

Figure 3.10 Residual d_{12} in the decentralized fault detection architecture with angular velocity measurement for 5% reduction in the torque effectiveness of actuator x of spacecraft #1.. 87

Figure 3.11 Residual d_{13} in the decentralized fault detection architecture with angular velocity measurement for 5% reduction in the torque effectiveness of actuator x of spacecraft #1.. 88

Figure 3.12 Residual d_{11} in the decentralized fault detection architecture with angular velocity measurement for 15% reduction in the torque effectiveness of actuator x of spacecraft #1.. 88

Figure 3.13 Residual d_{12} in the decentralized fault detection architecture with angular velocity measurement, for 15% reduction in the torque effectiveness of actuator x of spacecraft #1.. 89

Figure 3.14 Residual d_{13} in the decentralized fault detection architecture with angular velocity measurement, for 15% reduction in the torque effectiveness of actuator x of spacecraft #1.. 89

Figure 3.15 Residual d_{11} in the decentralized fault detection architecture with attitude measurement for 10% reduction in the torque effectiveness of actuator x of spacecraft #1..... 96

Figure 3.16 Residual d_{12} in the decentralized fault detection architecture with attitude measurement for 10% reduction in the torque effectiveness of actuator x of spacecraft

#1..... 96

Figure 3.17 Residual d_{13} in the decentralized fault detection architecture with attitude measurement for 10% reduction in the torque effectiveness of actuator x of spacecraft #1..... 97

Figure 3.18 Residual d_{11} in decentralized fault detection architecture with attitude measurement for 20% reduction in the torque effectiveness of actuator x of spacecraft #1..... 97

Figure 3.19 Residual d_{12} in the decentralized fault detection architecture with attitude measurement, for 20% reduction in the torque effectiveness of actuator x of spacecraft #1..... 98

Figure 3.20 Residual d_{13} in the decentralized fault detection architecture with attitude measurement, for 20% reduction in the torque effectiveness of actuator x of spacecraft #1..... 98

Figure 3.21 Residual d_1^1 in the semi-decentralized fault detection architecture with angular velocity measurement for 5% reduction in the torque effectiveness of actuator x of spacecraft #1..... 105

Figure 3.22 Residual d_2^1 in the semi-decentralized fault detection architecture with angular velocity measurement for 5% reduction in the torque effectiveness of actuator x of spacecraft #1..... 106

Figure 3.23 Residual d_3^1 in the semi-decentralized fault detection architecture with angular velocity measurement for 5% reduction in the torque effectiveness of actuator x of spacecraft #1..... 106

Figure 3.24 Residual d_1^1 in the semi-decentralized fault detection architecture with angular velocity measurement for 15% reduction in the torque effectiveness of actuator x of spacecraft #1..... 107

Figure 3.25 Residual d_2^1 in the semi-decentralized fault detection architecture with angular velocity measurement for 15% reduction in the torque effectiveness of actuator x of spacecraft #1..... 107

Figure 3.26 Residual d_3^1 in the semi-decentralized fault detection architecture with angular velocity measurement for 15% reduction in the torque effectiveness of actuator x of spacecraft #1..... 108

Figure 3.27 Residual d_1^1 in the semi-decentralized fault detection architecture with attitude measurement for 10% reduction in the torque effectiveness of actuator x of spacecraft #1... 115

Figure 3.28 Residual d_2^1 in the semi-decentralized fault detection architecture with attitude measurement for 10% reduction in the torque effectiveness of actuator x of spacecraft #1... 115

Figure 3.29 Residual d_3^1 in the semi-decentralized fault detection architecture with attitude measurement for 10% reduction in the torque effectiveness of actuator x of spacecraft #1... 116

Figure 3.31 Residual d_2^1 in the semi-decentralized fault detection architecture with attitude measurement for 20% reduction in the torque effectiveness of actuator x of spacecraft #1... 117

Figure 3.32 Residual d_3^1 in the semi-decentralized fault detection architecture with attitude measurement for 20% reduction in the torque effectiveness of actuator x of spacecraft #1... 117

Figure 3.33 Residual d_1 in the centralized fault detection architecture with angular velocity measurement for 5% reduction in the torque effectiveness of actuator x of spacecraft #1... 125

Figure 3.34 Residual d_2 in the centralized fault detection architecture with angular velocity, measurement for 5% reduction in the torque effectiveness of actuator x of spacecraft #1… 126

Figure 3.35 Residual d_3 in the centralized fault detection architecture with angular velocity measurement for 5% reduction in the torque effectiveness of actuator x of spacecraft #1… 126

Figure 3.36 Residual d_1 in the centralized fault detection architecture with angular velocity measurement, for 15% reduction in the torque effectiveness of actuator x of spacecraft #1… 127

Figure 3.37 Residual d_2 in the centralized fault detection architecture with angular velocity measurement, for 15% reduction in the torque effectiveness of actuator x of spacecraft #1… 127

Figure 3.38 Residual d_3 in the centralized fault detection architecture with angular velocity measurement, for 15% reduction in the torque effectiveness of actuator x of spacecraft #1… 128

Figure 3.39 Residual d_1 in the centralized fault detection architecture with attitude measurement for 10% reduction in the torque effectiveness of actuator x of spacecraft #1…… 135

Figure 3.39 Residual d_1 in the centralized fault detection architecture with attitude measurement for 10% reduction in the torque effectiveness of actuator x of spacecraft #1…… 135

Figure 3.40 Residual d_2 in the centralized fault detection architecture with attitude measurement for 10% reduction in the torque effectiveness of actuator x of spacecraft #1…… 135

Figure 3.41 Residual d_3 in the decentralized fault detection architecture with attitude measurement for 10% reduction in the torque effectiveness of actuator x of spacecraft

#1…… 136

Figure 3.42 Residual d_1 in the centralized fault detection architecture with attitude measurement for 20% reduction in the torque effectiveness of actuator x of spacecraft #1…… 137

Figure 3.43 Residual d_2 in the centralized fault detection architecture with attitude measurement for 20% reduction in the torque effectiveness of actuator x of spacecraft #1…… 137

Figure 3.44 Residual d_3 in the centralized fault detection architecture with attitude measurement for 20% reduction in the torque effectiveness of actuator x of spacecraft #1…… 138

Figure 3.45 Comparison of the accuracy for the decentralized, semi-decentralized, and centralized architectures with angular velocity measurement…… 144

Figure 3.46 Comparison of the false healthy for the decentralized, semi-decentralized, and centralized architectures with angular velocity measurement…… 145

Figure 3.47 Comparison of the true faulty for the decentralized, semi-decentralized, and centralized architectures with angular velocity measurement…… 146

Figure 3.48 Comparison of the precision for the decentralized, semi-decentralized, and centralized architectures with angular velocity measurement. …… 147

Figure 3.49 Comparison of the fault detection time delay for the decentralized, semi-decentralized, and centralized architectures with angular velocity measurement. …… 148

Figure 3.50 Comparison of the accuracy for the decentralized, semi-decentralized, and

centralized architectures with attitude measurement..... 149

Figure 3.51 Comparison of the false healthy for the decentralized, semi-decentralized, and centralized architectures with attitude measurement. 150

Figure 3.52 Comparison of the true faulty for the decentralized, semi-decentralized, and centralized architectures with attitude measurement. 151

Figure 3.53 Comparison of the precision for the decentralized, semi-decentralized, and centralized architectures with attitude measurement..... 152

Figure 3.54 Comparison of the fault detection delay for the decentralized, semi-decentralized, and centralized architectures with attitude measurement..... 153

Figure 3.55 Comparing the accuracy of attitude and angular velocity measurement in the decentralized architecture. 154

Figure 3.56 Comparing the false healthy of attitude and angular velocity measurement in the decentralized architecture. 155

Figure 3.57 Comparing the true faulty of attitude and angular velocity measurement in the decentralized architecture. 155

Figure 3.58 Comparing the precision of attitude and angular velocity measurement in the decentralized architecture. 156

Figure 3.59 Comparing the fault detection delay of attitude and angular velocity measurement in the decentralized architecture. 157

Figure 3.60 Comparing the accuracy of attitude and angular velocity measurement in the semi-decentralized architecture. 158

Figure 3.61 Comparing the false healthy of attitude and angular velocity measurement in the semi-decentralized architecture..…… 159

Figure 3.62 Comparing the true faulty of attitude and angular velocity measurement in the semi-decentralized architecture. …… 159

Figure 3.63 Comparing the precision of attitude and angular velocity measurement in the semi-decentralized architecture…… 160

Figure 3.64 Comparing the fault detection time of attitude and angular velocity measurement in semi-decentralized architecture. …… 161

Figure 3.65 Comparing the precision of attitude and angular velocity measurement in the centralized architecture.…… 162

Figure 3.66 Comparing the false healthy of attitude and angular velocity measurement in the centralized architecture. …… 162

Figure 3.67 Comparing the true faulty of attitude and angular velocity measurement in the centralized architecture. …… 163

Figure 3.68 Comparing the precision of attitude and angular velocity measurement in the centralized architecture. …… 163

Figure 3.69 Line chart for comparing the fault detection delay of attitude and angular velocity measurement in centralized architecture. …… 164

Figure 4.1 Comparison of the accuracy of decentralized, semi-decentralized, and centralized isolation techniques for angular velocity measurement. …… 234

Figure 4.2 Comparison of the accuracy of decentralized, semi-decentralized, and centralized isolation techniques for attitude measurement. …… 236

Figure 4.3 Comparison of the accuracy of decentralized isolation technique between angular velocity measurement and attitude measurement. …… 237

Figure 4.4 Comparison of the accuracy of semi-decentralized isolation technique between angular velocity measurement and attitude measurement. …… 238

Figure 4.5 Comparison of the accuracy of centralized isolation technique between angular velocity measurement and attitude measurement. …… 238

LIST OF TABLES

Table 3.1 Desired design specifications. …… 76

Table 3.2 Spacecraft control gains. …… 81

Table 3.3 Formation control gains. …… 81

Table 3.4 Confusion matrix definitions and terms. …… 83

Table 3.5 Confusion matrix for 5% reduction in the torque effectiveness. …… 90

Table 3.6 Confusion matrix for 6% reduction in the torque effectiveness.…… 91

Table 3.7 Confusion matrix for 7% reduction in the torque effectiveness. …… 91

Table 3.8 Confusion matrix for 8% reduction in the torque effectiveness. …… 91

Table 3.9 Confusion matrix for 10% reduction in the torque effectiveness. …… 92

Table 3.10 Confusion matrix for 15% reduction in the torque effectiveness. …… 92

Table 3.11 Confusion matrix for 20% reduction in the torque effectiveness. …… 92

Table 3.12 Confusion matrix for 25% reduction in the torque effectiveness. …… 93

Table 3.13 Confusion matrix evaluating parameters for the decentralized architecture with angular velocity output. …… 93

Table 3.14 Confusion matrix for 5% reduction in the torque effectiveness. …… 99

Table 3.15 Confusion matrix for 6% reduction in the torque effectiveness. …… 100

Table 3.16 Confusion matrix for 7% reduction in the torque effectiveness. …… 100

Table 3.17 Confusion matrix for 8% reduction in the torque effectiveness. …… 100

Table 3.18 Confusion matrix for 10% reduction in the torque effectiveness. …… 101

Table 3.19 Confusion matrix for 15% reduction in the torque effectiveness. …… 101

Table 3.20 Confusion matrix for 20% reduction in the torque effectiveness. …… 101

Table 3.21 Confusion matrix for 25% reduction in the torque effectiveness. …… 102

Table 3.22 Confusion matrix for the decentralized architecture with angular velocity output. …… 102

Table 3.23 Confusion matrix for 5% reduction in the torque effectiveness. …… 109

Table 3.24 Confusion matrix for 6% reduction in the torque effectiveness. …… 109

Table 3.25 Confusion matrix for 7% reduction in the torque effectiveness. …… 110

Table 3.26 Confusion matrix for 8% reduction in the torque effectiveness. …… 110

Table 3.27 Confusion matrix for 10% reduction in the torque effectiveness. …… 110

Table 3.28 Confusion matrix for 15% reduction in the torque effectiveness. …… 111

Table 3.29 Confusion matrix for 20% reduction in the torque effectiveness. …… 111

Table 3.30 Confusion matrix for 25% reduction in the torque effectiveness. …… 111

Table 3.31 Confusion matrix for the semi-decentralized architecture with angular velocity output. …… 112

Table 3.32 Confusion matrix for 5% reduction in the torque effectiveness. …… 118

Table 3.33 Confusion matrix for 6% reduction in the torque effectiveness. …… 119

Table 3.34 Confusion matrix for 7% reduction in the torque effectiveness. …… 119

Table 3.35 Confusion matrix for 8% reduction in the torque effectiveness. …… 119

Table 3.35 Confusion matrix for 8% reduction in the torque effectiveness. …… 119

Table 3.36 Confusion matrix for 10% reduction in the torque effectiveness. …… 120

Table 3.37 Confusion matrix for 15% reduction in the torque effectiveness. …… 120

Table 3.38 Confusion matrix for 20% reduction in the torque effectiveness.…… 120

Table 3.39 Confusion matrix for 25% reduction in the torque effectiveness. …… 121

Table 3.40 The evaluating parameters of confusion matrix for semi-decentralized architecture with attitude output. …… 122

Table 3.41 Confusion matrix for 5% reduction in the torque effectiveness. …… 129

Table 3.42 Confusion matrix for 6% reduction in the torque effectiveness. …… 129

Table 3.43 Confusion matrix for 7% reduction in the torque effectiveness. …… 130

Table 3.44 Confusion matrix for 8% reduction in the torque effectiveness. …… 130

Table 3.45 Confusion matrix for 10% reduction in the torque effectiveness.…… 130

Table 3.46 Confusion matrix for 15% reduction in the torque effectiveness. …… 131

Table 3.47 Confusion matrix for 20% reduction in the torque effectiveness. …… 131

Table 3.48 Confusion matrix for 25% reduction in the torque effectiveness. ……... 131

Table 3.49 Confusion matrix for the centralized architecture with angular velocity output. 132

Table 3.50 Confusion matrix for 5% reduction in the torque effectiveness. …… 139

Table 3.51 Confusion matrix for 6% reduction in the torque effectiveness. …… 139

Table 3.52 Confusion matrix for 7% reduction in the torque effectiveness. …… 140

Table 3.53 Confusion matrix for 8% reduction in the torque effectiveness. …… 140

Table 3.54 Confusion matrix for 10% reduction in the torque effectiveness. …… 140

Table 3.55 Confusion matrix for 15% reduction in the torque effectiveness. …… 141

Table 3.56 Confusion matrix for 20% reduction in the torque effectiveness. …… 141

Table 3.57 Confusion matrix for 25% reduction in the torque effectiveness. …… 141

Table 3.58 Evaluating parameters of confusion matrix for centralized architecture with attitude output. …… 142

Table 4.1 Confusion matrix for the decentralized isolation. …… 178

Table 4.2 Confusion matrix for the decentralized isolation of 25% reduction in loss of effectiveness. …… 180

Table 4.3 Confusion matrix for the decentralized isolation of 20% reduction in loss of effectiveness. …… 180

Table 4.4 Confusion matrix for the decentralized isolation of 15% reduction in loss of effectiveness. …… 181

Table 4.5 Confusion matrix for the decentralized isolation of 10% reduction in loss of effectiveness. …… 181

Table 4.6 Confusion matrix for the decentralized isolation of 8% reduction in loss of effectiveness. …… 182

Table 4.7 Confusion matrix for the decentralized isolation of 7% reduction in loss of effectiveness. …… 182

Table 4.8 Confusion matrix for the decentralized isolation of 6% reduction in loss of effectiveness. …… 183

Table 4.9 Confusion matrix for the decentralized isolation of 5% reduction in loss of effectiveness. …… 183

Table 4.10 Confusion matrix for the decentralized isolation of 25% reduction in loss of effectiveness. …… 185

Table 4.11 Confusion matrix for the decentralized isolation of 20% reduction in loss of effectiveness. …… 185

Table 4.12 Confusion matrix for the decentralized isolation of 15% reduction in loss of effectiveness. …… 186

Table 4.13 Confusion matrix for the decentralized isolation of 10% reduction in loss of effectiveness. …… 186

Table 4.15 Confusion matrix for the decentralized isolation of 7% reduction in loss of effectiveness. …… 187

Table 4.16 Confusion matrix for the decentralized isolation of 6% reduction in loss of effectiveness. …… 188

Table 4.17 Confusion matrix for the decentralized isolation of 5% reduction in loss of effectiveness. …… 188

Table 4.18 Confusion matrix for the semi-centralized isolation. ……... 192

Table 4.19 Confusion matrix for the semi-decentralized isolation of 25% reduction in loss of

effectiveness. …… 194

Table 4.19 Confusion matrix for the semi-decentralized isolation of 25% reduction in loss of effectiveness. …… 194

Table 4.20 Confusion matrix for the semi-decentralized isolation of 20% reduction in loss of effectiveness. …… 195

Table 4.21 Confusion matrix for the semi-decentralized isolation of 15% reduction in loss of effectiveness. …… 196

Table 4.22 Confusion matrix for the semi-decentralized isolation of 10% reduction in loss of effectiveness. …… 197

Table 4.23 Confusion matrix for the semi-decentralized isolation of 8% reduction in loss of effectiveness. …… 198

Table 4.24 Confusion matrix for the semi-decentralized isolation of 7% reduction in loss of effectiveness . …… 199

Table 4.25 Confusion matrix for the semi-decentralized isolation of 6% reduction in loss of effectiveness. …… 200

Table 4.26 Confusion matrix for the semi-decentralized isolation of 5% reduction in loss of effectiveness. …… 201

Table 4.27 Confusion matrix for the semi-decentralized isolation of 25% reduction in loss of effectiveness. …… 203

Table 4.28 Confusion matrix for the semi-decentralized isolation obtained of 20% reduction in loss of effectiveness. …… 204

Table 4.29 Confusion matrix for the semi-decentralized isolation of 15% reduction in loss of

effectiveness. …… 205

Table 4.30 Confusion matrix for the semi-decentralized isolation of 10% reduction in loss of effectiveness. …… 206

Table 4.31 Confusion matrix from the semi-decentralized isolation of 8% reduction in loss of effectiveness. …… 207

Table 4.32 Confusion matrix for the semi-decentralized isolation of 7% reduction in loss of effectiveness. …… 208

Table 4.33 Confusion matrix for the semi-decentralized isolation of 6% reduction in loss of effectiveness. …… 209

Table 4.34 Confusion matrix for the semi-decentralized isolation of 5% reduction in loss of effectiveness. …… 210

Table 4.35 Confusion matrix for the centralized isolation. …… 214

Table 4.36 Confusion matrix for the centralized isolation of 25% reduction in loss of effectiveness.…… 216

Table 4.37 Confusion matrix for the centralized isolation of 20% reduction in loss of effectiveness. …… 217

Table 4.38 Confusion matrix for the centralized isolation of 15% reduction in loss of effectiveness. …… 218

Table 4.39 Confusion matrix for the centralized isolation of 10% reduction in loss of effectiveness. …… 219

Table 4.40 Confusion matrix for the centralized isolation of 8% reduction in loss of effectiveness. …….. 220

Table 4.41 Confusion matrix for the centralized isolation of 7% reduction in loss of effectiveness. 221

Table 4.42 Confusion matrix for the centralized isolation of 6% reduction in loss of effectiveness. 222

Table 4.43 Confusion matrix for the centralized isolation of 5% reduction in loss of effectiveness. 223

Table 4.44 Confusion matrix for the centralized isolation of 25% reduction in loss of effectiveness. 225

Table 4.45 Confusion matrix for the centralized isolation of 20% reduction in loss of effectiveness. 226

Table 4.46 Confusion matrix for the centralized isolation of 15% reduction in loss of effectiveness. 227

Table 4.47 Confusion matrix for the centralized isolation of 10% reduction in loss of effectiveness. 228

Table 4.48 Confusion matrix for the centralized isolation of 8% reduction in loss of effectiveness.. 229

Table 4.49 Confusion matrix for the centralized isolation of 7% reduction in loss of effectiveness. 230

Table 4.50 Confusion matrix for the centralized isolation of 6% reduction in loss of effectiveness. 231

Table 4.51 Confusion matrix for the centralized isolation of 5% reduction in loss of effectiveness. 232

LIST OF ABBREVIATIONS

DS	Deep Space
POE	Planetary orbital Environment
AFRL	Air Force Research Laboratory
EO	Earth Orbiter
EOS	Earth Observing Systems
ESSP	Earth System Science Pathfinder
CNES	Centre National d'Etudes Spatiales
FDI	Fault Detection and Isolation
DOS	Dedicated Observer Scheme
LTI	Linear Time Invariant
PCA	Principal Component Analysis
PLS	Partial Least Square
GSFC	Goddard Space Flight Center
FFC	Formation Flying Control
MIMO	Multiple-Input Multi-Output

L/F	Leader Follower
LL	Low Level
HL	High Level
FL	Formation Level
FDIR	Fault Detection and Isolation and Reconfiguration
ACS	Attitude Control Subsystem
IGRF	International Geometric Reference Filed
LOE	Loss of Effectiveness
LIP	Lock in Place
HOP	Hardover Failure
ARMA	Autoregressive Moving Average
EKF	Extended Kalman Filter

Chapter 1: INTRODUCTION

1.1. MOTIVATION

There are several advantages in spacecraft formation flying concept. The ability to make formation more robust by eliminating single point failures is one of the most important advantages of formation flying. This multiple spacecraft approach will also impose less requirements and limitations on launch vehicles and, therefore, reducing the mission cost. Higher reliability and redundancy, higher resolution, simpler design and faster built time are other advantages of using multiple smaller spacecraft over a single large spacecraft.

Formation flying missions are categorized into two main classes: Deep Space missions (DS) and Planetary Orbital Environment (POE). In POE, the spacecraft are affected by orbital dynamics as well as environmental disturbances, while in DS the absolute and relative spacecraft dynamics can be represented by double integrators [1].

There are limited experiences of formation flying missions. TechSat-21 was a POE project from US's Air Force Research Laboratory (AFRL) which was intended to demonstrate a formation of three micro-spacecraft flying in formation to operate as a virtual spacecraft. However, the technical issues on the project were "far more challenging than originally thought," forcing the Air Force to "restructure the program," according to Maj. Gen. Paul Nielsen, director of the Air Force Research Laboratory. TechSat21 experiment has been terminated in 2003 **Error! Reference source not found.**.

New Millennium Program Earth Orbiter (EO-1) was a NASA-Goddard spacecraft

which launched in November 2000, in to a circular, sun-synchronous polar orbit at an altitude of 705 Kilometers. EO-1 flew in formation with Landsat-7, EOS AM-1 (Terra), and SAC-C- which is the first constellation of Earth observing spacecraft. Formation flying is defined to be the autonomous on-orbit position maintenance of multiple spacecraft relative to measured separation errors. The currently proposed formation flying technologies on EO-1 will not enable true formation flying in the sense of the definition given above because of a variety of budget and time constraints. Although incomplete, this demonstration will validate many of the formation flying components necessary to achieve the ultimate goal of true formation flying [1], [4].

The "A-Train" spacecraft formation consists of two of the major Earth Observing Systems (EOS) missions, three Earth System Science Pathfinder (ESSP) missions, and a French Centre National d'Etudes Spatiales (CNES) mission flying in close proximity. The A-Train (Afternoon Train) is a constellation of spacecraft in a polar orbit include GCOM-W1, Aqua, CALIPSO, CloudSat, PARASOL, and Aura, which are in Earth-observing spacecraft that closely follow one after another along the same orbital track. Aqua is the lead member of the formation and Aura is in the rear. OCO-2 is scheduled to join the configuration in 2013 which will cross the equator fifteen minutes ahead of Aqua and, thus, become the new leader of the formation of Figure 1.1. On November 16, 2011, PARASOL was lowered to 9.5 km under the A-Train and continues its nominal mission observing clouds and aerosols. PARASOL will exit the A-Train fully in the fall of 2013 [5], [6].

Missions for these spacecraft formations include understanding of water in the Earth's climate system and the global water cycle, understanding of additional components of the Earth's climate system and their interactions, weather forecasting, studying the clouds, measure total solar irradiance for long-term climate studies,

studying stratospheric ozone layer, controlling air quality, CO2 monitoring, and a variety of other science studies and technology demonstrations [8].

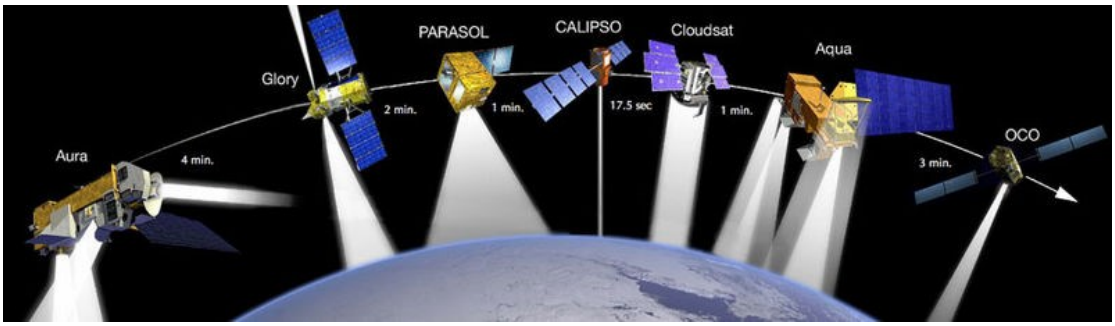

Figure 1.1 The various satellites that fly in constellation in the "A-Train" [7]

It is well-known that the efficiency and reliability of the formation can be degraded as a consequence of occurrence of a fault in the components of the spacecraft. Therefore, autonomous, real-time and on-line fault detection and isolation (FDI) strategies are required in order to diagnose faults before they cause severe damage and lead to catastrophic failure in the entire networked formation system.

1.2. LITERATURE REVIEW

In this section, relevant literature review regarding fault detection and isolation in formation flying is presented. The quantitative model-based, qualitative model-based and history-based methods in the literature are reviewed, the spacecraft formation flying concepts and issues are investigated, and the FDI approaches presented in the literature for formation flying are studied.

1.2.1. Fault Detection and Isolation (FDI)

A fault diagnosis algorithm consists of fault detection, isolation, and identification steps. Fault detection is the process of identifying the occurrence of a fault in the

system, while fault isolation and identification is a step further and implies the pinpointing of the faulty component [11].

Information redundancy is the basis of most FDI approaches. Hardware redundancy requires at least a dual set of physical devices, such as multiple sensors, actuators, or computers, but it faces the problem of extra equipment, maintenance cost, additional space and weight. An alternative approach is analytical redundancy which uses a model instead of using extra hardware. In **Error! Reference source not found.** and 0, *Frank* reviews different concepts of model-based fault detection and isolation and discussed the analytical redundancy approach to FDI in dynamic systems. In quantitative modeling, the system is expressed in terms of mathematical functional relationships between the inputs and outputs of the system. In qualitative modeling, these relationships are expressed in terms of qualitative functions which only require heuristic information e.g. the sign of the variables, the tendencies of the variables, order and/or relative magnitude. In the case that even the qualitative model is difficult to obtain, the model free approach can be used which is based on historical process data [11].

Quantitative model-based techniques use available input and output information measured from the monitored system and *a priori* information represented by the system's mathematical model to generate a fault indicating signal. These techniques can be categorized into three main approaches: observer based approach, parity space approach, and parameter estimation approach [12]-[15].

In observer-based approach, the weighted output error (or innovation in stochastic case) between the measured process output and model output is generated, which is named as residual [11]. Then, by setting a threshold (fixed or variable) on each residual

signal, the faults are detected. Each residual can be designed to have a special sensitivity to individual faults in different locations of the system [16]. The most common observers are Luenberger observer which is used in a deterministic setting and Kalman filter which is used in a stochastic setting [15]. In **Error! Reference source not found.**, *Clark* introduces the Dedicated Observer Scheme (DOS) as a functional redundancy approach for the problem of detecting instrument failure in operating systems. In 0-[22], *Patton et al.* demonstrated the eigenstructure assignment approach to robust detection through disturbance decoupling. In [23], *Massumnia* proposed a geometric approach for solving the problems related to designing failure detection and identification filters for continuous LTI systems. In [24], *White* and *Speyer* generated formulations for detection filters by assignment of the closed-loop eigenstructure under certain constraints. In [25], *Douglas* and *Speyer* proposed the h_∞ bound detection filter, and in [26], a game theoretic fault detection filter is designed by *Chung* and *Speyer*. For obtaining more information on different approaches that have been studied in the literature for observer and filter design you can refer to [27]-[42].

The parity space approach is based on checking the parity of the sensor measurements of the monitored system over a time window [43]-[52]. In this method, the mathematical model of the process is rearranged to obtain the parity equations which are algebraic equations that indicate an explicit relation between input and output time-sequence data vector. In [46], *Chow* and *Willsky* formulated the parity space design as an optimization problem. In [48], *Massumnia* and *Velde* constructed generalized parity relations by resource to transfer matrix description of system. They construct the parity relation of minimum length that depends only on the output of a single sensor. In [51], *Chen* and *Zhang* proposed a simple parity vector scheme which derives the redundant measurement by using the prediction of the state and the output

of the system.

The parameter estimation approach is based on system identification techniques [53]-[59]. In this method, the parameters of the actual process are estimated online using the parameter estimation methods and then compared with the parameters of the reference model obtained in fault free condition. In [55]-[57], *Isermann* has shown how parameter estimation methods can be used for detecting process faults in continuous time systems.

Qualitative model-based techniques can be classified into structural graphs causal models, fault trees, qualitative physics, and abstraction hierarchy [62], [63]-[73]. In the cases that the fault cannot be described in analytical models, the online information available is not given by quantitative measurements, or that the system structure is not precisely known, the diagnosis has to be based on heuristic information. In [68], *Lunze* and *Schiller* utilize the causal structure of the dynamic system to restrict the search space of the resolution system. They use a qualitative mode of the dynamical process and a causality graph, to describe the direction of cause-effect relations. In [69], *Fathi et al.* have integrated the symbolic reasoning of the knowledge-based systems techniques with quantitative analysis of analytical redundancy methods to reduce the analytical complexity of analytical algorithms and increase the effectiveness of knowledge-based systems.

In the case that a precise model of the process is not available, the history-based technique can be applied which is based on availability of large amount of historical process data. Feature extraction is the way of transforming the *a priory* data to use in a diagnosis system. Feature extraction can be categorized into quantitative and qualitative techniques. Qualitative feature extraction techniques include expert systems

[74]-[75], fuzzy logic [76], pattern recognition [77], frequency and time-frequency analysis, and qualitative trend analysis [78]-[79]. The methods that extract quantitative information can be classified into two types of statistical and non-statistical methods. Principal Component Analysis (PCA)/Partial Least Square (PLS) and statistical pattern classifiers are the two basic methods of statistical analysis, while neural networks is the most applied non-statistical feature extraction method[79]-[83].

1.2.2. Spacecraft Formation Flying

Among the several definitions proposed for the formation flight of spacecraft, NASA's Goddard Space Flight Center (GSFC) has proposed a definition that most of the space's community accepted as the definition of spacecraft formation flying: The tracking or maintenance of a desired relative separation, orientation or position between or among spacecraft [1].

Spacecraft formation flying has several benefits over a single flight spacecraft. Distributing the tasks of one large spacecraft among several smaller, less expensive, and cooperative spacecraft, reduces cost, increases instrument resolution, improves system reliability, and enhances system robustness. These precious advantages of formation flying have attracted researchers' attention in recent years [85]-[87].

Formation control strategies have been classically categorized into centralized approaches and decentralized approaches. In a fully centralized system, one spacecraft serves as a reference and has access to all of the states of the system and has the capability to communicate the optimal control commands to each actuator in the overall system. Since this spacecraft has complete knowledge of the formation, it has the responsibility of collision avoidance, formation keeping, guidance and control. Therefore, this reference spacecraft demands greater relative navigation hardware and

software [88], [91].

In a fully decentralized system, each spacecraft has an awareness of all other spacecraft in the formation. In this scheme, there is no supervisor and the feedback is only the relative states of each spacecraft respecting its neighbor agents. A global relative state is shared throughout the formation, and control is applied independently at each node [89], [90].

The centralized formation control could represent a good strategy for a small team, when it is implemented with a single computer and a single sensor to monitor and control the whole team. However, when considering a team with a large number of agents, the need of greater computational capacity and a large communication bandwidth, it may be preferable to use the decentralized formation control which distributes the computational load equally throughout the formation. Another advantage of decentralized approach, in contrast to the centralized approach, is its robustness to a single-point failure. The decentralized approach utilizes the inherent robustness advantages associated with a distributed system [88], [91].

1.2.3. Formation Control Architectures

In the literature, the Formation Flying Control (FFC) is divided into five FFC architectures: Multiple-Input Multi-Output (MIMO), Leader Follower (L/F), Virtual Structure, Behavioral Based, and Cyclic [85].

In MIMO architecture, the entire formation is considered as a multiple input-multiple output plant and the formation control is designed based on a dynamical model of the entire formation. The advantages of this structure are its optimality of the entire formation and feasibility of its stability analysis. However, the MIMO structure is

not robust to local faults [104]-[106].

The Leader Follower (L/F) architecture is the most studied formation flying architecture. In L/F configuration, which is also known as Chief/Deputy, Master/Slave, or Target-Case, one or more agents are selected as leaders and they are responsible for guiding the formation and the rest of the agents are controlled to follow the leaders and named follower agents. The L/F uses a hierarchical arrangement of individual spacecraft controllers that reduces formation control to individual tracking problems [107]-[109].

In Virtual Structure architecture, the spacecraft are treated as rigid bodies embedded in an overall virtual rigid body. Motions of the virtual structure and the constant specified positions and orientations of the spacecraft within the virtual structure are used to generate reference trajectories for the spacecraft to follow. Individual spacecraft controllers are used to track the generated reference trajectories [110], [111].

In Behavioral Based architecture, the desired behaviors for each agent are prescribed and then the control action is made from the weighted average of the control for each behavior. In fact, this architecture combines multiple controllers for achieving different behaviors. Possible behaviors include collision avoidance, obstacle avoidance, goal seeking, and formation keeping [112]-[114].

The Cyclic architecture is similar to L/F in this aspect that the formation controller is a connection between individual spacecraft controllers. But in the Cyclic, the individual controllers are not connected hierarchically and each spacecraft controls itself relative to neighboring spacecraft, which makes a cyclic control dependency directed graph [115]-[116].

In this thesis, formation flying of spacecraft is considered to be accomplished by controllers that are designed through the decentralized virtual structure approach. The advantages of the decentralized virtual structure approach are its capability to maintain the formation tightly during the spacecraft maneuver, to prescribe the coordinated behavior of the team, and to resolve and remedy the limitations of the centralized solution and configurations that introduces a single point of failure for the entire system [111].

1.2.4. Spacecraft Fault Diagnosis

Various methods have been proposed in the literature for the FDI problem of a single spacecraft. In [117], *Qing-xian et al.* investigated the robust nonlinear un-known input observer for satellite attitude control system. In [118], *Wang et al.* have proposed a nonlinear adaptive observer under the Lipschitz condition of the nonlinear part for the actuator fault diagnosis. In [119], *Jiang et al.* have developed residual generators based on least-squares parameter estimation techniques for FDIR of satellite's attitude and orbital model. In [120]-[122], *Tudoroiu et al.* have proposed isolation and detection interacting multiple model (IMM) algorithms for partial (soft) or total (hard) reaction wheel failures in the spacecraft attitude control system. Their FDI method is based on interactive bank of Kalman filter and interactive bank of unscented Kalman filter. In [123], *Qing* and *Saif* have investigated an actuator fault estimation and isolation scheme using a bank of repetitive learning observers for a class of discrete-time nonlinear systems. *Khorasani et al.* proposed in [124]-[128] neural network-based FDI approaches for FDI of satellite's actuator. In [129], *Zhao-hui et al.* have developed an online FDI scheme based on wavelet and dynamic neural network which is capable of processing time-varying signals in real time.

Cooperative fault estimation in formation flight of spacecraft is an open criteria and has new challenges. Many complexities and computational constraints are produced in formation flight of spacecraft at different levels, including: component, subsystem, system, spacecraft, and formation. No standard or conventional methodology exists that describes the communication scheme among the different system levels to achieve the most efficient fault diagnosis under various possible scenarios. Therefore, the cooperation and information exchange among different levels of diagnosis system leads to new issues and research problems. Investigating different possible faulty scenarios in the formation and the corresponding cooperation algorithms among different levels of diagnosis system are the open research area in this field [135].

Meskin and *Khorasani* in [130]-[131] developed three FDI architectures, namely, centralized, decentralized, and semi-decentralized for a network of unmanned vehicles with relative state measurements and compared these architectures. The problem for dependent fault signatures, time delay systems and linear impulsive systems have also been investigated in their work using the geometric approach.

Barua and *Khorasani* in [132]-[134] developed a decomposition hierarchical framework through a Bayesian network based model, namely Component Dependence Model (CDM). The CDM structure specifies the network parameters using node fault diagnosis performance data and domain experts' beliefs.

Azizi and *Khorasani* in [135]-[136], considered three levels for fault estimation and recovery in formation flight, namely, Low Level (LL), High Level (HL) and Formation Level (FL). The LL module corresponds to the vehicle components; a conventional quantitative model-based method is used for fault estimation and conventional linear

controllers are designed for fault recovery. The HL module is a supervisor that monitors the behaviors of all of the vehicles and if it observes any degradation in the performance of the fault recovery in LL, it forwards the tasks to FL. In FL, the vehicles are considered as one integrated unit and the fault severities are estimated cooperatively using distributed estimation filters, namely sub-observers. The HL supervisor is responsible for cooperation among different levels of this hierarchical scheme and the data fusion.

As mentioned, the literature review for FDI in formation flight of spacecraft is limited to [130]-[136]. However, reviewing the research that has been done on FDI of multi agent systems and networks can also be helpful. In [137], *Guo et al.* proposed a decentralized and real-time fault detection framework for two different cooperative multi agent system models based on communication or relative state sensing. In [138], *Shames et al.* constructed a bank of unknown input observers for networks of interconnected second-order linear time-invariant systems. In [139], *Mendes* and *Costa* have proposed a hybrid architecture based on horizontal layers of fault detection agents for networked control process. They have applied neural networks models for residuals generation with adaptive threshold. In [140], *Tousi et al.* have developed a hybrid fault detection, isolation, and recovery for a team of unmanned vehicle. Their approach consists of FDIR units for both low level and high level. The low level unit, complement the high level supervisor by monitoring the agents for the detection and identification of the faults. The high level supervisor isolate the faults by reconstructing the low level observers and analyzing the results.

1.3. OBJECTIVE OF THE THESIS

The main objective of this thesis is to provide a solution for the fault detection and

isolation of formation flying spacecraft missions with faults affecting the actuators of the attitude control subsystem. In order to fulfill this objective, the spacecraft attitude dynamics and attitude control subsystem for formation flying is presented and described. Extended Kalman filter has been chosen as the fault detection technique because of its model-based and nonlinear characteristics [98]. Finally, the fault detection and isolation problem in formation flying of spacecraft is investigated by designing three different FDI architectures, namely, Decentralized, Centralized, and Semi-Decentralized, to analyze and represent the advantages and disadvantages of each architecture versus the others.

The application of the developed fault detection architectures are not limited to spacecraft formation flying and can be extended to any other multi-vehicle formations with nonlinear dynamics.

The cost of formation flying missions can be reduced by implementing the presented FDI systems. Less engineer and professional time are required in ground stations for monitoring the formation behavior and for diagnosing the possible faults occurring.

1.4. THESIS CONTRIBUTION

- A novel fault detection and isolation scheme for the Attitude Control Subsystem (ACS) of spacecraft formation flying has been proposed based on the extended Kalman filter, which is the nonlinear version of the Kalman filter and is utilized for estimating the states of the system. The extended Kalman filter is integrated in three different architectures, namely, decentralized, centralized, and semi-decentralized to model the FD system in formation flying.

- Based on our results, in the formation with angular velocity measurement, the centralized detection architecture has the most success in announcing the occurrence of the faults, but it has also more false alarms relative to the two other architectures. Besides, the decentralized detection architecture has the least percentage in announcing the occurrence of the faults, but it has also the least amount of false alarms.

- It is shown that in the formation with attitude measurement, the centralized detection architecture has the most success in announcing the occurrence of the faults, and it has also the least number of false alarms relative to the two other architectures. Besides, the decentralized detection architecture has the least percentage in announcing the occurrence of the faults; however it has fewer false alarms relative to semi-decentralized detection architecture.

- In all three detection architectures, the results that are obtained from the angular velocity measurements show more desired performance for accuracy, true faulty, false healthy, true healthy, false faulty, precision, and fault detection delay relative to attitude measurement. This implies that the angular velocity sensors can make the missions more secure and safe, because the faults are more detectable by using the information provided with them.

- Novel isolation methods are proposed for decentralized, semi-decentralized, and decentralized architectures based on structured residual set technique. Using the criteria developed in these methods, the fault location is identified and the occurrence of one actuator fault is decoupled from the occurrence of other actuator faults in the formation.

- Our results demonstrate that the centralized isolation technique has the most desired performance among the three proposed isolation techniques.

- Furthermore, the presented results show that in all three isolation techniques, namely, decentralized, centralized and semi-decentralized, the formation with angular velocity measurement have higher isolation accuracy than the formation with attitude measurement.

1.5. ORGANIZATION OF THE THESIS

In Chapter 2, first the attitude dynamics of spacecraft is explained based on reference frames, kinematics and dynamics equations of angular motion. Then, the environment disturbances which affect the spacecraft dynamics are modelled. The different formation flying control architectures presented in the literature are introduced briefly, while the decentralized virtual structure control topology is discussed completely as the selected formation control methodology. The decentralized virtual structure is utilized for simulation in this thesis. In the next section, types of faults are introduced and the fault modeling in the state space system is explained. Then, the classifications of fault detection and isolation methods which exist in the literature are presented with a more detailed explanation on model-based FDI methods. Finally, an introduction for the concept of FDI in spacecraft formation flying is provided. At the end of the chapter, the simulation results for the controlled spacecraft formation flying using the virtual structure topology is provided.

In Chapter 3, first the concept of graph-based modeling is explained and then its application in spacecraft formation flying is discussed. Fault detection architectures for

formation flying, namely, decentralized, centralized and semi-decentralized architectures, are designed and presented. The residual generation and threshold selection method are proposed for each architecture. At the end of the chapter, first the simulation results for the behavior of the controlled spacecraft formation flying using the virtual structure topology is provided, and then the results that are obtained by implementing the proposed fault detection methods on formation flying are presented. The results are interpreted and discussed using confusion matrix tables, variables, and graphs.

In Chapter 4, isolation techniques based on structured residual set is proposed for decentralized, centralized, and semi-decentralized architectures to isolate the actuator faults in the formation. At the end of the chapter, the simulation results obtained by implementing the proposed method on spacecraft formation flying are presented and discussed.

Conclusions and future work are presented in Chapter 5.

Chapter 2: BACKGROUND

In this chapter, a review of the background required to realize the fault detection and isolation techniques proposed in this thesis is presented. First the model of spacecraft attitude dynamics is described based on kinematics and dynamics of angular motion. This is followed by a brief introduction of flight formation control approaches proposed in the literature, and a more detailed explanation on virtual structure control topology.

Afterwards, a review of basic concepts of fault is provided. The faulty model of a control system is introduced and modified to be used in the spacecraft attitude control systems. Then the various fault diagnosis approaches are introduced with a more detailed description on Kalman filtering methods. Finally an introduction is provided for the fault detection and isolation concept in spacecraft formation flying.

2.1. SPACECRAFT ATTITUDE DYNAMICS

The path of a spacecraft through space is called its orbit, and the orientation of a spacecraft in space is called its attitude. These two types of motion require two types of control systems, attitude control system and orbital control system. Since the fault detection and isolation in the attitude control subsystem of spacecraft formation flying is studied in this thesis, before confronting the formation flight definition, we require certain basic descriptions of spacecraft orientation, reference frames and attitude dynamics [141], [142].

2.1.1. Reference Frames

This section explains different frames for representing spacecraft attitude and orbital motion.

2.1.1.1. INERTIAL FRAME

Inertial frame F_0 is a non-accelerated reference frame in which Newton's laws are valid. The origin of this frame is located at the center of Earth. The z-axis is oriented toward the North Pole, the x-axis points toward the point where the plane of the Earth's orbit crosses the Equator, going from South to North. The y axis completes the right handed system.

2.1.1.2. ORBIT FRAME

The origin of this frame is at the center of mass of the spacecraft. The y-axis is toward the direction of motion tangentially to the orbit. The z-axis is toward the center of Earth, and x-axis completes the right handed system.

2.1.1.3. BODY FRAME

This frame is a moving frame which is fixed on the spacecraft body. The origin is at the center of mass of the spacecraft, the x-axis is forward and z-axis is downward. Y-axis completes the right handed system.

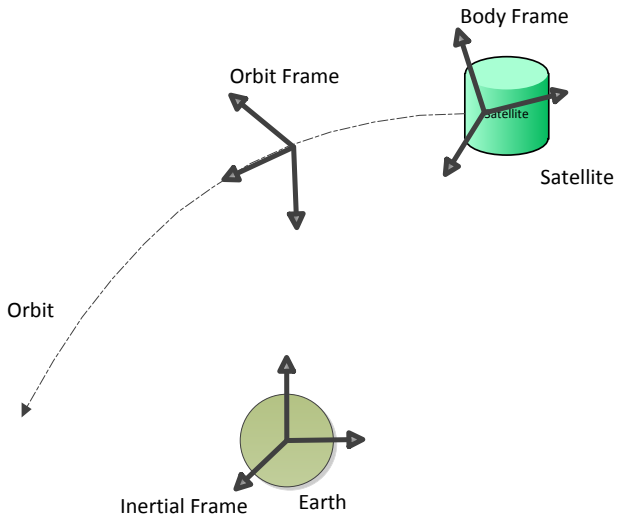

Figure 2.1 Spacecraft reference frames.

2.1.2. Kinematics and Dynamics Equations of Angular Motion

Spacecraft attitude dynamics relies on "rigid body" dynamics and its orientation behavior can be explained through this basis. A rigid body has six degrees of freedom, three of which are rotational parameters. Spatial rotations of a rigid body in three dimensions can be parameterized in several ways. These include the classical Euler angles, sequential rotations about the body axes, direction cosines, and the Eulerian parameters or "quaternions". In this thesis, we use quaternions to describe the rotation of a spacecraft, because it has several advantages over the use of Euler angles or direction cosines. Quaternions involve the use of algebraic relations to determine the elements of the rotation matrix instead of trigonometric functions. The computations are faster and there are no singularities which may occur in the Euler angle formulation. Moreover, fewer multiplications are required for propagating successive incremental rotations [141], [142].

2.1.2.1. QUATERNIONS

A quaternion has four elements, one of these elements is a scalar and three others construct a vector. The vector part describes the axis of rotation and the scalar part is the angle of rotation around that axis. A quaternion $\vec{q}$ is expressed as

$$\vec{q} = iq_1 + jq_2 + kq_3 + q_4 \tag{2.1}$$

$$\vec{\varepsilon} = \begin{bmatrix} q_1 \\ q_2 \\ q_3 \end{bmatrix} \tag{2.2}$$

$$\eta = q_4 \tag{2.3}$$

where

$$q_1 = a_1 \sin\frac{\phi}{2} \tag{2.4}$$

$$q_2 = a_2 \sin\frac{\phi}{2} \tag{2.5}$$

$$q_3 = a_3 \sin\frac{\phi}{2} \tag{2.6}$$

$$q_4 = \cos\frac{\phi}{2} \tag{2.7}$$

where a_1, a_2 and a_3 are direction cosines of the Euler vector $\vec{\varepsilon}$, and ϕ is the rotation angle about $\vec{\varepsilon}$.

The condition

$$\varepsilon^T\varepsilon+\eta^2=q_1{}^2+q_2{}^2+q_3{}^2+q_4{}^2=1 \tag{2.8}$$

is automatically satisfied and can be used for numerical control of machine computations.

2.1.2.2. ATTITUDE KINEMATICS AND DYNAMICS EQUATION

The attitude kinematics and dynamics equations of a spacecraft relative to the inertial frame F_0 respectively are

$$\dot{} \quad \begin{bmatrix} \dot{} & +\eta I_{3\times3} \\ \dot{} & -\varepsilon^T \end{bmatrix} \omega \tag{2.9}$$

$$J\dot{} \qquad J\omega)+\tau \tag{2.10}$$

where

$$\omega=\begin{bmatrix}\omega_1\\ \omega_2\\ \omega_3\end{bmatrix} \tag{2.11}$$

The vector ω is the angular velocity of the spacecraft relative to the inertial frame with ω_1 as the angular velocity of axis x, ω_2 as the angular velocity of axis y, and ω_3 is the angular velocity of axis z.

The matrix

$$J=\begin{bmatrix} I_{xx} & -I_{xy} & -I_{xz} \\ -I_{yx} & I_{yy} & -I_{yz} \\ -I_{xz} & -I_{yz} & I_z \end{bmatrix} \tag{2.12}$$

is the tensor of inertia about the center of mass of the spacecraft and with respect to the xyz axes. The spacecraft that is considered in this thesis is assumed to be symmetric with respect to the plane $x=0$, then, we will have $I_{xy}=I_{xz}=I_{yz}=0$. Now the inertia tensor can be written as

$$J=\begin{bmatrix} I_{xx} & 0 & 0 \\ 0 & I_{yy} & 0 \\ 0 & 0 & I_{zz} \end{bmatrix} \tag{2.13}$$

The vector

$$\tau=\begin{bmatrix} \tau_1 \\ \tau_2 \\ \tau_3 \end{bmatrix} \tag{2.14}$$

is the control torque with τ_1 as the torque produced in the actuator of axis x, τ_2 as the torque produced in the actuator of axis y, and τ_3 as the torque produced in the actuator of axis z.

The cross-product operate is defined as

$$\varepsilon^{\times}=\begin{bmatrix} 0 & -q_3 & q_2 \\ q_3 & 0 & -q_1 \\ -q_2 & q_1 & 0 \end{bmatrix} \tag{2.15}$$

The equations (2.9) and (2.10) can be combined and described in one matrix which can be written as

$$\begin{bmatrix} -\frac{1}{2}(\omega_2 q_3 - \omega_3 q_2) + \frac{1}{2} q_4 \omega_1 \\ -\frac{1}{2}(\omega_3 q_1 - \omega_1 q_3) + \frac{1}{2} q_4 \omega_2 \\ \dot{q}_3 \\ \dot{q}_4 \\ \dot{\omega}_1 \\ \dot{\omega}_2 \\ \dot{\omega}_3 \end{bmatrix} \begin{bmatrix} \frac{1}{2}(\omega_1 q_2 - \omega_2 q_1) + \frac{1}{2} q_4 \omega_3 \\ \frac{1}{2}(q_1 \omega_1 + q_2 \omega_2 + q_3 \omega_3) \\ \frac{I_y - I_z}{I_x} \omega_2 \omega_3 + \frac{1}{I_x} \tau_1 \\ \frac{I_z - I_x}{I_y} \omega_1 \omega_3 + \frac{1}{I_y} \tau_2 \\ \frac{I_x - I_y}{I_z} \omega_1 \omega_2 + \frac{1}{I_z} \tau_3 \end{bmatrix} \tag{2.16}$$

As stated in equation (2.8), q_4 can be calculated directly from q_1, q_2 and q_3 with the equation $q_4 = \sqrt{1 - q_1^2 - q_2^2 - q_3^2}$, and it is not required to have an extra differential equation for q_4. Therefore the equation $\dot{q}_4 = \frac{1}{2}(q_1\omega_1 + q_2\omega_2 + q_3\omega_3)$ can be eliminated from the above vectors.

The nonlinear dynamics of (2.16) can be written as the following

$$\begin{aligned} \dot{x} &= f(x(t)) + Bu(t) + w(t) \\ y(t) &= Cx(t) + v(t) \end{aligned} \tag{2.17}$$

where

$$x = \begin{bmatrix} q_1 \\ q_2 \\ q_3 \\ \omega_1 \\ \omega_2 \\ \omega_3 \end{bmatrix}, \quad y = \begin{bmatrix} \omega_1 \\ \omega_2 \\ \omega_3 \end{bmatrix}$$

are respectively the state vector and the output vector, and

$$u = \begin{bmatrix} u_1 \\ u_2 \\ u_3 \end{bmatrix}$$

is the control torque τ, produced in three actuators of three different axes, and $w(t) \in \Re^6$ and $v(t) \in \Re^3$ are white Gaussian noise with zero mean and covariance respectively $Q(t)$ and $R(t)$.

In order to achieve (2.17), $f\left(x(t)\right)$ can be defined with two vectors $f_1(x)$ and $f_2(x)$ explored from (2.16) as following:

$$f(x) = \begin{bmatrix} f_1(x) \\ f_2(x) \end{bmatrix} \tag{2.18}$$

$$f_1(x) = \begin{bmatrix} -\frac{1}{2}\left(\omega_2 q_3 - \omega_3 q_2\right) + \frac{1}{2} q_4 \omega_1 \\ -\frac{1}{2}\left(\omega_3 q_1 - \omega_1 q_3\right) + \frac{1}{2} q_4 \omega_2 \\ -\frac{1}{2}\left(\omega_1 q_2 - \omega_2 q_1\right) + \frac{1}{2} q_4 \omega_3 \end{bmatrix} \tag{2.19}$$

$$f_2(x) = \begin{bmatrix} k_4 \omega_2 \omega_3 \\ k_5 \omega_1 \omega_3 \\ k_6 \omega_1 \omega_2 \end{bmatrix} \tag{2.20}$$

where

$$k_1 = \frac{I_y - I_z}{I_x}$$
$$k_2 = \frac{I_z - I_x}{I_y}$$
$$k_3 = \frac{I_x - I_y}{I_z} \tag{2.21}$$

The control matrix B for the system (2.17) is extracted from equation (2.16) and it is

$$B = \begin{bmatrix} 0 & 0 & 0 \\ 0 & 0 & 0 \\ 0 & 0 & 0 \\ \frac{1}{I_x} & 0 & 0 \\ 0 & \frac{1}{I_y} & 0 \\ 0 & 0 & \frac{1}{I_z} \end{bmatrix} \tag{2.22}$$

The output matrix for the system 0 is

$$C = \begin{bmatrix} 0 & 0 & 0 & 1 & 0 & 0 \\ 0 & 0 & 0 & 0 & 1 & 0 \\ 0 & 0 & 0 & 0 & 0 & 1 \end{bmatrix} \tag{2.23}$$

for the angular velocity output measurement and

$$C = \begin{bmatrix} 1 & 0 & 0 & 0 & 0 & 0 \\ 0 & 1 & 0 & 0 & 0 & 0 \\ 0 & 0 & 1 & 0 & 0 & 0 \end{bmatrix} \tag{2.24}$$

for the attitude output measurement.

2.1.3. Modeling Environmental Disturbances

A spacecraft orbiting the Earth is influenced by many perturbing forces, torques and disturbances. Non-symmetric and non-homogenous characteristics of the Earth produce gravitational perturbation $J2$ and gravitational torque in lower altitudes [143], [144]. The other affecting disturbance in lower altitudes is atmospheric drag whereas for high altitude orbits it may be ignored [142], [143]. Solar radiation [145] and solar wind [143], the magnetic field of the Earth, and the gravitational force of the Moon and the Sun [146], [1] are other major perturbing factors.

The effect of disturbance in different altitudes is shown in Figure 2.2.

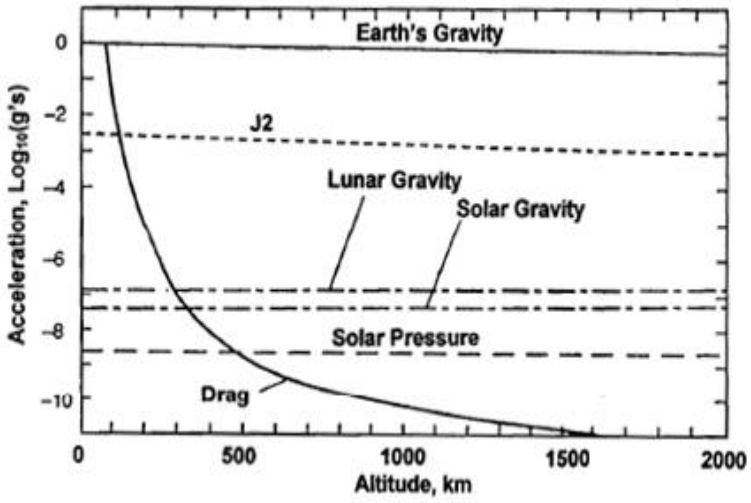

Figure 2.2 Effect of disturbance in different altitudes [148].

The dominant sources of environmental disturbance torques on the spacecraft attitude are the solar radiation pressure, aerodynamic drag and Earth's gravitational and magnetic fields [149]. Also, there are orbital perturbations like $J2$ perturbation that must be considered in orbital control. The solar radiation pressure is effective on the attitude of the spacecraft for altitudes higher than 1000 km. The gravity gradient disturbance is most significant below 1000 km. Aerodynamic perturbations are most

effective below 500 km and negligible over 1000 km altitudes.

The state space model 0 in the presence of disturbance is represented by

$$\begin{aligned} \dot{} \quad & (t)) + Bu(t) + w(t) + D_{ext}(t) \\ y(t) &= Cx(t) + v(t) \end{aligned} \tag{2.25}$$

where $D_{ext} \in R^6$ is the environmental disturbance and is the sum of T_g gravity gradient torque, T_{sp} solar radiation torque, T_a aerodynamic drag, and T_m magnetic disturbance torque, as follows

$$D_{ext}(t) = T_g + T_{sp} + T_a + T_m \tag{2.26}$$

In the following, mathematical models of the disturbances are presented.

2.1.3.1. GRAVITY GRADIENT TORQUE

Any non-symmetrical object in the orbit is affected by a gravitational torque because of the variation in the Earth's gravitational force over the object. There are many mathematical models for gravity gradient torque. The most common one is derived by assuming homogeneous mass distribution of the Earth:

$$T_g = \frac{3\mu\left(I_z - I_y\right)\sin\left(2\theta\right)}{2R^3} \tag{2.27}$$

where T_g is the max gravity torque, μ is the Earth's gravity constant ($3.986 \times 10^{14}\ {}^{m^3}/_{s^2}$), R is the orbit radius (m), θ is the maximum deviation of the z-axis from local vertical in radians, I_z and I_y are moments of inertia about z and y axes in $kg.m^2$[149].

2.1.3.2. SOLAR RADIATION TORQUE

The photons from the sun produce a force which results in a torque about the center of mass of the spacecraft. This disturbance is the influence of surface reflectivity and spacecraft geometry.

Solar radiation pressure is highly dependent on the type of surface being illuminated. In general, solar arrays are absorbers and the spacecraft body is a reflector. The worst case solar radiation torque is,

$$T_{sp} = F_s\left(c_{ps} - c_g\right) \tag{2.28}$$

where F_s is the solar constant,1367 W/m^2 , A_s is the surface area, c_{ps} is the location of the surface of solar pressure, and c_g is the center of gravity [149].

2.1.3.3. AERODYNAMIC DRAG

This disturbance is most effective on spacecraft orbiting below 400-500 km. The drag force created by the air molecule interaction with the spacecraft body produces a torque on the spacecraft, thus reducing its velocity and resulting in a lower orbit for the spacecraft. This torque is derived as:

$$T_a = F\left(c_{pa} - c_g\right) = FL \tag{2.29}$$

where $F = 0.5[\rho C_d A V^2]$ being the force, C_d the drag coefficient (usually between 2 and 2.5), ρ the atmosphere density, A the surface area, V the spacecraft velocity, c_{pa} the center of aerodynamic pressure and c_g the center of gravity [149].

2.1.3.4. MAGNETIC DISTURBANCE TORQUE

This torque is the result of the interaction of the geomagnetic field and spacecraft's residual magnetic field. The torque acting on the spacecraft is given by,

$$T_m = DB \tag{2.30}$$

where T_m is the magnetic torque on the spacecraft, D is the residual dipole of the vehicle and B is the earth's magnetic field in Tesla. The required magnetic field measurements for evaluating this torque can be obtained by using IGRF [149].

2.2. FORMATION CONTROL

2.2.1. Formation Flying Using Virtual Structure Architecture

As discussed in Section 1.2.3, five architectures for formation flying control are proposed in the literature including Multiple Input-Multiple Output, Leader/Follower, Virtual Structure, Cyclic, and Behavioral Based [1]. In this thesis, formation flying of spacecraft is considered to be accomplished by controllers that are designed through the *decentralized virtual structure* approach. The advantages of the decentralized virtual structure approach are its capability to maintain the formation tightly during the spacecraft maneuver, to prescribe the coordinated behavior of the team, and to resolve and remedy the limitations of the centralized solution and configurations that introduces a single point of failure for the entire system [111].

2.2.1.1. DECENTRALIZED VIRTUAL STRUCTURE

In [111], Ren and Beard have proposed the idea of decentralized virtual structure. In this approach, the entire formation is treated as a single structure which is called

virtual structure. The virtual structure evolves in time as a rigid body with a specified direction and maintains desired geometric relationships among the agents. It has a frame located in the virtual mass center of the formation which is known as the formation frame and indicated by F_F, while the inertial frame is indicated by F_0.

The virtual structure then has attitude q_F, and angular velocity ω_F relative to F_0. The attitude of the i-th spacecraft relative to the inertial frame F_0 is q_i, and its angular velocity relative to the inertial frame is ω_i. Similarly the attitude and angular velocity of the i-th spacecraft relative to the formation frame F_F is denoted by q_{iF} and ω_{iF}.

Assume place holders for each spacecraft that show their desired states relative to formation frame F_F. The spacecraft are supposed to track the states of these place holders. The attitude and angular velocity of the i-th place holder relative to formation frame F_F is q_{iF}^d and ω_{iF}^d. The desired attitude and angular velocity of each spacecraft, denoted by q_i^d and ω_i^d, are computed with 0, using the actual states of virtual structure and the desired states of spacecraft related to the virtual structure. The formation is supposed to preserve its shape during each maneuver. Then the attitude q_{iF}^d should be constant during the maneuver and the angular velocity ω_{iF}^d should be zero. The attitude and angular velocity of the i-th spacecraft relative to inertial frame are given by

$$\left[q_i^d\right]_0 = \left[q_F\right]_0 \left[q_{iF}^d\right]_F \,,\ \left[\omega_i^d\right]_0 = \left[\omega_F\right]_0$$
$$\left[\dot{\ } \quad \cdot \quad\right] \,,\ \left[\dot{\ } \quad \cdot \quad\right] \tag{2.31}$$

The formation pattern is the desired states of the virtual structure $\left[q_F^d, \omega_F^d\right]$. In piecewise rigid formation maneuvers the desired angular velocity of the formation is zero, $\omega_F^d = 0$. Each spacecraft is supposed to track the desired states that make the

formation to keep its shape and the virtual structure states achieve their desired amounts.

The coordinate frame geometry is shown in Figure 2.3. Frame F0 is an inertial frame. The formation frame is located at Ff. the labels S1, S2, S3 and S4 are the symbols for indicating the spacecraft. the labels Sd1, Sd2, Sd3 and Sd4 are the symbols for desired locations of the spacecraft.

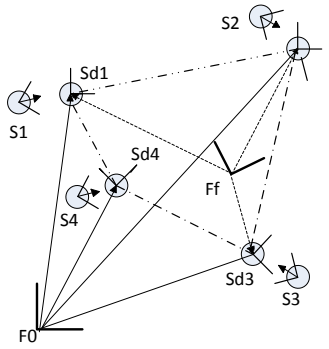

Figure 2.3 Coordinate frame geometry [110].

Among the different network topologies, such as Ring, Mesh, Star, Line, Fully Connected, Tree, and Bus, in this thesis the bidirectional Ring topology is used for the state communication among the spacecraft. In this topology, each spacecraft has communication with its two neighbors, one on the left hand side and one on the right hand side as shown in Figure 2.4.

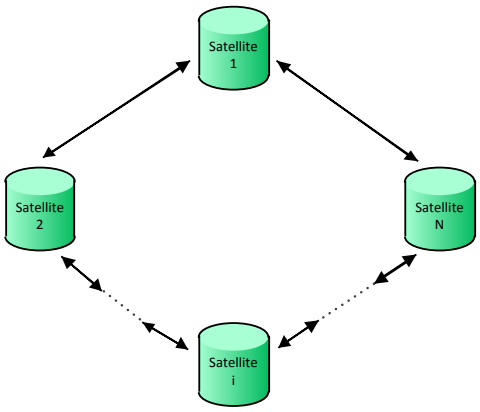

Figure 2.4 Ring topology.

2.2.1.2. FORMATION CONTROL STRATEGY FOR EACH SPACECRAFT

For the i-th spacecraft, $x_i = \left[q_i^T, \omega_i^T \right]^T$ is the actual state and $x_i^d = \left[q_i^{dT}, \omega_i^{dT} \right]^T$ is the desired state. Error state for the i-th spacecraft is defined by [illegible].

The attitude dynamics for the spacecraft are stated in Section 2.1. The control torque presented in [111] for the i-th spacecraft is given by

$$\tau_i = J_i \dot{[illegible]} \; J_i \left(\omega_i + \omega_i^d \right) - k_{qi} \left\langle q_i^{d*} q_i \right\rangle - k_{\omega i} \left(\omega_i - \omega_i^d \right) \tag{2.32}$$

where J_i is the moment of inertia of the i-th spacecraft, k_{qi} is a positive scalar, $k_{\omega i}$ is a symmetric positive definite matrix. The conjugate of a quaternion is defined by

$$q* = \begin{bmatrix} -q_1 \\ -q_2 \\ -q_3 \\ q_4 \end{bmatrix} \tag{2.33}$$

and $\langle q \rangle$ represents the vector part of the quaternion.

2.2.1.3. FORMATION CONTROL STRATEGY FOR EACH VIRTUAL STRUCTURE INSTANTIATION

The i-th virtual structure instantiation states are defined with $x_{Fi} = \left[q_{Fi}^T, \omega_{Fi}^T \right]^T$ as the actual states and $x_F^d = \left[q_F^{d^T}, \omega_F^{d^T} \right]^T$ as the desired states. The error states for the i-th virtual structure instantiation is defined with .~ ~ . The objectives of the control strategy are to synchronize the instantiations $x_{F1} = x_{F2} = \cdots$, and to achieve the desired goal $x_F^d = \left[q_F^{d^T}, \omega_F^{d^T} \right]^T$. The control torque τ_{Fi} proposed by [111] is given by

$$\tau_{Fi} = -k_G \left\langle q_F^{d^*} q_{Fi} \right\rangle - \Gamma_{Gi} \omega_{Fi} - k_s \left\langle q_{F(i+1)}^* q_{Fi} \right\rangle - D_s \left[\omega_{Fi} - \omega_{F(i+1)} \right] - k_s \left\langle q_{F(i-1)}^* q_{Fi} \right\rangle - D_s \left[\omega_{Fi} - \omega_{F(i-1)} \right] \quad (2.34)$$

where $k_G > 0$ and $k_s \geq 0$ are scalars, D_s is a symmetric positive definite matrix, and $\langle q \rangle$ represents the vector part of the quaternion. The matrix Γ_{Gi} is defined as $\Gamma_{Gi} = D_G + K_F e_{Ti}$ to bring formation feedback from the i-th spacecraft to the i-th virtual structure implementation where D_G and K_F are symmetric positive definite matrices and $e_{Ti} = \|.~$ is the tracking performance of the i-th spacecraft. The closed loop control for virtual structure control of spacecraft formation flying is shown in Figure 2.5.

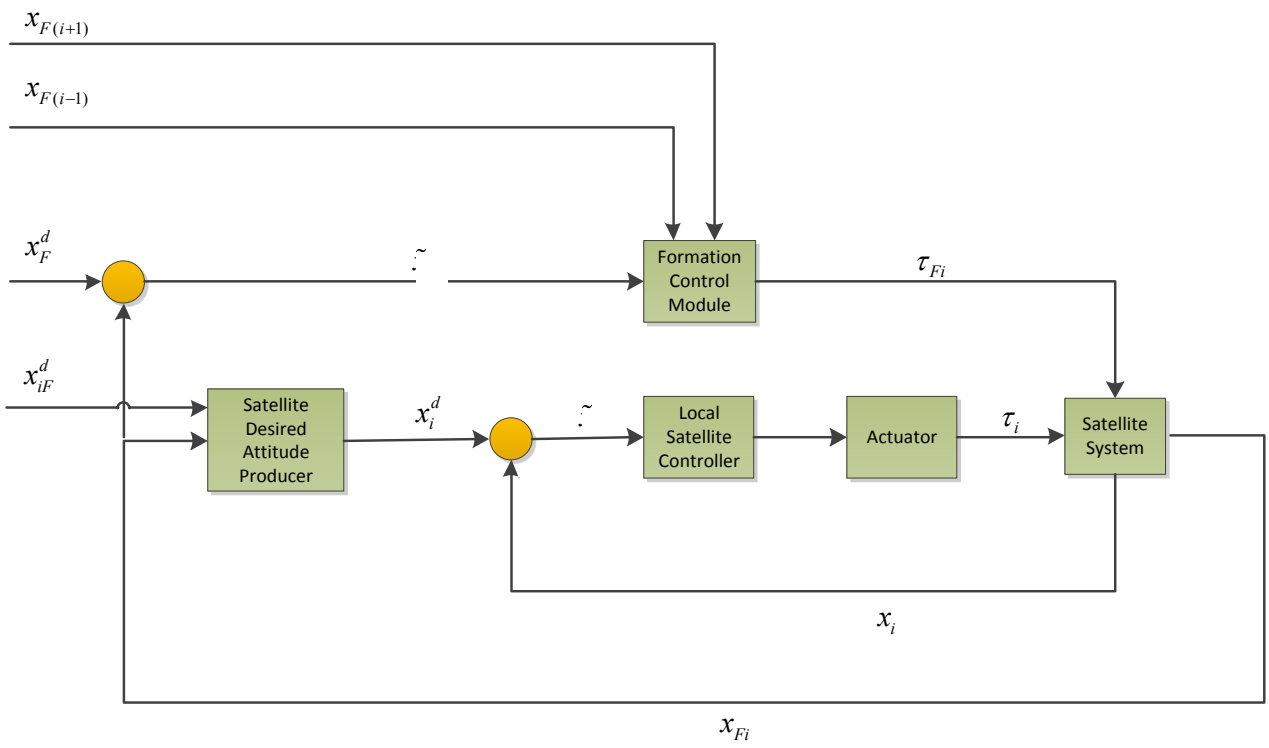

Figure 2.5 Closed loop system for virtual structure control of spacecraft formation flying.

2.3. FAULT DETECTION AND ISOLATION

Fault is regarded as an unpermitted deviation, of at least one characteristic property, or feature of the system from acceptable, usual or standard condition. Fault is the result of a defect in a component or subsystem which leads to degrade the functionality and performance of the system. A permanent fault may lead to a failure and terminate the ability of a subsystem or the whole system to perform its required function [92].

2.3.1. Fault Types

Faults can be categorized from different aspects. They can be classified based on the physical location of their occurrence such as sensors, actuators, system/plant components, and controllers. Also they can be categorized based on the way they are added to the system as additive and multiplicative faults, and based on the time behavior of faults they can be classified as abrupt and incipient faults. Another classification is based on the persistence of the faults. A permanent fault is a total failure of a component and remains until the component is repaired or replaced. Transient fault is a temporary malfunction of a component, while intermittent faults are repeated occurrences of transient faults.

In this thesis we investigate the actuator faults of the spacecraft, because actuators are the components that are among the most critical and vital parts of a spacecraft. Sensor redundancy can be a low cost solution for handling sensor faults, but for actuators it is not possible to have always extra actuators to recover from the possibility of actuator fault occurrence.

The actuator faults can be classified into four types, namely: lock-in-place, hard-over failure, float, and loss-of-effectiveness [93] . These faults may be formally represented as follows:

$$B_i^f u = \begin{cases} B_i u_i & \text{No Fault} \\ \left(B_i + f_i\right) u_i = B_i \left(I - \Gamma_i\right) u_i & \text{Loss of Effectiveness (LOE)} \\ 0 & \text{Float} \\ B_i u_i^{Lock} & \text{Lock in Place (LIP)} \\ B_i u_i^{\min} \ \ or \ \ B_i u_i^{\max} & \text{Hard over Failure (HOF)} \end{cases} \tag{2.35}$$

where B_i is the healthy actuator control matrix, u is the control input, B_i^f is the faulty

actuator control matrix, $f_i = -B_i\Gamma_i$ is a negative semi-definite matrix with diagonal matrix $\Gamma_i = diag(\gamma_{ik})$ where $\gamma_{ik} = [\gamma_{i1} \quad \gamma_{i2} \quad \gamma_{i3}]^T$ includes the LOE parameters $0 < \gamma_{ij} < 1$. The $U_i^{\max}$ and $U_i^{\min}$ are the minimum and maximum actuation, and $U_i^{Lock}\left(U_i^{\min} < U_i^{Lock} < U_i^{\max}\right)$ is a constant level of actuation [135].

In this thesis, we consider Loss of Effectiveness (LOE) actuator fault which is the most common fault in spacecraft actuators. For this fault the applied control signal becomes a percentage of the desired control signal.

2.3.2. Modeling of Faults

Three types of models for faulty system representations are: transfer functions, ARMA model, and state space model. In this work, we model our faulty system using state space modelling. Assume that the healthy system is modelled by the following state space representation

$$\begin{aligned} \dot{} \quad & \quad \varepsilon(t)) + Bu(t) \\ y(t) &= Cx(t) \end{aligned} \tag{2.36}$$

where $x \in R^n$ is the system state vector, $u \in R^m$ is the control input, $y \in R^p$ is the output measurement vector, and $f(x(t)) \in R^n$ is the nonlinear system model. The matrices $B \in R^{n\times m}$, and $C \in R^{p\times n}$ are respectively the input, and output matrices.

The system with actuator faults that is modelled by Loss of Effectiveness (LOE) faults can be written as

$$\dot{} \quad \varepsilon(t)) + B^f(t)u(t) \tag{2.37}$$

where $B^f \in R^{n\times m}$ is the post fault control matrix and is related to the nominal control

matrix B with

$$B^f(t) = B - \Delta B = B - B\Gamma(t) \tag{2.38}$$

where

$$\Gamma(t) = \begin{bmatrix} \gamma_1(t) & 0 & \cdots & \\ 0 & \gamma_2(t) & \ddots & \\ \vdots & \ddots & \ddots & \vdots \\ 0 & 0 & \cdots & \end{bmatrix} \tag{2.39}$$

The $\gamma_i = 0$ denotes the healthy i-th actuator and the $\gamma_i = 1$ indicates complete failure in the i-th actuator. In general the $0 < \gamma_i < 1$ shows the partial loss in control effectiveness of the i -th actuator.

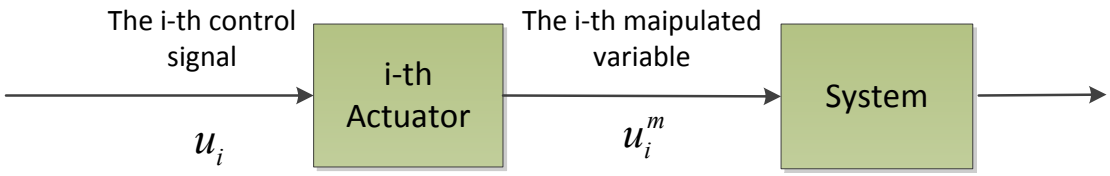

Figure 2.6 Block diagram for the input and output signals of the actuator and system.

In Figure 2.6, the signal u_i^m is the actuation produced by the i-th actuator. For a healthy actuator we have

$$u_i^m = u_i \tag{2.40}$$

and for a faulty actuator we have

$$u_i^m = (1-\gamma_i)u_i \tag{2.41}$$

which implies $\gamma \times 100\%$ reduction in the actuation effectiveness.

By substituting equation (2.38) into the equation (2.37), we obtain

$$\therefore \qquad \text{ć}(t)) + B(I - \Gamma(t))u(t) \tag{2.42}$$

An alternative representation of this equation is formulated as

$$\therefore \qquad \text{ć}(t)) + Bu(t) - \begin{bmatrix} b_1\gamma_1 & b_2\gamma_2 & \cdots \end{bmatrix} \begin{bmatrix} u_1 \\ \vdots \\ u_m \end{bmatrix} \tag{2.43}$$

which can be written in a more compact form with

$$\therefore \qquad \text{ć}(t)) + Bu(t) - \sum_{i=1}^{m} b_i\gamma_i u_i \tag{2.44}$$

This equation will be used in this thesis as the description of a faulty spacecraft attitude control subsystem.

2.3.3. Fault Diagnosis

Fault diagnosis system is a monitoring system that is being used to detect faults and diagnose their location and significance. This system normally consists of the following main tasks [11]:

- Fault detection: The task of this module is to make a decision between two facts; the system is healthy and everything is fine or a fault has occurred and something is going wrong.
- Fault isolation: The task of this unit is to find the location of the fault and to

determine which component or subsystem is the source of this malfunction.

- Fault identification: Estimating the size, type and nature of the fault is the responsibility of this unit.

Fault detection is the inseparable part of the procedure, and fault isolation is also an important part because of the requirement of determining the source of the fault to make a proper decision. The identification task is more needed for the reconfiguration process. Certainly it can be helpful to have a more complete awareness about the fault but it is not fundamental for fault diagnosis. In this thesis, our method consists of fault detection and isolation in actuators of the formation flight of spacecraft.

2.3.4. Fault Detection and Isolation (FDI) Approaches

FDI approaches can be classified by two main categories: Model-free and model-based methods. Model-free methods can also be classified by two main groups; Signal-based methods, and knowledge-based methods. Among the several techniques that exist in literature, the following are the most recognized techniques [92]:

Signal-based methods:

- Limit checking
- Signal Processing

Knowledge-based methods:

- Fault tree
- Pattern recognition
- Expert systems
- Fuzzy logic

- Neural networks

Model-based methods:

- State estimation methods
- Parameter estimation methods
- Parity space approaches

In model-based approaches it is assumed that a quantitative or qualitative model of the underlying system is known. In contrast, signal-based and knowledge-based approaches which can also be called data-based methods do not require such a model. They detect faults by exploring the actual measured data and finding the abnormality from the data behavior which is the effect of fault in the system. These approaches are well suited for systems in which mathematical models are not available.

Given the availability of a mathematical model of spacecraft formation flying, we use a model-based approach as our FDI method.

2.3.5. Model-Based Approaches for Fault Detection and Isolation

Model-based fault diagnosis is defined as detection, isolation and characterization of faults of a system, by comparing the actual system measurements with *a priori* information of the system obtained from its mathematical model [94].

In this approach, the idea is to generate residual signals from the difference between real information of the system and information obtained from the mathematical model. Then the behavior of the residual signal is evaluated to detect the fault and specify its characteristics. Figure 2.7 shows the two main stages in the structure of model-based fault diagnosis.

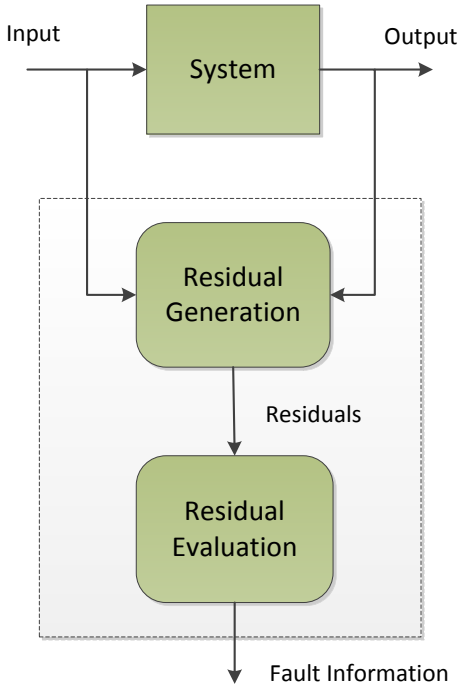

Figure 2.7 Structure for model-based fault diagnosis.

- **Residual Generation:**

Its purpose is to generate residuals using the input and output information of the system and the mathematical model. In the healthy condition of the system the residual is normally zero or close to zero, but in the faulty situation the residual remarkably diverges from zero. The residual behavior should contain information about the characteristics of the fault and it should be independent from the system inputs and outputs [11].

- **Residual Evaluation:**

The goal of residual evaluation is to make the decision if any fault has occurred or not and explore the fault information such as location, time, and severity from the characteristics of the residual. In order to achieve this goal one

may use a simple threshold test on the instantaneous value or average of residuals, or may use methods of statistical decision theory [11].

2.3.6. Model-based Residual Generation

The classification of the quantitative model-based residual generation methods can be shown in Figure 2.8.

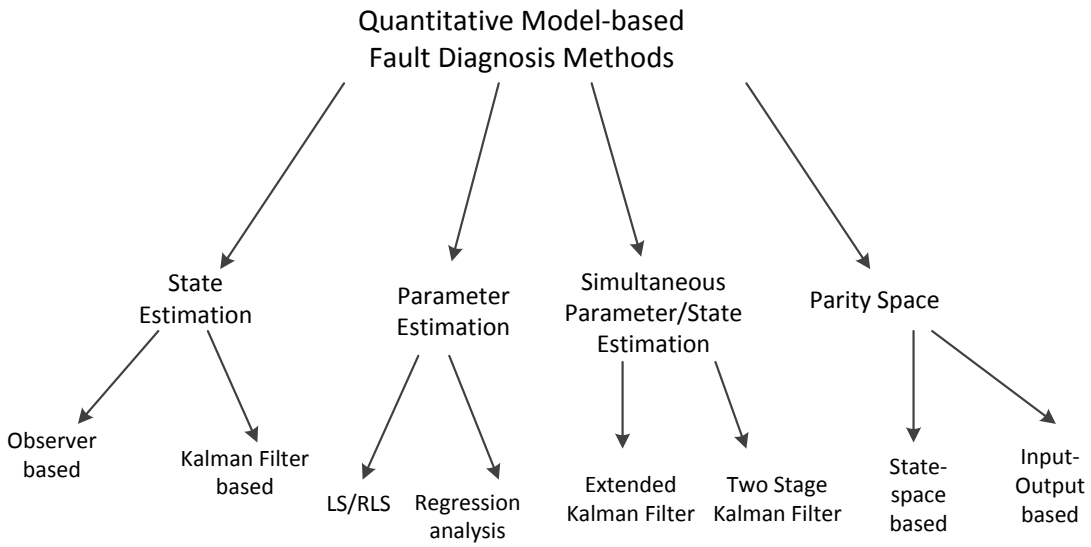

Figure 2.8 Classification of the model-based residual generation methods.

The attitude dynamics of the spacecraft as mentioned in Section 2.1 describes a nonlinear system. Therefore, extended Kalman filter (EKF) is a proper FDI method, which gives an approximation of the optimal estimate by linearizing the nonlinear system model around the last state estimate. Extended Kalman filter can be categorized as a stochastic state estimation method among the model-based methods.

In the following, first we explain the Kalman filter method and then describe the extended Kalman filter which is highly similar to the Kalman filter. The filters have both the discrete-time and the continuous-time representations. Here we explain the

continuous-time type for both of them because the model of our system is continuous-time.

2.3.6.1. KALMAN FILTER

Consider the following state space model describing a linear system:

$$\begin{aligned} \dot{} \qquad &)x(t)+B(t)u(t)+w(t) \\ y(t) &= C(t)x(t)+v(t) \end{aligned} \tag{2.45}$$

where $w(t)$ and $v(t)$ are the process and observation noise which are both assumed to be zero mean with covariances $Q(t)$ and $R(t)$, respectively. The initial state $x(t_0)$ is a random vector with known mean $\mu(t_0)=E\left[x(t_0)\right]$ and covariance $P(t_0)=E\left[\left(x(t_0)-\mu(t_0)\right)\left(x(t_0)-\mu(t_0)\right)^T\right]$.

Dimension and description of the variables are as follows:

$x(t)$	$n\times 1$	_ State vector
$w(t)$	$n\times 1$	_ Process noise vector
$y(t)$	$m\times 1$	_ Observation vector
$v(t)$	$m\times 1$	_ Measurement noise vector
$\mathrm{u}(t)$	$p\times 1$	_ Input vector
$Q(t)$	$n\times n$	_ Process noise covariance matrix
$R(t)$	$m\times m$	_ Measurement noise covariance matrix
$A(t)$	$n\times n$	_ State matrix
$B(t)$	$n\times p$	_ Input matrix
$\mathrm{C}(t)$	$m\times n$	_ Output matrix

The objective of the Kalman filter is to obtain an estimate of the state vector $\hat{x}(t)$

using the state dynamics and a sequence of measurements as accurate as possible. Kalman filter is an optimal estimator, and if all the noise is Gaussian it minimise the mean square error of the estimated parameters, according to

$$\begin{aligned}\frac{d}{dt}\hat{x}(t) &= A(t)\hat{x}(t)+B(t)u(t)+K(t)\tilde{} \\ &= A(t)\hat{x}(t)+B(t)u(t)+K(t)\left(y(t)-C(t)\hat{x}(t)\right)\end{aligned} \tag{2.46}$$

with the gain

$$K(t)=E\left(x(t)\tilde{}\qquad\right)^{-1}=P(t)C(t)^{T}R(t)^{-1} \tag{2.47}$$

The covariance may be computed by

$$\frac{d}{dt}P(t)=A(t)P(t)+P(t)A(t)^{T}-K(t)C(t)P(t)+Q(t) \tag{2.48}$$

In this process, the $r(t)=y(t)-\hat{y}(t)$, which denotes the difference between the actual observation $y(t)$ and the expected observation , $\hat{y}(t)$ is a random process and is usually known as an innovation process or innovation sequence. The innovation sequence can be used as a residual.

In the healthy condition, the difference between system states and their estimates is zero or very close to zero in steady state. However, in a faulty system, the residual $r(t)$ distinguishably diverges from zero.

2.3.6.2. EXTENDED KALMAN FILTER

Consider the following continuous-time nonlinear system, described by the differential equation and the observation model with an additive noise

$$\begin{aligned} \dot{x} &= f\left(x(t),u(t)\right)+w(t) \\ y(t) &= h\left(x(t)\right)+v(t) \end{aligned} \tag{2.49}$$

where $w(t)$ and $v(t)$ are the process and observation noise which are both assumed to be zero mean with covariances $Q(t)$ and $R(t)$, respectively. The initial state $x(t_0)$ is a random vector with known mean $\mu(t_0)=E\left[x(t_0)\right]$ and covariance $P(t_0)=E\left[\left(x(t_0)-\mu(t_0)\right)\left(x(t_0)-\mu(t_0)\right)^T\right]$.

Dimension and description of the variables are as follows

$x(t)$	$n\times 1$	_ State vector
$w(t)$	$n\times 1$	_ Process noise vector
$y(t)$	$m\times 1$	_ Observation vector
$v(t)$	$m\times 1$	_ Measurement noise vector
$\mathrm{u}(t)$	$p\times 1$	_ Input vector
$f(.)$	$n\times 1$	_ Process nonlinear vector function
$h(.)$	$m\times 1$	_ Observation nonlinear vector function
$Q(t)$	$n\times n$	_ Process noise covariance matrix
$R(t)$	$m\times m$	_ Measurement noise covariance matrix

The idea is to linearize the nonlinear function around the current state estimate by expanding $f\left(x(t),u(t)\right)$ and $h\left(x(t)\right)$ in Taylor series and using the lower order terms of the series to approximate the prediction and the next estimate of $x(t)$. In order to achieve this aim, the matrix of partial derivatives, that is the Jacobian, is computed.

At each time step, the Jacobian is evaluated with current predicted states. These matrices can be used in the Kalman filter equations. This process essentially linearizes the nonlinear function around the current estimate according to

$$F(t) = \frac{\partial f}{\partial x}|_{\hat{x}(t),u(t)} \tag{2.50}$$

$$H(t) = \frac{\partial h}{\partial x}|_{\hat{x}(t)} \tag{2.51}$$

The filter dynamics can be written as

$$\begin{aligned} \frac{d}{dt}\hat{x}(t) &= f\left(\hat{x}(t), u(t)\right) + K(t)\tilde{} \\ &= f\left(\hat{x}(t), u(t)\right) + K(t)\left(y(t) - h\left(\hat{x}(t)\right)\right) \end{aligned} \tag{2.52}$$

with the gain

$$K(t) = P(t)H(t)^T R(t)^{-1} \tag{2.53}$$

The covariance may be computed by

$$\frac{d}{dt}P(t) = F(t)P(t) + P(t)F(t)^T - K(t)H(t)P(t) + Q(t) \tag{2.54}$$

The innovation sequence $r(t) = y(t) - \hat{y}(t)$ is the difference between the actual observation and expected observation, and we can use it as the residual for the fault detection purpose.

2.3.7. Fault Detection and Isolation in Formation Flight of Spacecraft

Fault detection and isolation (FDI) problems for the formation flight of spacecraft is not as simple as for one spacecraft and has more challenges. Fault in one spacecraft can disturb the ideal cooperation desired for the formation keeping, stability, reliability, and performing the mission in formation flight. Also the effect of fault occurrence in one spacecraft can propagate to other parts of the formation and affects their

performance directly. These facts make FDI more vital and serious for formation flight.

In this thesis, three model-based architectures are proposed for fault detection and isolation in the formation flight of spacecraft: centralized architecture, decentralized architecture, and semi-decentralized architecture.

First, in Chapter 3, we discuss our fault detection method and explain how we use the extended Kalman filter in each of the centralized, decentralized, and semi-decentralized architectures to detect the actuator faults in the formation flight of spacecraft. Then, in Chapter 4 we present our isolation method for the architectures to distinguish the location of the faulty spacecraft and the faulty actuator.

2.4. CONCLUSION

In this chapter, attitude dynamics of the spacecraft is discussed and the formation control strategies developed in the literature is introduced briefly. Furthermore, the virtual structure formation control method is explained completely which is used as our formation control method in the simulations. The concept of fault, different types of actuator faults, and the fault modeling in attitude control system of the spacecraft is explained. The fault diagnosis methods proposed in the literature are introduced with a complete investigation on Kalman filter and extended Kalman filter concepts. Finally, fault detection and isolation problem in spacecraft formation flying are described which will be discussed further in the next chapters.

Chapter 3: FAULT DETECTION IN A FORMATION FLIGHT MISSION

In this chapter, the implementation of the extended Kalman filter (EKF) on spacecraft attitude model is explored. Finally, we propose our own architectures of the EKF for fault detection in formation flight of spacecraft. At the end of the chapter, the simulation results obtained by implementing the fault detection architectures on formation flight of spacecraft are presented and discussed.

3.1. GRAPH BASED FORMATION FLIGHT MODELLING

In order to formulate the problem, we describe the formation flight model by using the graph-based modeling for networked systems. First, some basic definitions and concepts in graph theory are presented and then we apply them to express the graph model for the formation flight.

3.1.1. Basic Concepts and Notations in Graph Theory

Graph G is defined with its nodes and edges that are represented respectively with $V=\{1,...,N\}$ and $E\subset V\times V$ [107]. Then $V(G)$ is the node set and $E(G)$ is the edge set of graph G. In order to display a graph, the nodes are shown with nodes and the edges are shown with lines. For example, Figure 3.1 shows a graph on $V=\{1,2,3,4\}$ with the edges $E=\{(1,2),(1,3),(1,4),(2,3),(2,4)\}$.

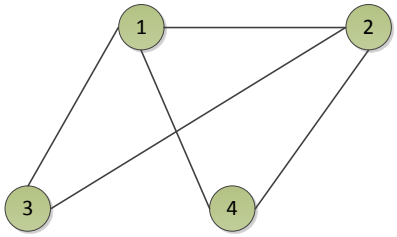

Figure 3.1 Graph G with nodes $V=\{1,2,3,4\}$ and edges $E=\{(1,2),(1,3),(1,4),(2,3),(2,4)\}$.

The number of nodes of a graph is called its *order* and the number of edges is called *degree* which are shown respectively with $|V(G)|$ and $|E(G)|$.

Two nodes i and j are called *neighbors* or *adjacent* if $(i,j)\subset E(G)$ and this neighborhood is shown with notation $i\sim$. The neighbor set of node i is shown with $N_G(i)=\{j\in V(G)\,|\,j\sim$. The number of neighbors of a node is called its *degree*. The *adjacency* matrix of a graph with order N is an $N\times N$ matrix which is defined by

$$\left[A(G)\right]_{ij}=\begin{cases}1 & \text{if } ij\in E(G)\\ 0 & \text{otherwise}\end{cases} \tag{3.1}$$

As an example, the adjacency matrix for the graph G shown in Figure 3.1 is given by

$$A(G)=\begin{bmatrix}0&1&1&1\\1&0&1&1\\1&1&0&0\\1&1&0&0\end{bmatrix} \tag{3.2}$$

By using the definitions and notations introduced above, we are able to model a formation flight with a graph. The spacecraft are denoted with nodes and the inter-agent communication links are denoted by edges.

3.2. MODELLING THE FORMATION FLIGHT OF SPACECRAFT

In this section, the problem of fault detection in a formation flight of N spacecraft is formalized.

The formation of N spacecraft can be described by a graph with N interconnected nodes. This graph is denoted by $S(V,E)$, where $V \triangleq$ is the vertex set, and $E \subset V \times V$ is the set of m edges. If there is a communication link between vertices i and j, and vertex i send information to vertex j or vice versa, then the pair (i,j) shows the edge incident on vertices i and j. Furthermore, $N_i = \{ j \in V(S) \mid j \sim$ is the neighborhood set of vertex i, and $\bar{N}_i = N_i \cup$.

It is assumed that each spacecraft dynamics is governed by the following nonlinear model

$$\therefore \qquad x_i(t)) + Bu_i(t) \tag{3.3}$$

where $x_i \in R^6$ is the state of the i-th spacecraft, $f(x_i(t)) \in R^6$ is the dynamic model of the i-th spacecraft which has been explained in Section 2.1, and $u_i \in R^3$ is the input signal of the i-th spacecraft which is given by

$$u_i = \{ g(x_i, x_j) : j \in N_i \} \tag{3.4}$$

where $g(x_i, x_j)$ is the control function to calculate the control input of the i-th spacecraft, $x_i \in R^6$ is the state of the i-th spacecraft, $x_j \in R^6$ is the state of the j-th spacecraft, and N_i is the neighboring set of spacecraft # i . The above equation conveys this meaning that the control input of a spacecraft in the formation flight is not only

dependent on its own states, but it is also dependent on the state information of the neighboring spacecraft.

In presence of an actuator fault, equation (3.3) can be remodeled as

$$\therefore \qquad x_i(t)) + B(I - \Gamma_i)u_i(t) \tag{3.5}$$

where Γ_i is the effectiveness factor of spacecraft $\#i$. For a spacecraft with three control channels, the effectiveness factor is given by $\Gamma_i = diag(\gamma_{ik})$ where $0 \le \gamma_{ik} < 1$, $k = 1,2,3$ represents the partial loss in the torque effectiveness of axis k of spacecraft $\#i$.

By expanding the effectiveness factor Γ_i, equation (3.5) can be rewritten as

$$\therefore \qquad x_i(t)) + Bu_i(t) - \sum_{k=1}^{3} b_k \gamma_{ik} u_{ik}(t) \tag{3.6}$$

In order to model a fault in the k-th actuator of spacecraft $\#i$, b_k is chosen as the k-th column of matrix B, γ_{ik} is the partial loss in the torque effectiveness of axis k of spacecraft $\#i$, and $u_{ik}(t)$ is the control signal for the k-th actuator of spacecraft $\#i$. Matrix B is assumed to be a full column rank matrix.

Defining $\rho_{ik}(t) = -\gamma_{ik} u_{ik}(t)$ as the actuator fault mode with dimension three, equation (3.6) can be rewritten as

$$\therefore \qquad x_i(t)) + Bu_i(t) + \sum_{k=1}^{3} b_k \rho_{ik}(t) \tag{3.7}$$

Each spacecraft has the following state measurements

$$y_i(t) = Cx_i(t) \tag{3.8}$$

where C is defined based on the output measurements that has been chosen. For attitude measurement it is defined by

$$C = \begin{bmatrix} 1 & 0 & 0 & 0 & 0 & 0 \\ 0 & 1 & 0 & 0 & 0 & 0 \\ 0 & 0 & 1 & 0 & 0 & 0 \end{bmatrix} \tag{3.9}$$

and in the case of angular velocity measurement it can be written as

$$C = \begin{bmatrix} 0 & 0 & 0 & 1 & 0 & 0 \\ 0 & 0 & 0 & 0 & 1 & 0 \\ 0 & 0 & 0 & 0 & 0 & 1 \end{bmatrix}. \tag{3.10}$$

3.3. ARCHITECTURES FOR FAULT DETECTION OF ACTUATOR FAULTS IN FORMATION FLIGHT OF SPACECRAFT

Occurrence of a fault in the actuator of a spacecraft in the formation not only affects the performance of the faulty spacecraft, but also disturbs the dynamic behavior of its neighboring spacecraft. Due to the control signal $u_i = \left\{ g\left(x_i, x_j\right) : j \in N_i \right\}$, the effect of fault in spacecraft $\#\, j$ can impact spacecraft $\#\, i$ and affect its dynamical behavior. The degree of this effect is dependent on the control function $g\left(x_i, x_j\right)$ and is not the same for different control topologies. This effect can be utilized in detection of low severity faults which are not detectable by using standard fault detection (FD) methods. Therefore, fault detection in formation flight has new challenges and needs new solutions.

Based on the possible information transfer among the FD units of spacecraft, three FD architectures are defined: centralized architecture, decentralized architecture, and

semi-decentralized architecture.

3.3.1. Decentralized Architecture

In decentralized architecture, shown in Figure 3.2, each spacecraft has its own FD unit and there is no communication among the spacecraft for the purpose of fault detection. Therefore, spacecraft $\#i$ detects the actuator faults which exist in the formation only based on the information of its own output y_i and control signal u_i. The system for this architecture has the following representation

$$\begin{aligned} \because \quad & x_i(t)) + Bu_i(t) + \sum_{k=1}^{3} b_k \rho_{ik}(t) \\ & y_i(t) = Cx_i(t) \end{aligned} \tag{3.11}$$

The state $x_i \in R^6$, the output $y_i \in R^3$, the control input $u_i \in R^3$, the dynamic model $f(x_i)$, the control input matrix B, the output matrix C, and the actuator fault mode $\rho_{ik} = -\gamma_{ik} u_{ik}$ describe the mathematical model for decentralized architecture of spacecraft $\#i$. The vector b_k is the k-th column of control input matrix B.

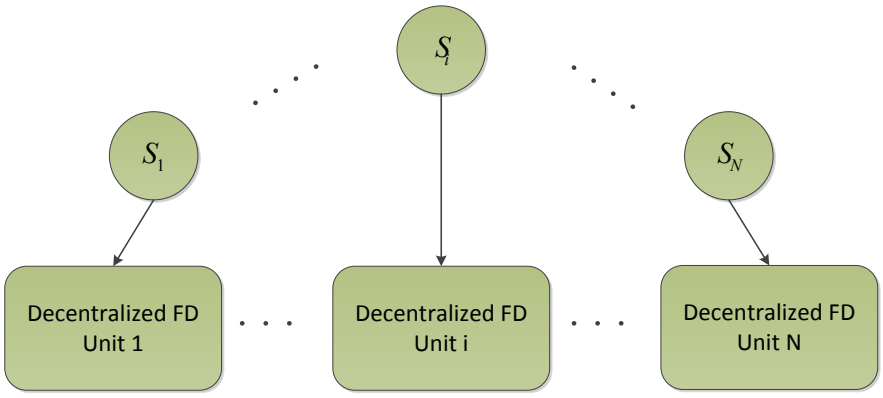

Figure 3.2 Decentralized FD architecture.

3.3.2. Semi-Decentralized Architecture

In the semi-decentralized architecture, the FD unit for each spacecraft receives the output measurement and control input information of its neighboring spacecraft. This information gives the FD unit the capability to detect and isolate the actuator faults of its neighboring spacecraft not only based on the effect of $u_i = \left\{ g\left(x_i, x_j\right) : j \in N_i \right\}$, but also by using the direct output measurement and control signal information received from them.

The neighbor set of spacecraft $\#i$ is shown with $N_i = \left\{ j \in V\left(S\right) \mid j \sim \right.$. The set that includes spacecraft $\#i$ is denoted by $\bar{N}_i = N_i \bigcup$, and the notation $\left|\bar{N}_i\right|$ symbolizes the number of spacecraft in this set.

The system for semi-decentralized architecture has the following representation

$$\begin{aligned} &\dot{x}_{\bar{N}_i} = \left(x_{\bar{N}_i}\right) + B^{|\bar{N}_i|} u_{\bar{N}_i}\left(t\right) + \sum_{k=1}^{|\bar{N}_i|} \sum_{j=1}^{3} \bar{b}_{kj} \rho_{kj} \\ &y_{\bar{N}_i}\left(t\right) = C^{|\bar{N}_i|} x_{\bar{N}_i}\left(t\right) \end{aligned} \tag{3.12}$$

where $B^{|\bar{N}_i|} = I^{|\bar{N}_i|} \otimes B$, $C^{|\bar{N}_i|} = I^{|\bar{N}_i|} \otimes C$, $\otimes$ denotes the Kronecker product, $I^{|\bar{N}_i|}$ is an $\left|\bar{N}_i\right| \times \left|\bar{N}_i\right|$ identity matrix, and $\bar{b}_{kj}$ is the $\left(k-1\right)\times 3 + j$-th column of $B^{|\bar{N}_i|}$, and

$$x = \begin{bmatrix} x_1 \\ \vdots \\ x_{\bar{N}_i} \end{bmatrix} \qquad \begin{bmatrix} f\left(x_1\right) \\ \vdots \\ f\left(x_{\bar{N}_i}\right) \end{bmatrix}$$

$$u = \begin{bmatrix} u_1 \\ \vdots \\ u_{\bar{N}_i} \end{bmatrix} \qquad \begin{bmatrix} y_1 \\ \vdots \\ y_{\bar{N}_i} \end{bmatrix}$$

For each formation control problem the semi-decentralized architecture has different presentation. In Figure 3.3, we use a specific example to display connections among the assumed neighboring spacecraft and then show the semi-decentralized architecture for this example.

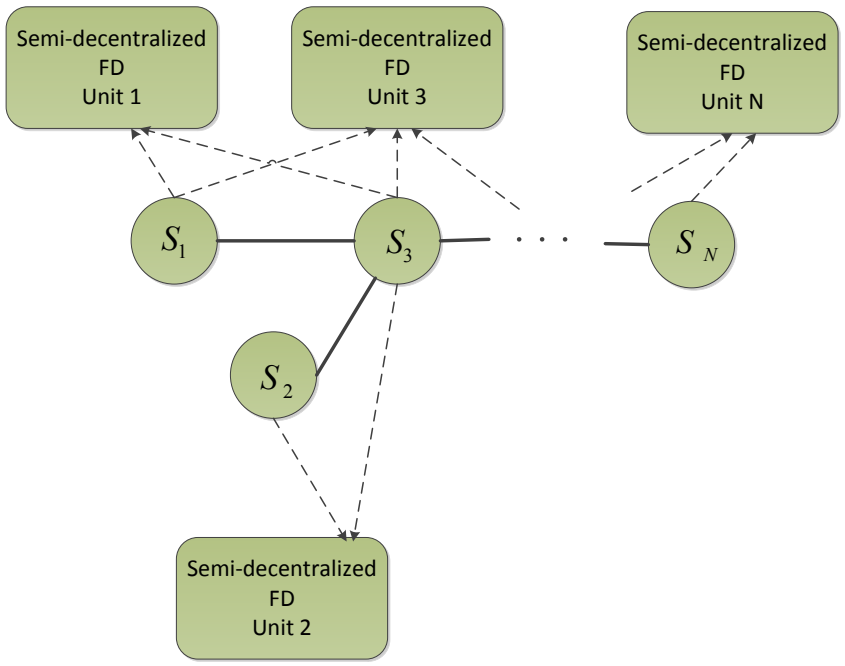

Figure 3.3 Semi-decentralized FD architecture.

3.3.3. Centralized Architecture

In the centralized architecture, one FD center is considered for the fault detection and isolation of the whole formation. All spacecraft send their state and control input information to this FD center, as shown in Figure 3.4. Considering a formation with N

spacecraft, the system for the centralized architecture has the following representation

$$\begin{aligned} \dot{x} &= f(x) + B^N u(t) + \sum_{i=1}^{N}\sum_{k=1}^{3} \bar{b}_{ik}\rho_{ik} \\ z(t) &= C^N x(t) \end{aligned} \tag{3.13}$$

where $B^N = I^N \otimes B$, $C^N = I^N \otimes C$, and $\otimes$ denotes the Kronecker product, I^N is an $N \times N$ identity matrix, and $\bar{b}_{ik}$ is the $(i-1)\times 3 + k$-th column of B^N, and

$$x = \begin{bmatrix} x_1 \\ \vdots \\ x_N \end{bmatrix} \qquad \begin{bmatrix} f(x_1) \\ \vdots \\ f(x_N) \end{bmatrix}$$

$$u = \begin{bmatrix} u_1 \\ \vdots \\ u_N \end{bmatrix} \qquad \begin{bmatrix} y_1 \\ \vdots \\ y_N \end{bmatrix}$$

The state $x_i \in R^6$, the output $y_i \in R^3$, the control input $u_i \in R^3$, and the dynamic model $f(x_i)$, with $i = 1, \ldots$ denotes the information received from the i-th spacecraft in a formation with N spacecraft.

The actuator fault mode $\rho_{ik} = -\gamma_{ik} u_{ik}$ shows reduction of torque effectiveness in the k-th actuator of the i-th spacecraft, where u_{ik} is the k-th entry of u_i and γ_{ik} is the partial loss in the torque effectiveness of axis k of spacecraft $\# i$.

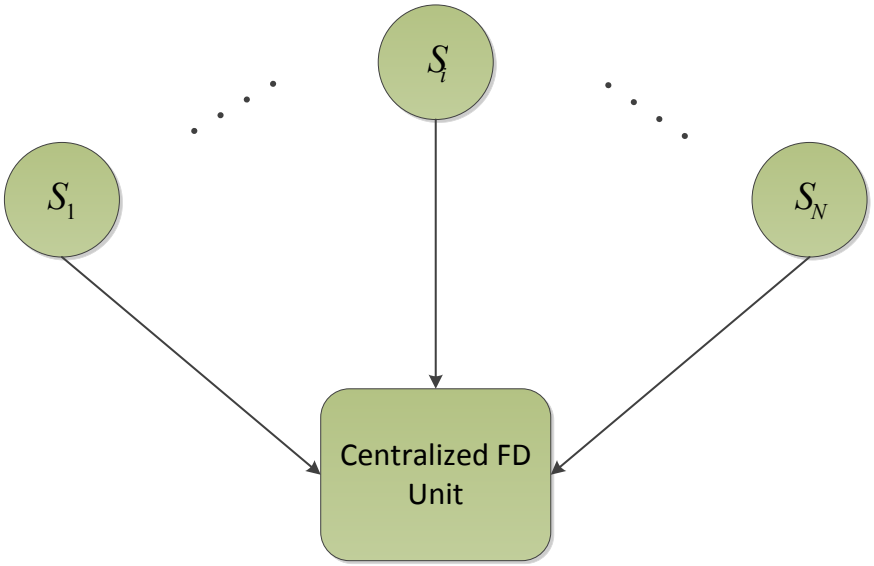

Figure 3.4 Centralized FD architecture.

In the centralized architecture, the FD unit is able to detect and isolate the actuator faults of a spacecraft in the formation based on the output measurement and control input signal received of that spacecraft.

3.4. Fault Detection in Formation Flight

Model-based fault detection techniques can be categorized to three main groups: process identification, parity equation, and state estimation methods. Extended Kalman filter, which is a version of Kalman filter, is one of the state estimation methods for FD of nonlinear systems. In this method, Jacobian matrices linearize the nonlinear function around the current estimate at each time step, and then these linearized matrices are used in the Kalman Filter equations.

Discrete-time extended Kalman Filter, continuous-time extended Kalman filter, and continuous-discrete extended Kalman filter, are three different descriptions of EKF.

Our model for spacecraft attitude dynamics is continuous-time, and therefore, we use the continuous-time EKF to estimate the states of the system.

3.4.1. Extended Kalman Filter for Decentralized Architecture

Considering the decentralized architecture described in Section 3.3.1, N fault detection units are constructed to detect the actuator faults for all spacecraft. Assume the following system as the decentralized architecture for spacecraft formation in the presence of additive noise

$$\begin{aligned} \dot{} \quad & x_i(t)) + Bu_i(t) + \sum_{j=1}^{3} b_j \rho_{ij}(t) + w_i(t) \\ y_i(t) &= Cx_i(t) + v_i(t) \end{aligned} \tag{3.14}$$

where $w_i(t) \in \Re^6$ and $v_i(t) \in \Re^3$ are white Gaussian noise with covariance matrices $Q^i(t) \in \Re^{6\times 6}$ and $R^i(t) \in \Re^{3\times 3}$, respectively.

3.4.1.1. STATE ESTIMATION

Predict and update equations for the continuous-time extended Kalman filtering of a decentralized architecture are described by the following equations.

Updated State Estimate:

$$\dot{} \quad \hat{x}_i(t)) + Bu_i(t) + K^i(t)(y_i(t) - C\hat{x}_i(t)) \tag{3.15}$$

Differential Riccati Equation:

$$\dot{} \quad (t)P^i(t) + P^i(t)\left(F^i(t)\right)^T - P^i(t)C^T(t)\left(R^i(t)\right)^{-1} C(t)P^i(t) + Q^i(t) \tag{3.16}$$

Kalman Gain:

$$K^i(t) = P^i(t)C(t)^T \left(R^i(t)\right)^{-1} \tag{3.17}$$

where the observation matrix $F(t)$ is defined by following Jacobian

$$F^i(t) = \frac{\partial f}{\partial x}|_{\hat{x}_i(t),u_i(t)} \tag{3.18}$$

The initial state $\hat{x}_i(t_0)$ is a random vector with known mean $\mu_i(t_0) = E\left[x_i(t_0)\right]$ and covariance $P^i(t_0) = E\left[\left(x_i(t_0) - \mu_i(t_0)\right)\left(x_i(t_0) - \mu_i(t_0)\right)^T\right]$.

3.4.1.2. RESIDUAL GENERATION

By applying the decentralized EKF estimator to the system (3.14), estimated state vector $\hat{x}_i$ is obtained. The residual $e_i(t) = y_i(t) - C\hat{x}_i(t)$ is the difference between the actual outputs and estimated outputs of the i-th spacecraft. The residual vector $e_i(t)$ is a vector with three residuals:

$$e_i(t) = \begin{bmatrix} e_{i1}(t) \\ e_{i2}(t) \\ e_{i3}(t) \end{bmatrix} \tag{3.19}$$

For the spacecraft system with attitude measurement, the residual $e_i(t)$ is given by

$$e_i(t) = \tilde{\ } \qquad t) - \hat{q}_i(t) \tag{3.20}$$

$$e_{ij}(t)|_{j=1,2,3} = \tilde{\ } \qquad (t) - \hat{q}_{ij}(t) \tag{3.21}$$

and for the spacecraft system with angular velocity measurement, the residual $e_i(t)$ is

given by

$$e_i(t) = \tilde{\iota} \qquad (t) - \hat{\omega}_i(t) \tag{3.22}$$

$$e_{ij}(t)|_{j=1:3} = \tilde{\iota} \qquad (t) - \hat{\omega}_{ij}(t) \tag{3.23}$$

The norm of the residual vector of spacecraft in the decentralized architecture is chosen as the residual evaluation function vector $J_i(t)$ according to

$$J_i(t) = \begin{bmatrix} J_{i1}(t) \\ J_{i2}(t) \\ J_{i3}(t) \end{bmatrix} = \begin{bmatrix} |e_{i1}(t)| \\ |e_{i2}(t)| \\ |e_{i3}(t)| \end{bmatrix} \tag{3.24}$$

where $J_{ij}(t)$, $i \in 1:N$ and $j \in 1:3$, is the j-th residual evaluation function of the i-th spacecraft.

A fault in the i-th spacecraft can be detected by comparing the mean value of the residual evaluation function J_{ij}, namely d_{ij}, with a threshold function T_{ij}. According to the test given below, if d_{ij} surpasses the threshold, the occurrence of fault is declared in one of the actuators of spacecraft $\#i$:

$$\begin{aligned} d_{ij}(m) &\le T_{ij} \quad \text{if} \quad \{\rho_{ij}(m) = 0 |\ j \in 1,2,3\} \\ d_{ij}(m) &> T_{ij} \quad \text{if} \quad \{\rho_{ij}(m) \neq 0 |\ j \in 1,2,3\} \end{aligned} \tag{3.25}$$

The mean value of the residual evaluation function over the time window length of M can be obtained by using the following equation:

$$d_{ij}(m) = \frac{1}{M} \sum_{n=m-M+1}^{m} J_{ij}(n) \tag{3.26}$$

where m is the sample number, and M is the window length. The value for the window length M, and the decision threshold T_{ij} must be determined in such a way that a trade-off is made between the probability of false alarm and the probability of missed alarm.

3.4.1.3. THRESHOLD SELECTION

The residual is different from zero even when no fault occurs. Then a threshold must be used in the residual evaluation stage. The threshold is selected as the sum of the mean and standard deviation of the norm of the residual evaluation function.

By considering the worst case analysis of the residual evaluation functions corresponding to the healthy operation of the satellites that are subject to the measurement noise, the threshold for the j-th residual evaluation function of the i-th decentralized FD unit is defined by

$$T_{ij} = mean\left(\left|J_{ij}(t)\right|\right) + \sqrt{\mathrm{var}\left(J_{ij}(t)\right)} \tag{3.27}$$

3.4.2. Extended Kalman Filter for Semi-Decentralized Architecture

For a semi-decentralized architecture as described in Section 3.3.2, with N spacecraft in the formation, it is assumed that each vehicle has an FD unit and local communication links between each spacecraft and its neighbors. In this architecture, the dimension of FD unit is different for each spacecraft, because it is dependent on the number of neighbors of that spacecraft. Assuming the following system in the presence of additive noise

$$\dot{x}(t) = A^N x(t) + B^N u(t) + \sum_{i=1}^{N} \sum_{j=1}^{3} \bar{b}_{ij} \rho_{ij} + w(t)$$
$$y(t) = C^N x(t) + v(t) \tag{3.28}$$

where i is the spacecraft's number, $w_{\bar{N}_i}(t) \in \Re^{6|\bar{N}_i|}$ and $v_{\bar{N}_i}(t) \in \Re^{3|\bar{N}_i|}$ are white Gaussian noise with covariance matrices $Q(t) \in \Re^{6|\bar{N}_i| \times 6|\bar{N}_i|}$ and $R(t) \in \Re^{3|\bar{N}_i| \times 3|\bar{N}_i|}$, respectively.

3.4.2.1. STATE ESTIMATION

Predict and update equations for the continuous-time extended Kalman filtering of semi-decentralized architecture are described by the following equations.

Updated State Estimate:

$$\dot{\hat{x}}_{\bar{N}_i}(t) = A^{|\bar{N}_i|} \hat{x}_{\bar{N}_i}(t) + B^{|\bar{N}_i|} u_{\bar{N}_i}(t) + K^{|\bar{N}_i|}(t)(y_{\bar{N}_i}(t) - C^{|\bar{N}_i|} \hat{x}_{\bar{N}_i}(t)) \tag{3.29}$$

Differential Riccati Equation:

$$\dot{P}^{|\bar{N}_i|}(t) = A^{|\bar{N}_i|}(t) P^{|\bar{N}_i|}(t) + P^{|\bar{N}_i|}(t) \left(F^{|\bar{N}_i|}(t)\right)^T - P^{|\bar{N}_i|}(t) \left(C^{|\bar{N}_i|}(t)\right)^T \left(R(t)\right)^{-1} C^{|\bar{N}_i|}(t) P^{|\bar{N}_i|}(t) + Q(t) \tag{3.30}$$

Kalman Gain:

$$K^{|\bar{N}_i|}(t) = P^{|\bar{N}_i|}(t) \left(F^{|\bar{N}_i|}\right)^T (t) R^{-1}(t) \tag{3.31}$$

where the observation matrix $F^{|\bar{N}_i|}(t)$ is defined by the following Jacobian

$$F^{|\bar{N}_i|}(t) = \frac{\partial f}{\partial x} |_{\hat{x}_{\bar{N}_i}(t), u_{\bar{N}_i}(t)} \tag{3.32}$$

The initial state $\hat{x}_{\bar{N}_i}(t_0)$ is a random vector with known mean $\mu_{\bar{N}_i}(t_0) = E\left[x_{\bar{N}_i}(t_0)\right]$ and covariance $P^{|\bar{N}_i|}(t_0) = E\left[\left(x_{\bar{N}_i}(t_0) - \mu_i(t_0)\right)\left(x_{\bar{N}_i}(t_0) - \mu_i(t_0)\right)^T\right]$.

3.4.2.2. RESIDUAL GENERATION

By applying the semi-decentralized EKF estimator to the system (3.28), estimated state vector $\hat{x}_{\bar{N}_i}$ is obtained. The residual $e_{\bar{N}_i}(t) = y_{\bar{N}_i}(t) - C^{|\bar{N}_i|}\hat{x}_{\bar{N}_i}(t)$ is a comparison between the actual outputs and estimated outputs. The residual vector $e(t)$ is a vector with $3\times|\bar{N}_i|$ residuals that includes $|\bar{N}_i|$ vectors of $e_{l,\bar{N}_i}(t) \in R^3$, where $l = 1$ indicates the i-th spacecraft and $l \in \{2,\ldots$ indicates the neighbor spacecraft as follows

$$e_{\bar{N}_i}(t) = \begin{bmatrix} e_{1,\bar{N}_i}(t) \\ \vdots \\ e_{|\bar{N}_i|,\bar{N}_i}(t) \end{bmatrix} \tag{3.33}$$

$$e_{l,\bar{N}_i}{}^T(t) = \begin{bmatrix} e_{l,\bar{N}_i,1}(t) \\ e_{l,\bar{N}_i,2}(t) \\ e_{l,\bar{N}_i,3}(t) \end{bmatrix} \tag{3.34}$$

The residual $e_{l,\bar{N}_i,j}(t)$ is the difference between the actual output and estimation output for the j-th actuator of the l-th spacecraft which belongs to $\bar{N}_i$, the neighborhood set of spacecraft $\#i$.

For the spacecraft system with attitude measurement, the residual $e_k(t)$ is given by

$$e_{l,\bar{N}_i}(t)|_{l=1,\ldots} \quad -\tilde{\iota} \qquad {}_{l,\bar{N}_i}(t)-\hat{q}_{l,\bar{N}_i}(t) \tag{3.35}$$

$$e_{l,\bar{N}_i,j}(t)|_{j=1:3}^{l=1:|N_i|}=\tilde{\iota} \qquad q_{l,\bar{N}_i,j}(t)-\hat{q}_{l,\bar{N}_i,j}(t) \tag{3.36}$$

and for the spacecraft system with angular velocity measurement, the residual $e_{l,\bar{N}_i}(t)$ is given by

$$e_{l,\bar{N}_i}(t)|_{l=1,\ldots} \quad -\tilde{\iota} \qquad \upsilon_{l,\bar{N}_i}(t)-\hat{\omega}_{l,\bar{N}_i}(t) \tag{3.37}$$

$$e_{l,\bar{N}_i,j}(t)|_{j=1:3}^{l=1:|N_i|}=\tilde{\iota} \qquad \omega_{l,\bar{N}_i,j}(t)-\hat{\omega}_{l,\bar{N}_i,j}(t) \tag{3.38}$$

In order to detect the fault in the formation level by using the threshold testing, first, matrix $J^i(t)\in R^{|N_i|\times 3}$ is defined. Each array of $J^i(t)$ is computed as the norm of the difference between the residual of spacecraft $\#i$, $e_{1,\bar{N}_i,j}$, and the residual of its nearest neighbor spacecraft, $e_{l.\bar{N}_i,j}$, where $l\in\{2,\ldots$.

The kj-th array of matrix $J^i(t)$ is defined by

$$J^i_{kj}(t)=\left|e_{l,|\bar{N}_i|,j}-e_{1,|\bar{N}_i|,j}\right| \tag{3.39}$$

where $k=l-1$.

The k-th row of matrix $J^i(t)$ can be written as

$$\left(J^i_k\right)^T(t)=\begin{Vmatrix}\left|e_{l,|\bar{N}_i|,1}-e_{1,|\bar{N}_i|,1}\right|\\ \left|e_{l,|\bar{N}_i|,2}-e_{1,|\bar{N}_i|,2}\right|\\ \left|e_{l,|\bar{N}_i|,3}-e_{1,|\bar{N}_i|,3}\right|\end{Vmatrix} \tag{3.40}$$

Now, we define the residual $S^i(t)$ which is the sum of the rows of $J^i(t)$ as follows

$$S^i(t) = \sum_{k=1}^{|\bar{N}_i|-1} J_k^i(t) = \begin{bmatrix} S_1^i(t) \\ S_2^i(t) \\ S_3^i(t) \end{bmatrix} \tag{3.41}$$

A fault can be detected by comparing the elements of the residual evaluation function with threshold functions $T_j^i(t)$ according to the residual evaluation test given below:

$$\begin{aligned} d_j^i(m) &\le T_j^i \quad \text{for} \quad \{\rho_{lj}(t) = 0 | l \in \bar{N}_i,\ j \in 1,\dots \\ d_j^i(m) &> T_j^i \quad \text{for} \quad \{\rho_{lj}(t) \neq 0 | l \in \bar{N}_i,\ j \in 1,\dots \end{aligned} \tag{3.42}$$

where

$$d_j^i(m) = \frac{1}{M} \sum_{n=m-M+1}^{m} S_j^i(n) \tag{3.43}$$

where n is the sample number and M is the window length.

This test implies that if one of the elements of the residual evaluation function becomes greater than the threshold T_j^i, a fault has occurred in the formation.

3.4.2.3. THRESHOLD SELECTION

The threshold is selected as the sum of the mean and standard deviation of the norm of residual evaluation function. By considering the worst case analysis of the residual evaluation functions corresponding to the healthy operation of the satellites that are subject to the measurement noise, the thresholds for semi-decentralized

architecture are defined by

$$T_j^i = mean\left(\left|S_j^i(n)\right|\right) + \sqrt{\text{var}\left(S_j^i(n)\right)} \tag{3.44}$$

3.4.3. Extended Kalman Filter for Centralized Architecture

Considering the centralized architecture as described in Section 3.3.3, one fault detection center is constructed to detect the actuator faults of all spacecraft in the formation. Assume the following system as the centralized architecture for spacecraft formation in the presence of additive noise

$$\begin{aligned} \dot{x}(t) &= \quad c) + B^N u(t) + \sum_{i=1}^{N}\sum_{j=1}^{3} \bar{b}_{ij}\rho_{ij} + w(t) \\ y(t) &= C^N x(t) + v(t) \end{aligned} \tag{3.45}$$

where $w(t) \in \Re^{6N}$ and $v(t) \in \Re^{3N}$ are white Gaussian noise with covariance matrices $Q(t) \in \Re^{6N\times 6N}$ and $R(t) \in \Re^{3N\times 3N}$, respectively.

3.4.3.1. STATE ESTIMATION

Predict and update equations for the continuous-time extended Kalman filtering of a centralized architecture are described by the following equations.

Updated State Estimate:

$$\dot{\hat{x}}(t) = \quad \hat{x}(t)) + B^N u(t) + K^N(t)(y(t) - C^N \hat{x}(t)) \tag{3.46}$$

Differential Riccati Equation:

$$\dot{P}(t) = \quad {}^{N}(t)P^N(t) + P^N(t)\left(F^N(t)\right)^T - P^N(t)\left(C^N\right)^T(t)R^{-1}(t)C^N(t)P^N(t) + Q(t) \tag{3.47}$$

Kalman Gain:

$$K^N(t) = P^N(t)\left(C^N(t)\right)^T R^{-1}(t) \tag{3.48}$$

where the observation matrix $F(t)$ is defined by the following Jacobian

$$F^N(t) = \frac{\partial f}{\partial x}|_{\hat{x}(t),u(t)} \tag{3.49}$$

The initial state $\hat{x}(t_0)$ is a random vector with known mean $\mu(t_0) = E\left[x(t_0)\right]$ and covariance $P^N(t_0) = E\left[\left(x(t_0) - \mu(t_0)\right)\left(x(t_0) - \mu(t_0)\right)^T\right]$.

3.4.3.2. RESIDUAL GENERATION

By applying the centralized EKF estimator to the integrated system of spacecraft 0, the estimated state vector $\hat{x}(t)$ is obtained. The residual $e(t) = y(t) - C^N\hat{x}(t)$ is a comparison between the actual outputs and estimated outputs. The residual matrix $e(t)$ is a $N \times 3$ matrix that includes N vectors of $e_i(t) \in R^3$, where $i \in 1,\ldots$ is the number of spacecraft.

$$e(t) = \begin{bmatrix} e_1(t) \\ \vdots \\ e_N(t) \end{bmatrix} \tag{3.50}$$

$$e_i^T(t) = \begin{bmatrix} e_{i1}(t) \\ e_{i2}(t) \\ e_{i3}(t) \end{bmatrix} \tag{3.51}$$

The residual entry e_{ij} is the difference between the estimation and actual output

for the j-th output of the i-th spacecraft.

For the spacecraft system with attitude measurement, the residual $e_i(t)$ is given by

$$e_i(t)|_{i=1,\ldots} \quad \tilde{} \quad t) - \hat{q}_i(t) \tag{3.52}$$

$$e_{ij}(t)|_{j=1:3}^{i=1:N} = \tilde{} \quad (t) - \hat{q}_{ij}(t) \tag{3.53}$$

and for the spacecraft system with angular velocity measurement, the residual $e_i(t)$ is given by

$$e_i(t)|_{i=1,\ldots} \quad \tilde{} \quad (t) - \hat{\omega}_i(t) \tag{3.54}$$

$$e_{ij}(t)|_{j=1:3}^{i=1:N} = \tilde{} \quad (t) - \hat{\omega}_{ij}(t) \tag{3.55}$$

In order to detect the fault in the formation level by using the threshold testing, first, a matrix $J(t) \in R^{(N-1)\times 3}$ is defined where $N-1$ is the number of the communication links among the centralized spacecraft and other spacecraft in the formation. Norm of the difference between the residual of the centralized spacecraft and the residual of other spacecraft in the formation generates the matrix $J(t)$.

The kj-th array of $J(t)$ is the norm of the difference between the j-th residual of the $(k+1)$-th spacecraft, $k \in \{1,\ldots$, and the j-th residual of the centralized spacecraft (spacecraft #1).

$$J_{kj}(t) = \left| e_{1j} - e_{(k+1)j} \right| \tag{3.56}$$

The k-th row of $J(t)$ can be written as

$$J_k^T(t) = \begin{bmatrix} J_{k1}(t) \\ J_{k2}(t) \\ J_{k3}(t) \end{bmatrix} = \begin{bmatrix} |e_{11} - e_{k1}| \\ |e_{12} - e_{k2}| \\ |e_{13} - e_{k3}| \end{bmatrix} \tag{3.57}$$

Now, we define the residual $S(t)$ which is the sum of the rows of $J(t)$ as follows

$$S(t) = \sum_{k=1}^{N-1} J_k(t) = \begin{bmatrix} S_1(t) \\ S_2(t) \\ S_3(t) \end{bmatrix} \tag{3.58}$$

A fault in the formation can be detected by comparing the mean value of the residual evaluation function S_j, namely d_j, with a threshold function T_j. According to the test given below, if d_j surpasses the threshold, the occurrence of fault is declared in an actuator of one of the spacecraft in the formation:

$$\begin{aligned} d_j(m) \le T_j \quad & if \quad \{\rho_{ij}(t) = 0 | i \in 1, \ldots \quad \ldots \\ d_j(m) > T_j \quad & if \quad \{\rho_{ij}(t) \neq 0 | i \in 1, \ldots \quad \ldots \end{aligned} \tag{3.59}$$

The mean value of the residual evaluation function over the time window length of M can be obtained by using the following equation:

$$d_j(m) = \frac{1}{M} \sum_{n=m-M+1}^{m} S_j(n) \tag{3.60}$$

where n is the sample number, and M is the window length. The value for the window length M, and the decision threshold T_j must be made in such a way that a trade-off is made between the probability of false alarm and the probability of missed alarm.

3.4.3.3. THRESHOLD SELECTION

The threshold is selected as the sum of the mean and standard deviation of the norm of the residual evaluation function. By considering the worst case analysis of the residual evaluation functions corresponding to the healthy operation of the satellites that are subject to the measurement noise, the thresholds in centralized architecture are defined by

$$T_j = mean\left(\left|S_j(n)\right|\right) + \sqrt{\mathrm{var}\left(S_j(n)\right)} \tag{3.61}$$

3.4.4. Stochastic Stability of the Architectures

Reif et al. in [98] proposed the conditions for stochastic stability of continuous-time extended Kalman filter. Based on their work, in this section, the conditions for stochastic stability of decentralized, centralized, and semi decentralized extended Kalman filters are investigated.

3.4.4.1. STOCHASTIC STABILITY OF DECENTRALIZED KALMAN FILTER

Consider the nonlinear stochastic decentralized architecture (3.14) and the decentralized extended Kalman filter as in Section 3.4.1.1.

In this thesis, we will refer to the following assumptions as the general assumptions [98].

1. There are positive real numbers $\bar{a}, \bar{q}, \bar{r} > 0$ such that the following bounds on various matrices are fulfilled for every $t \geq 0$, that is

$$\left\| F^i(t) \right\| \le \bar{a} \tag{3.62}$$

$$\bar{q}I \le Q^i(t) \tag{3.63}$$

$$\bar{r}I \le R^i(t) \tag{3.64}$$

2. There are positive real numbers $\varepsilon_\phi, \kappa_\phi > 0$ such that the nonlinear function ϕ which is the remaining term of the Taylor expansion,

$$f\left(x_i(t)\right) - f\left(\hat{x}_i(t)\right) = F^i(t)\left[x_i(t) - \hat{x}_i(t)\right] + \phi\left[x_i(t), \hat{x}_i(t)\right] \tag{3.65}$$

is bounded via

$$\left\| \phi\left(x_i, \hat{x}_i\right) \right\| \le \kappa_\phi \left\| x_i - \hat{x}_i \right\|^2 \text{ with } \left\| x_i - \hat{x}_i \right\| \le \varepsilon_\phi \tag{3.66}$$

3. $F^i(t)$ is non-singular for every $t \ge 0$.

4. There exist real constants $p, \bar{p}$ such that

$$pI \le P^i(t) \le \bar{p}I \tag{3.67}$$

Then it can be shown that along the same lines as those invoked in [98], for some $\delta, \varepsilon > 0$ the initial estimation error satisfies

$$\left\| e_i(0) \right\| \le \varepsilon \tag{3.68}$$

and the covariance matrices are bounded via

$$Q^i(t) \le \delta I \tag{3.69}$$

$$R^i(t) \le \delta I \tag{3.70}$$

Then the estimation error $e_i(t)$ given by

$$e_i(t) = y_i(t) - C\hat{x}_i(t) \tag{3.71}$$

is exponentially bounded with the probability one.

3.4.4.2. STOCHASTIC STABILITY OF SEMI-DCENTRALIZED KALMAN FILTER

Consider the nonlinear stochastic semi-decentralized architecture (3.28) and the semi-decentralized extended Kalman filter as in Section 3.4.2.1.

In this thesis, we will refer to the following assumptions as the general assumptions [98].

1) There are positive real numbers $\bar{a}, \bar{q}, \bar{r} > 0$ such that the following bounds on various matrices are fulfilled for every $t \ge 0$, that is

$$\left\| F^{|\bar{N}_i|}(t) \right\| \le \bar{a} \tag{3.72}$$

$$\bar{q}I \le Q(t) \tag{3.73}$$

$$\bar{r}I \le R(t) \tag{3.74}$$

2) There are positive real numbers $\varepsilon_\phi, \kappa_\phi > 0$ such that the nonlinear function ϕ which is the remaining term of the Taylor expansion,

$$f\left(x_{\bar{N}_i}(t)\right) - f\left(\hat{x}_{\bar{N}_i}(t)\right) = F^{|\bar{N}_i|}(t)\left[x_{\bar{N}_i}(t) - \hat{x}_{\bar{N}_i}(t)\right] + \phi\left[x_{\bar{N}_i}(t), \hat{x}_{\bar{N}_i}(t)\right] \tag{3.75}$$

is bounded via

$$\left\|\phi\left(x_{\bar{N}_i},\hat{x}_{\bar{N}_i}\right)\right\| \le \kappa_\phi \left\|x_{\bar{N}_i}-\hat{x}_{\bar{N}_i}\right\|^2 \text{ with } \left\|x_{\bar{N}_i}-\hat{x}_{\bar{N}_i}\right\| \le \varepsilon_\phi \tag{3.76}$$

3) $F^{|\bar{N}_i|}(t)$ is non-singular for every $t \ge 0$.

4) There exist real constants $p, \bar{p}$ such that

$$pI \le P^{|\bar{N}_i|}(t) \le \bar{p}I \tag{3.77}$$

Then it can be shown that along the same lines as those invoked in [98], for some $\delta, \varepsilon > 0$ the initial estimation error satisfies

$$\left\|e_{\bar{N}_i}(0)\right\| \le \varepsilon \tag{3.78}$$

and the covariance matrices are bounded via

$$Q(t) \le \delta I \tag{3.79}$$

$$R(t) \le \delta I \tag{3.80}$$

Then the estimation error $e(t)$ given by

$$e_{\bar{N}_i}(t) = y_{\bar{N}_i}(t) - C^{|\bar{N}_i|}\hat{x}_{\bar{N}_i}(t) \tag{3.81}$$

is exponentially bounded with the probability one.

3.4.4.3. STOCHASTIC STABILITY OF CENTRALIZED KALMAN FILTER

Consider the nonlinear stochastic centralized architecture (3.44) and the centralized extended Kalman filter as in Section 3.4.3.1.

In this thesis, we will refer to the following assumptions as the general assumptions [98].

1) There are positive real numbers $\bar{a}, \bar{q}, \bar{r} > 0$ such that the following bounds on various matrices are fulfilled for every $t \geq 0$, that is

$$\left\| F^N(t) \right\| \leq \bar{a} \tag{3.82}$$

$$\bar{q} I \leq Q(t) \tag{3.83}$$

$$\bar{r} I \leq R(t) \tag{3.84}$$

2) There are positive real numbers $\varepsilon_\phi, \kappa_\phi > 0$ such that the nonlinear function ϕ which is the remaining term of the Taylor expansion,

$$f\left(x(t)\right) - f\left(\hat{x}(t)\right) = F^N(t)\left[x(t) - \hat{x}(t)\right] + \phi\left[x(t), \hat{x}(t)\right] \tag{3.85}$$

is bounded via

$$\left\| \phi(x, \hat{x}) \right\| \leq \kappa_\phi \left\| x - \hat{x} \right\|^2 \text{ with } \left\| x - \hat{x} \right\| \leq \varepsilon_\phi \tag{3.86}$$

3) $F^N(t)$ is non-singular for every $t \geq 0$.

4) There exist real constants $p, \bar{p}$ such that

$$pI \leq P^N(t) \leq \bar{p} I \tag{3.87}$$

Then it can be shown that along the same lines as those invoked in [98], for some $\delta, \varepsilon > 0$ the initial estimation error satisfies

$$\left\| e(0) \right\| \leq \varepsilon \tag{3.88}$$

and the covariance matrices are bounded via

$$Q(t) \le \delta I \tag{3.89}$$

$$R(t) \le \delta I \tag{3.90}$$

Then the estimation error $e(t)$ given by

$$e(t) = y(t) - C\hat{x}(t) \tag{3.91}$$

is exponentially bounded with the probability one.

3.5. SIMULATION FOR ATTITUDE CONTROL OF SPACECRAFT FORMATION FLYING BY USING THE VIRTUAL STRUCTURE

Here we present a healthy scenario for virtual structure formation flight control strategy. Consider a four-spacecraft formation flight system in the planetary orbital environment, whose formation diagraph is shown in Figure 3.5. They are assumed on a sun-synchronize orbit with altitude of 680 km. The major environmental disturbance in this altitude is gravity gradient of order 10^{-3}. The noise is a Gaussian random signal with zero mean and standard deviation of 0.05 degree in attitude measurement and 0.01 degree/second in angular velocity measurement. The information exchange is in the form of bidirectional ring topology. The four spacecraft are assumed to have the $120\ kg$ mass, the axis x inertia of $9.8\ kg.m^2$, the axis y inertia of $9.7\ kg.m^2$, and the axis z inertia of $9.73\ kg.m^2$, and distributed equally along a circle with diameter of 0.7 km. Our results show that the four spacecraft formation evolves as a rigid body and the formation shape is preserved and each spacecraft preserves a fixed relative orientation within the formation throughout the manoeuvres.

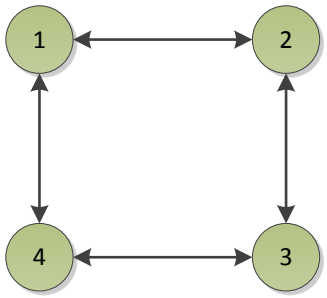

Figure 3.5 Four spacecraft formation flying topology.

The dynamic model of spacecraft used in our simulation is the same as those described in Section 2.1.2.2. The desired specifications to design the controllers are selected as:

Specification	Desired value
Settling time (t_s)	<= 500 sec
Tracking error	<=0.001

Table 3.1. Desired design specifications.

Given that the primary emphasis in spacecraft operations is safety rather than a fast transient response, the settling time of 500 sec is quite reasonable for a low Earth orbit that generally lasts 100 minutes [95].

In order to show the performance of the formation control method, we present the results corresponding to a healthy scenario. We simulate a scenario when the four

spacecraft start from the rest to rotate with the same desired attitude relative to the formation frame. The initial attitude condition for the formation and for each spacecraft with respect to the reference frame is [0, 0, 0] degree which is equal to [0, 0, 0, 1] in the quaternion. The desired attitude for formation is [1, 1.5, 2] degree which is equal to [0.0085 0.0132 0.0173 0.9997] in the quaternion. The desired attitude of each spacecraft with respect to the formation frame is [3 4 5] degree which is equal to [0.0246 0.0360 0.0426 0.9981] in the quaternion.

By using the equation (2.31), the desired attitude of each spacecraft with respect to the reference frame will be [4.13 5.405 7.0709] degree which is equal to [0.0330 0.0492 0.0598 0.9964] in the quaternion. In Figure 3.6 to Figure 3.8, the attitude, angular velocity, and attitude tracking error of spacecraft #1, without loss of any generality, during the first 1000 sec of its mission are presented.

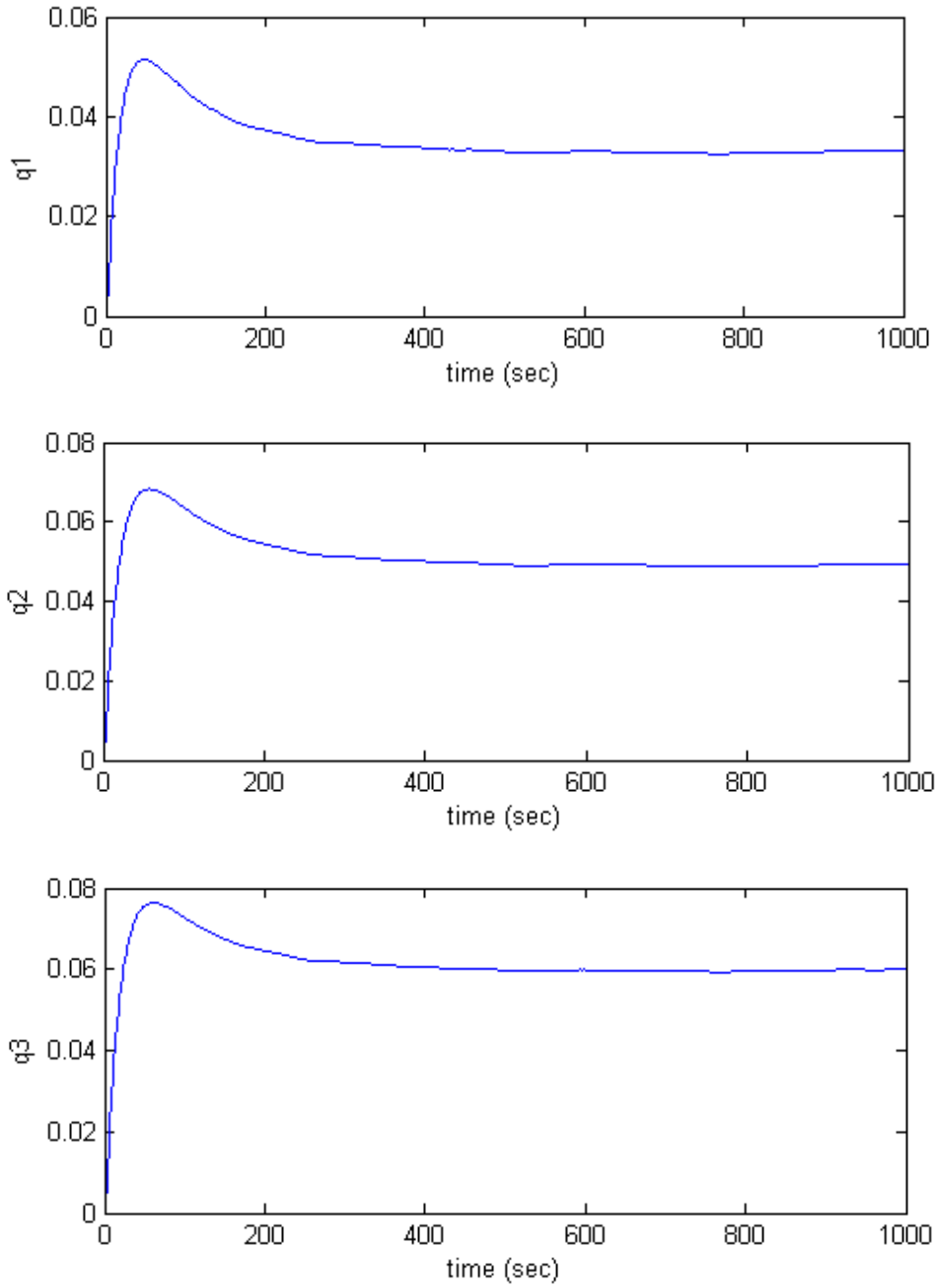

Figure 3.6 Attitude parameters q_1, q_2, q_3 for the formation flight of spacecraft controlled by the virtual structure.

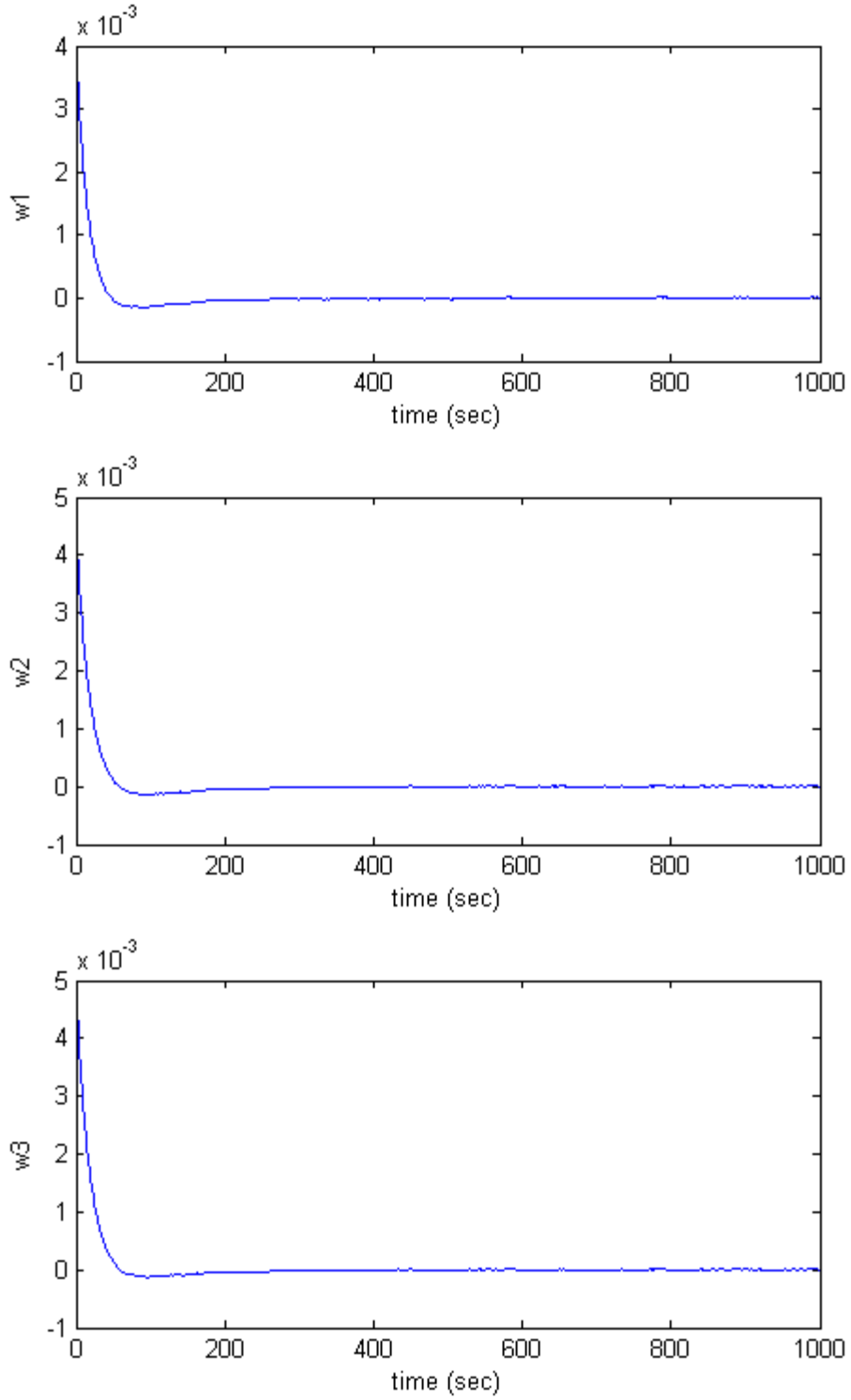

Figure 3.7 Angular velocity parameters $\omega_1, \omega_2, \omega_3$ for formation flight of spacecraft controlled by the virtual structure.

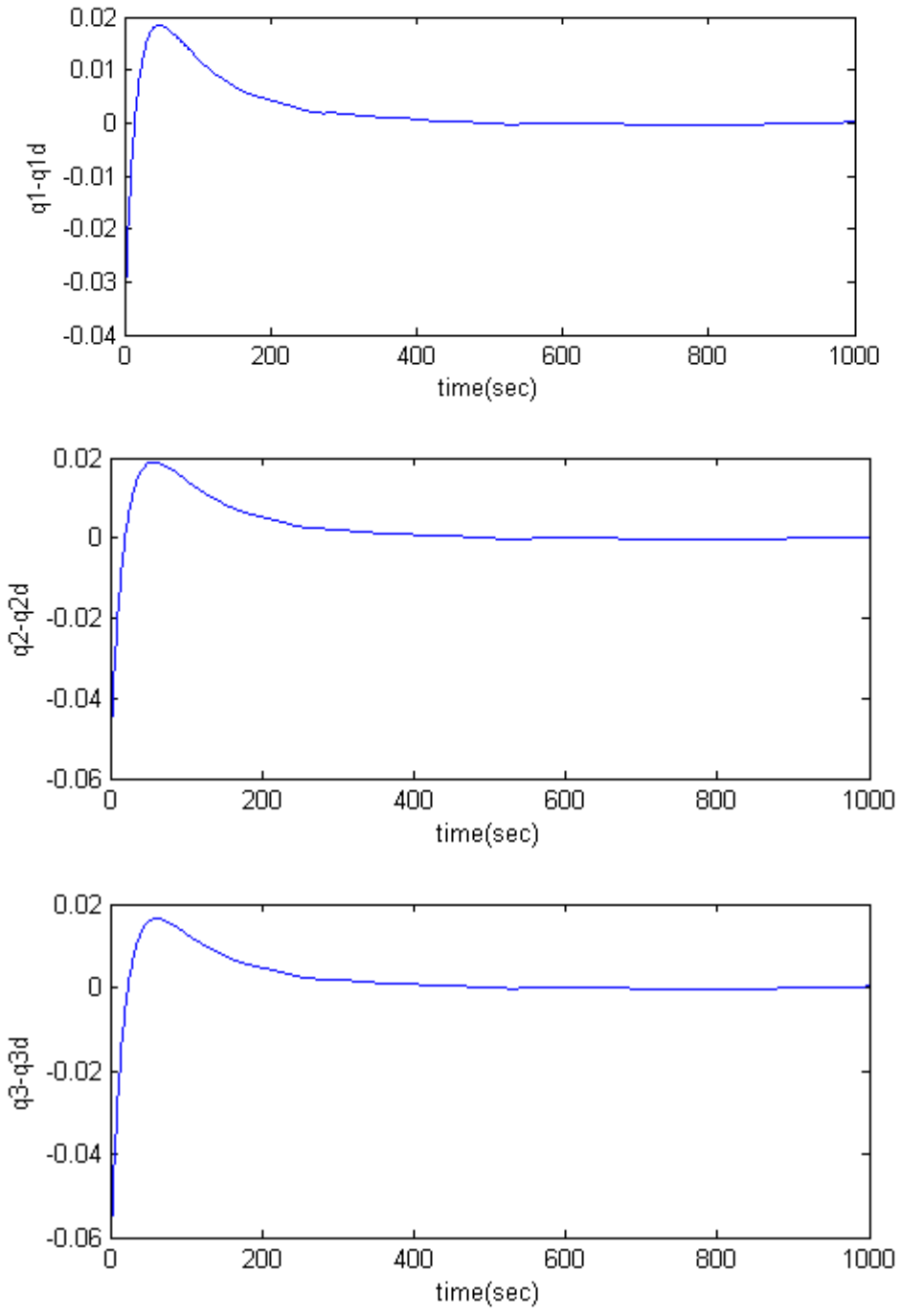

Figure 3.8 Attitude error for the formation flight of spacecraft controlled by the virtual structure.

Figure 3.6 and Figure 3.7 show that the settling time of spacecraft #1 is less than 500 sec, and Figure 3.8 shows that the tracking error is less than 0.001, which are our desired specifications for controller design.

The spacecraft attitude control gains and formation control gains which have been applied to equations (2.32) and (2.34) to obtain the above desired performance are given respectively in Table 3.2 and Table 3.3.

Spacecraft Control Gain Parameter	Control Gain Value
kq	[60 0 0; 0 60 0; 0 0 60]
kw	[1200 0 0; 0 1200 0; 0 0 1200]

Table 3.2. Spacecraft control gains.

Formation Control Gain Parameter	Control Gain Value
KG	[1 0 0; 0 1 0; 0 0 1]
KS	[1 0 0; 0 1 0; 0 0 1]
Ds	[1 0 0; 0 1 0; 0 0 1]
Dg	[100 0 0; 0 100 0; 0 0 100]
Kf	[10 0 0; 0 10 0; 0 0 10]

Table 3.3. Formation control gains.

3.6. SIMULATION RESULTS FOR FAULT DETECTION

In order to compare the performance of the fault detection architectures proposed in this thesis, and to show the significance and improvement of centralized and semi-decentralized architectures over the decentralized architecture, different faulty scenarios are experimented on the spacecraft formation flying.

The formation control topology is ring, which is a symmetric scheme and the control architecture is decentralized control. In the previous section, we presented the simulation results for one spacecraft that can be generalized to other spacecraft in the formation. However, this argument does not include all other formation architectures. In semi-decentralized and centralized formation control topologies, and also in non-symmetric decentralized control topology the dynamic behaviors of various spacecraft are different and their responses to faulty scenarios may not be similar.

The confusion matrix approach is used to evaluate the performance of the proposed fault detection methods, as shown in Table 3.4. Parameter A is the number of faulty scenarios that are detected correctly as faulty, which is named as true faulty detection. Parameter B is the number of faulty scenarios that are misclassified as healthy, which is named as false healthy detection. Parameter C is the number of healthy scenarios that are misclassified as faulty, which is named as false faulty detection. Parameter D is the number of healthy scenarios that are classified correctly as healthy, which is named as true healthy detection. The evaluation parameters in this approach are accuracy, true healthy, false healthy, true faulty, false faulty, and precision, those are defined as following:

		Predicted	
		Faulty	Healthy
Actual	Faulty	A	B
	Healthy	C	D

Table 3.4. Confusion matrix definitions and terms.

$$\text{Accuracy} = \frac{A+D}{A+B+C+D} \tag{3.92}$$

$$\text{True Healthy} = \frac{D}{C+D} \tag{3.93}$$

$$\text{False Healthy} = \frac{B}{A+B} \tag{3.94}$$

$$\text{True Faulty} = \frac{A}{A+B} \tag{3.95}$$

$$\text{False Faulty} = \frac{C}{C+D} \tag{3.96}$$

$$\text{Precision} = \frac{D}{B+D} \tag{3.97}$$

In order to evaluate and compare the results of different architectures, various fault scenarios are tested on the spacecraft formation flight model as described in Chapter 2. As discussed in Chapter 2, the actuator fault is modeled by using the partial

effectiveness factor which shows as reduction in the torque effectiveness of the actuators of the spacecraft.

Eight different faulty scenarios are considered for the actuator x of spacecraft #1. The partial effectiveness factors for theses faults are assumed to be $\gamma_1 = 25\%, 20\%, 15\%, 10\%, 8\%, 7\%, 6\%$ and 5% . Confusion matrix table corresponding to each of these fault scenarios is presented and the evaluation parameters are computed. The results of the confusion matrices are plotted in graphs to make comparisons among the efficiency of decentralized, semi-decentralized, and centralized methods, and also between the efficiency of attitude measurement and angular velocity measurement possible.

In addition, for each of the fault detection architectures, the figures obtained from residual evaluation functions for two different fault scenarios are presented.

3.6.1. Decentralized Fault Detection Architecture

In this section, the results that are obtained by implementing the decentralized fault detection method on spacecraft formation flying are presented. The results that are obtained from the system with angular velocity measurement are presented in Section 3.6.1.1, and the results that are obtained from the system with attitude measurement are presented in Section 3.6.1.2.

3.6.1.1. ANGULAR VELOCITY MEASUREMENT

According to equation (3.26), the decentralized fault detection unit of spacecraft #1 generates three residual evaluation functions $\{d_{ij} \mid i = 1, j = 1,2,3\} = \{d_{11}, d_{12}, d_{13}\}$. By considering the worst case analysis of the residuals corresponding to the healthy

operation of the satellites that are subject to the measurement noise, threshold values $T_1 = 0.0080$, $T_2 = 0.0085$ and $T_3 = 0.0084$ are selected for the fault detection logic evaluation and analysis. To obtain these thresholds, 30 different missions are applied to the formation and the threshold value for each of these missions is calculated by using the equation (3.27). The mean value of those thresholds is considered as the final threshold.

Figure 3.9 to Figure 3.14 show the residual evaluation functions obtained by implementing the decentralized fault detection architecture of spacecraft #1. The initial attitude condition for each spacecraft with respect to the reference frame is [-58, -41, 66] degree which is equal to [0.3062, -0.7802, -0.2153, 0.5013] in the quaternion. The initial condition for the formation is [40, 60, 50] degree which is equal to [0.0700, 0.5508, 0.1890, 0.8100] in the quaternion. The desired attitude for formation is [1, 1.5, 2] degree which is equal to [0.0085, 0.0132, 0.0173, 0.9997] in the quaternion. The desired attitude of each spacecraft with respect to the formation frame is [9, 11, 2] degree which is equal to [0.0764, 0.0968, 0.0098, 0.9923] in the quaternion.

Figure 3.9 to Figure 3.11 present the results that are obtained from 5% reduction in the torque effectiveness of actuator x of spacecraft #1, and Figure 3.12 to Figure 3.14 present the results that are obtained from 15% reduction in the torque effectiveness of actuator x of spacecraft #1. The missions are 92 second (685 samples) long and the faults have occurred at $t = 50$ second (sample #406). The solid horizontal lines show the threshold lines. The points that the residuals surpass the threshold lines before sample #406, are considered as false alarms. The first moment that a residual surpasses the threshold line, after sample #406, is considered as fault detection time which is shown with data cursor on the figure. The parameter X in the data cursor box shows the detection time, and the parameter Y shows the threshold value.

The window length is chosen by considering a trade-off between the fault detection delay and the number of false faulty detections. With increasing the window length, the number of false faulty detections will decrease, but the fault detection delay will increase. In our simulations, the window length M for the equation (3.26) is selected as 40.

The solid horizontal lines show the threshold lines. The samples of d_{ij}, that surpass the threshold line before sample #406, the moment that fault has occurred, are considered as false faulty detection. The samples of d_{ij}, that does not surpasses the threshold line before sample #406, the moment that fault has occurred, are considered as true healthy detection. The first moment that one of the residuals d_{11}, d_{12}, or d_{13} surpasses the threshold line, after sample #406, is considered as the fault detection time which is shown with the data cursor on the figure. The parameter X in the data cursor box shows the detection time, and the parameter Y shows the threshold value. The samples of d_{ij} that does not surpass the threshold line, after sample #406, are considered as false healthy detection. The samples of d_{ij} that surpass the threshold line, after sample #406, are considered as true healthy detection.

If all of these three residuals do not surpass the threshold line and detect a sample as a healthy sample, then the fault detection unit will consider that sample as a healthy sample. However, if at least one of the residuals surpasses the threshold line in a specific time, then the fault detection unit will consider that sample as a faulty sample.

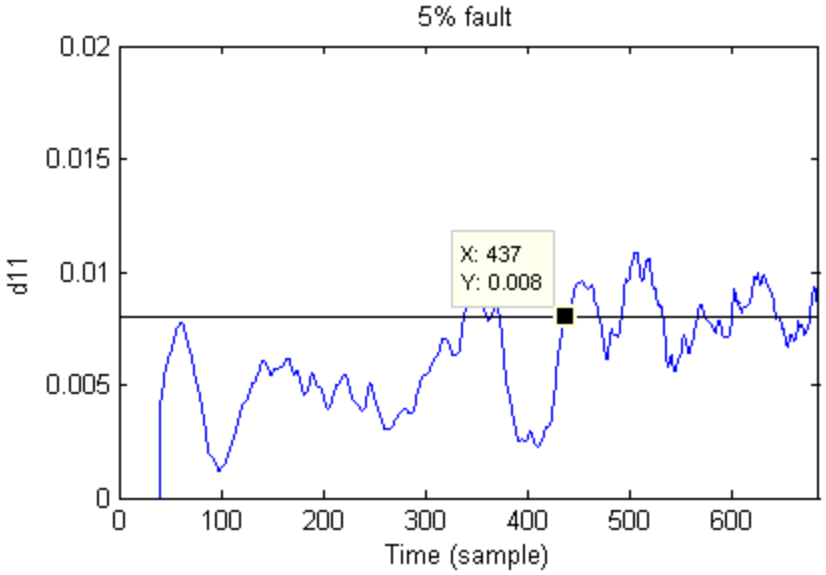

Figure 3.9 Residual d_{11} in the decentralized fault detection architecture with angular velocity measurement for 5% reduction in the torque effectiveness of actuator x of spacecraft #1.

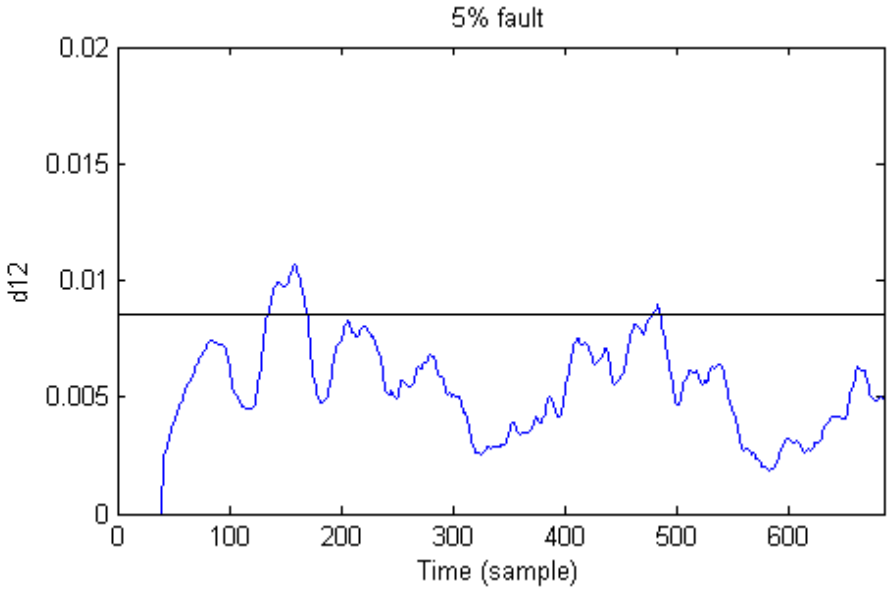

Figure 3.10 Residual d_{12} in the decentralized fault detection architecture with angular velocity measurement for 5% reduction in the torque effectiveness of actuator x of spacecraft #1.

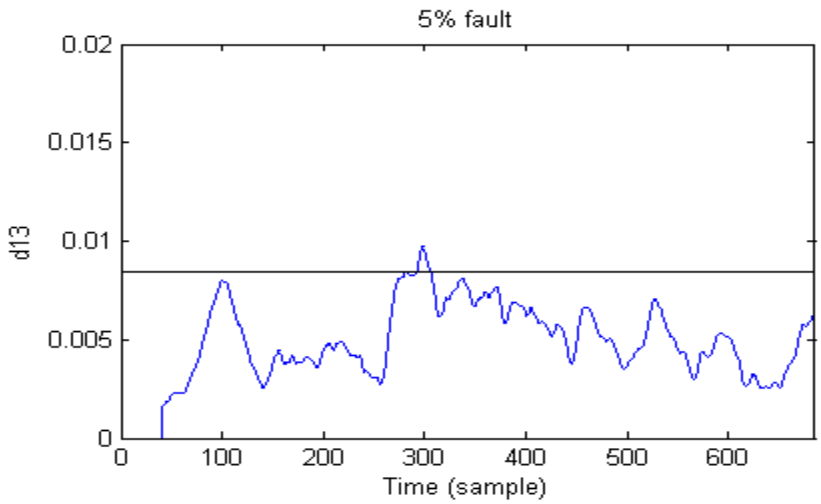

Figure 3.11 Residual d_{13} in the decentralized fault detection architecture with angular velocity measurement for 5% reduction in the torque effectiveness of actuator x of spacecraft #1.

As can be seen in Figure 3.9 to Figure 3.11, the first time that a residual surpasses the threshold after sample #406, has occurred for the residual d_{11} of Figure 3.9 at sample #437. Therefore, sample #437 is the fault detection time. There are 31 samples delay in detecting the fault.

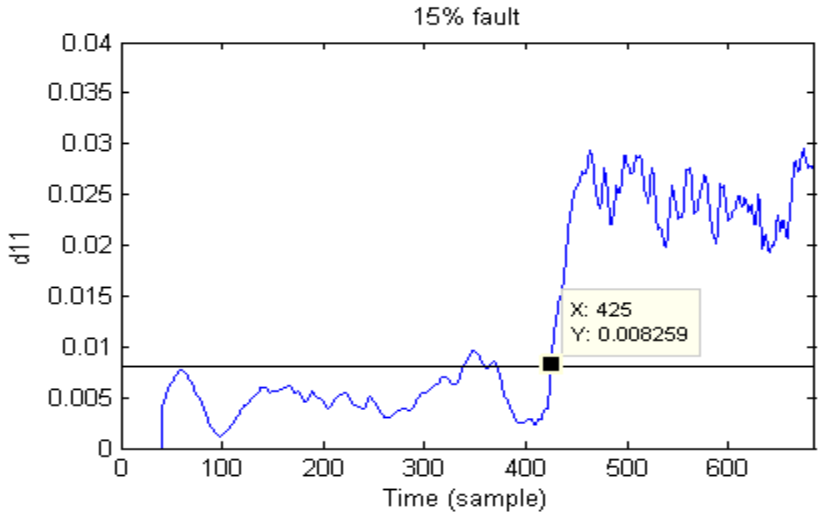

Figure 3.12 Residual d_{11} in the decentralized fault detection architecture with angular velocity measurement for 15% reduction in the torque effectiveness of actuator x of spacecraft #1.

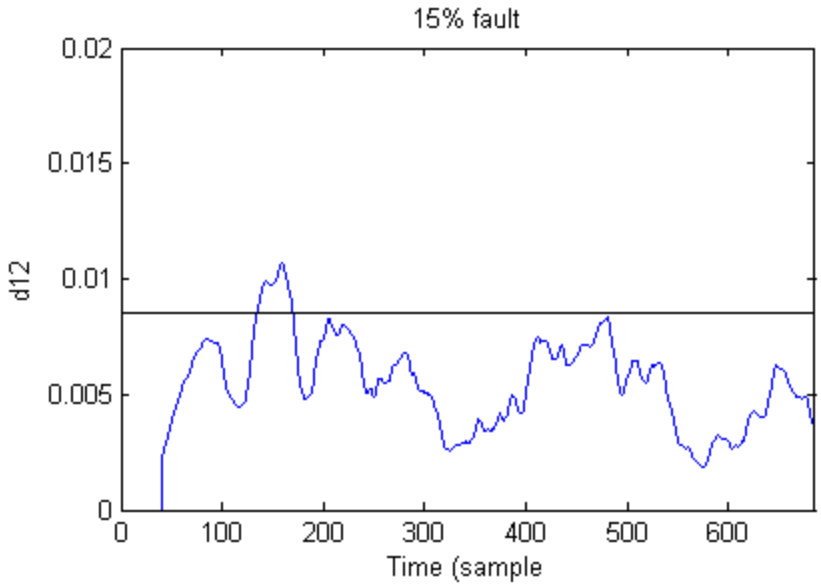

Figure 3.13 Residual d_{12} in the decentralized fault detection architecture with angular velocity measurement, for 15% reduction in the torque effectiveness of actuator x of spacecraft #1.

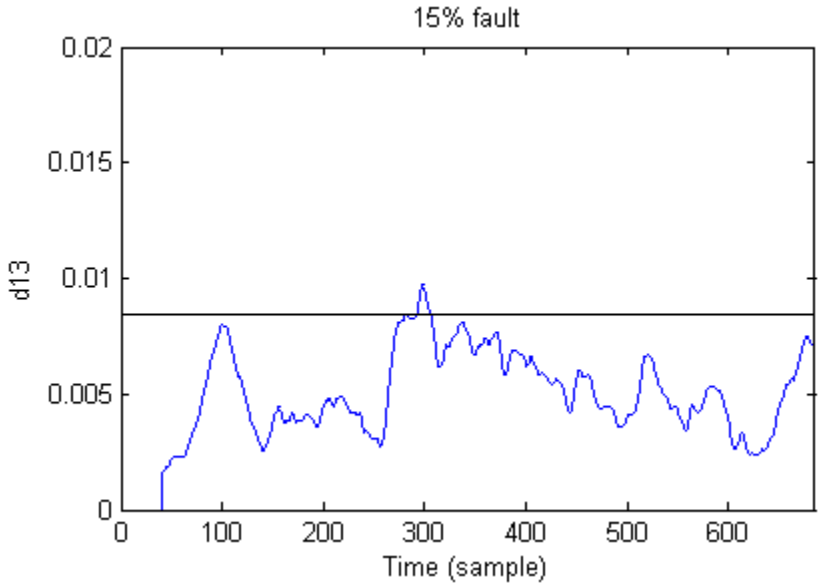

Figure 3.14 Residual d_{13} in the decentralized fault detection architecture with angular velocity measurement, for 15% reduction in the torque effectiveness of actuator x of spacecraft #1.

As can be seen in Figure 3.12 to Figure 3.14, the first time that a residual surpasses

the threshold line after sample #406, has occurred for the residual d_{11} of Figure 3.12 at sample #425. Therefore, sample #425 is the fault detection time. There are 19 samples delay in detecting the fault. In this scenario the fault is more severe than the last scenario, which leads to larger residual during the occurrence of the fault and smaller fault detection delay.

- **Confusion Matrix Results:**

Confusion matrix tables are computed based on Table 3.4, for 5%, 6%, 7%, 8%, 10%, 15%, 20%, and 25% reduction in the torque effectiveness of actuator x of spacecraft #1. The initial attitude condition for each spacecraft with respect to the reference frame is [-50, 35, 80] degree which is equal to [0.1337, 0.4676, 0.4582, 0.7440] in the quaternion. The initial condition for the formation is [29, 67, 8] degree which is equal to [0.1710, 0.5474, -0.0814, 0.8152] in the quaternion. The desired attitude for formation is [1, 1.5, 2] degree which is equal to [0.0085, 0.0132, 0.0173, 0.9997] in the quaternion. The desired attitude of each spacecraft with respect to the formation frame is [18, 38, 39] degree which is equal to [0.0321, 0.3523, 0.2636, 0.8974] in the quaternion. The missions are 100 second (701 samples), and the faults have occurred at $t = 50$ second (sample #358).

		Predicted	
		Faulty	Healthy
Actual	Faulty	118	225
	Healthy	36	322

Table 3.5. Confusion matrix for 5% reduction in the torque effectiveness.

		Predicted	
		Faulty	Healthy
Actual	Faulty	231	112
	Healthy	36	322

Table 3.6. Confusion matrix for 6% reduction in the torque effectiveness.

		Predicted	
		Faulty	Healthy
Actual	Faulty	269	74
	Healthy	36	322

Table 3.7. Confusion matrix for 7% reduction in the torque effectiveness.

		Predicted	
		Faulty	Healthy
Actual	Faulty	273	70
	Healthy	36	322

Table 3.8. Confusion matrix for 8% reduction in the torque effectiveness.

		Predicted	
		Faulty	Healthy
Actual	Faulty	277	66
	Healthy	36	322

Table 3.9. Confusion matrix for 10% reduction in the torque effectiveness.

		Predicted	
		Faulty	Healthy
Actual	Faulty	288	55
	Healthy	36	322

Table 3.10. Confusion matrix for 15% reduction in the torque effectiveness.

		Predicted	
		Faulty	Healthy
Actual	Faulty	290	53
	Healthy	36	322

Table 3.11. Confusion matrix for 20% reduction in the torque effectiveness.

		Predicted	
		Faulty	Healthy
Actual	Faulty	291	52
	Healthy	36	322

Table 3.12. Confusion matrix for 25% reduction in the torque effectiveness.

By using the equations (3.92)-(3.97) and based on the results of Table 3.5 to Table 3.12, the confusion matrix parameters are computed and presented in Table 3.13.

Decentralized	$\gamma_1 = 25\%$	$\gamma_1 = 20\%$	$\gamma_1 = 15\%$	$\gamma_1 = 10\%$	$\gamma_1 = 8\%$	$\gamma_1 = 7\%$	$\gamma_1 = 6\%$	$\gamma_1 = 5\%$
Accuracy	87.4%	87.3%	87.0%	85.4%	84.9%	84.3%	78.9%	62.8%
False Healthy	15.2%	15.4%	16.0%	19.2%	20.4%	21.6%	32.6%	65.6%
True Faulty	84.8%	84.5%	84.0%	83.58%	79.6%	78.4%	67.3%	34.4%
True Healthy	89.9%	89.9%	89.9%	89.9%	89.9%	89.9%	89.9%	89.9%
False Faulty	10.1%	10.1%	10.1%	10.1%	10.1%	10.1%	10.1%	10.1%
Precision	86.1%	85.9%	85.4%	83.0%	82.1%	81.3%	74.2%	58.9%
Detection Time (Sample)	411	412	417	427	430	432	440	459

Table 3.13. Confusion matrix evaluating parameters for the decentralized architecture with angular velocity output.

According to Table 3.13, the accuracy, true faulty, and precision parameters increase with increasing the fault severity and false healthy parameter decreases; as for higher severity faults, the residual deviation from zero becomes more significant and improves the fault detection results.

3.6.1.2. ATTITUDE MEASUREMENT

In this section, the results that are obtained by implementing the proposed decentralized fault detection architecture on spacecraft #1 with attitude measurement are presented. According to equation (3.26), the decentralized fault detection unit of spacecraft #1 generates three residual evaluation functions $\left\{d_{ij} \mid i=1, j=1,2,3\right\}=\left\{d_{11}, d_{12}, d_{13}\right\}$. By considering the worst case analysis of the residuals corresponding to the healthy operation of the satellites that are subject to the measurement noise, threshold of values $T_{11}=0.0063$, $T_{12}=0.0065$ and $T_{13}=0.0060$ are selected for the fault detection logic evaluation and analysis. To obtain these thresholds, 30 different missions are applied to the formation and the threshold values for each of these missions are calculated by using the equation (3.27). The mean value of thresholds is the considered as the final threshold.

Figure 3.15 to Figure 3.20 show the residual evaluation functions obtained by implementing the decentralized fault detection architecture of spacecraft #1. The initial attitude condition for each spacecraft with respect to the reference frame is [-58, -41, 66] degree which is equal to [0.3062, -0.7802, -0.2153, 0.5013] in the quaternion. The initial condition for the formation is [40, 60, 50] degree which is equal to [0.0700, 0.5508, 0.1890, 0.8100] in the quaternion. The desired attitude for formation is [1, 1.5, 2] degree which is equal to [0.0085, 0.0132, 0.0173, 0.9997] in the quaternion. The desired attitude of each spacecraft with respect to the formation frame is [9, 11, 2] degree which is equal to

[0.0764, 0.0968, 0.0098, 0.9923] in the quaternion.

Figure 3.15 to Figure 3.17 represent the results that are obtained from the 10% reduction in the torque effectiveness of actuator x of spacecraft #1, and Figure 3.18 to Figure 3.20 represent the results that are obtained from the 20% reduction in the torque effectiveness of actuator x of spacecraft #1. The missions are 92 second (685 samples) long and the faults have occurred at $t = 50$ second (sample #406).

This window length is chosen by considering a trade-off between the fault detection delay and the number of false faulty detections. With increasing the window length, the number of false faulty detections will decrease, but the fault detection delay will increase. In our simulations, the window length M for the equation (3.26) is selected as 40.

The solid horizontal lines show the threshold lines. The samples of d_{ij} that surpass the threshold line before sample #406, the moment that fault has occurred, are considered as false faulty detection. The samples of d_{ij} that do not surpasses the threshold line before sample #406, the moment that fault has occurred, are considered as true healthy detection. The first moment that one of the residuals d_{11}, d_{12}, or d_{13} surpasses the threshold line, after sample #406, is considered as the fault detection time which is shown with the data cursor on the figure. The parameter X in the data cursor box shows the detection time, and the parameter Y shows the threshold value. The samples of d_{ij} that do not surpass the threshold line, after sample #406, are considered as false healthy detection. The samples of d_{ij} that surpass the threshold line, after sample #406, are considered as true healthy detection.

If all of these three residuals do not surpass the threshold line and detect a sample

as a healthy sample, then the fault detection unit will consider that sample as a healthy sample. However, if at least one of the residuals surpasses the threshold line in a specific time, then the fault detection unit will consider that sample as a faulty sample.

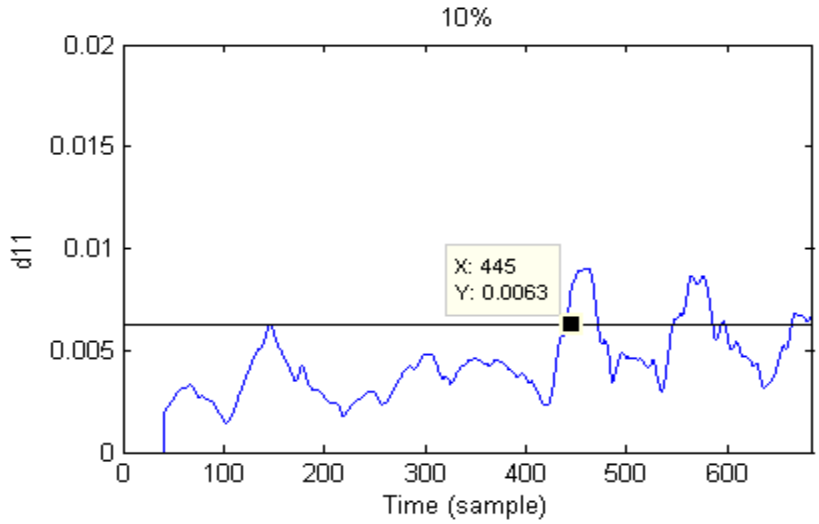

Figure 3.15 Residual d_{11} in the decentralized fault detection architecture with attitude measurement for 10% reduction in the torque effectiveness of actuator x of spacecraft #1.

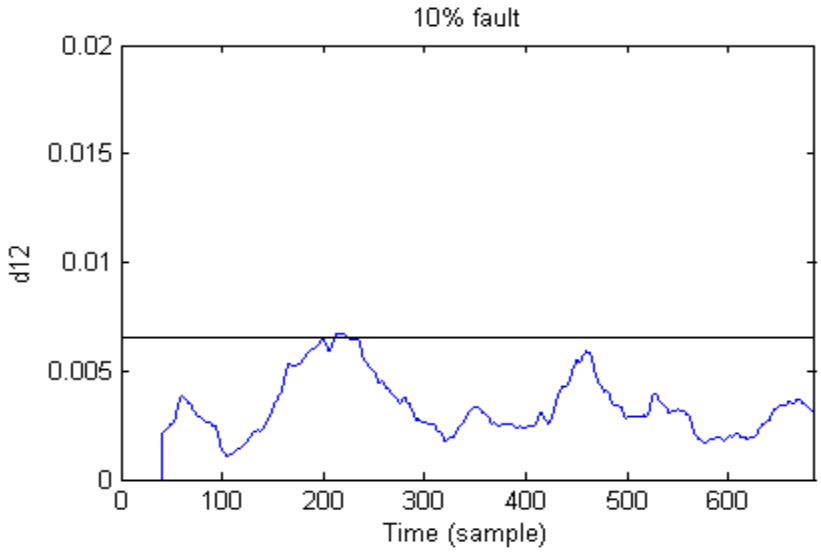

Figure 3.16 Residual d_{12} in the decentralized fault detection architecture with attitude measurement for 10% reduction in the torque effectiveness of actuator x of spacecraft #1.

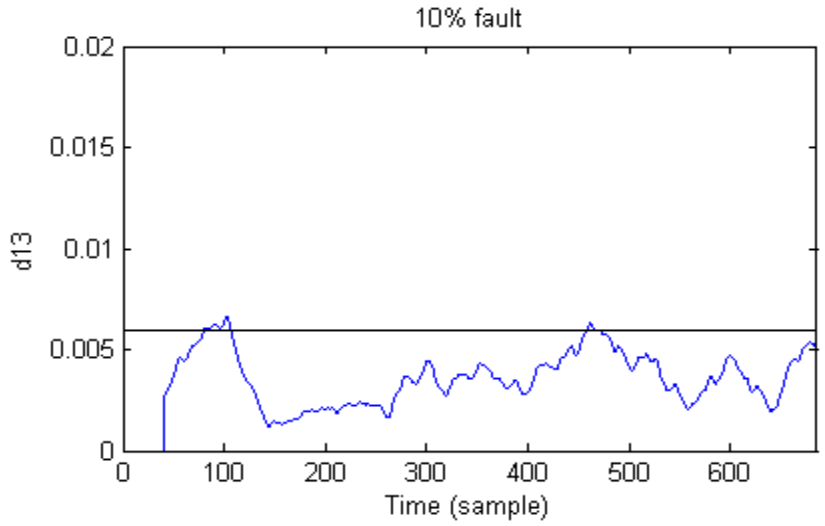

Figure 3.17 Residual d_{13} in the decentralized fault detection architecture with attitude measurement for 10% reduction in the torque effectiveness of actuator x of spacecraft #1.

As can be seen in Figure 3.15 to Figure 3.17, the first time that a residual surpasses the threshold line after sample #406, has occurred for the residual d_{11} of Figure 3.15 at sample #445. Therefore, sample #445 is the fault detection time. There are 39 samples delay in detecting the fault.

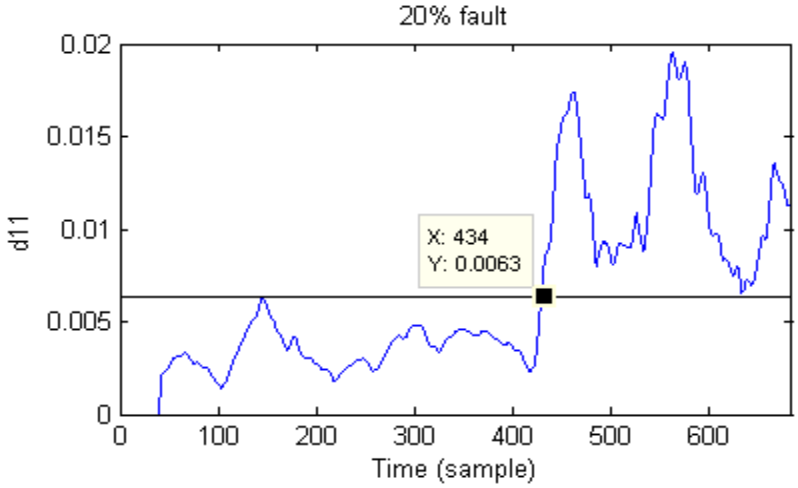

Figure 3.18 Residual d_{11} in decentralized fault detection architecture with attitude measurement for 20% reduction in the torque effectiveness of actuator x of spacecraft #1

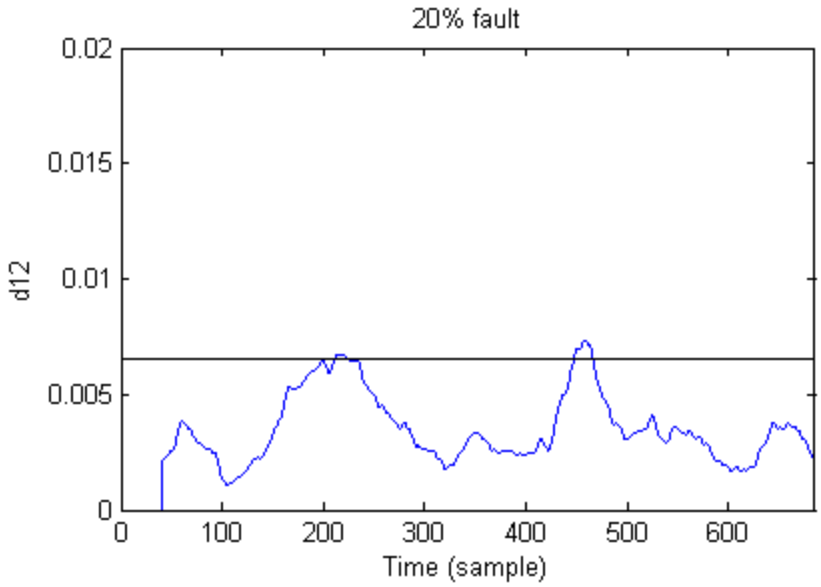

Figure 3.19 Residual d_{12} in the decentralized fault detection architecture with attitude measurement, for 20% reduction in the torque effectiveness of actuator x of spacecraft #1.

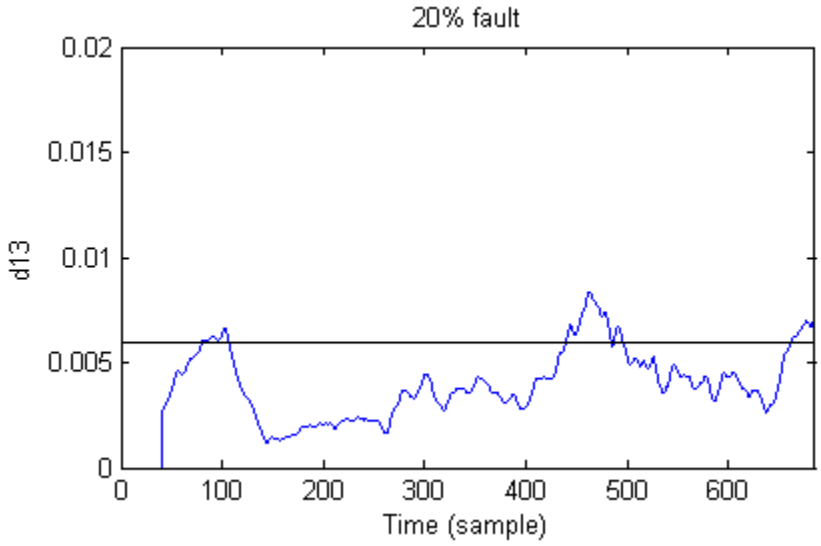

Figure 3.20 Residual d_{13} in the decentralized fault detection architecture with attitude measurement, for 20% reduction in the torque effectiveness of actuator x of spacecraft #1.

As can be seen in Figure 3.18 to Figure 3.20, the first time that a residual surpasses the threshold line after sample #406, has occurred for the residual d_{11} of Figure 3.18 at

sample #434. Therefore, sample #434 is the fault detection time. There are 28 samples delay in detecting the fault. In this scenario the fault is more severe than the last scenario, which leads to larger residual during the occurrence of the fault and smaller fault detection delay.

- **Confusion Matrix Results:**

Confusion matrix tables are computed based on Table 3.4, for 5%, 6%, 7%, 8%, 10%, 15%, 20%, and 25% reduction in the torque effectiveness of actuator x of spacecraft #1. The initial attitude condition for each spacecraft with respect to the reference frame is [-50, 35, 80] degree which is equal to [0.1337, 0.4676, 0.4582, 0.7440] in the quaternion. The initial condition for the formation is [29, 67, 8] degree which is equal to [0.1710, 0.5474, -0.0814, 0.8152] in the quaternion. The desired attitude for formation is [1, 1.5, 2] degree which is equal to [0.0085, 0.0132, 0.0173, 0.9997] in the quaternion. The desired attitude of each spacecraft with respect to the formation frame is [18, 38, 39] degree which is equal to [0.0321, 0.3523, 0.2636, 0.8974] in the quaternion. The missions are 100 second (701 samples), and the faults have occurred at $t = 50$ second (sample #358).

		Predicted	
		Faulty	Healthy
Actual	Faulty	0	343
	Healthy	43	315

Table 3.14. Confusion matrix for 5% reduction in the torque effectiveness.

		Predicted	
		Faulty	Healthy
Actual	Faulty	5	338
	Healthy	43	315

Table 3.15. Confusion matrix for 6% reduction in the torque effectiveness.

		Predicted	
		Faulty	Healthy
Actual	Faulty	17	326
	Healthy	43	315

Table 3.16. Confusion matrix for 7% reduction in the torque effectiveness.

		Predicted	
		Faulty	Healthy
Actual	Faulty	24	319
	Healthy	43	315

Table 3.17. Confusion matrix for 8% reduction in the torque effectiveness.

		Predicted	
		Faulty	Healthy
Actual	Faulty	74	269
	Healthy	43	315

Table 3.18. Confusion matrix for 10% reduction in the torque effectiveness.

		Predicted	
		Faulty	Healthy
Actual	Faulty	181	162
	Healthy	43	315

Table 3.19. Confusion matrix for 15% reduction in the torque effectiveness.

		Predicted	
		Faulty	Healthy
Actual	Faulty	252	91
	Healthy	43	315

Table 3.20. Confusion matrix for 20% reduction in the torque effectiveness.

		Predicted	
		Faulty	Healthy
Actual	Faulty	276	67
	Healthy	43	315

Table 3.21. Confusion matrix for 25% reduction in the torque effectiveness.

By using the equations (3.92)-(3.97) and based on the results of Table 3.14 to Table 3.21, the confusion matrix parameters are computed and presented in Table 3.13.

Decentralized	$\gamma_1 = 25\%$	$\gamma_1 = 20\%$	$\gamma_1 = 15\%$	$\gamma_1 = 10\%$	$\gamma_1 = 8\%$	$\gamma_1 = 7\%$	$\gamma_1 = 6\%$	$\gamma_1 = 5\%$
Accuracy	84.3%	80.9%	70.8%	55.5%	48.4%	47.4%	45.6%	44.9%
False Healthy	19.5%	26.5%	47.2%	78.4%	93.0%	95.0%	98.5%	100%
True Faulty	80.5%	73.5%	52.8%	21.6%	7.0%	5.0%	1.5%	0%
True Healthy	88.0%	88.0%	88.0%	88.0%	88.0%	88.0%	88.0%	88.0%
False Faulty	12.0%	12.0%	12.0%	12.0%	12.0%	12.0%	12.0%	12.0%
Precision	82.5%	77.6%	66.0%	53.9%	49.7%	49.1%	48.2%	47.9%
Detection Time (Sample)	419	422	430	430	430	440	450	Not Detected

Table 3.22. Confusion matrix for the decentralized architecture with angular velocity output.

According to Table 3.22, the accuracy, true faulty and precision parameters increase with increasing the fault severity and false healthy parameter decreases; as for higher severity faults, the residual deviation from zero become more significant and improves the fault detection results.

3.6.2. Semi-decentralized Fault Detection Architecture

In this section, the results that are obtained by implementing the semi-decentralized fault detection method on spacecraft formation flying are presented. The results that are obtained from the system with angular velocity measurement are presented in Section 3.6.2.1, and the results that are obtained from the system with attitude measurement are presented in Section 3.6.2.2.

3.6.2.1. ANGULAR VELOCITY MEASUREMENT

In this section, the results that are obtained by implementing the proposed semi-decentralized fault detection architecture on spacecraft #1 with angular velocity measurement are presented. According to equation (3.43), the decentralized fault detection unit of spacecraft #1 generates three residual evaluation functions $\left\{ d_j^i \mid i=1, j=1,2,3 \right\} = \left\{ d_1^1, d_2^1, d_3^1 \right\}$. By considering the worst case analysis of the residuals corresponding to the healthy operation of the satellites that are subject to the measurement noise, threshold values of $T_1^1 = 0.0158$, $T_2^1 = 0.0184$, $T_3^1 = 0.0160$ are selected for the fault detection logic evaluation and analysis. To obtain theses thresholds, 30 different missions are applied to the formation and the threshold value for each of these missions are calculated by using the equation (3.44). The mean value of the thresholds is considered as the final threshold.

Figure 3.21 to Figure 3.26 show the residual evaluation functions obtained by

implementing the decentralized fault detection architecture of spacecraft #1. The initial attitude condition for each spacecraft with respect to the reference frame is [-58, -41, 66] degree which is equal to [0.3062, -0.7802, -0.2153, 0.5013] in the quaternion. The initial condition for the formation is [40, 60, 50] degree which is equal to [0.0700, 0.5508, 0.1890, 0.8100] in the quaternion. The desired attitude for formation is [1, 1.5, 2] degree which is equal to [0.0085, 0.0132, 0.0173, 0.9997] in the quaternion. The desired attitude of each spacecraft with respect to the formation frame is [9, 11, 2] degree which is equal to [0.0764, 0.0968, 0.0098, 0.9923] in the quaternion.

Figure 3.21 to Figure 3.23 represent the results that are obtained from 5% reduction in the torque effectiveness of actuator x of spacecraft #1, and Figure 3.24 to Figure 3.26 represent the results that are obtained from the 15% reduction in the torque effectiveness of actuator x of spacecraft #1. The missions are 92 second (685 samples) long and the faults have occurred at $t = 50$ second (sample #406).

This window length is chosen by considering a trade-off between the fault detection delay and the number of false faulty detections. With increasing the window length, the number of false faulty detections will decrease, but the fault detection delay will increase. In our simulations, the window length M for equation (3.43) is selected as 40.

The solid horizontal lines show the threshold lines. The samples of d_j^i that surpass the threshold line before sample #406, the moment that fault has occurred, are considered as false faulty detection. The samples of d_j^i that do not surpasses the threshold line before sample #406, the moment that fault has occurred, are considered as true healthy detection. The first moment that one of the residuals d_1^1, d_2^1, or d_3^1 surpass the threshold line, after sample #406, is considered as the fault detection time

which is shown with the data cursor on the figure. The parameter X in the data cursor box shows the detection time, and the parameter Y shows the threshold value. The samples of d_j^i that do not surpass the threshold line, after sample #406, are considered as false healthy detection. The samples of d_j^i that surpass the threshold line, after sample #406, are considered as true healthy detection.

If all of these three residuals do not surpass the threshold line and detect a sample as a healthy sample, then the fault detection unit will consider that sample as a healthy sample. However, if at least one of the residuals surpasses the threshold line in a specific time, then the fault detection unit will consider that sample as a faulty sample.

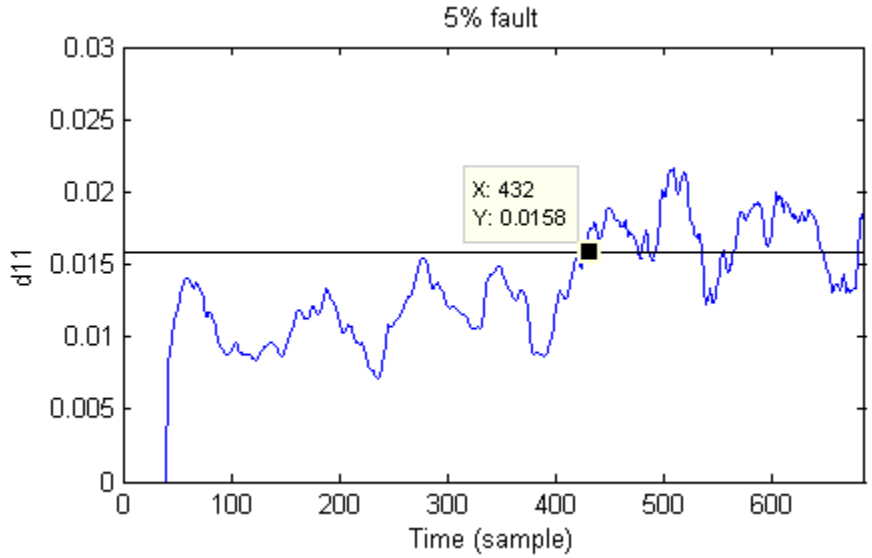

Figure 3.21 Residual d_1^1 in the semi-decentralized fault detection architecture with angular velocity measurement for 5% reduction in the torque effectiveness of actuator x of spacecraft #1.

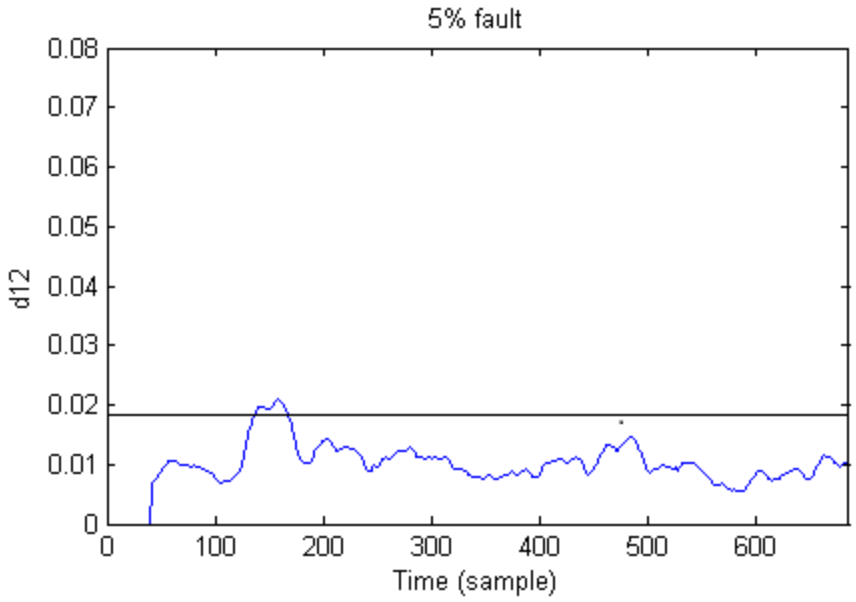

Figure 3.22 Residual d_2^1 in the semi-decentralized fault detection architecture with angular velocity measurement for 5% reduction in the torque effectiveness of actuator x of spacecraft #1.

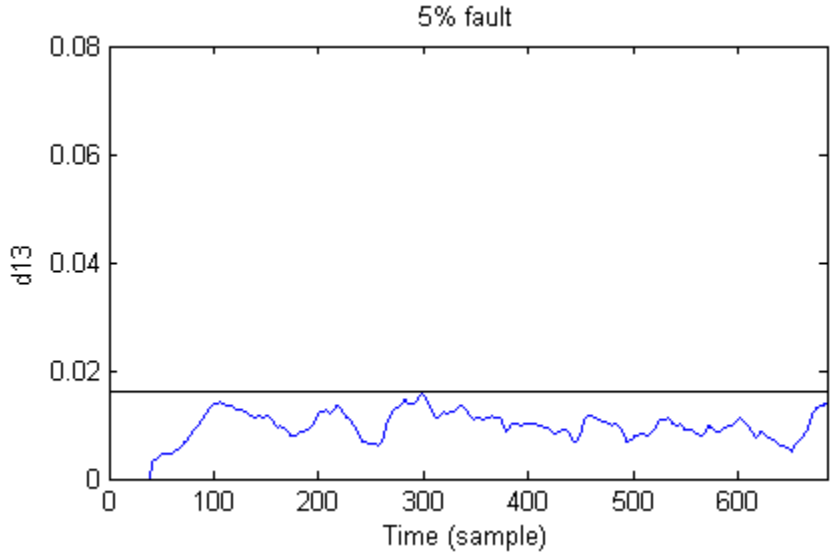

Figure 3.23 Residual d_3^1 in the semi-decentralized fault detection architecture with angular velocity measurement for 5% reduction in the torque effectiveness of actuator x of spacecraft #1.

As can be seen in Figure 3.21 to Figure 3.23, the first time that a residual surpasses the threshold line after sample #406, has occurred for the residual d_1^1 of Figure 3.18 at

sample #432. Therefore, sample #432 is the fault detection time. There are 26 samples delay in detecting the fault.

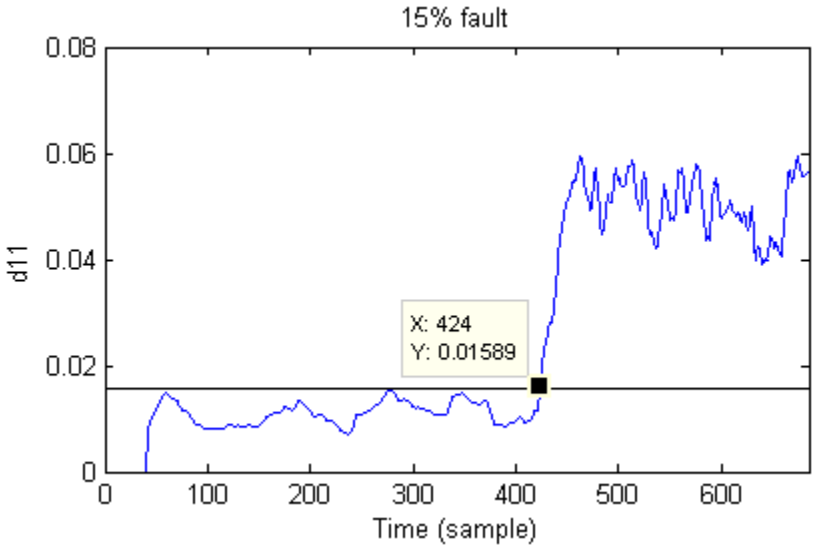

Figure 3.24 Residual d_1^1 in the semi-decentralized fault detection architecture with angular velocity measurement for 15% reduction in the torque effectiveness of actuator x of spacecraft #1.

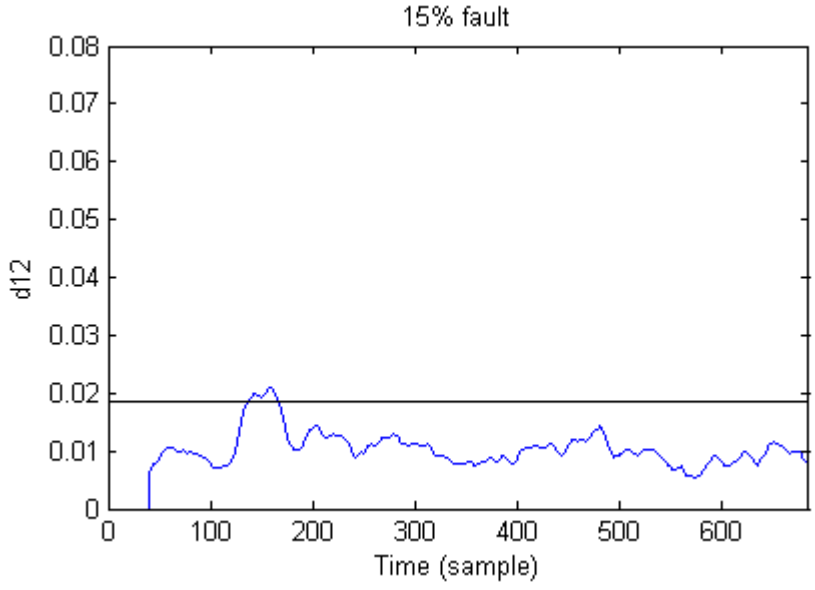

Figure 3.25 Residual d_2^1 in the semi-decentralized fault detection architecture with angular velocity measurement for 15% reduction in the torque effectiveness of actuator x of spacecraft #1.

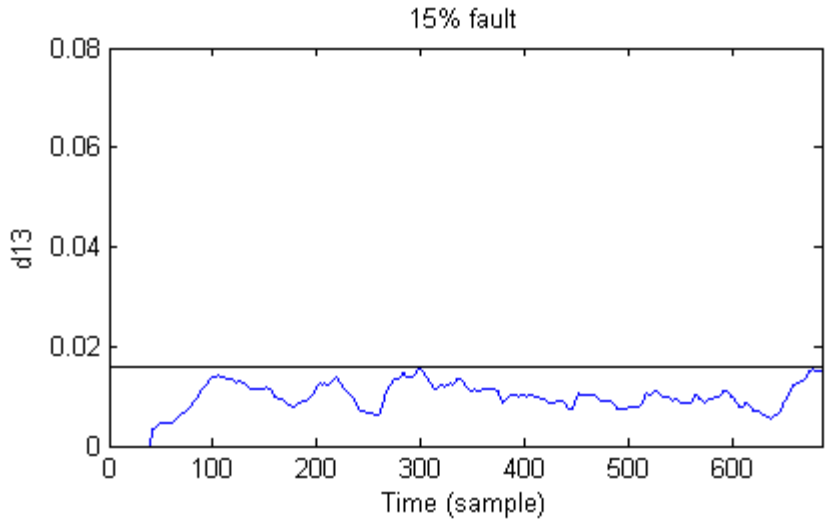

Figure 3.26 Residual d_3^1 in the semi-decentralized fault detection architecture with angular velocity measurement for 15% reduction in the torque effectiveness of actuator x of spacecraft #1.

As can be seen in Figure 3.24 to Figure 3.26, the first time that a residual surpasses the threshold line after sample #406, has occurred for the residual d_1^1 of Figure 3.24 at sample #424. Therefore, sample #424 is the fault detection time. There are 18 samples delay in detecting the fault. In this scenario the fault is more severe than the last scenario, which leads to larger residual during the occurrence of the fault and smaller fault detection delay.

- **Confusion Matrix Results:**

Confusion matrix tables are computed based on Table 3.4, for 5%, 6%, 7%, 8%, 10%, 15%, 20%, and 25% reduction in the torque effectiveness of actuator x of spacecraft #1. The initial attitude condition for each spacecraft with respect to the reference frame is [-50, 35, 80] degree which is equal to [0.1337, 0.4676, 0.4582, 0.7440] in the quaternion. The initial condition for the formation is [29, 67, 8] degree which is equal to [0.1710, 0.5474, -0.0814, 0.8152] in the quaternion. The desired attitude for formation is [1, 1.5, 2]

degree which is equal to [0.0085, 0.0132, 0.0173, 0.9997] in the quaternion. The desired attitude of each spacecraft with respect to the formation frame is [18, 38, 39] degree which is equal to [0.0321, 0.3523, 0.2636, 0.8974] in the quaternion. The missions are 100 second (701 samples) long, and the faults have occurred at $t = 50$ second (sample #358).

		Predicted	
		Faulty	Healthy
Actual	Faulty	160	183
	Healthy	79	279

Table 3.23. Confusion matrix for 5% reduction in the torque effectiveness.

		Predicted	
		Faulty	Healthy
Actual	Faulty	236	107
	Healthy	79	279

Table 3.24. Confusion matrix for 6% reduction in the torque effectiveness.

		Predicted	
		Faulty	Healthy
Actual	Faulty	273	70
	Healthy	79	279

Table 3.25. Confusion matrix for 7% reduction in the torque effectiveness.

		Predicted	
		Faulty	Healthy
Actual	Faulty	280	63
	Healthy	79	279

Table 3.26. Confusion matrix for 8% reduction in the torque effectiveness.

		Predicted	
		Faulty	Healthy
Actual	Faulty	287	56
	Healthy	79	279

Table 3.27. Confusion matrix for 10% reduction in the torque effectiveness.

		Predicted	
		Faulty	Healthy
Actual	Faulty	290	53
	Healthy	79	279

Table 3.28. Confusion matrix for 15% reduction in the torque effectiveness.

		Predicted	
		Faulty	Healthy
Actual	Faulty	292	51
	Healthy	79	279

Table 3.29. Confusion matrix for 20% reduction in the torque effectiveness.

		Predicted	
		Faulty	Healthy
Actual	Faulty	292	51
	Healthy	79	279

Table 3.30. Confusion matrix for 25% reduction in the torque effectiveness.

By using the equations (3.92)-(3.97) and based on the results of Table 3.23 to Table 3.30, the confusion matrix parameters are computed and presented in Table 3.31.

Semi-decentralized	$\gamma_1 = 25\%$	$\gamma_1 = 20\%$	$\gamma_1 = 15\%$	$\gamma_1 = 10\%$	$\gamma_1 = 8\%$	$\gamma_1 = 7\%$	$\gamma_1 = 6\%$	$\gamma_1 = 5\%$
Accuracy	%81.5	%81.5	%81.2	%80.7	%79.7	%78.7	%73.5	%65.9
False Healthy	%14.9	%14.9	%15.4	%16.3	%18.4	%20.4	%31.2	%46.6
True Faulty	%85.1	%85.1	%84.5	%83.7	%81.6	%79.6	%68.8	%53.3
True Healthy	%77.9	%77.9	%77.9	%77.9	%77.9	%77.9	%77.9	%77.9
False Faulty	%22.1	%22.1	%22.1	%22.1	%22.1	%22.1	%22.1	%22.1
Precision	%84.5	%84.5	%84.0	%83.3	%81.6	%79.9	%72.3	%63.5
Detection Time (Sample)	411	412	414	417	425	427	430	435

Table 3.31. Confusion matrix for the semi-decentralized architecture with angular velocity output.

According to Table 3.31, the accuracy, true faulty and precision parameters increase with increasing the fault severity and the false healthy parameter decreases; as for higher severity faults, the residual deviation from zero becomes more significant and improves the fault detection results.

3.6.2.2. ATTITUDE MEASUREMENT

In this section, the results that are obtained by implementing the proposed semi-decentralized fault detection architecture on spacecraft #1 with attitude measurement are presented. According to equation (3.43), the decentralized fault detection unit of spacecraft #1 generates three residual evaluation functions $\left\{d_j^i \mid i=1, j=1,2,3\right\}=\left\{d_1^1, d_2^1, d_3^1\right\}$. By considering the worst case analysis of the residuals corresponding to the healthy operation of the satellites that are subject to the measurement noise, threshold values of $T_1^1=0.0090$, $T_2^1=0.0090$, $T_3^1=0.0093$ are selected for the fault detection analysis. To obtain these thresholds, 30 different missions are applied to the formation and the threshold value for each of these missions is calculated by using the equation (3.44). The mean value of the thresholds is considered as the final threshold.

Figure 3.15 to Figure 3.20 show the residual evaluation functions obtained by implementing the decentralized fault detection architecture of spacecraft #1. The initial attitude condition for each spacecraft with respect to the reference frame is [-58, -41, 66] degree which is equal to [0.3062, -0.7802, -0.2153, 0.5013] in the quaternion. The initial condition for the formation is [40, 60, 50] degree which is equal to [0.0700, 0.5508, 0.1890, 0.8100] in the quaternion. The desired attitude for formation is [1, 1.5, 2] degree which is equal to [0.0085, 0.0132, 0.0173, 0.9997] in the quaternion. The desired attitude of each spacecraft with respect to the formation frame is [9, 11, 2] degree which is equal to [0.0764, 0.0968, 0.0098, 0.9923] in the quaternion.

Figure 3.15 to Figure 3.17 represent the results that are obtained from 10% reduction in the torque effectiveness of actuator x of spacecraft #1, and Figure 3.18 to Figure 3.20 represent the results that are obtained from the 20% reduction in the torque

effectiveness of actuator x of spacecraft #1. The missions are 92 second (685 samples) long and the faults have occurred at $t = 50$ second (sample #406).

This window length is chosen by considering a trade-off between the fault detection delay and the number of false faulty detections. With increasing the window length, the number of false faulty detections will decrease, but the fault detection delay will increase. In our simulations, the window length M for equation (3.43) is selected as 40.

The solid horizontal lines show the threshold lines. The samples of d_j^i that surpass the threshold line before sample #406, the moment that fault has occurred, are considered as false faulty detection. The samples of d_j^i that do not surpasses the threshold line before sample #406, the moment that fault has occurred, are considered as true healthy detection. The first moment that one of the residuals d_1^1, d_2^1, or d_3^1 surpass the threshold line, after sample #406, is considered as the fault detection time which is shown with the data cursor on the figure. The parameter X in the data cursor box shows the detection time, and the parameter Y shows the threshold value. The samples of d_j^i that do not surpass the threshold line, after sample #406, are considered as false healthy detection. The samples of d_j^i that surpass the threshold line, after sample #406, are considered as true healthy detection.

If all of these three residuals do not surpass the threshold line and detect a sample as a healthy sample, then the fault detection unit will consider that sample as a healthy sample. However, if at least one of the residuals surpasses the threshold line in a specific time, then the fault detection unit will consider that sample as a faulty sample.

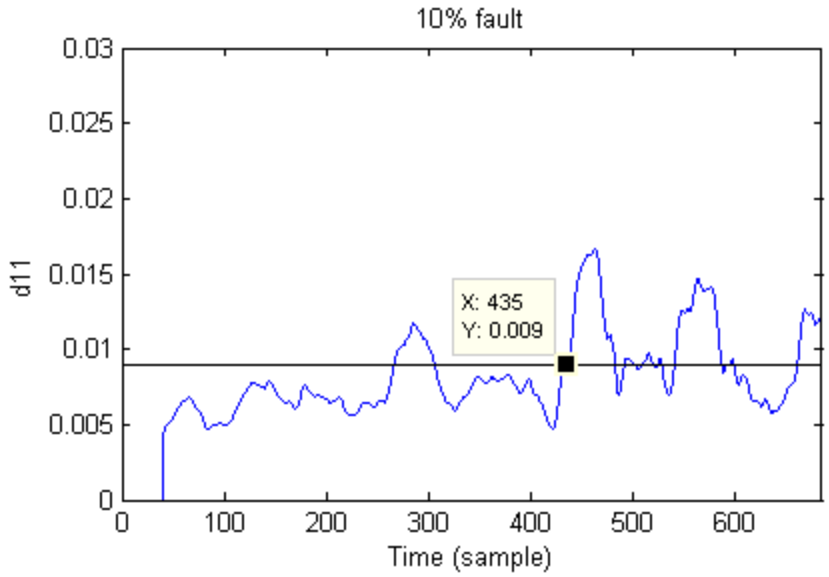

Figure 3.27 Residual d_1^1 in the semi-decentralized fault detection architecture with attitude measurement for 10% reduction in the torque effectiveness of actuator x of spacecraft #1.

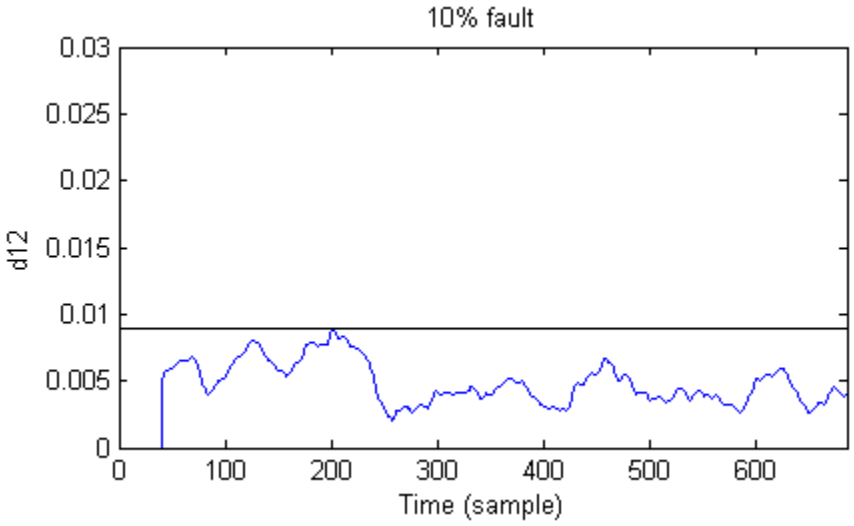

Figure 3.28 Residual d_2^1 in the semi-decentralized fault detection architecture with attitude measurement for 10% reduction in the torque effectiveness of actuator x of spacecraft #1.

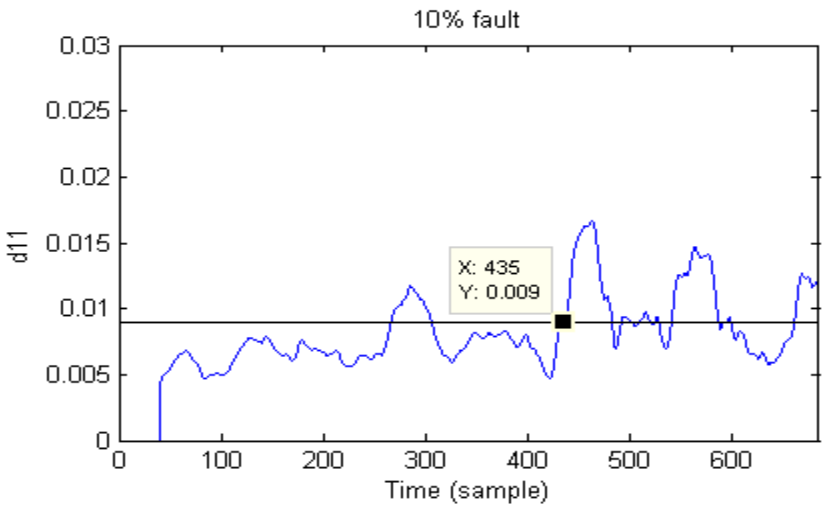

Figure 3.29 Residual d_3^1 in the semi-decentralized fault detection architecture with attitude measurement for 10% reduction in the torque effectiveness of actuator x of spacecraft #1.

As can be seen in Figure 3.27 to Figure 3.29, the first time that a residual surpasses the threshold line after sample #406, has occurred for the residual d_1^1 of Figure 3.27 at sample #435. Therefore, sample #435 is the fault detection time. There are 29 samples delay in detecting the fault.

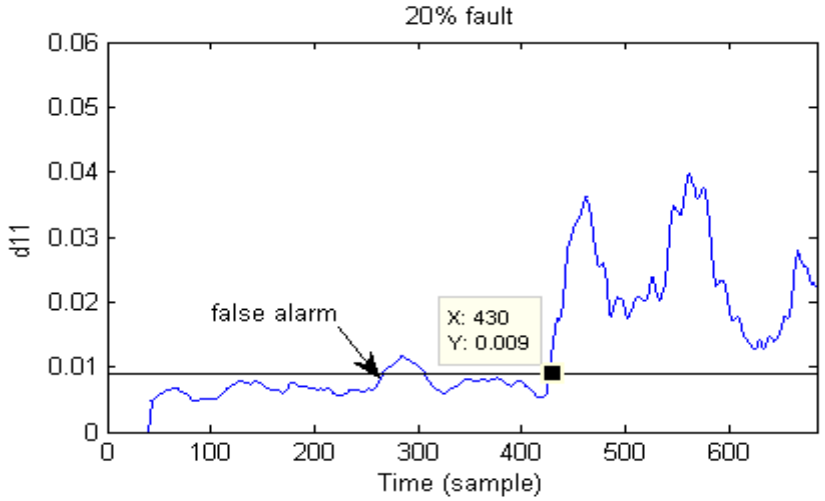

Figure 3.30 Residual d_1^1 in the semi-decentralized fault detection architecture with attitude measurement for 20% reduction in the torque effectiveness of actuator x of spacecraft #1.

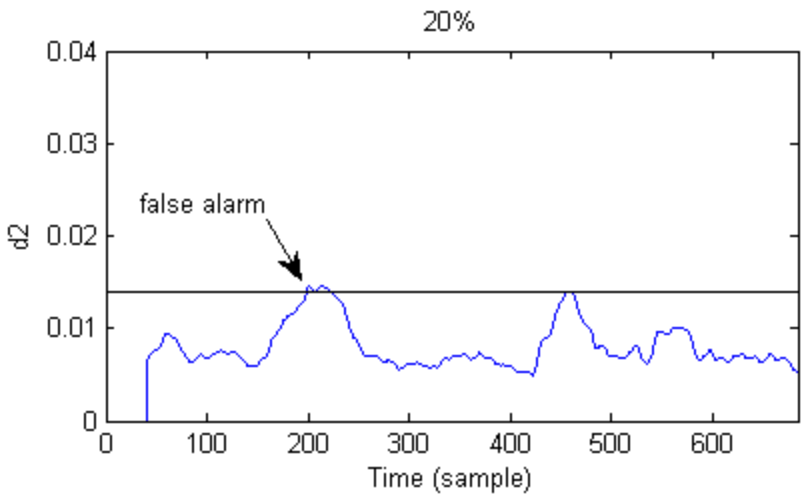

Figure 3.31 Residual d_2^1 in the semi-decentralized fault detection architecture with attitude measurement for 20% reduction in the torque effectiveness of actuator x of spacecraft #1.

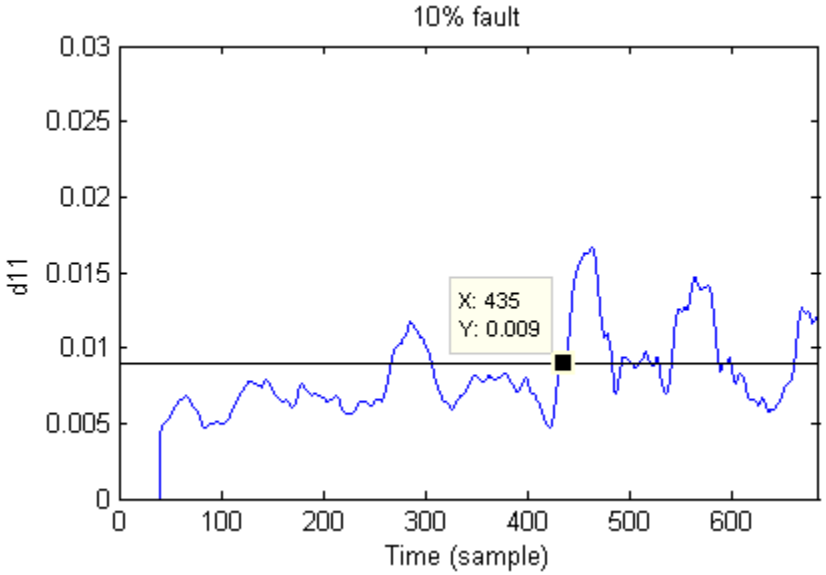

Figure 3.32 Residual d_3^1 in the semi-decentralized fault detection architecture with attitude measurement for 20% reduction in the torque effectiveness of actuator x of spacecraft #1.

As can be seen in Figure 3.30 to Figure 3.32, the first time that a residual surpasses the threshold line after sample #406, has occurred for the residual d_1^1 of Figure 3.30 at sample #435. Therefore, sample #429 is the fault detection time. There are 23 samples

delay in detecting the fault. In this scenario the fault is more severe than the last scenario, which leads to larger residual during the occurrence of the fault and smaller fault detection delay.

- **Confusion Matrix Results:**

Confusion matrix tables are computed based on Table 3.4, for 5%, 6%, 7%, 8%, 10%, 15%, 20%, and 25% reduction in the torque effectiveness of actuator x of spacecraft #1. The initial attitude condition for each spacecraft with respect to the reference frame is [-50, 35, 80] degree which is equal to [0.1337, 0.4676, 0.4582, 0.7440] in the quaternion. The initial condition for the formation is [29, 67, 8] degree which is equal to [0.1710, 0.5474, -0.0814, 0.8152] in the quaternion. The desired attitude for formation is [1, 1.5, 2] degree which is equal to [0.0085, 0.0132, 0.0173, 0.9997] in the quaternion. The desired attitude of each spacecraft with respect to the formation frame is [18, 38, 39] degree which is equal to [0.0321, 0.3523, 0.2636, 0.8974] in the quaternion. The missions are 100 second (701 samples) long, and the faults have occurred at $t = 50$ second (sample #358).

		Predicted	
		Faulty	Healthy
Actual	Faulty	47	296
	Healthy	79	279

Table 3.32. Confusion matrix for 5% reduction in the torque effectiveness.

		Predicted	
		Faulty	Healthy
Actual	Faulty	77	266
	Healthy	79	279

Table 3.33. Confusion matrix for 6% reduction in the torque effectiveness.

		Predicted	
		Faulty	Healthy
Actual	Faulty	93	250
	Healthy	79	279

Table 3.34. Confusion matrix for 7% reduction in the torque effectiveness.

		Predicted	
		Faulty	Healthy
Actual	Faulty	107	236
	Healthy	79	279

Table 3.35. Confusion matrix for 8% reduction in the torque effectiveness.

		Predicted	
		Faulty	Healthy
Actual	Faulty	149	194
	Healthy	79	279

Table 3.36. Confusion matrix for 10% reduction in the torque effectiveness.

		Predicted	
		Faulty	Healthy
Actual	Faulty	247	96
	Healthy	70	279

Table 3.37. Confusion matrix for 15% reduction in the torque effectiveness.

		Predicted	
		Faulty	Healthy
Actual	Faulty	277	66
	Healthy	70	279

Table 3.38. Confusion matrix for 20% reduction in the torque effectiveness.

		Predicted	
		Faulty	Healthy
Actual	Faulty	281	62
	Healthy	70	279

Table 3.39. Confusion matrix for 25% reduction in the torque effectiveness.

By using the equations (3.92)-(3.97) and based on the results of Table 3.50 to Table 3.57, the confusion matrix parameters are computed and presented in Table 3.13.

Semi-decentralized	$\gamma_1 = 25\%$	$\gamma_1 = 20\%$	$\gamma_1 = 15\%$	$\gamma_1 = 10\%$	$\gamma_1 = 8\%$	$\gamma_1 = 7\%$	$\gamma_1 = 6\%$	$\gamma_1 = 5\%$
Accuracy	79.9%	79.3%	75.0%	61.1%	55.1%	53.1%	50.8%	46.5%
False Healthy	18.1%	19.2%	28.0%	56.6%	68.8%	72.9%	77.5%	86.3%
True Faulty	81.9%	80.8%	72.0%	43.4%	31.2%	27.1%	22.4%	13.7%
True Healthy	77.9%	77.9%	77.9%	77.9%	77.9%	77.9%	77.9%	77.9%
False Faulty	22.1%	22.1%	22.1%	22.1%	22.1%	22.1%	22.1%	22.1%
Precision	81.8%	80.9%	72.4%	59.0%	54.2%	52.7%	51.2%	48.5%
Detection Time (Sample)	417	417	419	421	422	432	433	435

Table 3.40. The evaluating parameters of confusion matrix for semi-decentralized architecture with attitude output.

According to Table 3.40, the accuracy, true faulty and precision parameters increase with increasing the fault severity and the false healthy parameter decreases; as for higher severity faults, the residual deviation from zero becomes more significant and improves the fault detection results.

3.6.3. Centralized Fault Detection Architecture

In this section, the results that are obtained by implementing the centralized fault

detection method on spacecraft formation flying are presented. The results that are obtained from the system with angular velocity measurement are presented in Section 3.6.3.1, and the results that are obtained from the system with attitude measurement are presented in Section 3.6.3.2.

3.6.3.1. ANGULAR VELOCITY MEASUREMENT

In this section, the results that are obtained by implementing the proposed centralized fault detection architecture on spacecraft formation flying with angular velocity measurement are presented. According to the equation (3.60), the decentralized fault detection unit of spacecraft #1 generates three residual evaluation functions $\{d_j \mid j=1,2,3\}=\{d_1,d_2,d_3\}$. By considering the worst case analysis of the residuals corresponding to the healthy operation of the satellites that are subject to the measurement noise, threshold values of $T_1=0.0241$, $T_2=0.0265$, $T_3=0.0227$ are selected for the fault detection evaluation and analysis. The simulation time is 100 seconds (686 samples). To obtain theses thresholds, 30 different missions are applied to the formation and the threshold value for each of these missions are calculated by using the equation(3.61). The mean value of the thresholds is considered as the final threshold.

Figure 3.33 to Figure 3.38 show the residual evaluation functions obtained by implementing the decentralized fault detection architecture of spacecraft #1. The initial attitude condition for each spacecraft with respect to the reference frame is [-58, -41, 66] degree which is equal to [0.3062, -0.7802, -0.2153, 0.5013] in the quaternion. The initial condition for the formation is [40, 60, 50] degree which is equal to [0.0700, 0.5508, 0.1890, 0.8100] in the quaternion. The desired attitude for formation is [1, 1.5, 2] degree which is equal to [0.0085, 0.0132, 0.0173, 0.9997] in the quaternion. The desired attitude of each spacecraft with respect to the formation frame is [9, 11, 2] degree which is equal to

[0.0764, 0.0968, 0.0098, 0.9923] in the quaternion.

Figure 3.33 to Figure 3.35 represent the results that are obtained from 5% reduction in the torque effectiveness of actuator x of spacecraft #1, and Figure 3.36 to Figure 3.38 present the results that are obtained from 15% reduction in the torque effectiveness of actuator x of spacecraft #1. The missions are 92 second (685 samples) long and the faults have occurred at $t = 50$ second (sample #406). The solid horizontal lines show the threshold lines. The points that the residuals surpass the threshold lines before sample #406, are considered as false alarms. The first moment that a residual surpasses the threshold line after sample #406 is considered as fault detection time which is shown with data cursor on the figure. The parameter X in the data cursor box shows the detection time, and the parameter Y shows the threshold value.

This window length is chosen by considering a trade-off between the fault detection delay and the number of false faulty detections. With increasing the window length, the number of false faulty detections will decrease, but the fault detection delay will increase. In our simulations, the window length M for equation (3.60) is selected as 40.

The solid horizontal lines show the threshold lines. The samples of d_j that surpass the threshold line before sample #406, the moment that fault has occurred, are considered as false faulty detection. The samples of d_j that do not surpasses the threshold line before sample #406, the moment that fault has occurred, are considered as true healthy detection. The first moment that one of the residuals d_1, d_2, or d_3 surpass the threshold line, after sample #406, is considered as the fault detection time which is shown with the data cursor on the figure. The parameter X in the data cursor box shows the detection time, and the parameter Y shows the threshold value. The

samples of d_j that do not surpass the threshold line, after sample #406, are considered as false healthy detection. The samples of d_j that surpass the threshold line, after sample #406, are considered as true healthy detection.

If all of these three residuals do not surpass the threshold line and detect a sample as a healthy sample, then the fault detection unit will consider that sample as a healthy sample. However, if at least one of the residuals surpasses the threshold line in a specific time, then the fault detection unit will consider that sample as a faulty sample.

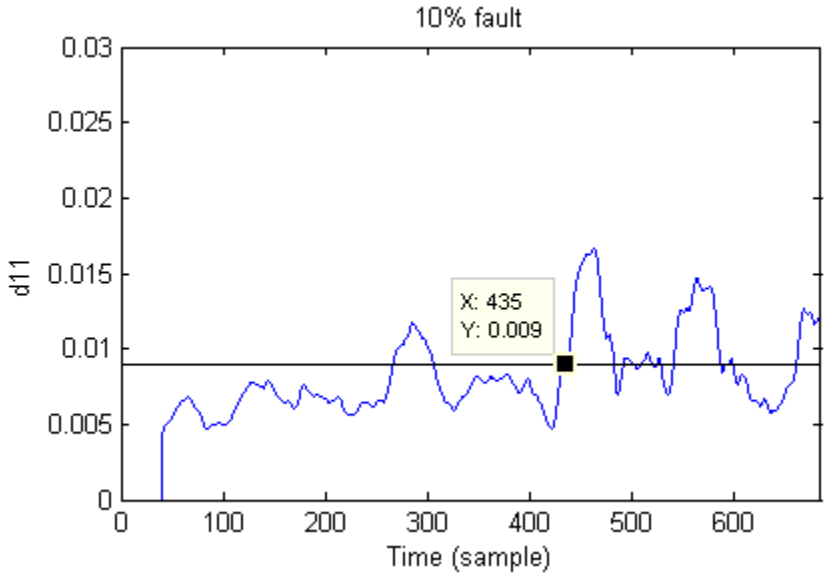

Figure 3.33 Residual d_1 in the centralized fault detection architecture with angular velocity measurement for 5% reduction in the torque effectiveness of actuator x of spacecraft #1.

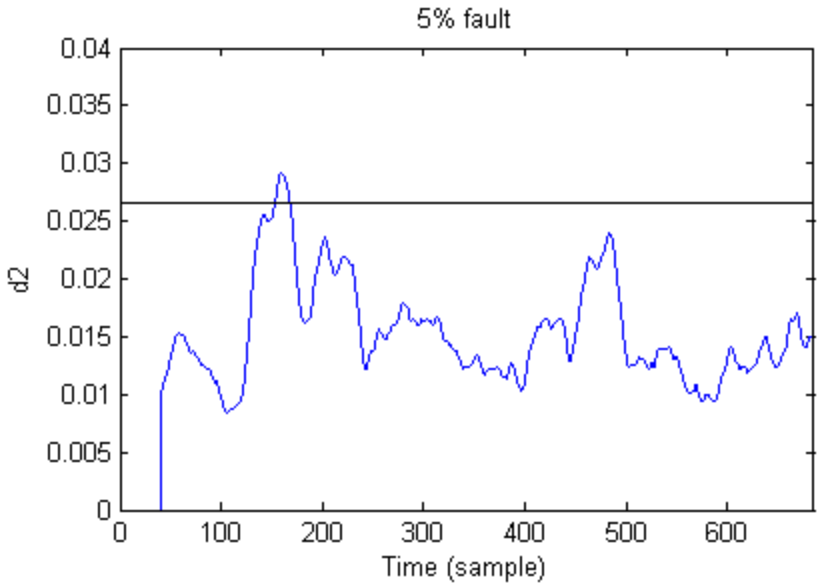

Figure 3.34 Residual d_2 in the centralized fault detection architecture with angular velocity, measurement for 5% reduction in the torque effectiveness of actuator x of spacecraft #1.

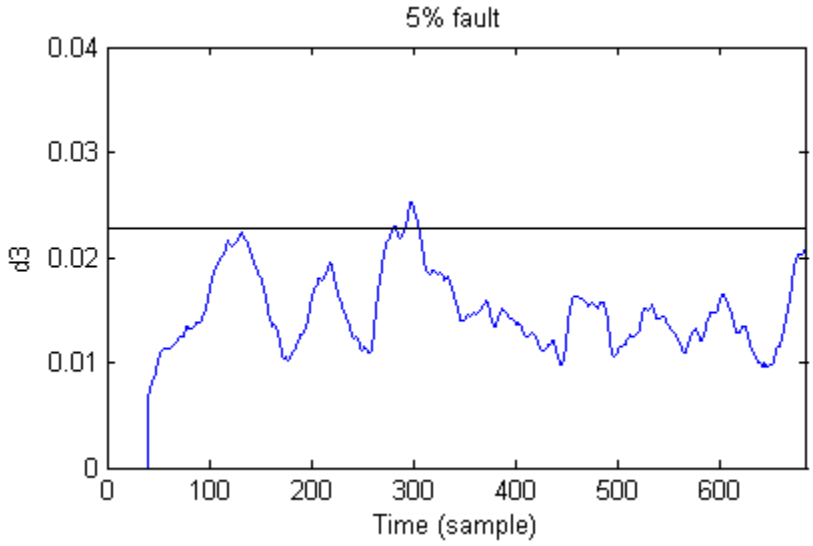

Figure 3.35 Residual d_3 in the centralized fault detection architecture with angular velocity measurement for 5% reduction in the torque effectiveness of actuator x of spacecraft #1.

As can be seen in Figure 3.33 to Figure 3.35, the first time that a residual surpasses the threshold line after sample #406, has occurred for the residual d_1 of Figure 3.33 at

sample #432. Therefore, sample #432 is the fault detection time. There are 26 samples delay in detecting the fault.

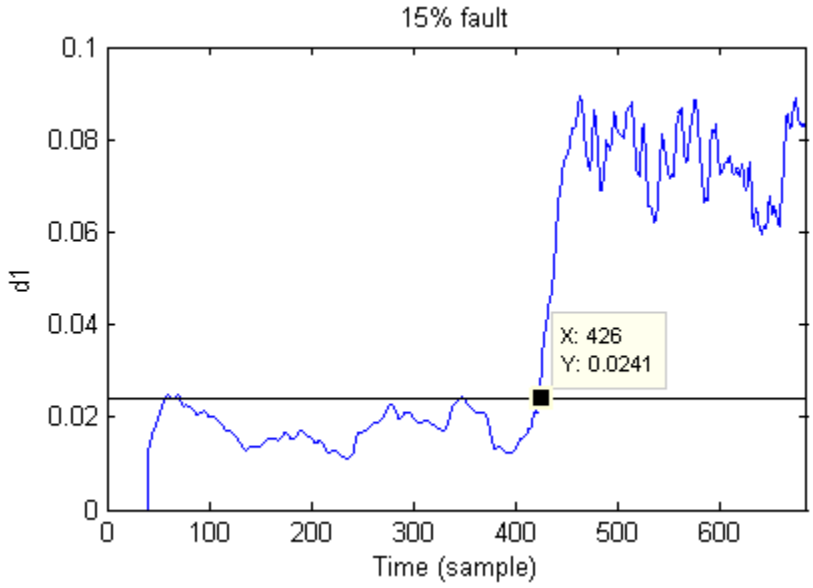

Figure 3.36 Residual d_1 in the centralized fault detection architecture with angular velocity measurement, for 15% reduction in the torque effectiveness of actuator x of spacecraft #1.

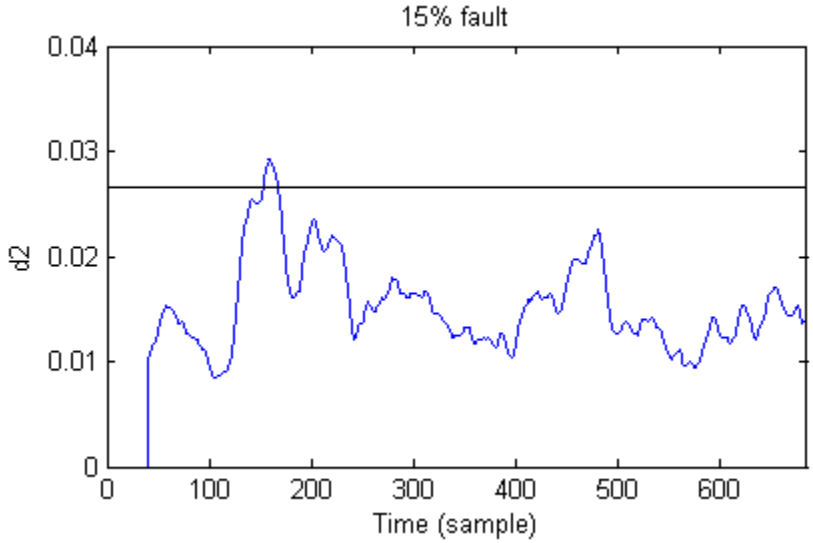

Figure 3.37 Residual d_2 in the centralized fault detection architecture with angular velocity measurement, for 15% reduction in the torque effectiveness of actuator x of spacecraft #1.

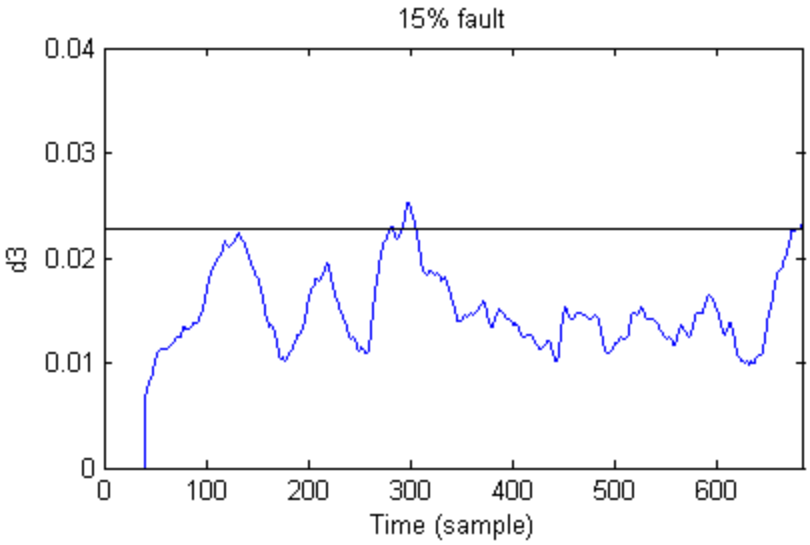

Figure 3.38 Residual d_3 in the centralized fault detection architecture with angular velocity measurement, for 15% reduction in the torque effectiveness of actuator x of spacecraft #1.

As can be seen in Figure 3.36 to Figure 3.38, the first time that a residual surpasses the threshold line after sample #406, has occurred for the residual d_1 of Figure 3.36 at sample #426. Therefore, sample #426 is the fault detection time. There are 20 samples delay in detecting the fault. In this scenario the fault is more severe than the last scenario, which leads to larger residual during the occurrence of the fault and smaller fault detection delay.

- **Confusion Matrix Results:**

Confusion matrix tables are computed based on Table 3.4, for 5%, 6%, 7%, 8%, 10%, 15%, 20%, and 25% reduction in the torque effectiveness of actuator x of spacecraft #1. The initial attitude condition for each spacecraft with respect to the reference frame is [-50, 35, 80] degree which is equal to [0.1337, 0.4676, 0.4582, 0.7440] in the quaternion. The initial condition for the formation is [29, 67, 8] degree which is equal to [0.1710, 0.5474, -0.0814, 0.8152] in the quaternion. The desired attitude for formation is [1, 1.5, 2]

degree which is equal to [0.0085, 0.0132, 0.0173, 0.9997] in the quaternion. The desired attitude of each spacecraft with respect to the formation frame is [18, 38, 39] degree which is equal to [0.0321, 0.3523, 0.2636, 0.8974] in the quaternion. The missions are 100 second (701 samples) long and the faults have occurred at $t = 50$ second (sample #358).

		Predicted	
		Faulty	Healthy
Actual	Faulty	196	147
	Healthy	85	273

Table 3.41. Confusion matrix for 5% reduction in the torque effectiveness.

		Predicted	
		Faulty	Healthy
Actual	Faulty	259	84
	Healthy	85	273

Table 3.42. Confusion matrix for 6% reduction in the torque effectiveness.

		Predicted	
		Faulty	Healthy
Actual	Faulty	276	67
	Healthy	85	273

Table 3.43. Confusion matrix for 7% reduction in the torque effectiveness.

		Predicted	
		Faulty	Healthy
Actual	Faulty	282	61
	Healthy	85	273

Table 3.44. Confusion matrix for 8% reduction in the torque effectiveness.

		Predicted	
		Faulty	Healthy
Actual	Faulty	287	56
	Healthy	85	273

Table 3.45. Confusion matrix for 10% reduction in the torque effectiveness.

		Predicted	
		Faulty	Healthy
Actual	Faulty	290	53
	Healthy	85	273

Table 3.46. Confusion matrix for 15% reduction in the torque effectiveness.

		Predicted	
		Faulty	Healthy
Actual	Faulty	290	53
	Healthy	85	273

Table 3.47. Confusion matrix for 20% reduction in the torque effectiveness.

		Predicted	
		Faulty	Healthy
Actual	Faulty	296	47
	Healthy	85	273

Table 3.48. Confusion matrix for 25% reduction in the torque effectiveness.

By using the equations (3.92)-(3.97) and based on the results of Table 3.41 to Table 3.48, the confusion matrix parameters are computed and presented in Table 3.49.

Centralized	$\gamma_1 = 25\%$	$\gamma_1 = 20\%$	$\gamma_1 = 15\%$	$\gamma_1 = 10\%$	$\gamma_1 = 8\%$	$\gamma_1 = 7\%$	$\gamma_1 = 6\%$	$\gamma_1 = 5\%$
Accuracy	%81.2	%80.6	%80.3	%79.9	%79.2	%78.3	%75.9	%66.9
False Healthy	%13.7	%14.9	%15.4	%16.3	%17.8	%19.5	%24.5	%42.9
True Faulty	%86.3	%85.1	%84.5	%83.7	%82.2	%80.5	%75.5	%57.1
True Healthy	%76.3	%76.3	%76.3	%76.3	%76.3	%76.3	%76.3	%76.3
False Faulty	%23.7	%23.7	%23.7	%23.7	%23.7	%23.7	%23.7	%23.7
Precision	%85.3	%84.3	%83.7	%83.0	%81.7	%80.3	%76.5	%65
Detection Time (Sample)	408	412	412	417	422	427	431	433

Table 3.49. Confusion matrix for the centralized architecture with angular velocity output.

According to Table 3.49, the accuracy, true faulty and precision parameters increase with increasing the fault severity and false healthy parameter decreases; as for higher severity faults, the residual deviation from zero becomes more significant and improves the fault detection results.

3.6.3.2. ATTITUDE MEASUREMENT

In this section, the results that are obtained by implementing the proposed

centralized fault detection architecture with attitude measurement are presented. According to equation (3.60), the centralized fault detection unit generates three residual evaluation functions $\{d_j \mid j=1,2,3\}=\{d_1,d_2,d_3\}$. By considering the worst case analysis of the residuals corresponding to the healthy operation of the satellites that are subject to the measurement noise, threshold values of $T_1=0.0140$, $T_2=0.0140$, and $T_3=0.0134$ are selected for the fault detection evaluation and analysis. To obtain these thresholds, 30 different missions are applied to the formation and the threshold value for each of these missions is calculated by using the equation (3.61). The mean value of the thresholds is considered as the final threshold.

Figure 3.39 to Figure 3.44 show the residual evaluation functions obtained by implementing the decentralized fault detection architecture. The initial attitude condition for each spacecraft with respect to the reference frame is [-58, -41, 66] degree which is equal to [0.3062, -0.7802, -0.2153, 0.5013] in the quaternion. The initial condition for the formation is [40, 60, 50] degree which is equal to [0.0700, 0.5508, 0.1890, 0.8100] in the quaternion. The desired attitude for formation is [1, 1.5, 2] degree which is equal to [0.0085, 0.0132, 0.0173, 0.9997] in the quaternion. The desired attitude of each spacecraft with respect to the formation frame is [9, 11, 2] degree which is equal to [0.0764, 0.0968, 0.0098, 0.9923] in the quaternion.

Figure 3.39 to Figure 3.41 represent the results that are obtained from 10% reduction in the torque effectiveness of actuator x of spacecraft #1, and Figure 3.42Figure 3.44 represent the results that are obtained from 20% reduction in the torque effectiveness of actuator x of spacecraft #1. The missions are 92 second (685 samples) long and the faults have occurred at $t=50$ second (sample #406). The solid horizontal lines show the threshold lines. The points that the residuals surpass the threshold lines

before sample #406, are considered as false alarms. The first moment that a residual surpasses the threshold line after sample #406 is considered as fault detection time which is shown with data cursor on the figure. The parameter X in the data cursor box shows the detection time, and the parameter Y shows the threshold value.

This window length is chosen by considering a trade-off between the fault detection delay and the number of false faulty detections. With increasing the window length, the number of false faulty detections will decrease, but the fault detection delay will increase. In our simulations, the window length M for equation (3.60) is selected as 40.

The solid horizontal lines show the threshold lines. The samples of d_j that surpass the threshold line before sample #406, the moment that fault has occurred, are considered as false faulty detection. The samples of d_j that do not surpass the threshold line before sample #406, the moment that fault has occurred, are considered as true healthy detection. The first moment that one of the residuals d_1, d_2, or d_3 surpass the threshold line, after sample #406, is considered as the fault detection time which is shown with the data cursor on the figure. The parameter X in the data cursor box shows the detection time, and the parameter Y shows the threshold value. The samples of d_j that do not surpass the threshold line, after sample #406, are considered as false healthy detection. The samples of d_j that surpass the threshold line, after sample #406, are considered as true healthy detection.

If all of these three residuals do not surpass the threshold line and detect a sample as a healthy sample, then the fault detection unit will consider that sample as a healthy sample. However, if at least one of the residuals surpasses the threshold line in a specific time, then the fault detection unit will consider that sample as a faulty sample.

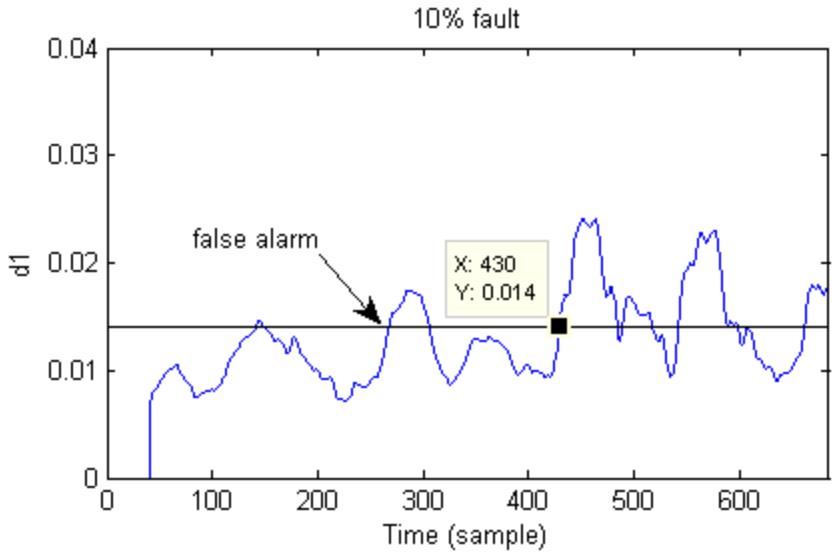

Figure 3.39 Residual d_1 in the centralized fault detection architecture with attitude measurement for 10% reduction in the torque effectiveness of actuator x of spacecraft #1.

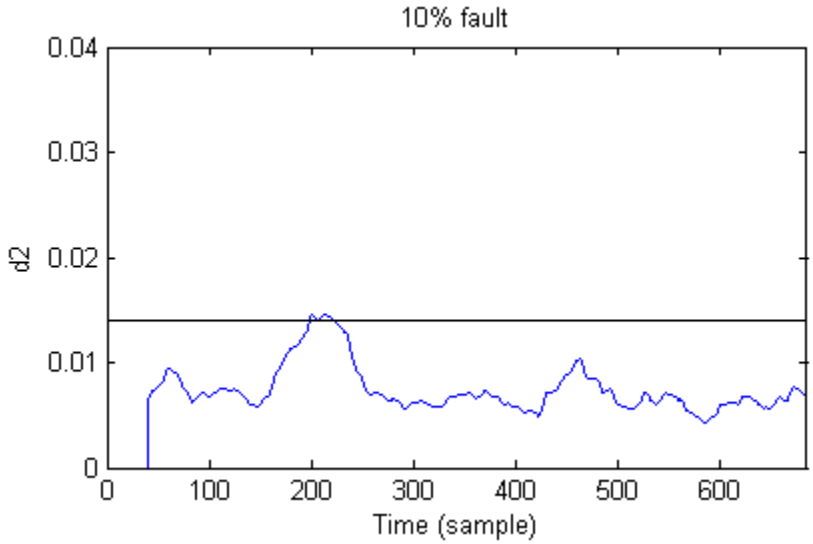

Figure 3.40 Residual d_2 in the centralized fault detection architecture with attitude measurement for 10% reduction in the torque effectiveness of actuator x of spacecraft #1.

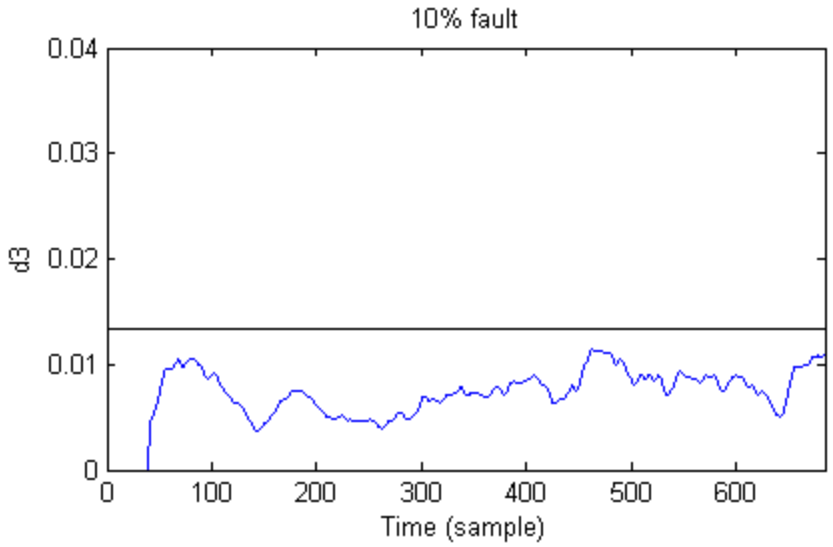

Figure 3.41 Residual d_3 in the decentralized fault detection architecture with attitude measurement for 10% reduction in the torque effectiveness of actuator x of spacecraft #1.

As can be seen in Figure 3.39 to Figure 3.41, the first time that a residual surpasses the threshold line after sample #406, has occurred for the residual d_1 of Figure 3.39 at sample #426. Therefore, sample #430 is the fault detection time. There are 24 samples delay in detecting the fault.

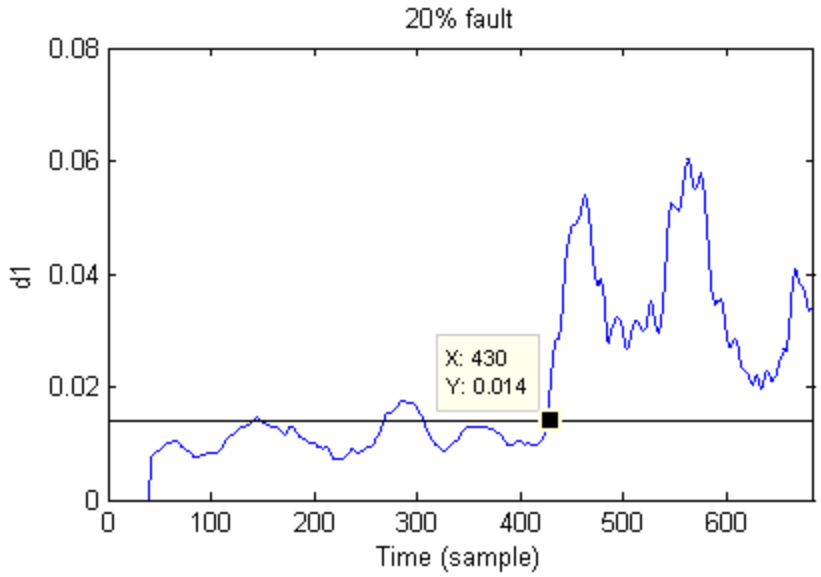

Figure 3.42 Residual d_1 in the centralized fault detection architecture with attitude measurement for 20% reduction in the torque effectiveness of actuator x of spacecraft #1.

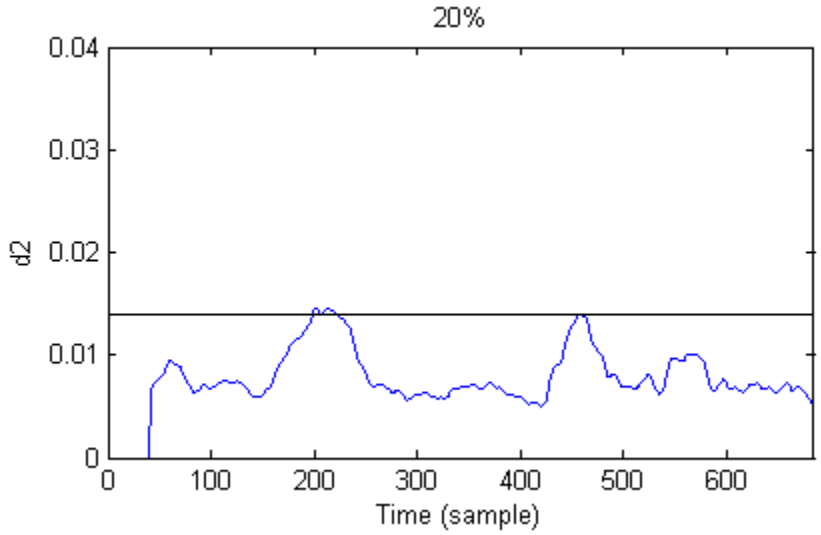

Figure 3.43 Residual d_2 in the centralized fault detection architecture with attitude measurement for 20% reduction in the torque effectiveness of actuator x of spacecraft #1.

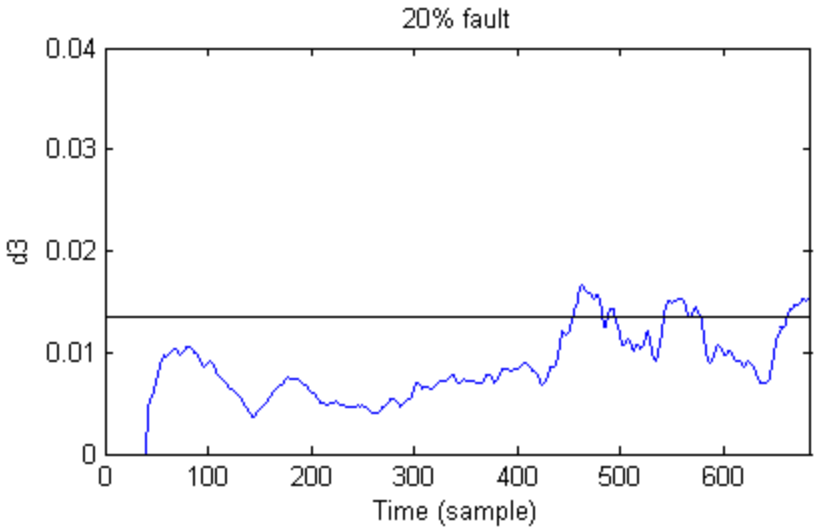

Figure 3.44 Residual d_3 in the centralized fault detection architecture with attitude measurement for 20% reduction in the torque effectiveness of actuator x of spacecraft #1.

As can be seen in Figure 3.42 to Figure 3.44, the first time that a residual surpasses the threshold line after sample #406, has occurred for the residual d_1 of Figure 3.42 at sample #426. Therefore, sample #430 is the fault detection time. There are 24 samples delay in detecting the fault. In this scenario the fault is more severe than the last scenario, which leads to larger residual during the occurrence of the fault.

- **Confusion Matrix Results:**

Confusion matrix tables are computed based on Table 3.4, for 5%, 6%, 7%, 8%, 10%, 15%, 20%, and 25% reduction in the torque effectiveness of actuator x of spacecraft #1. The initial attitude condition for each spacecraft with respect to the reference frame is [-50, 35, 80] degree which is equal to [0.1337, 0.4676, 0.4582, 0.7440] in the quaternion. The initial condition for the formation is [29, 67, 8] degree which is equal to [0.1710, 0.5474, -0.0814, 0.8152] in the quaternion. The desired attitude for formation is [1, 1.5, 2] degree which is equal to [0.0085, 0.0132, 0.0173, 0.9997] in the quaternion. The desired

attitude of each spacecraft with respect to the formation frame is [18, 38, 39] degree which is equal to [0.0321, 0.3523, 0.2636, 0.8974] in the quaternion. The missions are 100 second (701 samples) long, and the faults have occurred at $t = 50$ second (sample #358).

		Predicted	
		Faulty	Healthy
Actual	Faulty	52	291
	Healthy	35	323

Table 3.50. Confusion matrix for 5% reduction in the torque effectiveness.

		Predicted	
		Faulty	Healthy
Actual	Faulty	77	266
	Healthy	35	323

Table 3.51. Confusion matrix for 6% reduction in the torque effectiveness.

		Predicted	
		Faulty	Healthy
Actual	Faulty	97	246
	Healthy	35	323

Table 3.52. Confusion matrix for 7% reduction in the torque effectiveness.

		Predicted	
		Faulty	Healthy
Actual	Faulty	118	225
	Healthy	35	323

Table 3.53. Confusion matrix for 8% reduction in the torque effectiveness.

		Predicted	
		Faulty	Healthy
Actual	Faulty	153	190
	Healthy	35	323

Table 3.54. Confusion matrix for 10% reduction in the torque effectiveness.

		Predicted	
		Faulty	Healthy
Actual	Faulty	238	105
	Healthy	35	323

Table 3.55. Confusion matrix for 15% reduction in the torque effectiveness.

		Predicted	
		Faulty	Healthy
Actual	Faulty	275	68
	Healthy	35	323

Table 3.56. Confusion matrix for 20% reduction in the torque effectiveness.

		Predicted	
		Faulty	Healthy
Actual	Faulty	280	63
	Healthy	35	323

Table 3.57. Confusion matrix for 25% reduction in the torque effectiveness.

By using the equations (3.92)-(3.97) and based on the results of Table 3.50 to Table 3.57, the confusion matrix parameters are computed and presented in Table 3.58.

Centralized	$\gamma_1 = 25\%$	$\gamma_1 = 20\%$	$\gamma_1 = 15\%$	$\gamma_1 = 10\%$	$\gamma_1 = 8\%$	$\gamma_1 = 7\%$	$\gamma_1 = 6\%$	$\gamma_1 = 5\%$
Accuracy	86.0%	85.3%	80.0%	67.9%	62.9%	59.9%	57.1%	53.5%
False Healthy	18.4%	19.8%	30.6%	55.4%	65.6%	71.7%	77.5%	84.8%
True Faulty	81.6%	80.2%	69.4%	44.6%	34.4%	28.3%	22.4%	15.2%
True Healthy	90.2%	90.2%	90.2%	90.2%	90.2%	90.2%	90.2%	90.2%
False Faulty	9.8%	9.8%	9.8%	9.8%	9.8%	9.8%	9.8%	9.8%
Precision	83.7%	82.6%	75.5%	63.0%	58.9%	56.8%	54.8%	52.6%
Detection Time (Sample)	414	417	419	419	422	429	432	435

Table 3.58. Evaluating parameters of confusion matrix for centralized architecture with attitude output.

According to Table 3.58, the accuracy, true faulty and precision parameters increase with increasing the fault severity and the false healthy parameter decreases; as for the higher severity faults, residual deviation from zero becomes more significant and improves the fault detection results.

3.6.4. Performance Comparison of the Architectures Based on Confusion Matrix Results

In this section, the results that are obtained from the fault detection architectures are compared and discussed. In order to make a more objective comparison among the confusion matrix tables, the results are displayed with line charts.

3.6.4.1. ANGULAR VELOCITY MEASUREMENT

The confusion matrix parameters resulting from implementing the fault detection architectures on spacecraft formation flight with the angular velocity measurements are compared in this section.

Figure 3.45 displays the change of accuracy for decentralized, semi-decentralized, and centralized detection architectures. It shows that for low severity faults (5% loss of effectiveness), the centralized architecture has the highest accuracy among the three architectures. The second more accurate architecture for low severity faults is the semi-decentralized architecture. However, with increasing the severity of the fault, the decentralized architecture has more accurate detection results than the two other architectures. The accuracy of the semi-decentralized architecture for those faults is greater than the centralized architecture but so close together.

For faults with less than 8% loss of effectiveness, the accuracy change rate is much greater than the higher severity faults. For faults with loss of effectiveness more than 10%, the accuracy is almost constant.

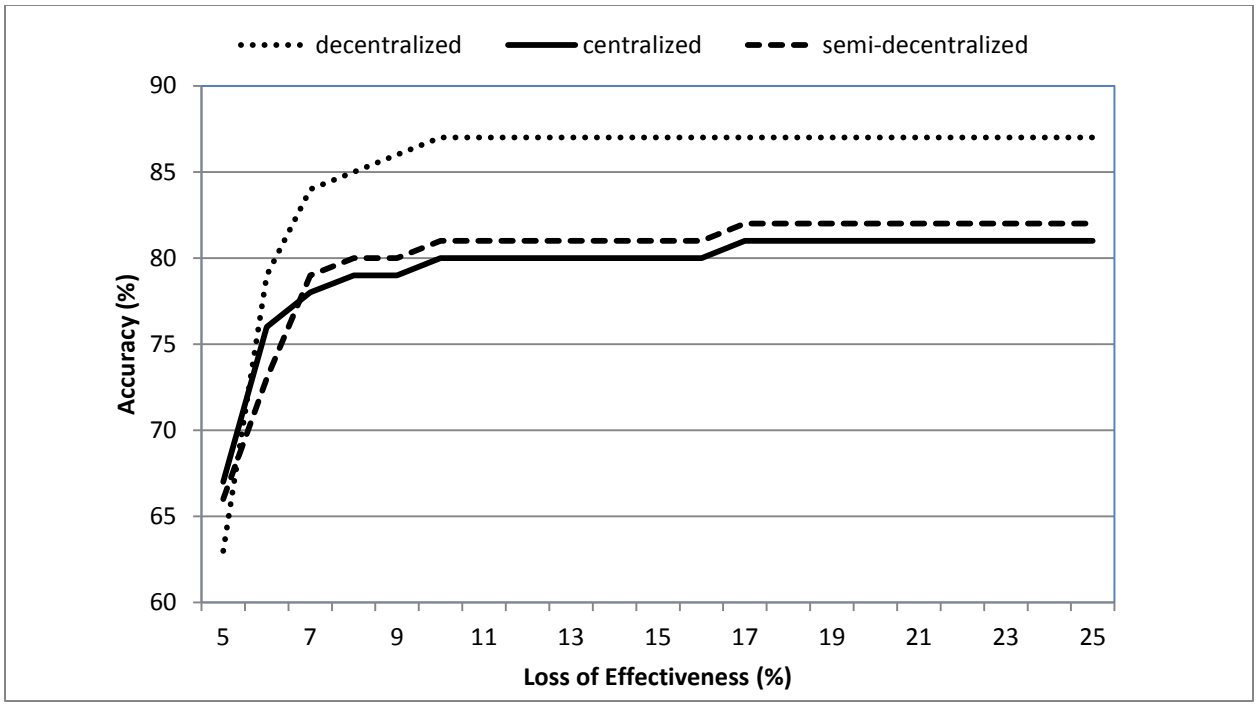

Figure 3.45 Comparison of the accuracy for the decentralized, semi-decentralized, and centralized architectures with angular velocity measurement.

Figure 3.46 shows the change of false healthy parameter for decentralized, semi-decentralized, and centralized architectures. According to this figure, the centralized architecture has the least false healthy misclassification for faults with loss of effectiveness less than 7%. The semi-decentralized architecture is the second architecture with less false healthy misclassification results for that severity of faults.

For faults with loss of effectiveness more than 7%, the centralized and semi-decentralized architectures show similar results. They demonstrate less false healthy misclassification than the decentralized architecture for faults between 7% and 13% loss of effectiveness. For faults with more than 13% loss of effectiveness, all of the three architectures have almost the same amount of false healthy misclassification.

For faults less than 8% loss of effectiveness, the false healthy change rate is much

greater than the higher severity faults. For faults with loss of effectiveness more than 14%, the false healthy result is almost constant.

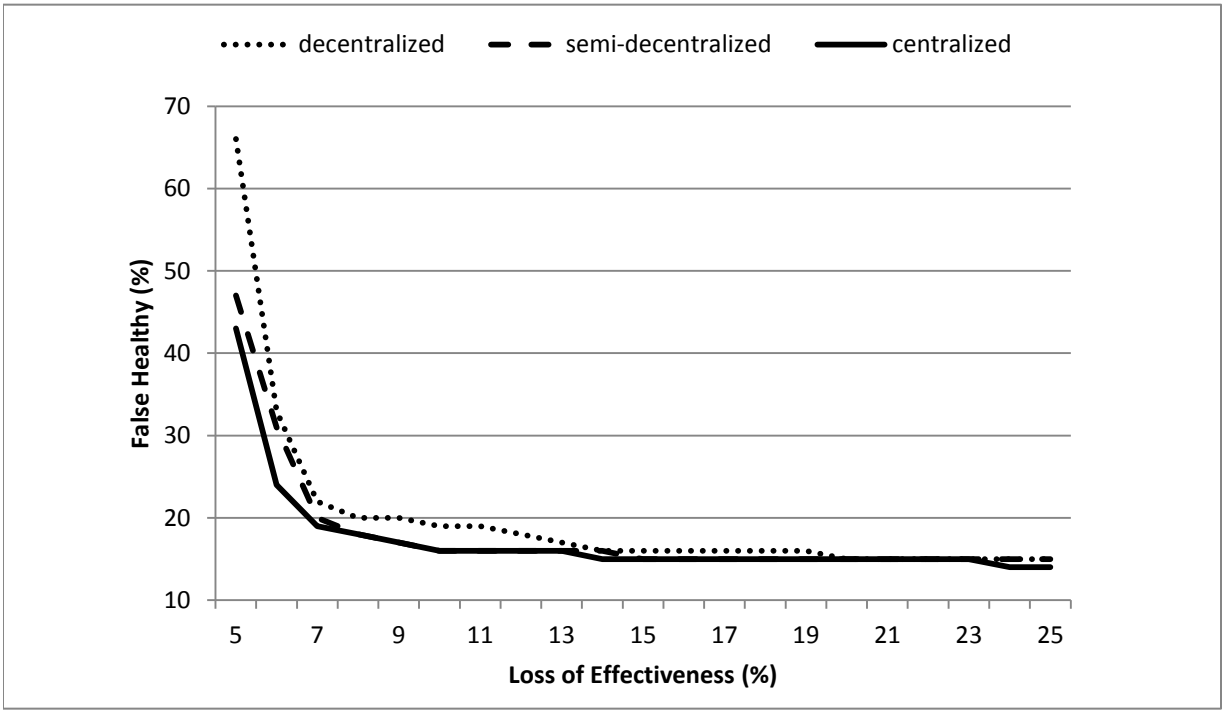

Figure 3.46 Comparison of the false healthy for the decentralized, semi-decentralized, and centralized architectures with angular velocity measurement.

Figure 3.47 shows the change of true faulty parameter for the decentralized, semi-decentralized, and centralized architectures. According to this figure, the centralized architecture has the highest true faulty detection for faults with loss of effectiveness less than 7%. The semi-decentralized architecture is the second architecture with higher true faulty results for that severity of faults.

For faults with loss of effectiveness more than 7%, the centralized and semi-decentralized architectures show similar results. They demonstrate more true fault detection than the decentralized architecture for faults between 7% and 13% loss of effectiveness. For the faults with more than 13% loss of effectiveness, all of the three

architectures have almost the same amount of true fault detection.

For faults with less than 8% loss of effectiveness, the true faulty change rate is much greater than higher severity faults. For faults with loss of effectiveness more than 14%, the true faulty result is almost constant.

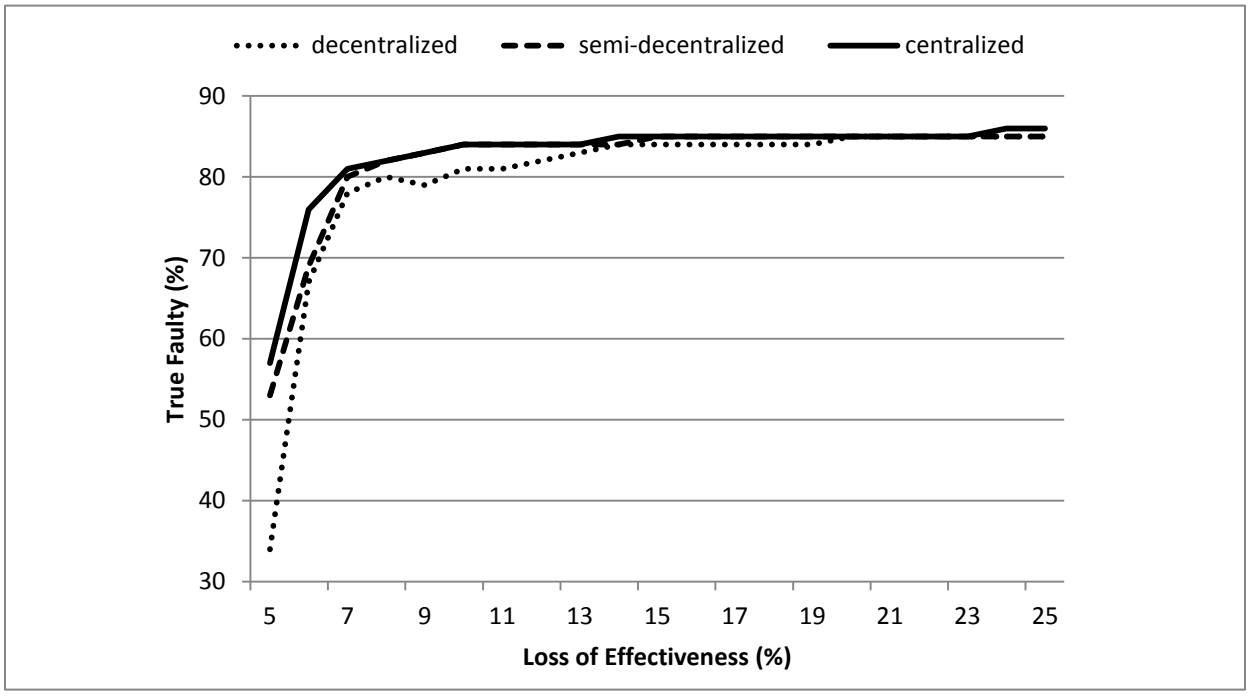

Figure 3.47 Comparison of the true faulty for the decentralized, semi-decentralized, and centralized architectures with angular velocity measurement.

Figure 3.48 shows the changes of the precision parameter for the decentralized, semi-decentralized, and centralized architectures. As can be seen in this figure, the centralized architecture has higher precision than the two other architectures for the faults less than 7% loss of effectiveness.

For faults more than 8% loss of effectiveness, the centralized and semi-decentralized architectures show the same results. The precision of the decentralized

architecture is more than the two other architectures for faults larger than 11% loss of effectiveness.

For faults with less than 8% loss of effectiveness, the precision change rate is much greater than for higher severity faults.

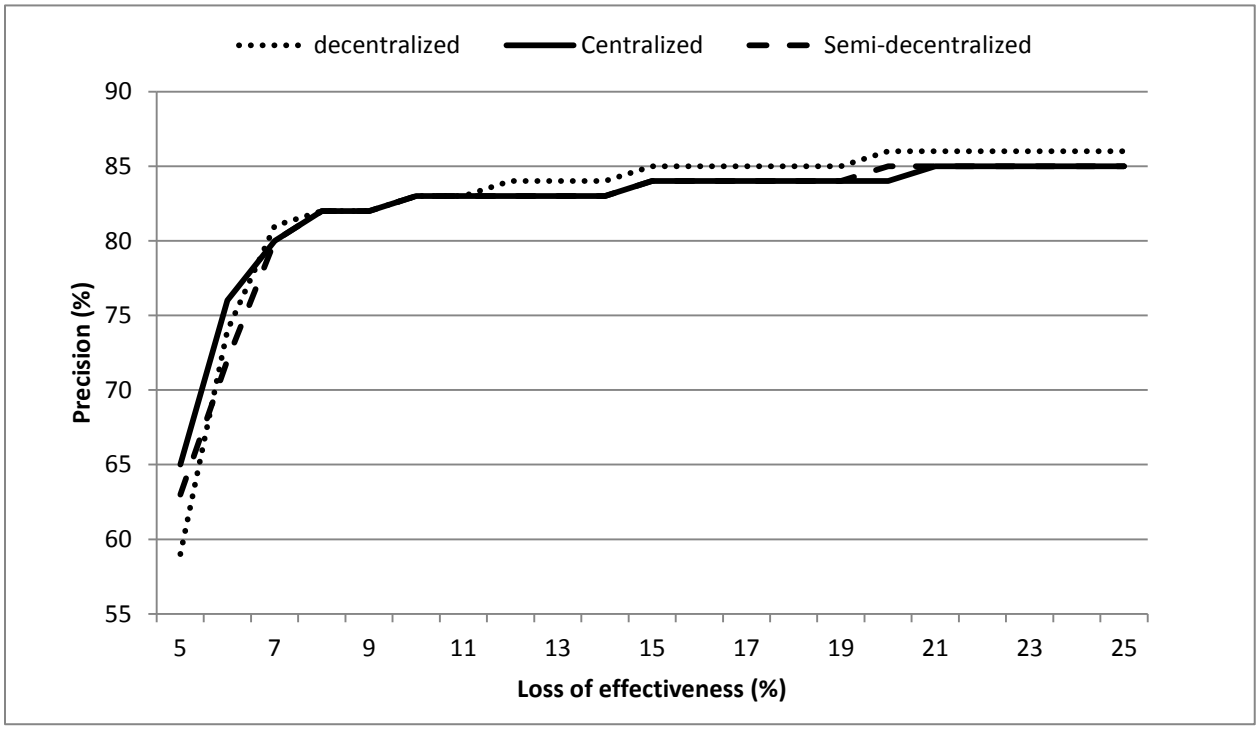

Figure 3.48 Comparison of the precision for the decentralized, semi-decentralized, and centralized architectures with angular velocity measurement.

Figure 3.49 shows the fault detection time delay for decentralized, semi-decentralized, and centralized architectures. According to this figure, the centralized architecture has the least time delay for all severity of faults. The performance of the semi-decentralized architecture is close to the centralized architecture. The decentralized architecture has the biggest time delays which increase faster with decreasing the fault.

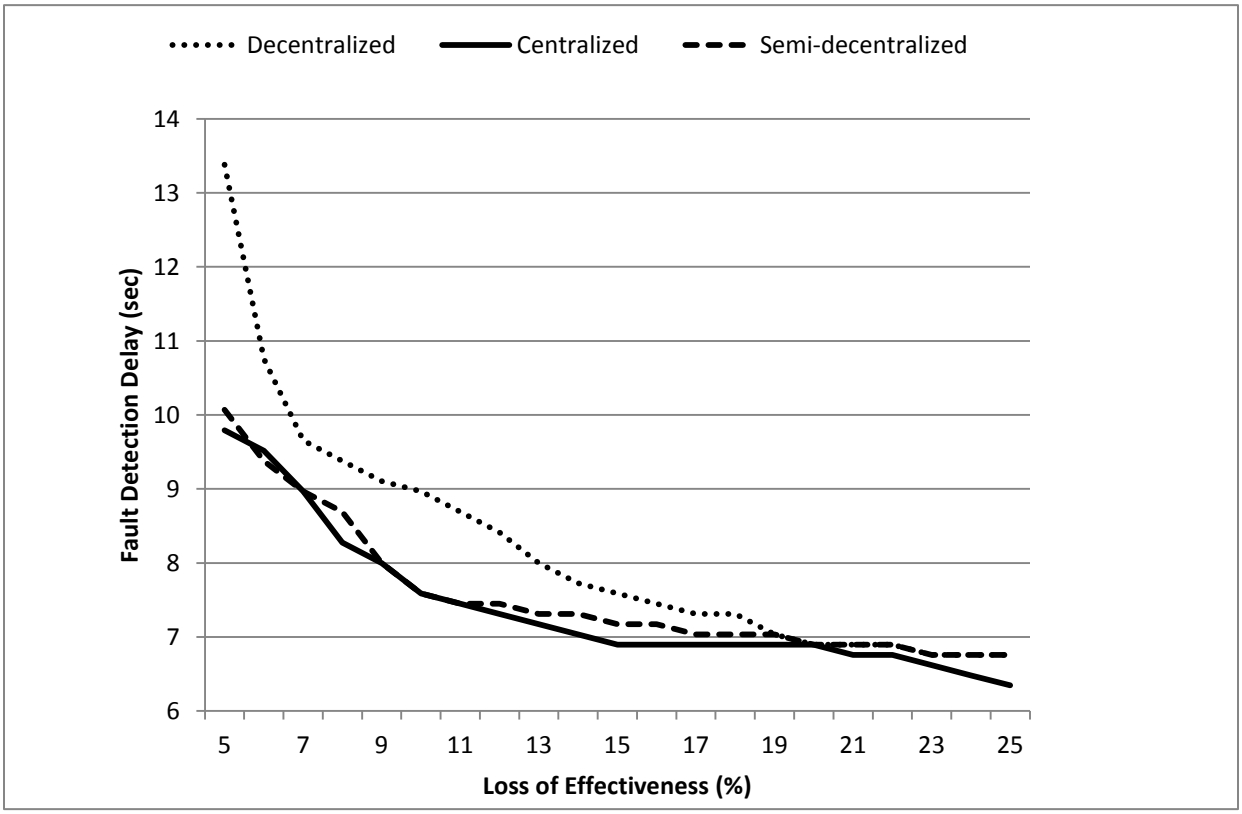

Figure 3.49 Comparison of the fault detection time delay for the decentralized, semi-decentralized, and centralized architectures with angular velocity measurement.

3.6.4.2. ATTITUDE MEASUREMENT

The confusion matrix parameters resulting from implementing the fault detection architectures on spacecraft formation flight with the attitude measurements are compared in this section.

Figure 3.50 displays the changes of accuracy for the decentralized, semi-decentralized, and centralized architectures with attitude measurements. As can be seen in this figure, the centralized architecture has the highest accuracy for all values of loss of effectiveness. For faults with less than 18% loss of effectiveness, the results of semi-decentralized architecture demonstrate more accuracy than the results of decentralized

architecture. However for faults with more than 18% loss of effectiveness, the decentralized architecture shows more accuracy than the semi-decentralized architecture.

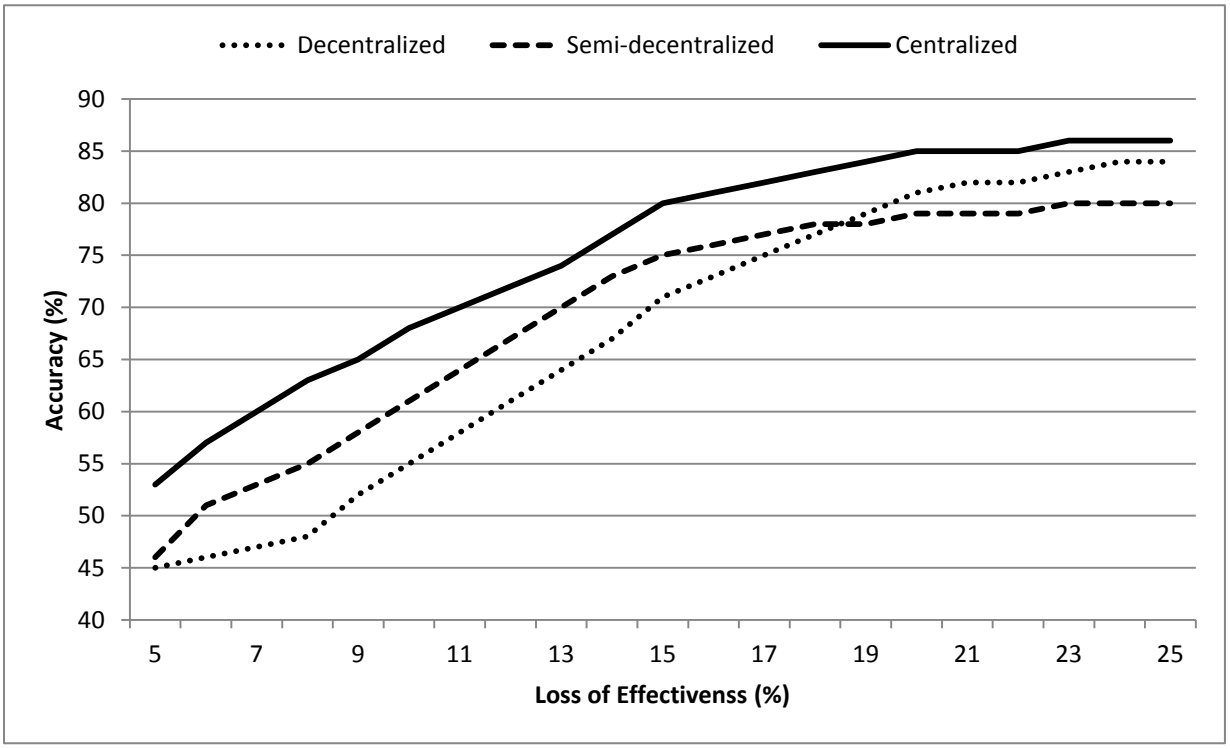

Figure 3.50 Comparison of the accuracy for the decentralized, semi-decentralized, and centralized architectures with attitude measurement.

Figure 3.51 displays the change of the false healthy parameter for the decentralized, semi-decentralized, and centralized architectures. According to this figure, the decentralized architecture has the highest amount of false healthy misclassification for all values of loss of effectiveness. The centralized and semi-decentralized architectures have similar results for false healthy parameter. With increasing the loss of effectiveness percentage, the performance of the decentralized architecture becomes closer to the performance of the semi-decentralized and centralized architectures.

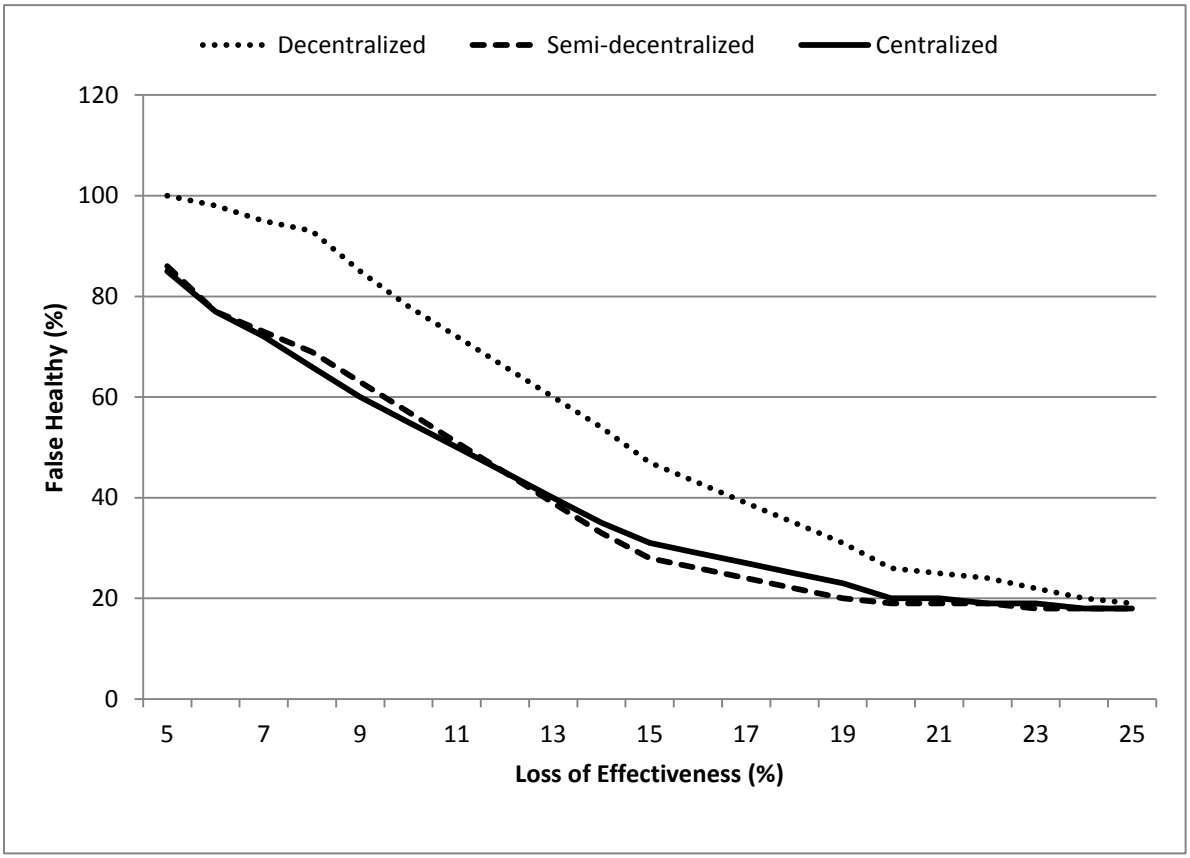

Figure 3.51 Comparison of the false healthy for the decentralized, semi-decentralized, and centralized architectures with attitude measurement.

Figure 3.52 displays the change of the true faulty parameter for decentralized, semi-decentralized, and centralized architectures. According to this figure, the centralized and semi-decentralized architectures have similar results for false healthy parameter and have the highest true faulty detection for all percentages of loss of effectiveness. With increasing the loss of effectiveness percentage, the performance of the decentralized architecture becomes closer to the performance of semi-decentralized and centralized architectures.

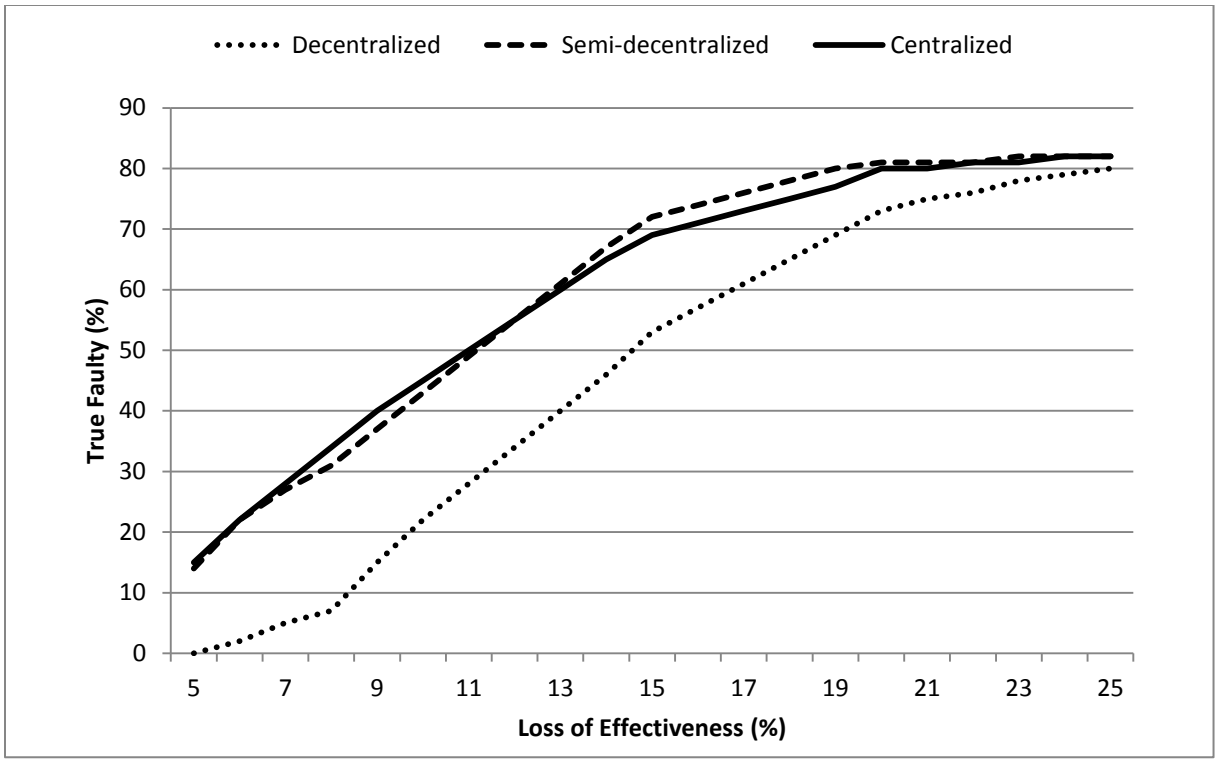

Figure 3.52 Comparison of the true faulty for the decentralized, semi-decentralized, and centralized architectures with attitude measurement.

Figure 3.53 shows the changes of precision for the decentralized, semi-decentralized, and centralized architectures. Based on this figure, the centralized architecture has the highest precision for all values of loss of effectiveness. The semi-decentralized architecture is the second architecture and the decentralized architecture is the last one based on the precision evaluation.

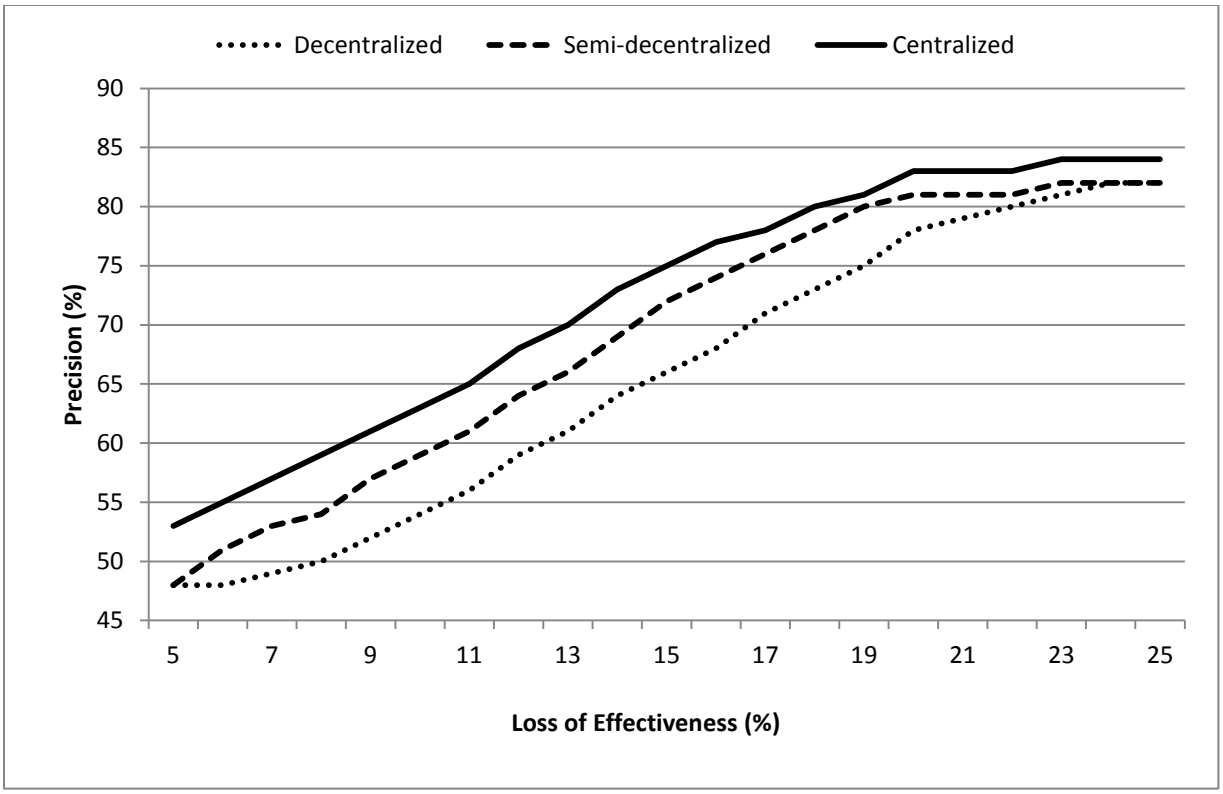

Figure 3.53 Comparison of the precision for the decentralized, semi-decentralized, and centralized architectures with attitude measurement.

Figure 3.54 displays the changes of fault detection time delay for the decentralized, semi-decentralized, and centralized architectures. According to this figure, the centralized architecture has the least amount of fault detection delay for all values of loss of effectiveness. The semi-decentralized performance is close to the centralized architecture, while the decentralized architecture shows the highest time delays for the fault detection.

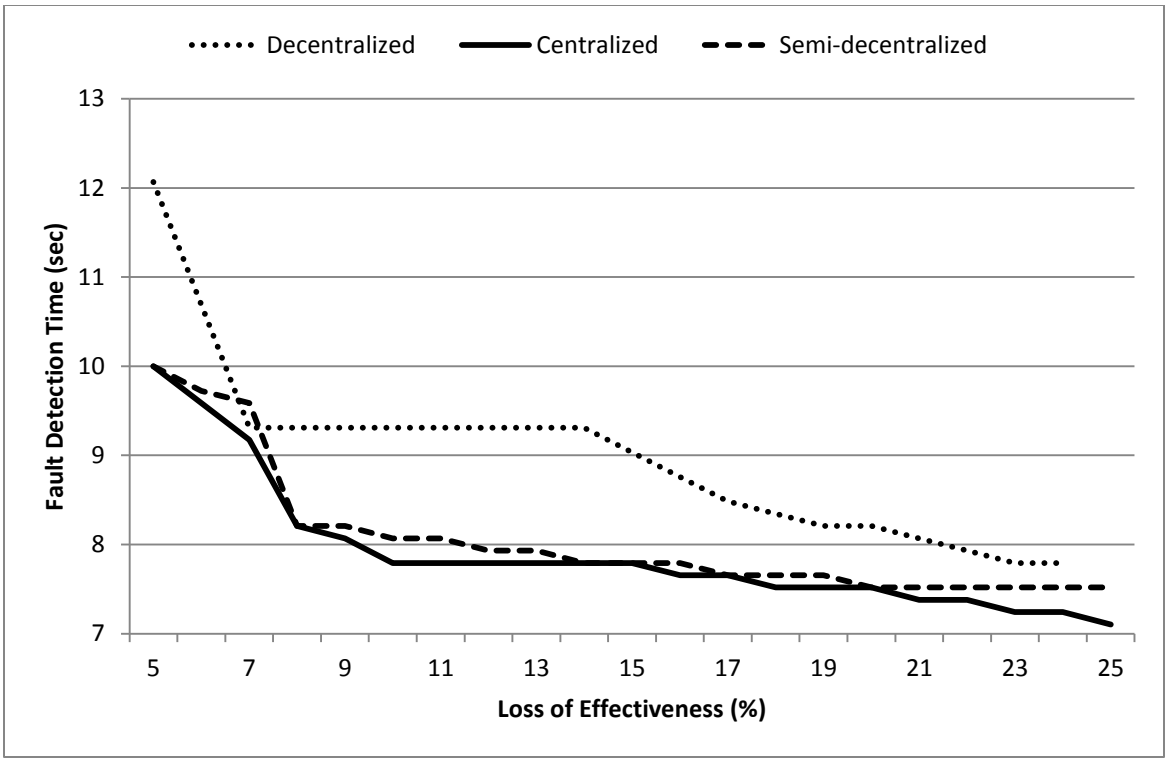

Figure 3.54 Comparison of the fault detection delay for the decentralized, semi-decentralized, and centralized architectures with attitude measurement.

3.6.5. Performance Comparison of the Attitude Measurement and the Angular Velocity Measurement

In this section, the fault detection results of spacecraft formation flight with angular velocity measurement and attitude measurement are compared. Accuracy, false healthy, true faulty, precision, and fault detection delay are the confusion matrix parameters that will be discussed for decentralized, semi-decentralized, and centralized architectures.

3.6.5.1. DECENTRALIZED ARCHITECTURE

Changes of accuracy, false healthy, true faulty and precision are respectively shown in Figure 3.55, Figure 3.56, Figure 3.57 and Figure 3.58. In all of these figures, the

spacecraft formation flight with angular velocity measurement demonstrates better performance than attitude measurement for all values of loss of effectiveness. With increasing the fault, their performance becomes closer. In angular velocity measurement, the parameters are changing fast for the faults with less than 8% loss of effectiveness, and for the more severe faults, the change rate is close to zero. However, the change rates of parameters in attitude measurement are almost constant for all values of loss of effectiveness.

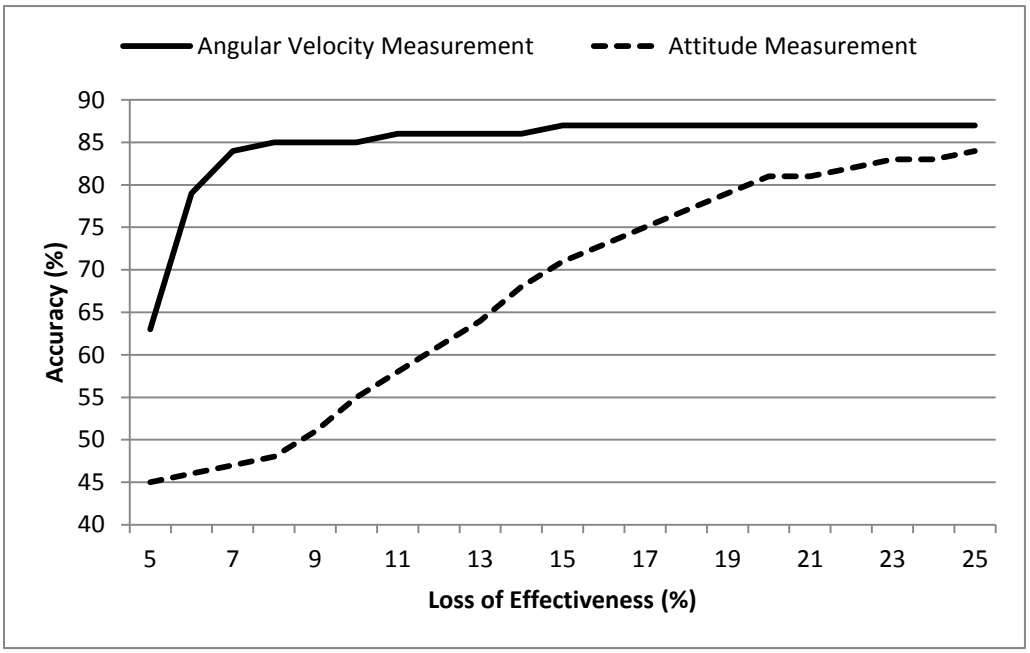

Figure 3.55 Comparing the accuracy of attitude and angular velocity measurement in the decentralized architecture.

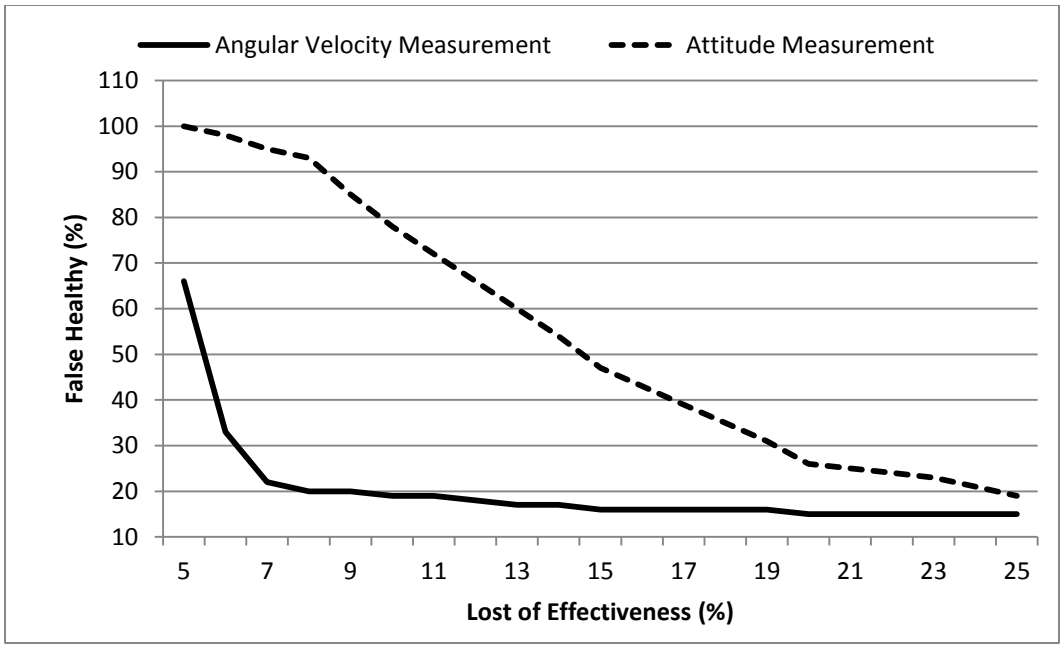

Figure 3.56 Comparing the false healthy of attitude and angular velocity measurement in the decentralized architecture.

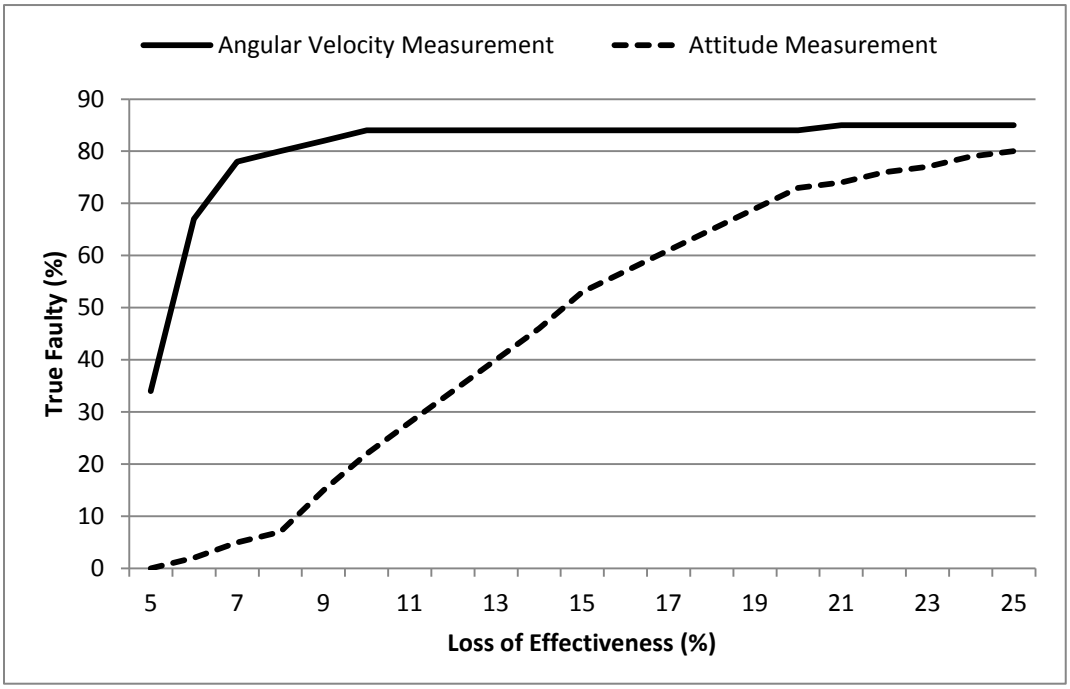

Figure 3.57 Comparing the true faulty of attitude and angular velocity measurement in the decentralized architecture.

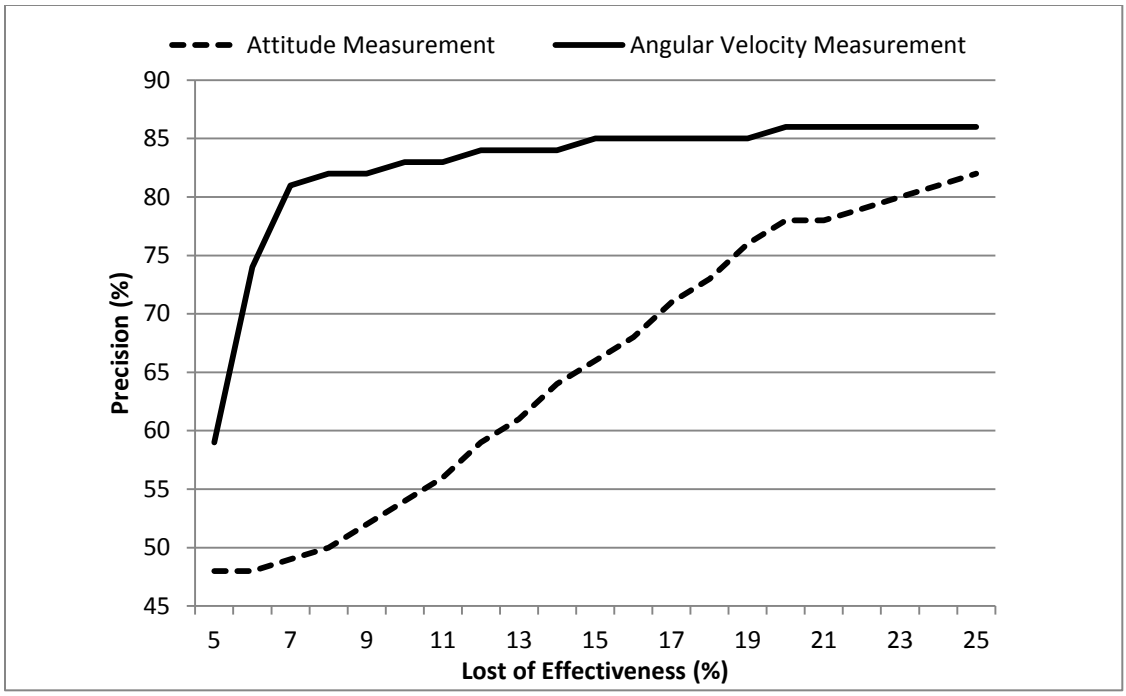

Figure 3.58 Comparing the precision of attitude and angular velocity measurement in the decentralized architecture.

Figure 3.59 shows the changes of fault detection delay. As can be seen in this figure, the attitude measurement has less fault detection delay for the faults with less than 6% loss of effectiveness. However, the angular velocity measurement shows better performance and less delay for the faults with more than 9% loss of effectiveness.

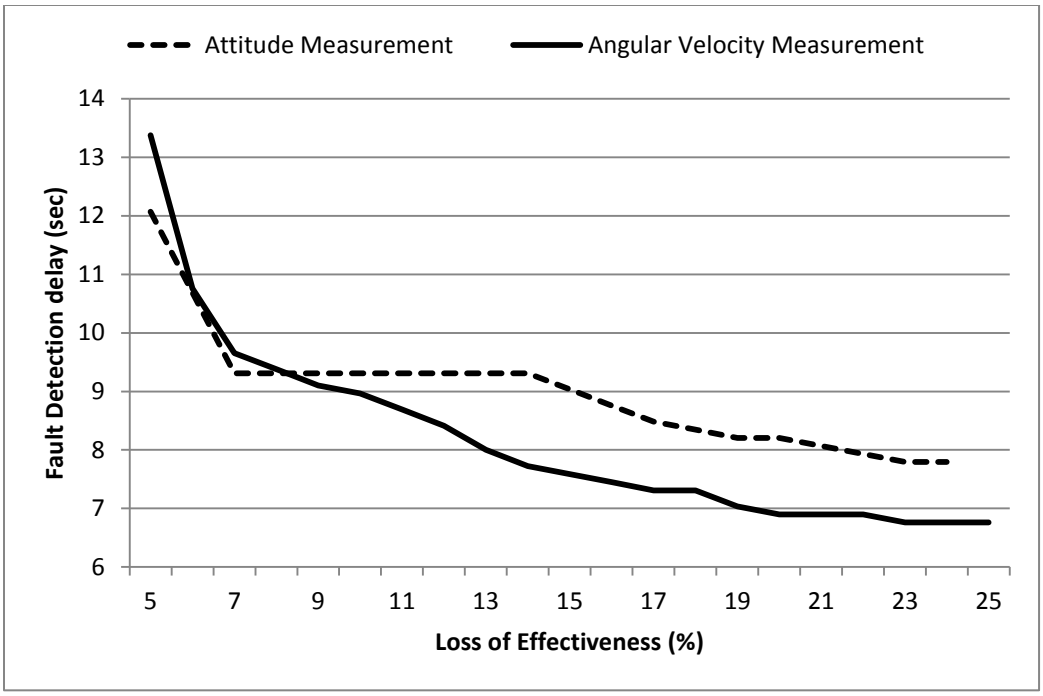

Figure 3.59 Comparing the fault detection delay of attitude and angular velocity measurement in the decentralized architecture.

3.6.5.2. SEMI-DECENTRALIZED ARCHITECTURE

Changes of accuracy, false healthy, true faulty and precision are respectively shown in Figure 3.60, Figure 3.61, Figure 3.62, and Figure 3.63.

In Figure 3.60, one can see that for faults with less than 16% loss of effectiveness, the angular velocity measurement has higher accuracy than the attitude measurement. However, for faults with more than 17% loss of effectiveness, the accuracy of attitude measurement is higher.

According to the Figure 3.61 to Figure 3.63, the change of false healthy, true faulty and precision parameters in a formation flight with angular velocity measurement are more acceptable than the attitude measurement. With increasing the severity of the fault, their performance becomes closer. In the angular velocity measurement, the

parameters are changing fast for those faults with less than 7% loss of effectiveness, and for the more severe faults, change rate is close to zero. However, the change rates of parameters in attitude measurement are almost constant for all values of loss of effectiveness.

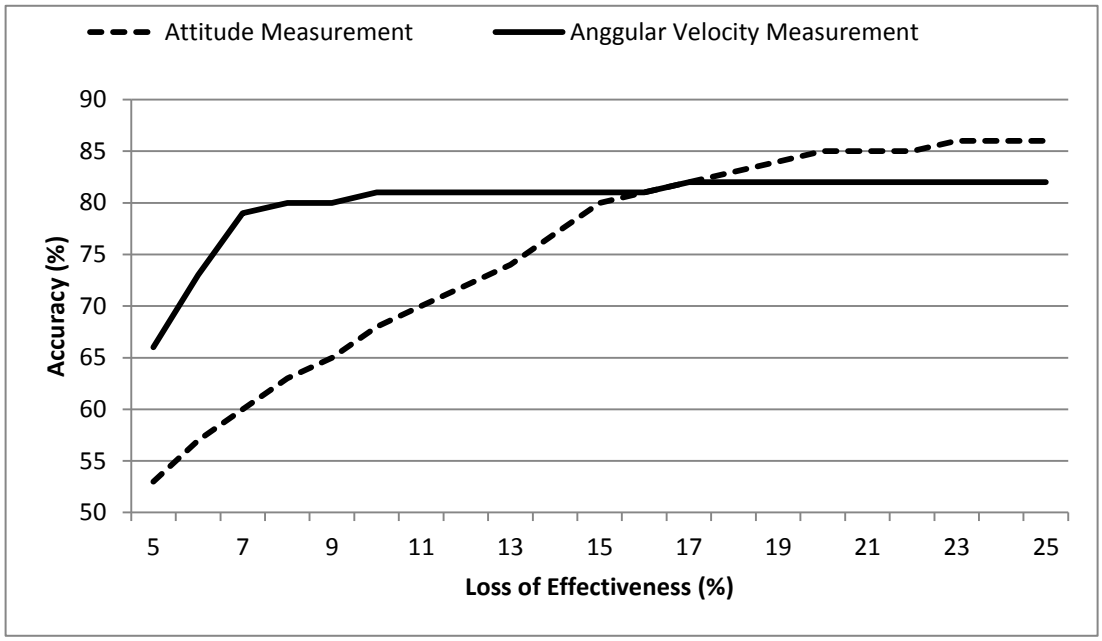

Figure 3.60 Comparing the accuracy of attitude and angular velocity measurement in the semi-decentralized architecture.

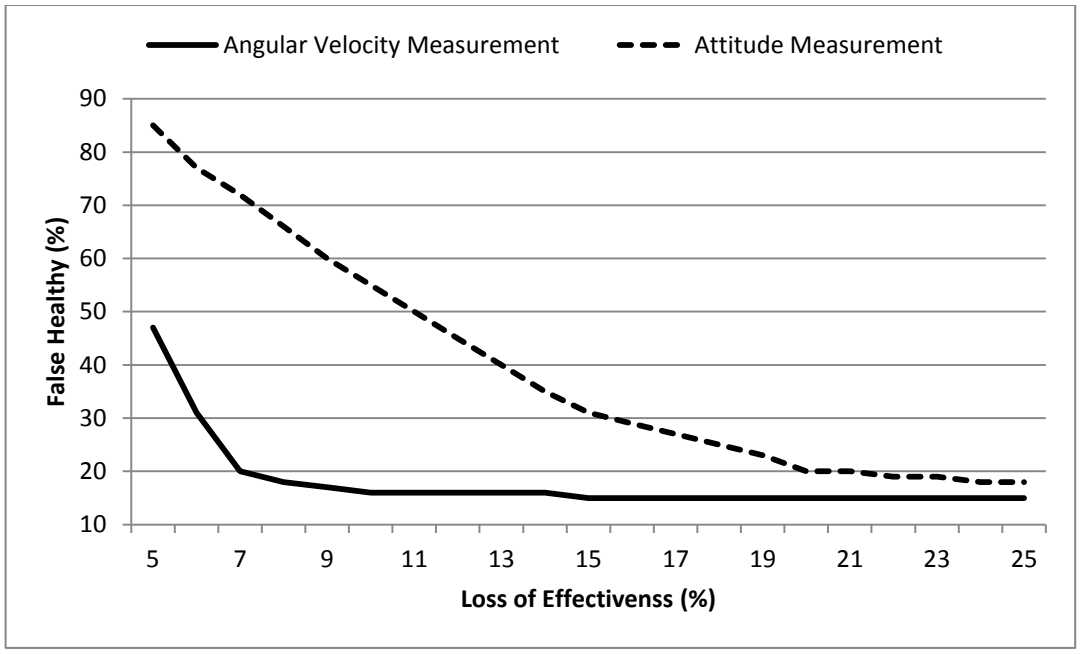

Figure 3.61 Comparing the false healthy of attitude and angular velocity measurement in the semi-decentralized architecture.

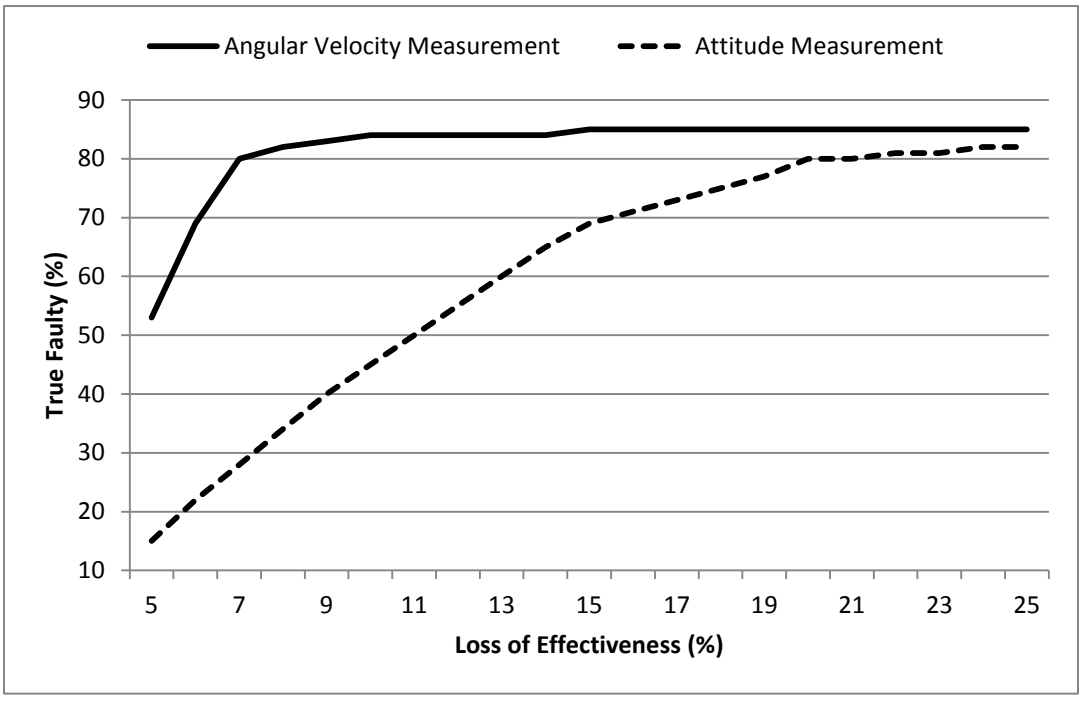

Figure 3.62 Comparing the true faulty of attitude and angular velocity measurement in the semi-decentralized architecture.

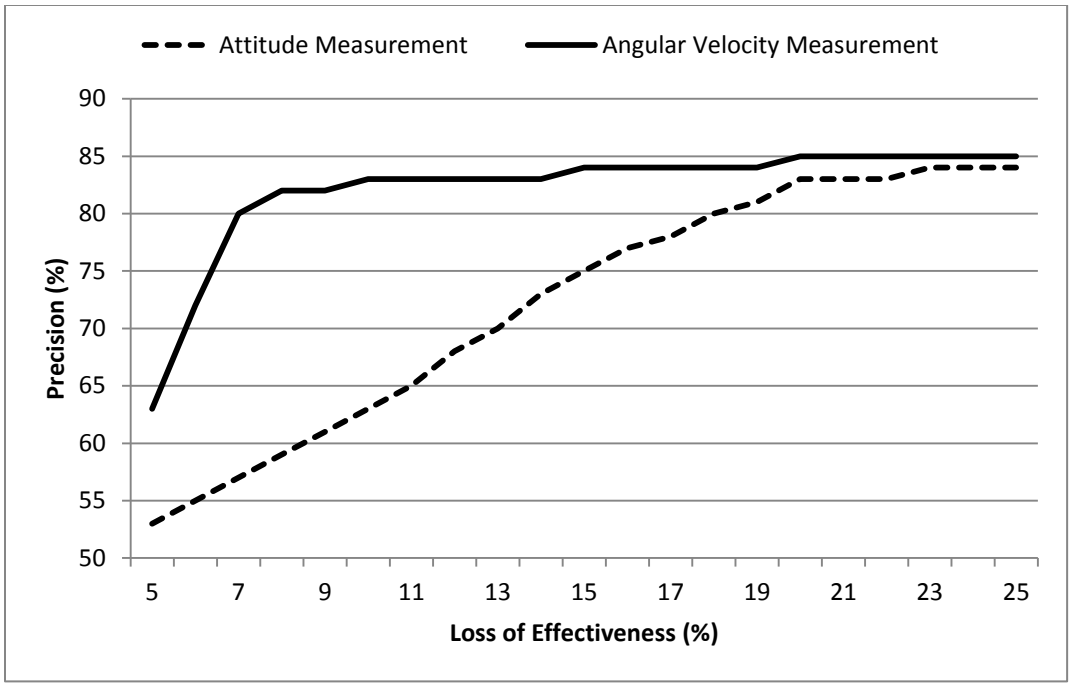

Figure 3.63 Comparing the precision of attitude and angular velocity measurement in the semi-decentralized architecture.

Figure 3.64 shows the fault detection delay. According to this figure, the detection delay in the angular velocity measurement is less than the detection delay in the attitude measurement for the faults severe than 9%. However, for fault less than 9%, their performance is fluctuating and is close together.

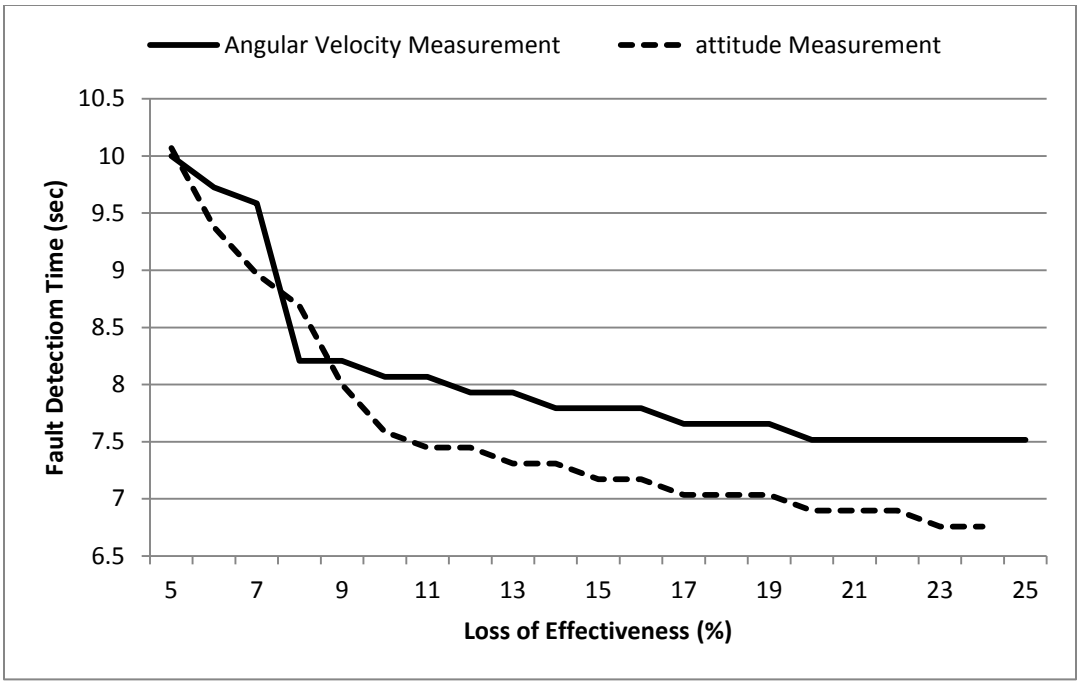

Figure 3.64 Comparing the fault detection time of attitude and angular velocity measurement in semi-decentralized architecture.

3.6.5.3. CENTRALIZED ARCHITECTURE

Changes of accuracy, false healthy, true faulty and precision are respectively shown in Figure 3.65, Figure 3.66, Figure 3.67 and Figure 3.68. In all of these figures, the spacecraft formation flight with the angular velocity measurement has better performance than the attitude measurement for all values of loss of effectiveness. With increasing the fault, their performance becomes closer. In angular velocity measurement, the parameters are changing fast for faults less than 8% loss of effectiveness and after that, the change rate is close to zero. However, the change rates of the parameters in the attitude measurement are almost constant for all values of loss of effectiveness.

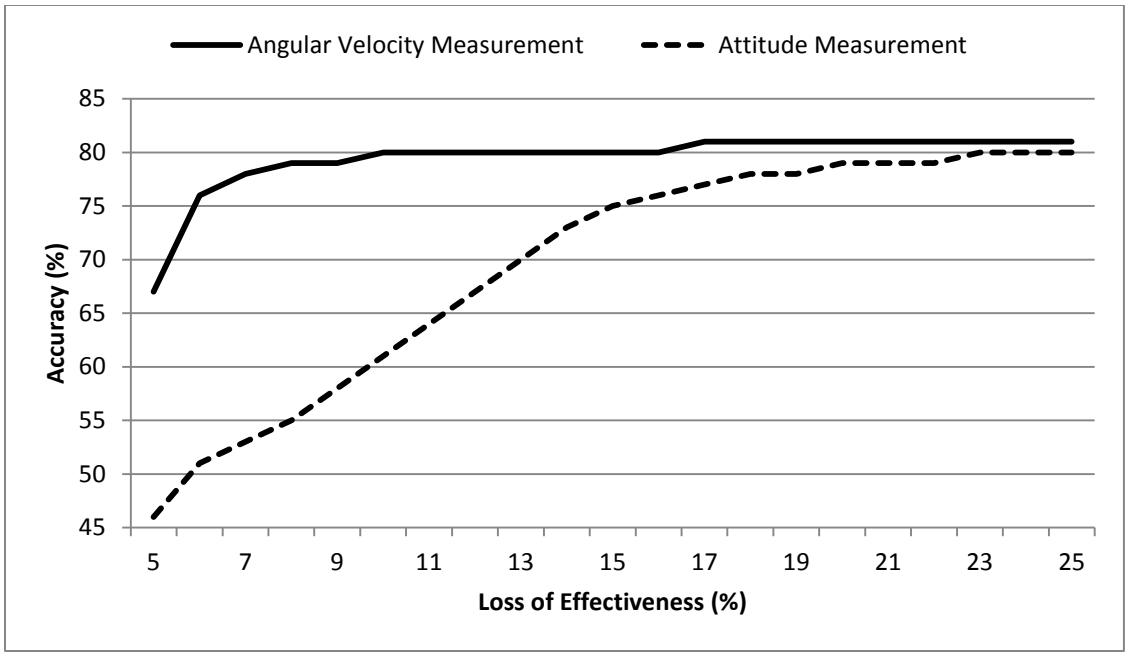

Figure 3.65 Comparing the precision of attitude and angular velocity measurement in the centralized architecture.

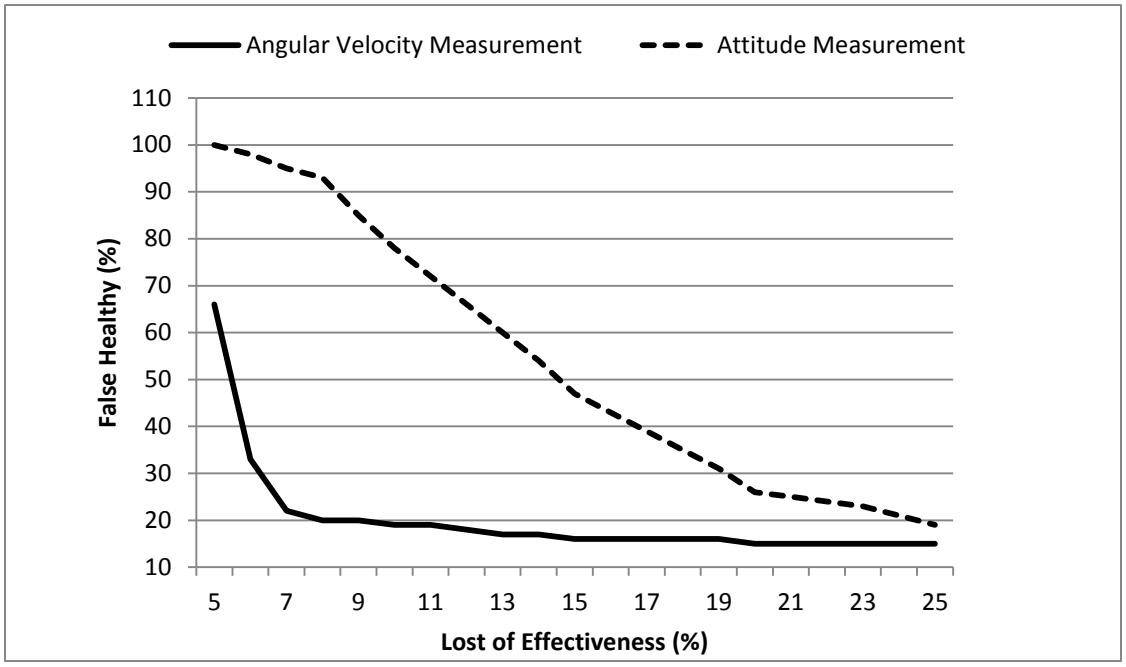

Figure 3.66 Comparing the false healthy of attitude and angular velocity measurement in the centralized architecture.

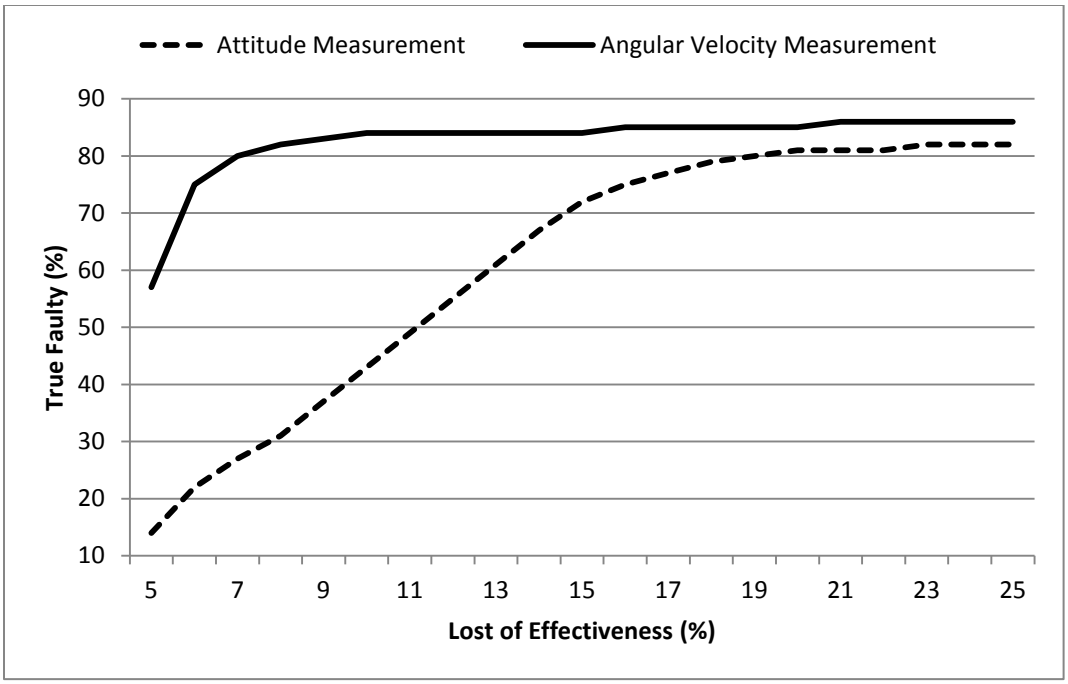

Figure 3.67 Comparing the true faulty of attitude and angular velocity measurement in the centralized architecture.

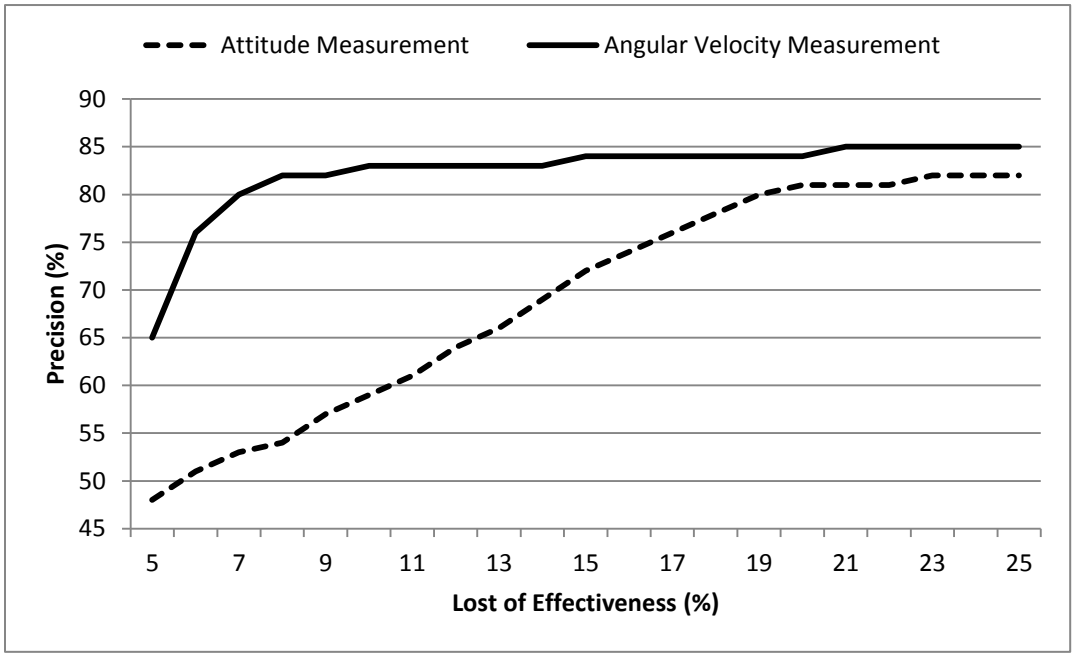

Figure 3.68 Comparing the precision of attitude and angular velocity measurement in the centralized architecture.

Figure 3.69 shows the changes of fault detection delay. According to this figure, for the faults with loss of effectiveness more than 10%, the formation with angular velocity measurement has more detection delay than the formation with attitude measurement. However, for faults less than 10%, the two measurements demonstrate close performance for the fault detection delay.

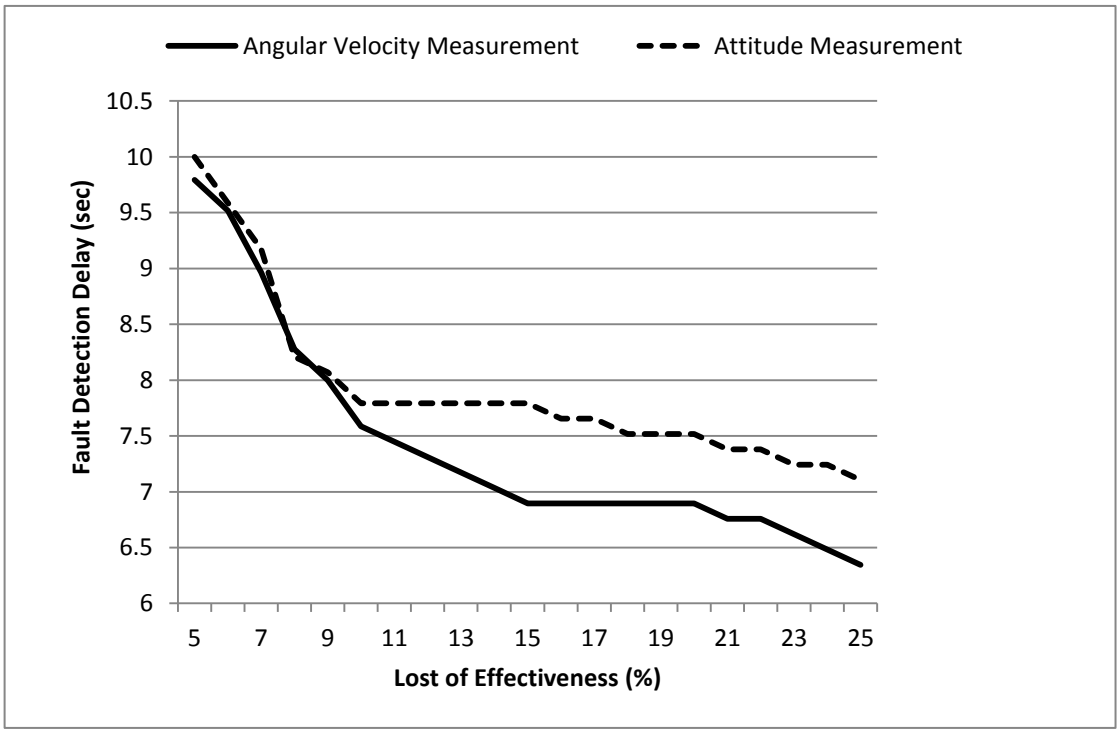

Figure 3.69 Line chart for comparing the fault detection delay of attitude and angular velocity measurement in centralized architecture.

In all three architectures, the figures related to the angular velocity measurement show higher reliability and performance than the attitude measurement.

3.7. CONCLUSION

In this chapter, to describe the formation flying model, graph theory concepts and notations are first explained; afterwards, the formation model for healthy and faulty situations are presented. Three fault detection architectures for spacecraft formation flying are introduced including: decentralized, semi-decentralized, and centralized architectures based on the extended Kalman filter. In the simulation section, first the simulation results obtained from controlling the formation flight of spacecraft by using the decentralized virtual structure approach are presented and discussed. The results show that the control approach provides a stable and precise formation, which can be utilized for testing our proposed fault detection method. The results that are obtained by implementing the fault detection architectures on formation flying mission are presented.

In the formation with angular velocity measurement, the fault detection delay of the centralized architecture is less than the two other architectures. Moreover, the semi-decentralized architecture has less fault detection delay relative to the decentralized architecture. The results also show the highest true faulty detections and the least false healthy misclassifications for centralized architecture. Moreover, the semi-decentralized architecture shows more satisfying results for true faulty and false healthy parameters relative to the decentralized architecture. The precision parameter does not display constant relative behaviors. For low severity faults (less than 7% loss of effectiveness), the centralized architecture has higher precision. Between 7% and 11% loss of effectiveness, the three architectures have the same precision, and after 11%, the decentralized architecture shows higher precision; while the precision of centralized and semi-decentralized architecture are equal for those faults. The accuracy of decentralized architecture is higher than the semi-decentralized architecture, and the

accuracy of semi-decentralized architecture is higher than the centralized architecture, for faults more than 6% loss of effectiveness. For lower severity faults, they show close accuracy performance. The false faulty and true healthy parameters present more desired performance for the decentralized architecture relative to the semi-decentralized, and for the semi-decentralized architecture relative to the centralized.

To summarize, in the formation with angular velocity measurement the centralized architecture has the most success in announcing the occurrence of faults, but it has also more false alarms relative to the two other architectures. Besides, the decentralized architecture has the least percentage in announcing the occurrence of faults, but it has also the least amount of false alarms.

In formations with attitude measurement, the fault detection delay of centralized architecture is less than the two other architectures. Moreover, the semi-decentralized architecture has less fault detection delay relative to the decentralized architecture. The true faulty and false healthy parameters have close behavior for the centralized and the semi-decentralized architectures. Their true faulty parameter is more than the true faulty parameter of decentralized architecture, and their false healthy parameter is less than the false healthy of decentralized architecture. The precision of the centralized architecture is more than the semi-decentralized, and the precision of the semi-decentralised architecture is more than the decentralized. The accuracy of centralized architecture is more than the semi-decentralized and decentralized architectures. The semi-decentralized architecture has higher accuracy than decentralized architecture for faults less than 18% loss of effectiveness. The false faulty and true healthy parameters have the best result in the centralized architecture. The decentralized architecture shows better results for these parameters relative to semi-decentralized architecture.

To summarize, in the formation with attitude measurement, the centralized architecture has the most success in announcing the occurrence of faults, and it has also the least number of false alarms relative to the two other architectures. Besides, the decentralized architecture has the least percentage in announcing the occurrence of faults and it has fewer false alarms relative to semi-decentralized architecture.

The final conclusion that can be made among the performance of the architectures is the better performance of the centralized architecture relative to the semi-decentralized and decentralized architectures. However, the higher cost of the centralized architecture should also be considered, which is the result of the larger amount of computations involved with this detection method. The semi-decentralized architecture shows more reliable performance relative to the decentralized architecture. However, its computation cost is also higher than the decentralized architecture.

The other conclusion that can be drawn from the results is the higher reliability of angular velocity measurement versus the attitude measurement in our fault detection method. In all three architectures, the results that are obtained from the angular velocity measurements show more desired performance for the accuracy, true faulty, false healthy, true healthy, false faulty, precision, and fault detection delay. This implies that the angular velocity sensors can make the missions more secure and safer, because the faults are more detectable by using the information provided with them.

Chapter 4: FAULT ISOLATION IN FORMATION FLIGHT OF SPACECRAFT

In this chapter, fault isolation algorithms are presented for isolating faults in decentralized, centralized, and semi-decentralized fault detection architectures which are proposed in Chapter 3. The objective of these algorithms is finding the exact location of fault in the formation based on evaluating the residual evaluation functions produced in the fault detection units.

In the first section of this chapter, the fault isolation concept and the techniques proposed in the literature are explained. In the next section, our isolation approach based on structured residual set technique is generated. The isolation method is developed for decentralized, centralized, and semi-decentralized architectures. At the end of the chapter, the simulation results that are obtained by implementing the methods on simulated spacecraft formation flight are provided.

4.1. FAULT ISOLATION

The successful detection of a fault is followed by the fault isolation procedure which will distinguish (isolate) a particular fault from the others. If a fault is distinguishable from other faults by using one residual set (or a residual vector), it can be said that this fault is isolable by using this residual set (or residual vector). In order to achieve the isolation, several principles exist; at least three different approaches can be distinguished as: fixed direction residuals, structured residuals, and structured hypothesis test [11].

The idea of fixed direction residuals [33] is to design a directional residual vector which lies in a fixed and fault-specified direction in the residual space, in response to a particular fault. This approach has not been used extensively in the literature because of the problems associated with designing a residual vector with desired properties.

The idea of structured residuals [96] is to design a set of structured residuals, where each residual is sensitive to a subset of faults and remains insensitive to the rest. The residual set which has the required sensitivity to specific faults and insensitivity to other faults is known as the structured residual set. Structured residuals have been widely used in the literature, in both theoretical and practical studies.

The basic idea of structured hypothesis test [97] is to construct the diagnosis system by combining a set of hypothesis tests. A structured hypothesis test is a generalization and formalization of the structured-residuals method. The procedure of how the isolation is formed from the residuals is formalized by using a standard interpretation of the functionality of each hypothesis test.

Following sections illustrate how the faults in spacecraft formation flying are isolated by using the structured residuals method and based on the residuals generated from the extended Kalman filter architectures.

4.2. FAULT ISOLATION BY USING THE STRUCTURED RESIDUAL SET

Assume a local extended Kalman filter for one single spacecraft. The innovation sequence generated from this EKF can be written as

$$e(t)=\begin{bmatrix} e_1(t) \\ e_2(t) \\ e_3(t) \end{bmatrix} \tag{4.1}$$

As discussed in Chapter 3, two types of output measurements can be considered for a spacecraft: the attitude measurement and the angular velocity measurement. The innovation sequence produced in extended Kalman filter is different for each of these measurements.

The innovation sequence obtained for the angular velocity measurements is given by

$$e(t)=\begin{bmatrix} e_1(t) \\ e_2(t) \\ e_3(t) \end{bmatrix}=\begin{bmatrix} \tilde{\omega} \\ \tilde{\omega} \\ \tilde{\omega} \end{bmatrix} \tag{4.2}$$

and the innovation sequence obtained for the attitude measurements is given by

$$e(t)=\begin{bmatrix} e_1(t) \\ e_2(t) \\ e_3(t) \end{bmatrix}=\begin{bmatrix} \tilde{q} \\ \tilde{q} \\ \tilde{q} \end{bmatrix} \tag{4.3}$$

The result of the occurrence of a fault in the actuator of a spacecraft is an undesired change in the torque of that actuator. According to the equation (2.16), it can be realized that the angular velocity parameters and quaternion parameters are not isolated, and changing the torque of one actuator can affect all parameters of the angular velocity and quaternion. But our simulation results show that changing the torque of the actuator of one axis have the most effect on the angular velocity around that specific axis. In the case of the attitude measurement, the innovation sequence vector (4.3) is based on the quaternion. Our simulation results also show that changing the torque of actuators x , y , and z have the most effect respectively on q_1, q_2, and q_3 . By using this fact, we propose our residual structured set method. At the end of this

chapter, we prove the truth of our claims by using the simulation results.

4.2.1. Fault Isolation in the Decentralized Architecture

In decentralized architecture, each spacecraft has an independent fault isolation (FI) unit which does not receive the output measurement or the control input information from other spacecraft in the formation.

Assume $J_i(t) \in R^3$ as the residual evaluation function obtained from the i-th FI unit of decentralized architecture described in Section 3.4.1, and the j-th entry of this vector is defined by $J_{ij}(t) = |e_{ij}(t)|$, where e_{ij} is the j-th innovation sequence of the i-th spacecraft. Using the arrays of this matrix we build our residual structured set.

The residual evaluation function obtained for the angular velocity measurements is given by

$$J_i(t) = \begin{bmatrix} J_{i1}(t) \\ J_{i2}(t) \\ J_{i3}(t) \end{bmatrix} = \begin{bmatrix} |e_{i1}(t)| \\ |e_{i2}(t)| \\ |e_{i3}(t)| \end{bmatrix} = \begin{bmatrix} |\omega_{i1} - \hat{\omega}_{i1}| \\ |\omega_{i2} - \hat{\omega}_{i2}| \\ |\omega_{i3} - \hat{\omega}_{i3}| \end{bmatrix} \tag{4.4}$$

and the residual evaluation function obtained for the attitude measurements is given by

$$J_i(t) = \begin{bmatrix} J_{i1}(t) \\ J_{i2}(t) \\ J_{i3}(t) \end{bmatrix} = \begin{bmatrix} |e_{i1}(t)| \\ |e_{i2}(t)| \\ |e_{i3}(t)| \end{bmatrix} = \begin{bmatrix} |q_{i1} - \hat{q}_{i1}| \\ |q_{i2} - \hat{q}_{i2}| \\ |q_{i3} - \hat{q}_{i3}| \end{bmatrix} \tag{4.5}$$

The mean value of $J_i(t)$ over the time window length of M can be obtained by

$$g_{ij}(m) = \frac{1}{M} \sum_{n=m-M+1}^{m} J_{ij}(n) \tag{4.6}$$

where m is the sample number and M is the window length.

In light of this illustration, it is convenient to introduce some notations. Fault f_{ij} is the occurrence of fault in the j-th actuator of spacecraft $\#i$. Our isolation method is based on the idea that the occurrence of fault f_{ij} causes g_{ij} to surpass the threshold T_{ij}. In this situation, the indicator r_{ij} changes from zero to one and announces the occurrence of fault in actuator $\#j$ of spacecraft $\#i$, that is

$$\begin{aligned} g_{ij}(m) > T_{ij} &\Rightarrow r_{ij}(m) = 1 \\ g_{ij}(m) < T_{ij} &\Rightarrow r_{ij}(m) = 0 \end{aligned} \tag{4.7}$$

The threshold T_{ij} is selected as the sum of the mean and standard deviation of g_{ij}. By considering the worst case analysis of g_{ij} corresponding to the healthy operation of spacecraft that are subject to the measurement noise, the thresholds are defined by

$$T_{ij} = mean\left(\left|g_{ij}(n)\right|\right) + \sqrt{\mathrm{var}\left(g_{ij}(n)\right)} \tag{4.8}$$

The simulation results that are obtained by implementing this isolation technique on the decentralized FI architecture of spacecraft formation flying is presented in Section 4.3.1.

4.2.2. Fault Isolation in the Semi-Decentralized Architecture

In the semi-decentralized architecture, each spacecraft has a fault isolation unit which receives the output measurement and control input information from the neighboring spacecraft. Consider the innovation sequence matrix $e_{|\bar{N}_i|}(t)$ defined in equations (3.33) and (3.34).

$$e_{\bar{N}_i(t)} = \begin{bmatrix} e_{1,\bar{N}_i,1}(t) & e_{1,\bar{N}_i,2}(t) & e_{1,\bar{N}_i,3}(t) \\ \vdots & \vdots & \vdots \\ e_{|\bar{N}_i|,\bar{N}_i,1}(t) & e_{|\bar{N}_i|,\bar{N}_i,2}(t) & e_{|\bar{N}_i|,\bar{N}_i,3}(t) \end{bmatrix} \tag{4.9}$$

where $e_{l,|\bar{N}_i|,j}(t)$ for the angular velocity measurements is given by

$$e_{l,|\bar{N}_i|,j}(t) = \omega_{l,|\bar{N}_i|,j} - \hat{\omega}_{l,|\bar{N}_i|,j} \tag{4.10}$$

and for the attitude measurements is given by

$$e_{l,|\bar{N}_i|,j}(t) = q_{l,|\bar{N}_i|,j} - \hat{q}_{l,|\bar{N}_i|,j} \tag{4.11}$$

In order to isolate the faults in the i-th semi-decentralized architecture of the formation, the three dimensional matrix $L^i \in \Re^{|\bar{N}_i|\times|\bar{N}_i|\times 3}$ is defined where each array is given by

$$L^i_{lkj}(t) = \left| e_{lj}(t) - e_{kj}(t) \right| \tag{4.12}$$

In the above definition, the effect of f^i_{lj} (fault of actuator $\#j$ of spacecraft $\#l$ in the semi-decentralized architecture $\#i$) on the k-th spacecraft of the formation is calculated, where $l,k \in \bar{N}_i$. The mean value of $L^i_{lkj}(t)$ over the time window length of M can be obtained by

$$g^i_{lkj}(m) = \frac{1}{M} \sum_{n=m-M+1}^{m} L^i_{lkj}(n) \tag{4.13}$$

where m is the sample number and M is the window length.

Using the test given below, the occurrence of faults in the i-th semi-decentralized

architecture can be isolated. The indicator r_{lj}^{i} changes from zero to one during the fault of f_{lj}^{i}, that is

$$\begin{aligned} &\left\{ g_{lkj}^{i} > T_{lkj}^{i} \mid \forall k \in \left\{ 1,\ldots \qquad : \neq l \right\} \right\} \Rightarrow r_{lj}^{i} = 1 \\ &\left\{ g_{lkj}^{i} < T_{lkj}^{i} \mid \exists k \in \left\{ 1,\ldots \qquad : \neq l \right\} \right\} \Rightarrow r_{lj}^{i} = 0 \end{aligned} \tag{4.14}$$

According to the above evaluation test, actuator $\#\, j$ of spacecraft $\#l$ in the semi-decentralized architecture $\#i$ is considered healthy if at least one g_{lkj}^{i} does not surpass the threshold. The threshold T_{lkj}^{i} is selected as the sum of the mean and standard deviation of g_{lkj}^{i}. By considering the worst case analysis of g_{lkj}^{i} corresponding to the healthy operation of spacecraft that are subject to the measurement noise, the thresholds are defined by

$$T_{lkj}^{i} = mean\left(\left| g_{lkj}^{i}\left(n \right) \right| \right) + \sqrt{\mathrm{var}\left(g_{lkj}^{i}\left(n \right) \right)} \tag{4.15}$$

The simulation results that are obtained by implementing this isolation technique on the semi-decentralized FD architecture of spacecraft formation flying is presented in Section 4.3.2.

4.2.3. Fault Isolation in the Centralized Architecture

In centralized architecture, one fault detection and isolation unit detects the faults that may occur in the actuators of all spacecraft in the formation.

Consider the innovation sequence matrix $e\left(t \right)$ defined in equations (3.50) and (3.51).

$$e(t)=\begin{bmatrix} e_{11}(t) & e_{12}(t) & e_{13}(t) \\ \vdots & \vdots & \vdots \\ e_{N1}(t) & e_{N2}(t) & e_{N3}(t) \end{bmatrix} \tag{4.16}$$

where $e_{ij}(t)$ for the angular velocity measurements is given by

$$e_{ij}(t)=\omega_{ij}-\hat{\omega}_{ij} \tag{4.17}$$

and for the attitude measurements is given by

$$e_{ij}(t)=q_{ij}-\hat{q}_{ij} \tag{4.18}$$

In order to isolate the faults in the formation, the three dimensional matrix $L\in\Re^{N\times N\times 3}$ is defined where each array is given by

$$L_{ikj}(t)=\left|e_{ij}(t)-e_{kj}(t)\right| \tag{4.19}$$

In the above definition, the effect of f_{ij} (fault of actuator $\#j$ of spacecraft $\#i$) on the k-th spacecraft of the formation is calculated, where $i,k\in\{1,\ldots$. The mean value of $L_{ikj}(t)$ over the time window length of M can be obtained by

$$g_{ikj}(m)=\frac{1}{M}\sum_{n=m-M+1}^{m}L_{ikj}(n) \tag{4.20}$$

where m is the sample number and M is the window length.

Using the test given below, the occurrence of fault can be declared in actuator $\#j$ of spacecraft $\#i$. In the faulty situation, the indicator r_{ij} changes from zero to one and shows the occurrence of fault f_{ij}. Based on this condition, actuator $\#j$ of spacecraft $\#i$

is considered healthy if at least one g_{ikj} does not surpass the threshold, that is

$$\begin{aligned} &\left\{ g_{ikj} > T_{ikj} \mid \forall k \in \{1,\ldots \qquad \vdots k \right\} \Rightarrow r_{ij} = 1 \\ &\left\{ g_{ikj} < T_{ikj} \mid \exists k \in \{1,\ldots \qquad \neq k \right\} \Rightarrow r_{ij} = 0 \end{aligned} \tag{4.21}$$

The threshold T_{ikj} is selected as the sum of the mean and standard deviation of g_{ikj}. By considering the worst case analysis of g_{ikj} corresponding to the healthy operation of spacecraft that are subject to the measurement noise, the threshold is defined by

$$T_{ikj} = mean\left(\left|g_{ikj}(n)\right|\right) + \sqrt{\mathrm{var}\left(g_{ikj}(n)\right)} \tag{4.22}$$

The simulation results that are obtained by implementing this isolation technique on the centralized FI architecture of spacecraft formation flying is presented in Section 4.3.3.

4.3. SIMULATION RESULTS

In order to present the simulation results, three sections are considered for numerical confusion matrix tables. These sections are entitled as decentralized isolation, semi-decentralized isolation, and centralized isolation. Each of these sections includes two different parts. The first part shows the results that are obtained by employing the isolation technique on the system with angular velocity measurement, and the second part shows the results that are obtained by employing the isolation technique on the system with attitude measurement. After these three sections, the results are discussed and compared in a new section.

The formation flight is controlled with virtual structure control topology. The spacecraft parameters, control gain parameters, disturbances, and noise in the

simulations are the same as the conditions applied for implementing the simulations in Chapter 3. The fault scenarios include 5%, 6%, 7%, 8%, 10%, 15%, 20% and 25% loss of effectiveness in torque of actuator x, y, and z of spacecraft #1. For each fault scenario, 100 detected faults are considered for isolation.

The spacecraft formation flying mission is the same as the mission considered for the fault detection scenarios. The initial attitude condition for each spacecraft with respect to the reference frame is [-50, 35, 80] degree which is equal to [0.1337, 0.4676, 0.4582, 0.7440] in the quaternion. The initial condition for the formation is [29, 67, 8] degree which is equal to [0.1710, 0.5474, -0.0814, 0.8152] in the quaternion. The desired attitude for formation is [1, 1.5, 2] degree which is equal to [0.0085, 0.0132, 0.0173, 0.9997] in the quaternion. The desired attitude of each spacecraft with respect to the formation frame is [18, 38, 39] degree which is equal to [0.0321, 0.3523, 0.2636, 0.8974] in the quaternion.

The fault isolation time is the same as the fault detection time, because our isolation techniques are based on logical evaluations and does not contain any time delay.

4.3.1. Decentralized Isolation Architecture

In this section, the results that are obtained by implementing the decentralized isolation technique are presented. The results are provided by using the confusion matrix tables. Table 4.1 shows the confusion matrix arrangement for the decentralized isolation.

Reduction in Effectiveness Factor (%)		Actual		
		f_{11}	f_{12}	f_{13}
Predicted	f_{11}	XX	XY	XZ
	f_{12}	YX	YY	YZ
	f_{13}	ZX	ZY	ZZ
Axis Accuracy (%)		Acc_1	Acc_2	Acc_3
Total Accuracy (%)		Acc		

Table 4.1. Confusion matrix for the decentralized isolation.

In Table 4.1, f_{ij} is the occurrence of fault in actuator $\#j$ of spacecraft $\#i$. Parameter XX is the number of f_{11} faults that are isolated correctly. Parameter YX is the number of f_{11} faults that are misclassified as f_{12} fault. Parameter ZX is the number of f_{11} faults that are misclassified as f_{13} fault. Parameter XY is the number of f_{12} faults that are misclassified as fault f_{11}. Parameter YY is the number of f_{12} faults that are isolated correctly. Parameter ZY is the number of f_{12} faults that are misclassified as fault f_{13}. Parameter XZ is the number of f_{13} faults that are misclassified as fault f_{11}. Parameter YZ is the number of f_{13} faults that are misclassified as fault f_{12}. Parameter ZZ is the number of f_{13} faults that are isolated correctly.

Parameter Acc_1 is the isolation accuracy for fault of actuator #1, parameter Acc_2 is the isolation accuracy for faults of actuator #2, and parameter Acc_3 is the isolation

accuracy for faults of actuator #3. Parameter Acc is the mean of isolation accuracies of the actuators [150].

$$Acc_1 = \frac{XX}{XX + YX + ZX} \tag{4.23}$$

$$Acc_2 = \frac{YY}{XY + YY + ZY} \tag{4.24}$$

$$Acc_3 = \frac{ZZ}{XZ + YZ + ZZ} \tag{4.25}$$

$$Acc = \frac{Acc_1 + Acc_2 + Acc_3}{3} \tag{4.26}$$

The faulty scenarios are first detected by using the decentralized fault detection architecture. For each faulty scenario, 100 detected faulty cases are tested.

Parameter M of equation (4.6), which is the window length, is set to 40 samples for our simulations. The thresholds are selected by using equation (4.7). For each threshold, 30 different healthy simulation missions of spacecraft that are subject to the measurement noise are executed and the threshold in each mission is calculated. Finally, the average of the thresholds is considered as the final threshold.

4.3.1.1. ANGULAR VELOCITY MEASUREMENT

In this section, the isolation results obtained from applying the decentralized isolation technique on spacecraft formation flying with angular velocity measurements are presented by confusion matrix tables. The thresholds are $T_{11} = 0.0080,\ T_{12} = 0.0085,\ T_{13} = 0.0074$. Table 4.2 to Table 4.9 display the results.

25% Reduction in Effectiveness Factor (%)		Actual		
		f_{11}	f_{12}	f_{13}
Predicted	f_{11}	99	0	0
	f_{12}	0	98	0
	f_{13}	1	2	100
Axis Accuracy (%)		99%	99%	100%
Total Accuracy (%)		99.33%		

Table 4.2. Confusion matrix for the decentralized isolation of 25% reduction in loss of effectiveness.

20% Reduction in Effectiveness Factor (%)		Actual		
		f_{11}	f_{12}	f_{13}
Predicted	f_{11}	99	0	0
	f_{12}	0	99	0
	f_{13}	1	1	100
Axis Accuracy (%)		99%	99%	100%
Total Accuracy (%)		99.33%		

Table 4.3. Confusion matrix for the decentralized isolation of 20% reduction in loss of effectiveness.

15% Reduction in Effectiveness Factor (%)		Actual		
		f_{11}	f_{12}	f_{13}
Predicted	f_{11}	99	0	0
	f_{12}	0	96	0
	f_{13}	1	4	100
Axis Accuracy (%)		98%	96%	97%
Total Accuracy (%)		97%		

Table 4.4. Confusion matrix for the decentralized isolation of 15% reduction in loss of effectiveness.

10% Reduction in Effectiveness Factor (%)		Actual		
		f_{11}	f_{12}	f_{13}
Predicted	f_{11}	95	2	5
	f_{12}	0	90	0
	f_{13}	5	8	95
Axis Accuracy (%)		95%	90%	95%
Total Accuracy (%)		93.33%		

Table 4.5. Confusion matrix for the decentralized isolation of 10% reduction in loss of effectiveness.

8% Reduction in Effectiveness Factor (%)		Actual		
		f_{11}	f_{12}	f_{13}
Predicted	f_{11}	95	6	7
	f_{12}	0	84	0
	f_{13}	5	10	93
Axis Accuracy (%)		95%	84%	93%
Total Accuracy (%)		90%		

Table 4.6. Confusion matrix for the decentralized isolation of 8% reduction in loss of effectiveness.

7% Reduction in Effectiveness Factor (%)		Actual		
		f_{11}	f_{12}	f_{13}
Predicted	f_{11}	95	4	7
	f_{12}	0	82	0
	f_{13}	5	14	93
Axis Accuracy (%)		95%	82%	93%
Total Accuracy (%)		88%		

Table 4.7. Confusion matrix for the decentralized isolation of 7% reduction in loss of effectiveness.

6% Reduction in Effectiveness Factor (%)		Actual		
		f_{11}	f_{12}	f_{13}
Predicted	f_{11}	95	10	7
	f_{12}	0	65	0
	f_{13}	5	25	93
Axis Accuracy (%)		95%	65%	93%
Total Accuracy (%)		84.33%		

Table 4.8. Confusion matrix for the decentralized isolation of 6% reduction in loss of effectiveness.

5% Reduction in Effectiveness Factor (%)		Actual		
		f_{11}	f_{12}	f_{13}
Predicted	f_{11}	93	17	8
	f_{12}	0	38	0
	f_{13}	7	45	92
Axis Accuracy (%)		93%	38%	92%
Total Accuracy (%)		74.33%		

Table 4.9. Confusion matrix for the decentralized isolation of 5% reduction in loss of effectiveness.

According to Table 4.2 to Table 4.9, with decreasing the loss of effectiveness percentage, the accuracy of fault isolation is reduced. It also shows that for the faults with less than 10% loss of effectiveness, the faults of actuator y are isolated with less amount of accuracy in comparison with the faults of actuators x and z. Small changes in the torque of actuator y has less effect on ω_{12} in comparison with the effect of the same changes in torque of actuator x on ω_{11}, and effect of the same changes in torque of actuator z on ω_{13}. This difference can cause an increase in the false healthy detection of low severity faults of actuator y in comparison with the same severity faults in actuator x and z. Therefore, the numbers of false faulty detections among the 100 faulty detected scenarios of actuator y are higher than the two other actuators. Then, lower accuracy of fault isolation for actuator y is the result of fault isolation for more false faulty detections comparing to actuators x and z.

4.3.1.2. ATTITUDE MEASUREMENT

In this section, the isolation results obtained from applying the decentralized isolation technique on spacecraft formation flying with attitude measurements are presented by confusion matrix tables. The thresholds are $T_{11} = 0.0106$, $T_{12} = 0.0099$, $T_{13} = 0.0090$. Table 4.10 to Table 4.17 display the results.

25% Reduction in Effectiveness Factor (%)		Actual		
		f_{11}	f_{12}	f_{13}
Predicted	f_{11}	77	0	5
	f_{12}	5	82	15
	f_{13}	18	18	80
Axis Accuracy (%)		77%	83%	80%
Total Accuracy (%)		80.33%		

Table 4.10. Confusion matrix for the decentralized isolation of 25% reduction in loss of effectiveness.

20% Reduction in Effectiveness Factor (%)		Actual		
		f_{11}	f_{12}	f_{13}
Predicted	f_{11}	89	0	0
	f_{12}	2	87	7
	f_{13}	9	13	93
Axis Accuracy (%)		89%	88%	93%
Total Accuracy (%)		90%		

Table 4.11. Confusion matrix for the decentralized isolation of 20% reduction in loss of effectiveness.

15% Reduction in Effectiveness Factor (%)		Actual		
		f_{11}	f_{12}	f_{13}
Predicted	f_{11}	88	0	0
	f_{12}	2	85	8
	f_{13}	10	15	92
Axis Accuracy (%)		89%	85%	92%
Total Accuracy (%)		88.33%		

Table 4.12. Confusion matrix for the decentralized isolation of 15% reduction in loss of effectiveness.

10% Reduction in Effectiveness Factor (%)		Actual		
		f_{11}	f_{12}	f_{13}
Predicted	f_{11}	88	0	1
	f_{12}	2	62	9
	f_{13}	10	38	90
Axis Accuracy (%)		88%	62%	90%
Total Accuracy (%)		80%		

Table 4.13. Confusion matrix for the decentralized isolation of 10% reduction in loss of effectiveness.

8% Reduction in Effectiveness Factor (%)		Actual		
		f_{11}	f_{12}	f_{13}
Predicted	f_{11}	85	3	2
	f_{12}	3	43	10
	f_{13}	12	54	88
Axis Accuracy (%)		85%	43%	88%
Total Accuracy (%)		72%		

Table 4.14. Confusion matrix for the decentralized isolation of 8% reduction in loss of effectiveness.

7% Reduction in Effectiveness Factor (%)		Actual		
		f_{11}	f_{12}	f_{13}
Predicted	f_{11}	79	3	2
	f_{12}	6	40	12
	f_{13}	15	57	86
Axis Accuracy (%)		79%	40%	86%
Total Accuracy (%)		68.66%		

Table 4.15. Confusion matrix for the decentralized isolation of 7% reduction in loss of effectiveness.

6% Reduction in Effectiveness Factor (%)		Actual		
		f_{11}	f_{12}	f_{13}
Predicted	f_{11}	73	5	3
	f_{12}	7	30	15
	f_{13}	20	65	82
Axis Accuracy (%)		73%	30%	82%
Total Accuracy (%)		62%		

Table 4.16. Confusion matrix for the decentralized isolation of 6% reduction in loss of effectiveness.

5% Reduction in Effectiveness Factor (%)		Actual		
		f_{11}	f_{12}	f_{13}
Predicted	f_{11}	60	5	3
	f_{12}	9	27	19
	f_{13}	31	68	78
Axis Accuracy (%)		60%	27%	78%
Total Accuracy (%)		55%		

Table 4.17. Confusion matrix for the decentralized isolation of 5% reduction in loss of effectiveness.

According to Table 4.10 to Table 4.17, for the faults with equal to and less than 20% severity, the faults of actuator y are isolated with less amount of accuracy in comparison with the faults of actuators x and z. The reason is similar to the reason explained for the angular velocity results. Small changes in the torque of actuator y has less effect on q_{12} in comparison with the effect of the same changes in torque of actuator x on q_{11}, and effect of the same changes in torque of actuator z on q_{13}. This difference can cause an increase in the false healthy detection of low severity faults of actuator y in comparison with the same severity faults in actuators x and z. Therefore, the numbers of false faulty detections among the 100 faulty detected scenarios of actuator y are higher than the two other actuators. Then, lower accuracy of fault isolation for actuator y is the result of fault isolation for more false faulty detections comparing to actuators x and z.

According to Table 4.10 to Table 4.17, with decreasing the loss of effectiveness percentage, the accuracy of fault isolation is reduced. But, this is true for the faults with equal to and less than 20% loss of effectiveness. Table 4.10, Table 4.11, and Table 4.12 show that the fault isolation accuracy for 25% fault is less 20% and 15% fault. The reason of this behavior change is the couplings that exist among the quaternions. The coupling effect is more significant for larger changes in the torque of the actuators. Therefore, with increasing the fault severity, the coupling effect will increase and can cause to more incorrect isolation. We name the increasing of isolation accuracy relative to the increasing of fault, as the normal behavior. Here, it can said that in the attitude measurement, the coupling effect overcome the normal behavior of isolation accuracy for the faults more than 15% loss of effectiveness.

4.3.2. Semi-decentralized Isolation Architecture

In this section, the results that are obtained by implementing the semi-

decentralized isolation technique on spacecraft #1 of formation flight are presented. The results are provided by using the confusion matrix tables. Table 4.18 shows the confusion matrix arrangement for the semi-centralized isolation.

In Table 4.18, f_{ij} is the occurrence of fault in actuator $\#j$ of spacecraft $\#i$. Parameter A_1 is the number of f_{11} faults that are isolated correctly. Parameter A_2 is the number of f_{11} faults that are misclassified as f_{12} fault. Parameter A_3 is the number of f_{11} faults that are misclassified as f_{13} fault. Parameter A_4 is the number of f_{11} faults that are misclassified as f_{21} fault. Parameter A_5 is the number of f_{11} faults that are misclassified as f_{22} fault. Parameter A_6 is the number of f_{11} faults that are misclassified as f_{23} fault. Parameter A_7 is the number of f_{11} faults that are misclassified as f_{31} fault. Parameter A_8 is the number of f_{11} faults that are misclassified as f_{32} fault. Parameter A_9 is the number of f_{11} faults that are misclassified as f_{33} fault.

Parameter B_1 is the number of f_{12} faults that are misclassified as f_{11} fault. Parameter B_2 is the number of f_{12} faults that are isolated correctly. Parameter B_3 is the number of f_{12} faults that are misclassified as f_{13} fault. Parameter B_4 is the number of f_{12} faults that are misclassified as f_{21} fault. Parameter B_5 is the number of f_{12} faults that are misclassified as f_{22} fault. Parameter B_6 is the number of f_{12} faults that are misclassified as f_{23} fault. Parameter B_7 is the number of f_{12} faults that are misclassified as f_{31} fault. Parameter B_8 is the number of f_{12} faults that are misclassified as f_{32} fault. Parameter B_9 is the number of f_{12} faults that are misclassified as f_{33} fault.

Parameter C_1 is the number of f_{13} faults that are misclassified as f_{11} fault. Parameter C_2 is the number of f_{13} faults that are misclassified as f_{12} fault. Parameter C_3

is the number of f_{13} faults that are isolated correctly. Parameter C_4 is the number of f_{13} faults that are misclassified as f_{21} fault. Parameter C_5 is the number of f_{13} faults that are misclassified as f_{22} fault. Parameter C_6 is the number of f_{13} faults that are misclassified as f_{23} fault. Parameter C_7 is the number of f_{13} faults that are misclassified as f_{31} fault. Parameter C_8 is the number of f_{13} faults that are misclassified as f_{32} fault. Parameter C_9 is the number of f_{13} faults that are misclassified as f_{33} fault.

Parameter Acc_1 is the isolation accuracy for fault of actuator #1, parameter Acc_2 is the isolation accuracy for faults of actuator #2, and parameter Acc_3 is the isolation accuracy for faults of actuator #3. Parameter Acc is the mean of isolation accuracies of the actuators.

$$Acc_1 = \frac{A_1}{A_1 + A_2 + A_3 + A_4 + A_5 + A_6 + A_7 + A_8 + A_9} \tag{4.27}$$

$$Acc_2 = \frac{B_2}{B_1 + B_2 + B_3 + B_4 + B_5 + B_6 + B_7 + B_8 + B_9} \tag{4.28}$$

$$Acc_3 = \frac{C_3}{C_1 + C_2 + C_3 + C_4 + C_5 + C_6 + C_7 + C_8 + C_9} \tag{4.29}$$

$$Acc = \frac{Acc_1 + Acc_2 + Acc_3}{3} \tag{4.30}$$

The faulty scenarios are first detected by using the semi-decentralized fault detection architecture. For each faulty scenario, 100 detected faulty cases are tested.

Parameter M of equation (4.13), which is the window length, is set to 40 samples for our simulations. The thresholds are selected by using the equation (4.15). For each threshold, 30 different healthy simulation missions of spacecraft that are subject to the

measurement noise are executed and the threshold in each mission is calculated. Finally, the average of the thresholds is considered as the final threshold.

Reduction in Effectiveness Factor (%)		Actual		
		f_{11}	f_{12}	f_{13}
Predicted	f_{11}	A_1	B_1	C_1
	f_{12}	A_2	B_2	C_2
	f_{13}	A_3	B_3	C_3
	f_{21}	A_4	B_4	C_4
	f_{22}	A_5	B_5	C_5
	f_{23}	A_6	B_6	C_6
	f_{31}	A_7	B_7	C_7
	f_{32}	A_8	B_8	C_8
	f_{33}	A_9	B_9	C_9
Axis Accuracy (%)		Acc_1	Acc_2	Acc_3
Accuracy (%)		Acc		

Table 4.18. Confusion matrix for the semi-centralized isolation.

4.3.2.1. ANGULAR VELOCITY MEASUREMENT

In this section, the isolation results obtained by applying the semi-decentralized isolation technique on spacecraft formation flying with angular velocity measurements are presented by confusion matrix tables. The thresholds are selected as

$$T_{121}^{1} = T_{211}^{1} = 0.0093$$
$$T_{122}^{1} = T_{212}^{1} = 0.0096$$
$$T_{123}^{1} = T_{213}^{1} = 0.0092$$
$$T_{141}^{1} = T_{411}^{1} = 0.0092$$
$$T_{142}^{1} = T_{412}^{1} = 0.0093$$
$$T_{143}^{1} = T_{413}^{1} = 0.0091$$
$$T_{241}^{1} = T_{421}^{1} = 0.0094$$
$$T_{242}^{1} = T_{422}^{1} = 0.0093$$
$$T_{243}^{1} = T_{423}^{1} = 0.0093$$

Table 4.19 to Table 4.26 display the results.

25% Reduction in Effectiveness Factor		Actual		
		f_{12}	f_{12}	f_{13}
Predicted	f_{11}	100	0	0
	f_{12}	0	99	0
	f_{13}	0	0	100
	f_{21}	0	0	0
	f_{22}	0	1	0
	f_{23}	0	0	0
	f_{31}	0	0	0
	f_{32}	0	0	0
	f_{33}	0	0	0
Axis Accuracy (%)		100%	99%	100%
Accuracy (%)		99.66%		

Table 4.19. Confusion matrix for the semi-decentralized isolation of 25% reduction in loss of effectiveness.

20% Reduction in Effectiveness Factor		Actual		
		f_{11}	f_{12}	f_{13}
Predicted	f_{11}	99	0	0
	f_{12}	0	98	0
	f_{13}	0	0	99
	f_{21}	1	0	0
	f_{22}	0	2	0
	f_{23}	0	0	1
	f_{31}	0	0	0
	f_{32}	0	0	0
	f_{33}	0	0	0
Axis Accuracy (%)		99%	98%	99%
Accuracy (%)		98.66%		

Table 4.20. Confusion matrix for the semi-decentralized isolation of 20% reduction in loss of effectiveness.

15% Reduction in Effectiveness Factor		Actual		
		f_{11}	f_{12}	f_{13}
Predicted	f_{11}	99	0	0
	f_{12}	0	96	0
	f_{13}	0	0	99
	f_{21}	1	0	0
	f_{22}	0	3	0
	f_{23}	0	0	1
	f_{31}	0	0	0
	f_{32}	0	1	0
	f_{33}	0	0	0
Axis Accuracy (%)		99%	96%	99%
Accuracy (%)		98%		

Table 4.21. Confusion matrix for the semi-decentralized isolation of 15% reduction in loss of effectiveness.

10% Reduction in Effectiveness Factor		Actual		
		f_{11}	f_{12}	f_{13}
Predicted	f_{11}	98	0	0
	f_{12}	0	90	0
	f_{13}	0	0	98
	f_{21}	2	0	0
	f_{22}	0	7	0
	f_{23}	0	0	2
	f_{31}	0	0	0
	f_{32}	0	3	0
	f_{33}	0	0	0
Axis Accuracy (%)		98%	90%	98%
Accuracy (%)		95.33%		

Table 4.22. Confusion matrix for the semi-decentralized isolation of 10% reduction in loss of effectiveness.

8% Reduction in Effectiveness Factor		Actual		
		f_{11}	f_{12}	f_{13}
Predicted	f_{11}	97	0	0
	f_{12}	0	84	0
	f_{13}	0	0	95
	f_{21}	2	0	0
	f_{22}	0	10	0
	f_{23}	0	1	5
	f_{31}	1	1	0
	f_{32}	0	4	0
	f_{33}	0	0	0
Axis Accuracy (%)		97%	84%	95%
Accuracy (%)		92%		

Table 4.23. Confusion matrix for the semi-decentralized isolation of 8% reduction in loss of effectiveness.

7% Reduction in Effectiveness Factor		Actual		
		f_{11}	f_{12}	f_{13}
Predicted	f_{11}	97	0	0
	f_{12}	0	81	0
	f_{13}	0	1	95
	f_{21}	2	0	0
	f_{22}	0	14	0
	f_{23}	0	0	5
	f_{31}	1	0	0
	f_{32}	0	4	0
	f_{33}	0	0	0
Axis Accuracy (%)		97%	81	95%
Accuracy (%)		91%		

Table 4.24. Confusion matrix for the semi-decentralized isolation of 7% reduction in loss of effectiveness

6% Reduction in Effectiveness Factor		Actual		
		f_{11}	f_{12}	f_{13}
Predicted	f_{11}	96	0	0
	f_{12}	0	72	0
	f_{13}	0	2	93
	f_{21}	2	0	0
	f_{22}	1	16	0
	f_{23}	0	3	4
	f_{31}	1	1	0
	f_{32}	0	3	0
	f_{33}	0	3	3
Axis Accuracy (%)		96%	72%	93%
Accuracy (%)		87%		

Table 4.25. Confusion matrix for the semi-decentralized isolation of 6% reduction in loss of effectiveness.

5% Reduction in Effectiveness Factor		Actual		
		f_{11}	f_{12}	f_{13}
Predicted	f_{11}	92	0	0
	f_{12}	0	58	0
	f_{13}	0	2	87
	f_{21}	3	3	0
	f_{22}	2	17	0
	f_{23}	0	5	11
	f_{31}	4	5	0
	f_{32}	0	5	0
	f_{33}	1	5	2
Axis Accuracy (%)		92%	585	87%
Accuracy (%)		79%		

Table 4.26. Confusion matrix for the semi-decentralized isolation of 5% reduction in loss of effectiveness.

According to Table 4.19 to Table 4.26, with decreasing the loss of effectiveness percentage, the accuracy of fault isolation is reduced. It also shows that the faults of actuator y are isolated with less amount of accuracy in comparison with the faults of actuators x and z.

4.3.2.2. ATTITUDE MEASUREMENT

In this section, the isolation results obtained from applying the semi-decentralized isolation technique on spacecraft formation flying with attitude measurements are presented by confusion matrix tables. The thresholds are selected as

$$
\begin{aligned}
T_{121}^{1} &= T_{211}^{1} = 0.0109 \\
T_{122}^{1} &= T_{212}^{1} = 0.0113 \\
T_{123}^{1} &= T_{213}^{1} = 0.0111 \\
T_{141}^{1} &= T_{411}^{1} = 0.0110 \\
T_{142}^{1} &= T_{412}^{1} = 0.0111 \\
T_{143}^{1} &= T_{413}^{1} = 0.0111 \\
T_{241}^{1} &= T_{421}^{1} = 0.0112 \\
T_{242}^{1} &= T_{422}^{1} = 0.0113 \\
T_{243}^{1} &= T_{423}^{1} = 0.0107
\end{aligned}
$$

Table 4.27 to Table 4.34 display the results.

25% Reduction in Effectiveness Factor		Actual		
		f_{11}	f_{12}	f_{13}
Predicted	f_{11}	87	1	2
	f_{12}	2	86	9
	f_{13}	8	8	85
	f_{21}	1	0	0
	f_{22}	0	2	0
	f_{23}	0	0	2
	f_{31}	2	0	0
	f_{32}	0	2	0
	f_{33}	0	1	2
Axis Accuracy		87%	86%	85%
Accuracy		86%		

Table 4.27. Confusion matrix for the semi-decentralized isolation of 25% reduction in loss of effectiveness.

20% Reduction in Effectiveness Factor		Actual		
		f_{11}	f_{12}	f_{13}
Predicted	f_{11}	93	1	1
	f_{12}	0	91	3
	f_{13}	2	3	89
	f_{21}	2	0	0
	f_{22}	0	2	0
	f_{23}	0	1	3
	f_{31}	2	0	0
	f_{32}	0	1	1
	f_{33}	1	1	3
Axis Accuracy		93%	91%	89%
Accuracy		91%		

Table 4.28. Confusion matrix for the semi-decentralized isolation obtained of 20% reduction in loss of effectiveness.

15% Reduction in Effectiveness Factor		Actual		
		f_{11}	f_{12}	f_{13}
Predicted	f_{11}	95	0	1
	f_{12}	0	89	2
	f_{13}	1	2	91
	f_{21}	3	0	0
	f_{22}	0	2	0
	f_{23}	0	0	2
	f_{31}	1	0	0
	f_{32}	0	4	0
	f_{33}	0	3	4
Axis Accuracy		95%	89%	91%
Accuracy		91.66%		

Table 4.29. Confusion matrix for the semi-decentralized isolation of 15% reduction in loss of effectiveness.

10% Reduction in Effectiveness Factor		Actual		
		f_{11}	f_{12}	f_{13}
Predicted	f_{11}	90	4	1
	f_{12}	0	79	0
	f_{13}	1	4	88
	f_{21}	3	2	0
	f_{22}	0	3	1
	f_{23}	1	0	3
	f_{31}	5	0	0
	f_{32}	0	5	0
	f_{33}	0	3	8
Axis Accuracy		90%	79%	88%
Accuracy		86.33%		

Table 4.30. Confusion matrix for the semi-decentralized isolation of 10% reduction in loss of effectiveness.

8% Reduction in Effectiveness Factor		Actual		
		f_{11}	f_{12}	f_{13}
Predicted	f_{11}	80	8	6
	f_{12}	3	68	0
	f_{13}	1	12	77
	f_{21}	2	0	0
	f_{22}	0	3	0
	f_{23}	3	0	8
	f_{31}	8	0	0
	f_{32}	1	7	0
	f_{33}	2	2	9
Axis Accuracy		80	68%	77%
Accuracy		75%		

Table 4.31. Confusion matrix from the semi-decentralized isolation of 8% reduction in loss of effectiveness.

7% Reduction in Effectiveness Factor		Actual		
		f_{11}	f_{12}	f_{13}
Predicted	f_{11}	87	6	17
	f_{12}	0	68	1
	f_{13}	0	8	50
	f_{21}	4	0	0
	f_{22}	0	6	3
	f_{23}	2	0	11
	f_{31}	7	0	0
	f_{32}	0	8	0
	f_{33}	0	4	18
Axis Accuracy		78%	60%	73%
Accuracy		70.33%		

Table 4.32. Confusion matrix for the semi-decentralized isolation of 7% reduction in loss of effectiveness.

6% Reduction in Effectiveness Factor		Actual		
		f_{11}	f_{12}	f_{13}
Predicted	f_{11}	71	5	25
	f_{12}	2	49	0
	f_{13}	2	15	68
	f_{21}	11	5	0
	f_{22}	1	18	2
	f_{23}	0	0	0
	f_{31}	10	0	0
	f_{32}	2	4	0
	f_{33}	1	4	5
Axis Accuracy		71%	49%	68%
Accuracy		62.66%		

Table 4.33. Confusion matrix for the semi-decentralized isolation of 6% reduction in loss of effectiveness.

5% Reduction in Effectiveness Factor		Actual		
		f_{11}	f_{12}	f_{13}
Predicted	f_{11}	68	15	20
	f_{12}	2	40	0
	f_{13}	2	20	64
	f_{21}	13	0	0
	f_{22}	1	10	5
	f_{23}	0	0	0
	f_{31}	12	1	0
	f_{32}	2	8	0
	f_{33}	0	6	11
Axis Accuracy		68%	40%	64%
Accuracy		57.33%		

Table 4.34. Confusion matrix for the semi-decentralized isolation of 5% reduction in loss of effectiveness.

According to Table 4.27 to Table 4.34, for the faults less 15% loss of effectiveness, with decreasing the loss of effectiveness percentage, the accuracy of fault isolation is reduced. But for the faults more than 15%, with increasing the loss of effectiveness, the isolation accuracy decrease. This nonconsistent behavior is the result of coupling that existed among the quaternions, which shows itself more for the high severity faults. It also shows that the faults of actuator y and z are isolated with less amount of accuracy in comparison with the faults of actuators x.

4.3.3. Centralized Isolation Architecture

In this section, the results that are obtained by implementing the centralized isolation technique are presented. The results are stated by using the confusion matrix tables. Table 4.35 shows the confusion matrix arrangement for the centralized isolation.

In Table 4.35, f_{ij} is the occurrence of fault in actuator $\#j$ of spacecraft $\#i$. Parameter A_1 is the number of f_{11} faults that are isolated correctly. Parameter A_2 is the number of f_{11} faults that are misclassified as f_{12} fault. Parameter A_3 is the number of f_{11} faults that are misclassified as f_{13} fault. Parameter A_4 is the number of f_{11} faults that are misclassified as f_{21} fault. Parameter A_5 is the number of f_{11} faults that are misclassified as f_{22} fault. Parameter A_6 is the number of f_{11} faults that are misclassified as f_{23} fault. Parameter A_7 is the number of f_{11} faults that are misclassified as f_{31} fault. Parameter A_8 is the number of f_{11} faults that are misclassified as f_{32} fault. Parameter A_9 is the number of f_{11} faults that are misclassified as f_{33} fault. Parameter A_{10} is the number of f_{11} faults that are misclassified as f_{41} fault. Parameter A_{11} is the number of f_{11} faults that are misclassified as f_{42} fault. Parameter A_{12} is the number of f_{11} faults that are misclassified as f_{43} fault.

Parameter B_1 is the number of f_{12} faults that are misclassified as f_{11} fault. Parameter B_2 is the number of f_{12} faults that are isolated correctly. Parameter B_3 is the number of f_{12} faults that are misclassified as f_{13} fault. Parameter B_4 is the number of f_{12} faults that are misclassified as f_{21} fault. Parameter B_5 is the number of f_{12} faults that are misclassified as f_{22} fault. Parameter B_6 is the number of f_{12} faults that are misclassified as f_{23} fault. Parameter B_7 is the number of f_{12} faults that are misclassified as f_{31} fault. Parameter B_8 is the number of f_{12} faults that are misclassified as f_{32} fault. Parameter B_9 is the number of f_{12} faults that are misclassified as f_{33} fault. Parameter B_{10} is the number of f_{12} faults that are misclassified as f_{41} fault. Parameter B_{11} is the number of f_{12} faults that are misclassified as f_{42} fault. Parameter B_{12} is the number of f_{12} faults that are misclassified as f_{43} fault.

Parameter C_1 is the number of f_{13} faults that are misclassified as f_{11} fault. Parameter C_2 is the number of f_{13} faults that are misclassified as f_{12} fault. Parameter C_3 is the number of f_{13} faults that are isolated correctly. Parameter C_4 is the number of f_{13} faults that are misclassified as f_{21} fault. Parameter C_5 is the number of f_{13} faults that are misclassified as f_{22} fault. Parameter C_6 is the number of f_{13} faults that are misclassified as f_{23} fault. Parameter C_7 is the number of f_{13} faults that are misclassified as f_{31} fault. Parameter C_8 is the number of f_{13} faults that are misclassified as f_{32} fault. Parameter C_9 is the number of f_{13} faults that are misclassified as f_{33} fault. Parameter C_{10} is the number of f_{13} faults that are misclassified as f_{41} fault. Parameter C_{11} is the number of f_{13} faults that are misclassified as f_{42} fault. Parameter C_{12} is the number of f_{13} faults that are misclassified as f_{43} fault.

Parameter Acc_1 is the isolation accuracy for fault of actuator #1, parameter Acc_2 is the isolation accuracy for faults of actuator #2, and parameter Acc_3 is the isolation accuracy for faults of actuator #3. Parameter Acc is the mean of isolation accuracies of the actuators.

$$Acc_1 = \frac{A_1}{A_1 + A_2 + A_3 + A_4 + A_5 + A_6 + A_7 + A_8 + A_9 + A_{10} + A_{11} + A_{12}} \tag{4.31}$$

$$Acc_2 = \frac{B_2}{B_1 + B_2 + B_3 + B_4 + B_5 + B_6 + B_7 + B_8 + B_9 + B_{10} + B_{11} + B_{12}} \tag{4.32}$$

$$Acc_3 = \frac{C_3}{C_1 + C_2 + C_3 + C_4 + C_5 + C_6 + C_7 + C_8 + C_9 + C_{10} + C_{11} + C_{12}} \tag{4.33}$$

$$Acc = \frac{Acc_1 + Acc_2 + Acc_3}{3} \tag{4.34}$$

The faulty scenarios are first detected by using the centralized fault detection architecture. For each faulty scenario, 100 detected faulty cases are tested.

Parameter M of equation (4.20), which is the window length, is set to 40 samples for our simulations. The thresholds are selected by using the equation (4.22). For each threshold, 30 different healthy simulation missions of spacecraft that are subject to the measurement noise are executed and the threshold in each mission is calculated. Finally, the average of the thresholds is considered as the final threshold.

Reduction in Effectiveness Factor (%)		Actual		
		f_{11}	f_{12}	f_{13}
Predicted	f_{11}	A_1	B_1	C_1
	f_{12}	A_2	B_2	C_2
	f_{13}	A_3	B_3	C_3
	f_{21}	A_4	B_4	C_4
	f_{22}	A_5	B_5	C_5
	f_{23}	A_6	B_6	C_6
	f_{31}	A_7	B_7	C_7
	f_{32}	A_8	B_8	C_8
	f_{33}	A_9	B_9	C_9
	f_{41}	A_{10}	B_{10}	C_{10}
	f_{42}	A_{11}	B_{11}	C_{11}
	f_{43}	A_{12}	B_{12}	C_{12}
Axis Accuracy (%)		Acc_1	Acc_2	Acc_3
Total Accuracy (%)		Acc		

Table 4.35. Confusion matrix for the centralized isolation.

4.3.3.1. ANGULAR VELOCITY MEASUREMENT

In this section, the isolation results obtained from applying the centralized isolation technique on spacecraft formation flying with angular velocity measurements are presented by confusion matrix tables. The thresholds are selected as

$$
\begin{aligned}
T_{121} &= T_{211} = 0.0093 \\
T_{122} &= T_{212} = 0.0096 \\
T_{123} &= T_{213} = 0.0092 \\
T_{131} &= T_{311} = 0.0094 \\
T_{132} &= T_{312} = 0.0092 \\
T_{133} &= T_{313} = 0.0088 \\
T_{141} &= T_{411} = 0.0092 \\
T_{142} &= T_{412} = 0.0093 \\
T_{143} &= T_{413} = 0.0091 \\
T_{231} &= T_{321} = 0.0095 \\
T_{232} &= T_{322} = 0.0093 \\
T_{233} &= T_{322} = 0.0090 \\
T_{241} &= T_{421} = 0.0094 \\
T_{242} &= T_{422} = 0.0093 \\
T_{243} &= T_{423} = 0.0093 \\
T_{341} &= T_{431} = 0.0094 \\
T_{342} &= T_{432} = 0.0091 \\
T_{343} &= T_{433} = 0.0091
\end{aligned}
.
$$

0-Table 4.43 display the results.

25% Reduction in Effectiveness Factor		Actual		
		f_{11}	f_{12}	f_{13}
Predicted	f_{11}	100	0	0
	f_{12}	0	99	0
	f_{13}	0	0	100
	f_{21}	0	0	0
	f_{22}	0	1	0
	f_{23}	0	0	0
	f_{31}	0	0	0
	f_{32}	0	0	0
	f_{33}	0	0	0
	f_{41}	0	0	0
	f_{42}	0	0	0
	f_{43}	0	0	0
Axis Accuracy		100%	99%	100%
Total Accuracy		99.67%		

Table 4.36. Confusion matrix for the centralized isolation of 25% reduction in loss of effectiveness.

20% Reduction in Effectiveness Factor		Actual		
		f_{11}	f_{12}	f_{13}
Predicted	f_{11}	100	0	0
	f_{12}	0	99	0
	f_{13}	0	0	100
	f_{21}	0	0	0
	f_{22}	0	1	0
	f_{23}	0	0	0
	f_{31}	0	0	0
	f_{32}	0	0	0
	f_{33}	0	0	0
	f_{41}	0	0	0
	f_{42}	0	0	0
	f_{43}	0	0	0
Axis Accuracy		100%	99%	100%
Total Accuracy		99.67%		

Table 4.37. Confusion matrix for the centralized isolation of 20% reduction in loss of effectiveness.

15% Reduction in Effectiveness Factor		Actual		
		f_{11}	f_{12}	f_{13}
Predicted	f_{11}	100	0	0
	f_{12}	0	99	0
	f_{13}	0	0	100
	f_{21}	0	0	0
	f_{22}	0	1	0
	f_{23}	0	0	0
	f_{31}	0	0	0
	f_{32}	0	0	0
	f_{33}	0	0	0
	f_{41}	0	0	0
	f_{42}	0	0	0
	f_{43}	0	0	0
Axis Accuracy		100%	99%	100%
Total Accuracy		99.67%		

Table 4.38. Confusion matrix for the centralized isolation of 15% reduction in loss of effectiveness.

10% Reduction in Effectiveness Factor		Actual		
		f_{11}	f_{12}	f_{13}
Predicted	f_{11}	100	0	0
	f_{12}	0	97	0
	f_{13}	0	0	97
	f_{21}	0	0	0
	f_{22}	0	1	0
	f_{23}	0	0	1
	f_{31}	0	0	0
	f_{32}	0	1	0
	f_{33}	0	0	0
	f_{41}	0	0	0
	f_{42}	0	1	1
	f_{43}	0	0	1
Axis Accuracy		100%	97%	97%
Total Accuracy		98%		

Table 4.39. Confusion matrix for the centralized isolation of 10% reduction in loss of effectiveness.

8% Reduction in Effectiveness Factor		Actual		
		f_{11}	f_{12}	f_{13}
Predicted	f_{11}	99	0	0
	f_{12}	0	93	0
	f_{13}	0	1	95
	f_{21}	1	0	0
	f_{22}	0	2	0
	f_{23}	0	0	2
	f_{31}	0	0	0
	f_{32}	0	1	1
	f_{33}	0	0	0
	f_{41}	0	0	0
	f_{42}	0	3	0
	f_{43}	0	0	2
Axis Accuracy		99%	93%	95%
Total Accuracy		95.67%		

Table 4.40. Confusion matrix for the centralized isolation of 8% reduction in loss of effectiveness.

7% Reduction in Effectiveness Factor		Actual		
		f_{11}	f_{12}	f_{13}
Predicted	f_{11}	97	0	0
	f_{12}	0	89	0
	f_{13}	0	0	94
	f_{21}	2	0	0
	f_{22}	0	7	0
	f_{23}	0	0	2
	f_{31}	0	0	0
	f_{32}	0	1	0
	f_{33}	0	0	2
	f_{41}	1	1	0
	f_{42}	0	2	0
	f_{43}	0	0	2
Axis Accuracy		97%	89%	94%
Total Accuracy		93.33%		

Table 4.41. Confusion matrix for the centralized isolation of 7% reduction in loss of effectiveness.

6% Reduction in Effectiveness Factor		Actual		
		f_{11}	f_{12}	f_{13}
Predicted	f_{11}	96	0	0
	f_{12}	0	83	0
	f_{13}	0	0	92
	f_{21}	2	0	0
	f_{22}	0	10	0
	f_{23}	0	0	3
	f_{31}	0	0	0
	f_{32}	0	4	0
	f_{33}	0	0	1
	f_{41}	2	0	0
	f_{42}	0	3	0
	f_{43}	0	0	4
Axis Accuracy		96%	83%	92%
Total Accuracy		90.33%		

Table 4.42. Confusion matrix for the centralized isolation of 6% reduction in loss of effectiveness.

5% Reduction in Effectiveness Factor		Actual		
		f_{11}	f_{12}	f_{13}
Predicted	f_{11}	90	0	0
	f_{12}	0	74	0
	f_{13}	0	0	88
	f_{21}	3	0	0
	f_{22}	0	15	0
	f_{23}	0	0	5
	f_{31}	0	0	0
	f_{32}	0	7	0
	f_{33}	0	0	0
	f_{41}	7	0	0
	f_{42}	0	4	0
	f_{43}	0	0	7
Axis Accuracy		90%	74%	88%
Total Accuracy		84%		

Table 4.43. Confusion matrix for the centralized isolation of 5% reduction in loss of effectiveness.

According to 0 to Table 4.43, with decreasing the loss of effectiveness percentage, the accuracy of fault isolation is reduced. It also shows that the faults of actuator y and z are isolated with less amount of accuracy in comparison with the faults of actuators x.

4.3.3.2. ATTITUDE MEASUREMENT

In this section, the isolation results obtained from applying the centralized isolation technique on spacecraft formation flying with attitude measurements are presented by confusion matrix tables. The thresholds are selected as

$$
\begin{aligned}
T_{121} &= T_{211} = 0.0109 \\
T_{122} &= T_{212} = 0.0113 \\
T_{123} &= T_{213} = 0.0111 \\
T_{131} &= T_{311} = 0.0111 \\
T_{132} &= T_{312} = 0.0106 \\
T_{133} &= T_{313} = 0.0106 \\
T_{141} &= T_{411} = 0.0110 \\
T_{142} &= T_{412} = 0.0111 \\
T_{143} &= T_{413} = 0.0111 \\
T_{231} &= T_{321} = 0.0110 \\
T_{232} &= T_{322} = 0.0110 \\
T_{233} &= T_{322} = 0.0105 \\
T_{241} &= T_{421} = 0.0112 \\
T_{242} &= T_{422} = 0.0113 \\
T_{243} &= T_{423} = 0.0107 \\
T_{341} &= T_{431} = 0.0111 \\
T_{342} &= T_{432} = 0.0109 \\
T_{343} &= T_{433} = 0.0108
\end{aligned}
.
$$

Table 4.44 to Table 4.51 display the results.

25% Reduction in Effectiveness Factor		Actual		
		f_{11}	f_{12}	f_{13}
Predicted	f_{11}	89	0	2
	f_{12}	1	90	6
	f_{13}	6	8	91
	f_{21}	0	0	0
	f_{22}	0	0	0
	f_{23}	0	0	0
	f_{31}	0	0	0
	f_{32}	0	0	0
	f_{33}	0	0	0
	f_{41}	4	0	0
	f_{42}	0	2	0
	f_{43}	0	0	1
Axis Accuracy		89%	90%	91%
Total Accuracy		90%		

Table 4.44. Confusion matrix for the centralized isolation of 25% reduction in loss of effectiveness.

20% Reduction in Effectiveness Factor		Actual		
		f_{11}	f_{12}	f_{13}
Predicted	f_{11}	97	0	1
	f_{12}	0	91	3
	f_{13}	3	5	92
	f_{21}	0	0	1
	f_{22}	0	1	0
	f_{23}	0	0	0
	f_{31}	0	0	1
	f_{32}	0	1	0
	f_{33}	0	0	0
	f_{41}	0	0	0
	f_{42}	1	1	1
	f_{43}	0	0	1
Axis Accuracy		97%	92%	92%
Total Accuracy		93.66%		

Table 4.45. Confusion matrix for the centralized isolation of 20% reduction in loss of effectiveness.

15% Reduction in Effectiveness Factor		Actual		
		f_{11}	f_{12}	f_{13}
Predicted	f_{11}	99	1	1
	f_{12}	0	94	2
	f_{13}	1	1	95
	f_{21}	0	1	0
	f_{22}	0	1	0
	f_{23}	0	0	0
	f_{31}	0	0	1
	f_{32}	0	0	0
	f_{33}	0	0	0
	f_{41}	0	0	0
	f_{42}	0	2	0
	f_{43}	0	0	1
Axis Accuracy		99%	94%	95%
Total Accuracy		96%		

Table 4.46. Confusion matrix for the centralized isolation of 15% reduction in loss of effectiveness.

10% Reduction in Effectiveness Factor		Actual		
		f_{11}	f_{12}	f_{13}
Predicted	f_{11}	96	2	1
	f_{12}	0	67	1
	f_{13}	0	16	88
	f_{21}	1	3	3
	f_{22}	0	2	0
	f_{23}	0	1	4
	f_{31}	0	0	0
	f_{32}	0	6	0
	f_{33}	0	0	2
	f_{41}	3	0	0
	f_{42}	0	2	0
	f_{43}	0	1	1
Axis Accuracy		95%	84%	91%
Total Accuracy		90%		

Table 4.47. Confusion matrix for the centralized isolation of 10% reduction in loss of effectiveness.

8% Reduction in Effectiveness Factor		Actual		
		f_{11}	f_{12}	f_{13}
Predicted	f_{11}	93	3	1
	f_{12}	0	70	1
	f_{13}	0	16	85
	f_{21}	0	7	4
	f_{22}	3	2	0
	f_{23}	0	0	5
	f_{31}	0	0	0
	f_{32}	0	0	0
	f_{33}	0	0	2
	f_{41}	4	0	0
	f_{42}	0	2	0
	f_{43}	0	0	2
Axis Accuracy		93%	70%	85%
Total Accuracy		82.66%		

Table 4.48. Confusion matrix for the centralized isolation of 8% reduction in loss of effectiveness.

7% Reduction in Effectiveness Factor		Actual		
		f_{11}	f_{12}	f_{13}
Predicted	f_{11}	84	3	0
	f_{12}	0	60	2
	f_{13}	0	23	81
	f_{21}	1	8	2
	f_{22}	0	0	0
	f_{23}	0	0	12
	f_{31}	5	0	0
	f_{32}	0	0	0
	f_{33}	0	0	3
	f_{41}	10	0	0
	f_{42}	0	6	0
	f_{43}	0	0	0
Axis Accuracy		84%	60%	81%
Total Accuracy		75%		

Table 4.49. Confusion matrix for the centralized isolation of 7% reduction in loss of effectiveness.

6% Reduction in Effectiveness Factor		Actual		
		f_{11}	f_{12}	f_{13}
Predicted	f_{11}	75	2	4
	f_{12}	3	4	70
	f_{13}	10	51	17
	f_{21}	0	23	3
	f_{22}	0	0	0
	f_{23}	0	16	0
	f_{31}	0	0	0
	f_{32}	0	0	3
	f_{33}	0	4	0
	f_{41}	12	0	0
	f_{42}	0	0	3
	f_{43}	0	0	0
Axis Accuracy		75%	51%	70%
Total Accuracy		68%		

Table 4.50. Confusion matrix for the centralized isolation of 6% reduction in loss of effectiveness.

5% Reduction in Effectiveness Factor		Actual		
		f_{11}	f_{12}	f_{13}
Predicted	f_{11}	72	10	9
	f_{12}	0	15	65
	f_{13}	5	0	22
	f_{21}	0	0	0
	f_{22}	7	0	0
	f_{23}	0	20	0
	f_{31}	0	0	0
	f_{32}	0	0	0
	f_{33}	0	0	0
	f_{41}	16	0	0
	f_{42}	0	0	0
	f_{43}	0	4	4
Axis Accuracy		72%	47%	65%
Total Accuracy		64%		

Table 4.51. Confusion matrix for the centralized isolation of 5% reduction in loss of effectiveness.

According to Table 4.44 to Table 4.51, for the fault less than 15% loss of effectiveness, with decreasing the loss of effectiveness percentage, the accuracy of fault isolation is reduced. But, for the faults with the loss of effectiveness more than 15%, with increasing the fault severity the accuracy decreases. The reason of this nonconsistant behavior is the coupling that exists among the quaternion parameters, which shows itself more for the high severity faults. It also shows that the faults of actuator y are isolated with less amount of accuracy in comparison with the faults of actuators x and z.

4.4. COMPARING AND DISCUSSING THE RESULTS

In this section, the results that are obtained by implementing the proposed isolation techniques, which have been presented in Section 4.3, are discussed. In order to make this discussion easier, we compare the performances by using a line chart. In each figure, the horizontal axis shows the change of loss of effectiveness factor from 5% to 25%, and the vertical axis shows the changes of accuracy with respect to the loss of effectiveness.

4.4.1. Comparing the Isolation Accuracy of the Decentralized, Centralized, and Semi-decentralized Architectures

As can be seen in Figure 4.1, for the formations with angular velocity measurements, with increasing the fault percentage, the accuracies are increased. The figure also demonstrates that the isolation results obtained by the centralized isolating technique are more accurate than the decentralized and semi-decentralized techniques. The results of semi-decentralized technique are also more accurate than the decentralized technique. In centralized isolation, the information of all of the satellites in the formation has been used. The computations are more than the two other

techniques, but the result is more accurate. In semi-decentralized isolation, the information of the nearest neighbor satellites have been used to find the location of the fault. The information used in this method are less than the centralized technique, but more than the decentralized technique. Therefore, the semi-decentralized isolation is less accurate than centralized isolation, but more accurate than the decentralized isolation. Also, the required computations in semi-decentralized technique are more than centralized technique and less than decentralized technique.

For the faults less than 8% loss of effectiveness, the change in the rate of accuracy is much greater than the higher severity faults. For the faults more than 15% loss of effectiveness, the accuracies are almost constant.

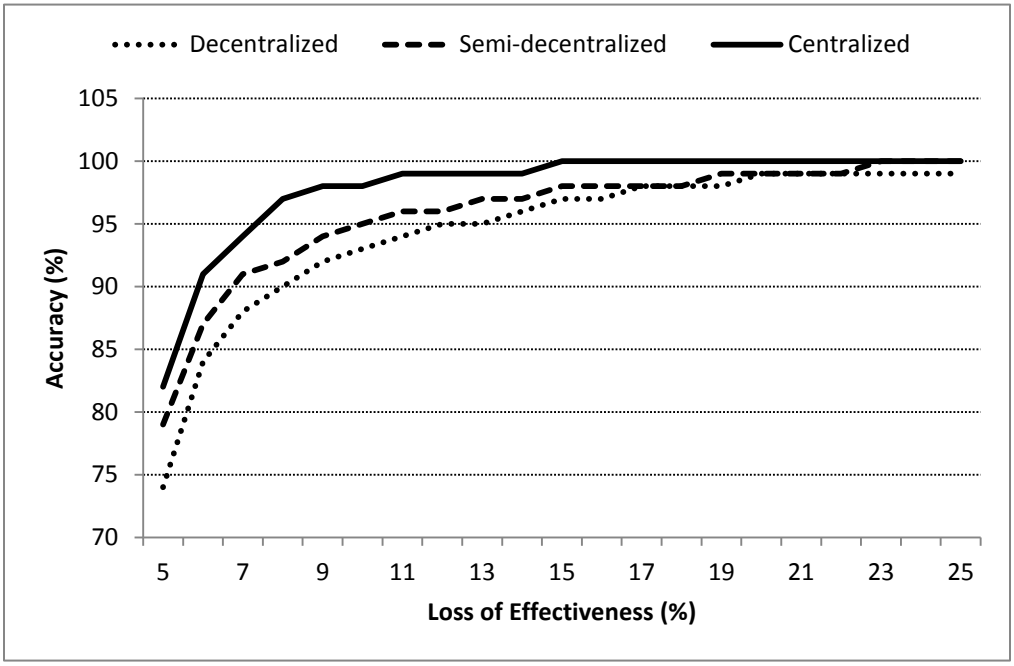

Figure 4.1 Comparison of the accuracy of decentralized, semi-decentralized, and centralized isolation techniques for angular velocity measurement.

With decreasing the loss of effectiveness percentage, the accuracy of fault isolation is reduced. But, this is true for the faults with less than 20% loss of effectiveness in

centralized and semi-decentralized techniques and less than 18% for decentralized technique. Figure 4.2 shows that the fault isolation accuracy for the 25% fault is less than 20% fault. The reason of this behavior change is the couplings that exist among the quaternions. The coupling effect is more significant for larger changes in the torque of the actuators. Therefore, with increasing the fault severity, the coupling effect will increase and can cause more incorrect isolation. We designate the increase of isolation accuracy relative to the increase of fault as the normal behavior. Here, it can be said that in the attitude measurement, the coupling effects overcome the normal behavior of isolation accuracy for the faults more than 20% loss of effectiveness in centralized and semi-decentralized techniques and less than 18% for decentralized technique. The reason that we do not see this coupling effect in Figure 4.1 is the higher decoupling that exist among the angular velocity parameters relative to the decoupling among the attitude parameters.

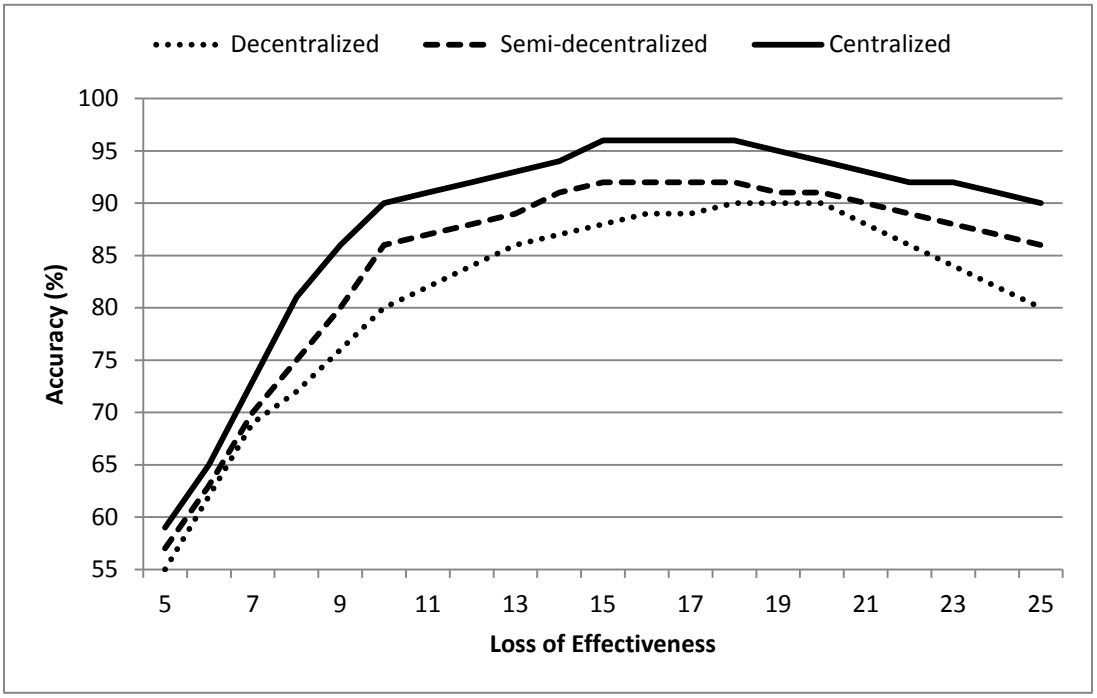

Figure 4.2 Comparison of the accuracy of decentralized, semi-decentralized, and centralized isolation techniques for attitude measurement.

Figure 4.2 shows that for all percentage of loss of effectiveness, the centralized isolation is more accurate than semi-decentralized isolation, and semi-decentralized isolation is more accurate than decentralized isolation. For the faults with less than 7% loss of effectiveness, the performances of the methods are close together. The accuracy change rate for the faults with less than 10% loss of effectiveness is more than the higher severe faults.

4.4.2. Comparing the Isolation Accuracy of the Formation with Angular Velocity Measurement and Attitude Measurement

According to Figure 4.3 to Figure 4.5, the results that are obtained by implementing the decentralized, semi-decentralized, and centralized isolation techniques to the formation with angular velocity measurements are more accurate than implementing those techniques to the formation with attitude measurements. In addition, because of more independency among the angular velocity parameters relative to the attitude parameters, the accuracy does not decrease for high severity faults in the angular velocity measurement line charts.

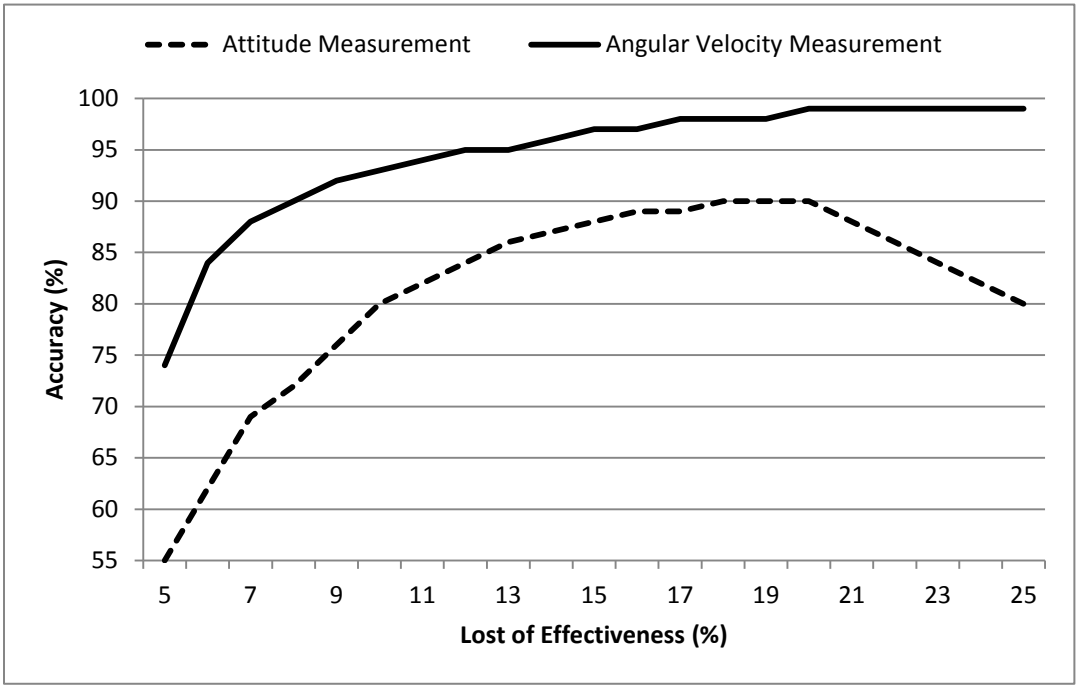

Figure 4.3 Comparison of the accuracy of decentralized isolation technique between angular velocity measurement and attitude measurement.

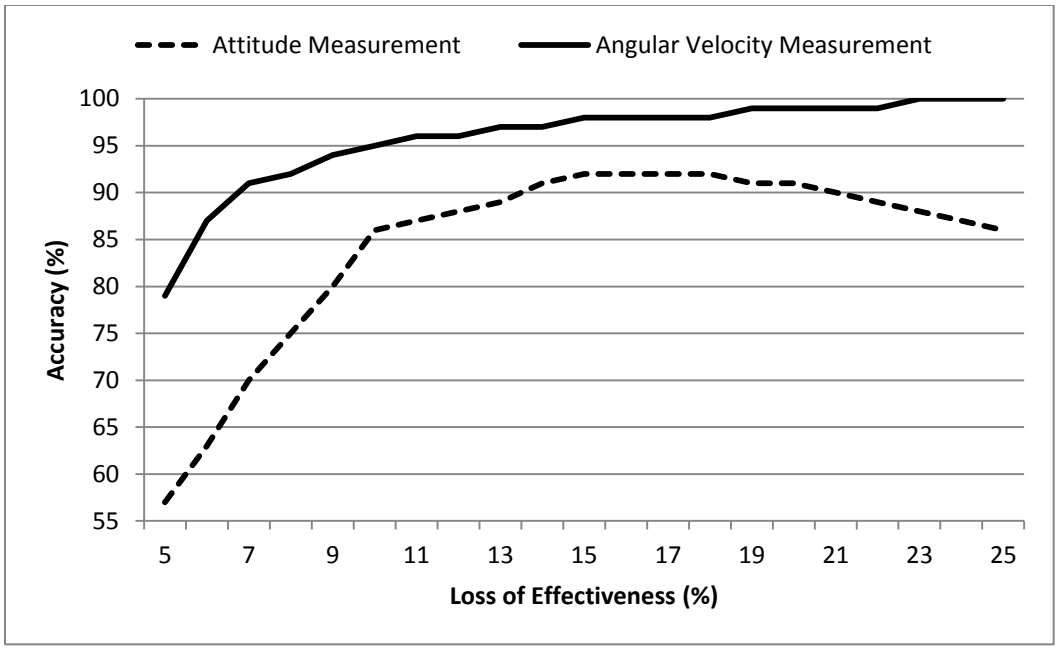

Figure 4.4 Comparison of the accuracy of semi-decentralized isolation technique between angular velocity measurement and attitude measurement.

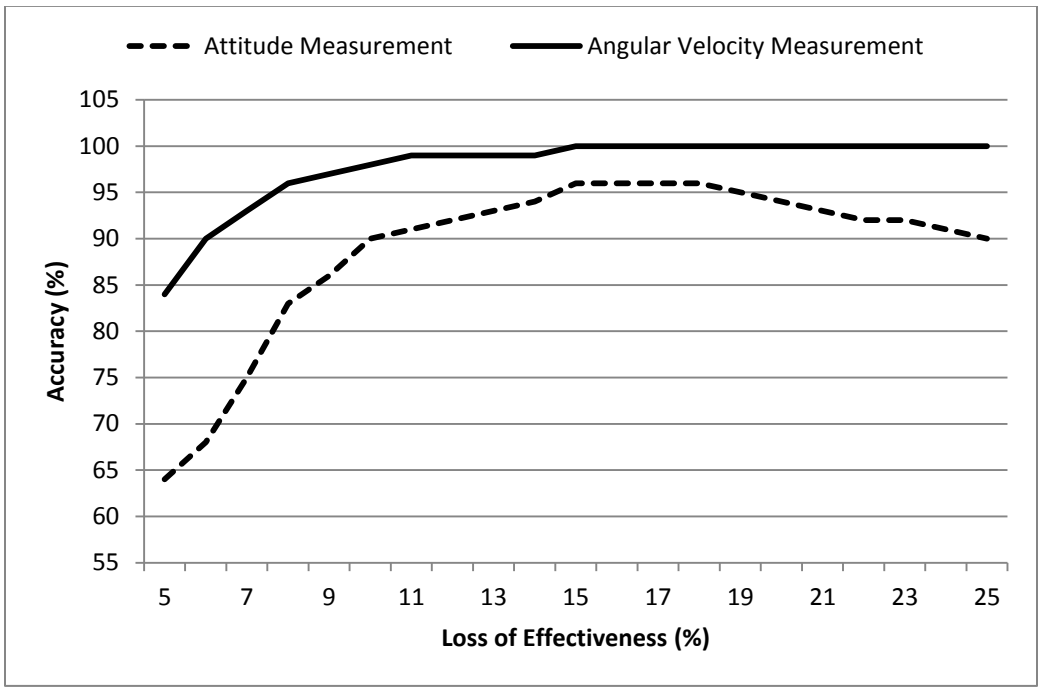

Figure 4.5 Comparison of the accuracy of centralized isolation technique between angular velocity measurement and attitude measurement.

4.5. CONCLUSION

In this chapter, isolation techniques are developed for the decentralized, semi-decentralized, and centralized architectures based on the idea of structured residuals set. The results that are obtained by implementing the isolation techniques on spacecraft formation flying are presented by using confusion matrix tables. At the end of the chapter, the results are compared and discussed.

Based on the simulation results, in the formation with angular velocity measurement, the centralized isolation technique has higher accuracy than the decentralized technique, and the results that are obtained by the semi-decentralized technique are more accurate than the decentralized technique.

In the formation with attitude measurement for the faults with less than 20% loss of effectiveness, with increasing of the fault severity, the isolation accuracy of the decentralized technique increases. For the faults with more than 20% loss of effectiveness, with increasing the loss of effectiveness the isolation accuracy decreases. For centralized and semi-decentralized techniques, this peak value is 18% loss of effectiveness. The reason of this non-consistent behavior is the coupling that existed among the quaternions, which shows itself more for the high severity faults. Furthermore, in the formation with attitude measurement, the accuracy of centralized architecture is more than the semi-decentralized architecture, and the accuracy of the semi-decentralized architecture is more than the decentralized architecture.

These results demonstrate that the centralized isolation technique has the most desired performance compared to the two other techniques; however, it should be considered that the amount of computations required for this technique is also higher.

Furthermore, the presented results show that in all three isolation techniques, the formation with angular velocity measurement has higher isolation accuracy than the formation with attitude measurement. Therefore, it will be more reliable to use angular velocity sensors instead of attitude sensors for fault isolation purposes.

Chapter 5: CONCLUSIONS AND FUTURE WORK

5.1. CONCLUSIONS

In this thesis, three different model based architectures were proposed for detection and isolation of actuator faults in spacecraft formation flight; namely, decentralized, semi-decentralized, and centralized. Extended Kalman filter was used as the state estimator in these architectures. In order to analyze and evaluate the performance of each architecture, several faulty scenarios were examined via simulations.

In the first chapter, a literature review on different aspects of our proposed problem was provided. First, experiences of formation flight missions and the importance of FDI problem during missions were discussed. Fault detection and isolation methods, spacecraft formation flying control strategies, formation control architectures, single spacecraft FDI, and formation flight FDI were reviewed from the literature.

In the second chapter, the background material that were required before proposing our methods were presented. First, using the reference frames, kinematics and dynamics equations of angular motion and modeling the environmental disturbances and the spacecraft attitude dynamics were analysed. The decentralized virtual structure control topology was explained, which has been used as the formation control strategy for our simulations. Various types of faults were introduced and the fault modeling in the state space system was clarified. Finally, after discussing the

model-based fault detection, isolation, and residual generation, the Kalman filter and extended Kalman filter methods were explained.

In the third chapter, our fault detection architectures were developed. First, graph based formation flight modeling is defined and then the formation flight of spacecraft was modelled. To achieve this, the model of a spacecraft in presence of actuator fault was developed and was applied to the frameworks of decentralized, semi-decentralized, and centralized architectures. This has been followed up by developing fault detection architectures based on the extended Kalman filter state estimation method. The residual generation and threshold selection techniques were developed. The conditions for stochastic stability of the proposed decentralized, centralized, and semi-decentralized extended Kalman filters were also investigated. Finally, the simulation results that are obtained by implementing the proposed fault detection architectures on the simulated spacecraft formation flight were provided. The results were summarized by confusion matrix tables and the evaluating parameters were extracted from the tables. Based on the acquired parameters, efficiencies of fault detection architectures were compared. The results show that in the formation with angular velocity measurement the centralized architecture has the most success in detecting the occurrence of faults, but it has also higher false alarms relative to the two other architectures. Furthermore, the decentralized architecture has the least percentage in announcing the occurrence of faults, but it has also the least amount of false alarms. In the formation with attitude measurement, the centralized architecture has the most success in announcing the occurrence of faults, and it has also the least number of false alarms relative to the two other architectures. Furthermore, the decentralized architecture has the least percentage in announcing the occurrence of faults and it has fewer false alarms relative to the semi-decentralized architecture. The other conclusion

that can be drawn from the results is the higher reliability of angular velocity measurement versus the attitude measurement in our fault detection method. In all three architectures, the results obtained from the angular velocity measurements show more desired performance for the accuracy, true faulty, false healthy, true healthy, false faulty, precision, and fault detection delay. This implies that the angular velocity sensors can make the missions more secure and safer, because the faults are more detectable by using the information provided with them.

In the fourth chapter, fault isolation techniques were developed for decentralized, semi-decentralized, and centralized architectures. First, different isolation approaches that have proposed in the literature were introduced. The structured residual set which was considered as our method was investigated. The decentralized, semi-decentralized, and centralized isolation strategies were developed based on generating residual functions, threshold testing, and decision making logic algorithms. Finally, the simulation results that were obtained by implementing the proposed isolation techniques on the spacecraft formation flight were presented. These results demonstrate that the centralized isolation technique has the most desired performance as compared to the two other techniques; however, it should be noted that the amount of computations required for this technique is also higher. Furthermore, the presented results show that in all three isolation techniques, the formation with angular velocity measurement has higher isolation accuracy than the formation with attitude measurement. Therefore, it will be more reliable to use angular velocity sensors instead of the attitude sensors.

5.2. FUTURE WORK

Based on the results obtained in this thesis, the suggested future work can be

focused on the following areas:

- **Fault identification:** A complete fault diagnosis method consists of fault detection, isolation, and identification. The methods generated in this thesis have been focused on detection and isolation problems. In order to design a fault tolerant control system, the severity of faults should be known which should encourage one to study fault identification in future work.

- **Threshold and window length selection:** The sensitivity of the presented fault detection method depends on the threshold selection and the window length selection. As illustrated in Chapter 3, a trade-off exists between the probability of false faulty alarm and false healthy detection. As a future work, stochastic based techniques can be used to make an optimized decision for choosing the threshold and the window length.

- **Formation based FDI:** The cooperative control function among spacecraft in a formation flight depends on the control architecture used to control the formation. Different control architectures have different control functions which affect the fault transfer among the spacecraft. As an extension to this work, the residual evaluation function can be defined separately for each control architecture, based on the fault transfer characteristics of the formation control law.

- **Isolation improvement:** With increasing the fault severity in the formation attitude measurement, the isolation accuracy increases. But after a significant fault severity, because of the coupling that exist among the quaternion parameters, the isolation accuracy decreases. In future, one can develop a completely decoupled isolation structure set for the formation with attitude measurement, to avoid the accuracy loss due to high severity faults.

REFERENCE

[1] D. P. Scharf, F. Y. Hadaegh, and S. R. Ploen, "A Survey of Spacecraft Formation Flying Guidance and Control (part I): Guidance," American Control Conference, Proceedings of the 2003, vol.2, no., pp. 1733-1739, June 2003.

[2] S. Chien, R. Sherwood, M. Burl, R. Knight, G. Rabideau, B. Engelhardt, ... & V. Baker, "The Techsat-21 autonomous sciencecraft constellation demonstration," In The 6th International Symposium on Artificial Intelligence, Robotics, and Automation in Space, April 2001.

[3] F. Bauer, J. Bristow, D. Folta, K. Hartman, D. Quinn, and J. P. How, "Spacecraft Formation Flying Using an Innovative Autonomous Control System (AUTOCON) Environment," AIAA Guidance Navigation And Control Conference, pp 657-666, 1997.

[4] S. Ungar, D. Mandl, P. Campbell, and E. Middleton, "Earth Observing One (EO-1) Celebrates 10 Years," The Earth Observer, Volume 22, Issue 6, November-December 2010.

[5] The Afternoon Constellation, available at: http://atrain.nasa.gov.

[6] "Formation Flying: The Afternoon "A-Train" Spacecraft Constellation," NASA Facts, Goddard Space Flight Center, Article in The Earth Enterprise Series, March 2003.

[7] Image Courtesy of Alex McClung, NASA/SSAI/GSFC.

[8] Missions Highlights, available at: http://www.nasa.gov/missions/index.html.

[9] P. M. Frank, "Fault Diagnosis in Dynamic Systems via State Estimation-A Survey," In System fault diagnostics, reliability and related knowledge-based approaches, pp. 35-98. Springer Netherlands, 1987.

[10] P. M. Frank, "Fault Diagnosis in dynamic System using analytical and Knowledge based Redundancy-A Survey and Some New Results," Automatica 26(3) : 459-474, 1990.

[11] J. Chen, and R. J. Patton, "Robust Model-Based Fault Diagnosis for Dynamic Systems," Kluwer Academic Publishers, 1999.

[12] R. J. Patton, P. M. Frank, and R. N. Clark, "Fault diagnosis in Dynamic Systems, Theory and Applications," Control Engineering Series, Prentice-Hall, New York, 1989.

[13] R. J. Patton, P. M. Frank, and R. N. Clark, "Issues of Fault Diagnosis for Dynamic Systems," Springer-Verlog, London, 2000.

[14] M. Basseville, and I. V. Nikiforov, "Detection of Abrupt Changes: Theory and Application," Information and System Science, Prentice-Hall, New-York, 1993.

[15] J. Gertler, "Fault Detection and Diagnosis in Engineering Systems," Marcel Dekker, New York, 1998.

[16] R.J. Patton, and J. Chen, "Observer-based Fault Detection and Isolation: Robustness and Applications," Control Engineering Practice, Volume 5, Issue 5, May 1997, Pages 671-682.

[17] R. N. Clark, D. C. Fostch, and V. M. Walton, “Detecting Instrument Malfunctions in Control Systems,” IEEE Transactions Aerospace & Electronic Systems, AES-11: 465-473, 1975.

[18] R. N. Clark, "The Dedicated Observer Approach to Instrument Failure Detection," In Decision and Control including the Symposium on Adaptive Processes, 1979 18th IEEE Conference on, vol. 18, pp. 237-241. IEEE, 1979.

[19] R. J. Patton, “Robust Fault Detection Using Eigen Structure Assignment,” 12th IMAC World Congress on Mathematical Modeling and Scientific Computation, Paris, Vol. 2, 431-434, 1988.

[20] R. J. Patton, S. M. Kangethe, “Robust Fault Diganosis Using Eigen Structure Assignment of Observers,” 99-154, 1989.

[21] R. J. Patton, J. Chen, “Robus Fault Detection of Jet Engine Sensor Systems by Using Eigen-structure Assignment,” AIAA Guidance, Navigation, and Control Conference, New Orleans, LA., 1991.

[22] R. J. Patton, J. Chen, "Robust Fault Detection Using Eigenstructure Assignment: A Tutorial Consideration and Some New Results," Proceedings of the 30th IEEE Conference on Decision and Control, pp. 2242-2247 vol.3, 11-13 Dec 1991.

[23] M. A. Massumnia, “A Geometric Approach to the Synthesis of Failure Detection Filters,” IEEE Transaction on Automatic Control, 31(9):839-846, 1986.

[24] J. E. White, and J. L. Speyer, “Detection Filter Design: Spectral Theory and

Algorithms," IEEE Transaction on Automatic Control, 32(7): 593-603, 1987.

[25] R. K. Douglas, and J. L. Speyer, "h_∞ Bound Detection Filter," AIAA Journal of Guidance, Control and Dynamics, 22(1): 129-138, 1999.

[26] W. H. Chung, and J. L. Speyer, "A Game Theoretic Fault Detection Filter," IEEE Transaction on Automatic Control, 43(2): 143-161, 1998.

[27] R. K. Douglas, and J. L. Speyer, "Robust Detection Filter Design," Proceedings of the American Control Conference, pages 91-96, 1995.

[28] R. H. Chen, and J. L. Speyer, "A Generalized Least-squares Fault Detection Filter," International Journal of Adaptive Control and Signal Processing, 14: 747-757, 2000.

[29] R. H. Chen, and J. L. Speyer, "Robust Multiple-fault Detection Filter," International Journal of Robust and Nonlinear Control, 12(8):675-696, 2002.

[30] J. H. Park, and G. Rizzoni, "A New Interpretation of the Fault Detection Filter, 1: Closed-form Algorithm," International Journal of Control, 60(5): 767-787, 1994.

[31] J. H. Park, and G. Rizzoni, "An Eigen-Structure Assignment Algorithm for the Design of Fault Detection Filters," IEEE Transaction Automatica, Control, 39(7):1521-1524, 1994.

[32] J. H. Park, G. Rizzoni, and W. B. Ribbens, "On the Representation of Sensor Faults in Fault Detection Filters," Automatica, 30(11): 1793-1795, 1994.

[33] R. V. Beard, "Failure Accommodation in Linear Systems through Self-

reorganization," PHD dissertation, Massachusetts Institute of Technology, 1971.

[34] R. K. Mehra, and J. Peschon, "An Innovations Approach to Fault Detection and Diagnosis in Dynamic Systems," Automatica 7: 637-640.

[35] A. S. Willsky, "A Survey of Design Methods for Failure Detection in Dynamic Sysems", Automatica 12(6): 601-611, 1976.

[36] M. Basseville, "Detecting Changes in Signals and Systems-A Survey," Automatica 24(3): 309-326, 1988.

[37] S. G. Tzafestas, and K. Watanabe, "Modern Approaches to System/Sensor Fault and Diagnosis," Journal A 31(4): 42-57.

[38] R. Da, and C. F. Lin, "Sensitivity Analysis Algorithm for the State Chi-Square Test," Journal of Guidance, Control & Dynamics 19(1): 219-222.

[39] A. Zolghadri, "An Algorithm for Real-Time Failure Detection in Kalman Filters," IEEE Transaction Automatic Control 41(10): 1537-1539.

[40] B. Sohlberg, "Monitoring and Failure Diagnosis of a Steel Strip Process," IEEE Transaction Control System Technology 6(2): 294-303.

[41] J. Y. Keller, L. Summer, M. Boutayeb, and M. Darouach, "Generalized Likelihood-ratio Approach for Fault Detection in Linear dynamic Stochastic Systems with Unknown Inputs," International Journal of System Science, 27(12):1231-1241, 1990.

[42] L. Berec, "A Multi-model Method to Fault Detection and Diagnosis: Bayesian

Solution. An Introductory Treatise," International Journal of Adaptive Control And Signal Processing, 44(6):1009-1016, 1998.

[43] I. E. Potter, and M. C. Suman, "Thresholdless Redundancy Management with Arrays of Skewed Instruments," Technical Report AGARDOGRAPH-244 (pp 15-11 to 15-25), AGARD. Integrity in Electronic Flight Control Systems, 1977.

[44] E. Gai, J. V. Harrison, and K. C. Daly, "Failure Detection and Isolation Performance of Two Redundancy Sensor Configurations," Position Location and Navigation Symposium (PLANS), San Diego, pp. 122-131, 1978.

[45] M. Desai, and A. Ray, "A Fault Detection and Isolation Methodology Theory and Application," American Control Conference, pp. 262-270.

[46] E. Y. Chow, and A. S. Willsky, "Analytical Redundancy and the Design of Robust Detection Systems," IEEE Transaction Automatic Control, AC-29(7): 603-614, 1984.

[47] X. Lou, A. S. Willsky, and G. C. Verghese, "Optimally Robust Redundancy Relations for Failure Detection in Uncertain Systems," Automatica 22(3): 333-344, 1986.

[48] M. A. Massoumnia, and W. E. Vander Velde, "Generating Parity Relations for Detecting and Identifying Control System Component Failures," Journal of Guidance, Control & Dynamics 11(1): 60-65, 1988.

[49] J. Gertler, and D. Singer, "A New Structural Framework for Parity Equation-Based Failure Detection and Isolation," Automatic 26(2): 381-388, 1990.

[50] R. J. Patton, and J. Chen, "A Review of Parity Space Approaches to Fault

Diagnosis Preprints of IFAC/IMACS Symposium: SAFEPROCESS'91, Baden-Baden, " pp. 239-255 (Vol.1). Invited Survey Paper, 1991.

[51] J. Chen, and H. Y. Zhang, "Parity vector Approach for Detecting Failures in Dynamic Systems," International Journal of Ssytem Science, 21(4):765-770.

[52] J. Gertler, "Fault Detection and Isolation Using Parity Relations," Control Engineering Practice 5(5): 653-661.

[53] C. Bakitois, J. Raymond, and A. Rault, "Parameter and Discriminant Analysis for Jet Engine Mechanical State Diagnosis," IEEE Conference on Decision & Control, Fort Laudredale, USA, 1979.

[54] G. Geiger, "Monitoring of an Electrical Driven Pump Using Continuous Time Parameter Estimation Methods," 6th IFAC Symposium On Identification and Parameter Estimation, Pergamon Press, Washington, 1982.

[55] R. Isermann, "Process Fault Detection Based on Modelling and Estimation Methods: A Survey," Automatica, 20(4): 387-404.

[56] R. Isermann, and B. Freyermuth, "Process Fault Diagnosis Based on Process Model Knowledge," Journal A 31(4): 58-65, 1990.

[57] R. Isermann, and B. Freyermuth, "Process Fault Diagnosis Based on Process Model Knowledge – Part I: Principles for Fault Diagnosis with Parameter Estimation," Journal Dynamic System, Measurement & Control – Transaction Of the ASME 113(4): 620-626, 1991.

[58] R. Isermann, "Supervision, Fault-Detection and Fault-Diagnosis Methods - An Introduction," Control Engineering Practice 5(5): 639-652, 1997.

[59] R. Isermann, and P. Balle, "Trends in the Application of Model-Based Fault Detection and Diagnosis of Technical Processes," Contr. Eng. Practice 5(5): 709-719, 1997.

[60] V. Venkatasubramanian, R. Rengaswamy, K. Yin, and S. N. Kavuri, "A Review of Process Fault Detection and Diagnosis Part I: Quantitative Model-Based Methods," Computers and Chemical Engineering 2003, 27, 293:311.

[61] V. Venkatasubramanian, R. Rengaswamy, and S. N. Kavuri, "A Review of Process Fault Detection and Diagnosis Part II: Qualitative Models and Search Strategies," El-sevier Journal of Computers and Chemical Engineering, 27(3):313-326, 2003.

[62] V. Venkatasubramanian, R. Rengaswamy, S. N. Kavuri, and K. Yin., "A Review of Process Fault Detection and Diagnosis Part III: Process History-Based Methods," Elsevier Journal of Computers and Chemical Engineering, 27(3):327-346, 2003.

[63] D. L. Dvorak, "Monitoring and Diagnosis of Continuous Dynamic Systems Using Semi-Quantitative Simulation," PHD Thesis, The University of Texas at Austin, Austin, Texas 78712, USA, 1992.

[64] R. Leitch, R. Kraft, and R. Luntz, "RESCU: A Real-time Knowledge Based System for Process Control," IEEE Proceedings: Control Theory and Application 138(3):217-227, 1991.

[65] R. Leitch, "Engineering Diagnosis: Match Problems to Solutions," Proceedings of International Conference on Fault Diagnosis: TOOLDIAG'93, Toulouse, pp. 837-844, 1993.

[66] Q. Shen, and R. Leitch, "Fuzzy Qualitative Simulation," IEEE Transaction On System, Man & Cybernetics SMC-23(4): 1038-1061.

[67] J. Lunze, "A Method for Logic Based Fault Diagnosis," Preprints of IFAC/IMACS Symposium: SAFEPROCESS'91, Baden-Based, pp. 45-52 (Vol.2), 1991.

[68] J. Lunze, and F. Schiller, "Logic Based Process Diagnosis Utilising the Causal Structure of Dynamical Systems," Preprints of IFAC/IFIP/IMACS International Symposium On Artificial Intelligence in Real-Time Control: AIRTC'92, Delft, pp. 649-654, 1992.

[69] Z. Fathi, W. F. Ramirez, and J. korbicz, "Analytical and Knowledge-Based Redundancy for Fault Diagnosis in Process Plants," AICHE J. 39(1): 42-56, 1993.

[70] I. C. Chang, C. C. Yu, and C. T. Liou, "Model-Based Approach for Fault Diagnosis. 1: Principles of Deep Model Algorithm," Industrial and Engineering Chemistry Research 33(6): 1542-1555.

[71] J. Howell, "Model-based Fault Detection in Information Poor Plants," Automatica 30(6): 929-943, 1994.

[72] L. Leyval, J. Montmain, and S. Gentil, "Qualitative Analysis for Decision-Making in Supervision of Industrial Continuous Processes," Mathematics and Computer in Simulation, 36(2): 149-163, 1994.

[73] G. Betta, M. Dapuzzo, A. Pietrosanto, "A Knowledge Approach to Instrument Fault detection and Isolation," IEEE Transaction On Instrumentation and

Measurement 44(6): 1009-1016, 1995.

[74] T. S. Ramesh, S. K. Shum, and J. F. Davis, "A Structured Framework for Efficient Problem-solving in Diagnostic Expert Systems," Computers and Chemical Engineering 9 - 10 (12), 891- 902, 1988.

[75] D. Leung, and J. Romagnoli, "Dynamic Probabilistic Model-based Expert Systemfor Fault Diagnosis," Computers and Chemical Engineering, 24(11): 2473-2492, 2000.

[76] E. Tarifa, and N. Scenna, "Fault Diagnosis, Directed Graphs, and Fuzzy Logic," Computers and Chemical Engineering 21, S649-654, 1997.

[77] R. Rengaswamy, and V. Venkatasubramanian, "A Syntactic Pattern-Recognition Approach for Process Monitoring and Fault Diagnosis," Engineering Applications of Artificial Intelligence 8 (1): 35-51, 1995.

[78] J. T. Cheung, and G. Stephanopoulos, "Representation of Process Trends Part I. A Formal Representation Framework," Computers and Chemical Engineering 14 (4 -5): 495- 510, 1990.

[79] R. Rengaswamy, and V. Venkatasubramanian, "A Syntactic Pattern-Recognition Approach for Process Monitoring and Fault Diagnosis," Engineering Applications of Artificial Intelligence 8 (1), 35- 51, 1995.

[80] S. Wold, "Cross-validatory Estimation of The Number of Components in Factor and Principal Components Model," Technometrics 20 (4): 397- 405, 1978.

[81] S. Wold, K. Esbensen, and P. Geladi, "Principal Component Analysis,"

Chemometrics and Intelligent Laboratory Systems 2 (1 -3): 37- 52, 1987.

[82] S. Wold, A. Ruhe, H. Wold, and W. Dunn, "The Collinearity Problem in Linear Regression. The Partial Least Squares (PLS) Approach to Generalized Inverses," SIAM Journal of Science Statistical Computer 5 , 735- 743, 1984.

[83] R. Vaidyanathan, and V. Venkatasubramanian, "Representing and Diagnosing Dynamic Process Data Using Neural Networks," Engineering Applications of Artificial Intelligence 5 (1), 11-21, 1992.

[84] V. Venkatasubramanian, and K. Chan, "A Neural Network Methodology for Process Fault Diagnosis," American Institute of Chemical Engineers Journal 35 (12), 1993_ 2002.

[85] D. P. Scharf, F. Y. Hadaegh, and S. R. Ploen, "A Survey of Space Formation Flying Guidance and Control (Part 2)," in Proceedings of the American Control Conference, Boston, Massachusetts, June 2004.

[86] R. W. Beard, J. Lawton, and F. Y. Hadaegh, "A Coordination Architecture for Spacecraft Formation Control," IEEE Transactions on Control Systems Technology, vol.9, no.6, pp.777-790, November 2001.

[87] K. T. Alfriend, S. R. Vadali, P. Gurfil, J. P. How, and L. S. Breger, "Spacecraft Formation Flying Dynamics, Control, and Navigation," Elsevir Ltd., 2010.

[88] R. Carelli, C. de la Cruz, and F. Roberti, "Centralized Formation Control of Non-holonomic Mobile Robot," Latin American Applied Research, 36 (2) (2006), pp. 63–70.

[89] J. Mueller, and S. Thomas, "Decentralized Formation Flying Control in a

Multiple-Team Hierarchy," Proceedings of the 2nd New Trends in Astrodynamics and Applications conference, Princeton, NJ, June 2005. Published in the Annals of the New York Academy of Sciences, Vol. 1065, pp. 112-138.

[90] J. B. Mueller, "A Multiple-Team Organization for the decentralized Guidance and Control of Formation Flying Spacecraft," AIAA Intelligent Systems Conference, 2004.

[91] J. B. Mueller, and S. J. Thomas, "Decentralized Formation Flying Control in a Multiple-Team Hierarchy," Annals of the New York Academy of Sciences 1065.1 (2005): 112-138.

[92] R. Isermann, "Fault-Diagnosis Systems: An introduction from Fault Detection to Fault Tolerance ," Springer, 2006.

[93] M. Staroswiecki, and N. E. Wu, "Fault Detection, Supervision and Safety of Technical Processes 2003," A Proceeding Volume from the 5th IFAC Symposium Washington, D.C, Volume 1, 2003.

[94] A. K. Samantaray, and B. O. Bouamama, "Model-based Process Supervision: A Bond Graph Approach," Springer, 2008.

[95] G. N. Ashtiani, "Fault Detection and Isolation in Spacecraft Attitude System Using Parity Space Method," Master of Science Thesis, Electrical and Computer Engineering Department, Concordia University, April 2007.

[96] J. Gertler, "Analytical Redundancy Methods in Fault Detection and Isolation," Proceedings of IFAC/IAMCS Symposium on Safe Process, Vol. 1, 1991.

[97] M. Nyberg, "Model-Based Fault Fiagnosis Using Structured Hypothesis Tests," Fault Detection, Supervision and Safety for Technical Processes, IFAC, Budapest, Hungary 2000.

[98] K. Reif, S. Gunther, E. Yaz, and R. Unbehauen, "Stochastic Stability of the Continuous-time Extended Kalman Filter," Control Theory and Applications, IEEE Proceedings, Vol. 147, No. 1. IET, 2000.

[99] J. R. Carpenter, "A Preliminary Investigation of Decentralized Control for Satellite Formations," Aerospace Conference Proceedings, 2000 IEEE , vol.7, no., pp.63-74 vol.7, 2000.

[100] A. Bemporad, and C. Rocchi, "Decentralized Linear Time-varying Model Predictive Control of a Formation of Unmanned Aerial Vehicles," 50th IEEE Conference on Decision and Control and European Control Conference (CDC-ECC) , vol., no., pp.7488-7493, 12-15, Dec. 2011.

[101] R. S. Smith, M. V. Subbotin, and F. Y. Hadaegh, "Decentralized Estimation and Control in High Precision Spacecraft Formations: Comparison Studies," Aerospace Conference, 2007 IEEE , vol., no., pp.1-11, 3-10 March 2007.

[102] J. Lavaei, A. Momeni, and A. G. Aghdam, "A Model Predictive Decentralized Control Scheme With Reduced Communication Requirement for Spacecraft Formation," Control Systems Technology, IEEE Transactions on , vol.16, no.2, pp.268-278, March 2008.

[103] F. Wang, A. Nabil, and A. Tsourdos ,"Centralized/Decentralized Control for Spacecraft Formation Flying Near Sun-Earth L2 Point," Industrial Electronics

and Applications, 2009. ICIEA 2009. 4th IEEE Conference on , vol., no., pp.1159-1166, 25-27 May 2009.

[104] Y. Ulybyshev, "Long-term Formation Keeping of Satellite Constellation Using Linear-quadratic Controller," Journal of Guidance, Control, and Dynamics 21.1 (1998).

[105] R. Olfati-Saber, and R.M. Murray, "Distributed Cooperative Control of Multiple Vehicle Formations Using Structural Potential Functions," IFAC World Congress. 2002.

[106] W.B. Dunbar, and R.M. Murray, "Model Predicitive Control of Coordinated Multi-Vehicle Formations," in IEEE Conference on Decision and Control, 2002, pp. 4631-4636 .

[107] M. Mesbahi, and F.Y. Hadaegh, "Formation Flying Control of Multiple Spacecraft via Graphs, Matrix Inequalities, and Switching," Control Applications, 1999. Proceedings of the 1999 IEEE International Conference on, vol.2, no., pp.1211-1216 vol. 2, 1999.

[108] P.K.C. Wang, and F.Y. Hadaegh, "Coordination and Control of Multiple Microspacecraft Moving in Formation," 1996.

[109] N. Wang, X. Jieqiong, "Leader-follower Formation Control of Networked Spacecraft in Deep Space," Advanced Computer Control (ICACC), 2010 2nd International Conference on , vol.3, no., pp.527-530, 27-29 March 2010.

[110] W. Ren, R. W. Beard, "Formation Feedback Control for Multiple Spacecraft via Virtual Structures," Control Theory and Applications, IEE Proceedings - ,

vol.151, no.3, pp. 357- 368, 23 May 2004.

[111] W. Ren, and R.W. Beard,"A Decentralized Scheme for Spacecraft Formation Flying via the Virtual Structure Approach," American Control Conference, Proceedings of the 2003 , vol.2, no., pp. 1746- 1751, June 4-6, 2003.

[112] M.R. Anderson, and A.C. Robbins, “Formation Flight As a Cooperative Game,” in AIAA Guidance Navigation and Control Conference, Boston, MA, 1998, pp. 244-251.

[113] T. Balch, and R.C. Arkin. "Behavior-Based Formation Control for Multirobot Teams," Robotics and Automation, IEEE Transactions on 14.6 (1998): 926-939.

[114] R.C. Arkin, "Behavior-Based Robotics,", MIT press, 1998.

[115] C.R. McInnes, “Autonomous Ring Formation for a Planar Constellation of Satellites,” Journal of Guidance, Control & Dynamics, Vol. 18, No. 5, pp. 1215-1217, 1995.

[116] P.K.C. Wang, and F. Y. Hadaegh, "Self-organizing Control of Multiple Free-Flying Miniature Spacecraft in Formation,” in AIAA Guidance Navigation and Control Conference, Denver, CO, 2000, AIAA Paper No. 2000-4437.

[117] J. Qing-xian, Z. Ying-chun, G. Yu, and W. Li-na, "Robust Nonlinear Unknown Input Observer-based Fault Diagnosis for Satellite Attitude Control System," Intelligent Control and Information Processing (ICICIP), 2011 2nd International Conference on , vol.1, no., pp.345-350, July 2011.

[118] J. Wang, B. Jian, and P. Shi, “Adaptive Observer Based Fault Diagnosis for

Satellite Attitude Control Systems," International Journal of Innovative Computing, Information and Control, vol.4, no.8, Auguest 2008.

[119] T. Jiang, K. Khorasani, and S. Tafazoli, "Parameter Estimation-Based Fault Detection, Isolation and Recovery for Nonlinear Satellite Models," Control Systems Technology, IEEE Transactions on, vol.16, no.4, pp.799-808, July 2008.

[120] N. Tudoroiu, K. Khorasani, "Fault Detection and Diagnosis for Reaction Wheels of Satellite's Attitude Control System Using a Bank of Kalman Filters," International Symposium on Signals, Circuits, and Systems, vol. 1, pp. 199-202, July 2005.

[121] N. Tudoroiu, and K. Khorasani, "Fault Detection and Diagnosis for Satellite's Attitude Control System Using an Interactive Multiple Model Approach," Proceedings of 2005 IEEE Conference on Control Applications, pp. 1287-1292, August 2005.

[122] N. Tudoroiu, E. Sobhani-Tehrani, and K. Khorasani, "Interactive Bank of Unscented Kalman Filters for Fault Detection and Isolation in Reaction Wheel Actuators of Satellite Attitude Control System," 32nd Annual Conference on IEEE Industrial Electronics, p.p. 264-269, November 2006.

[123] W. Qing, and M. Saif, "Repetitive Learning Observer Based Actuator Fault Detection, Isolation, and Estimation With Application to a Satellite Attitude Control system," American Control Conference, pp. 414-419, July 2007.

[124] H. A. Talebi, K. Khorasani, and S. Tafazoli, "A Recurrent Neural-Network-

Based Sensor and Actuator Fault Detection and Isolation for Nonlinear Systems With Application to the Satellite's Attitude Control Subsystem," Neural Networks, IEEE Transactions on , vol.20, no.1, pp.45-60, Jan. 2009.

[125] H. A. Talebi, and K. Khorasani, "A Robust Fault Detection and Isolation Scheme With Application to Magnetorquer Type Actuators for Satellites," IEEE International Conference on Systems, Man, and Cybernetics, pp. 3165-3170, October 2007.

[126] H. A. Talebi, R.V. Patel, and K. Khorasani, "Fault Detection and Isolation for Uncertain Nonlinear Systems with Application to a Satellite Reaction Wheel Actuator", IEEE International Conference on Systems, Man, and Cybernetics, pp. 3140-3145, October 2007.

[127] A. Valdes, K. Khorasani, "Dynamic Neural Network Based Pulsed Plasma Thruster Fault Detection and Isolation for the Attitude Control System of a Satellite", IEEE International Joint Conference on Neural Networks, pp. 2689-2695, 2008.

[128] I.A.D. Al-Zyoud, and K. Khorasani, "Neural Network Based Actuator Fault Diagnosis for Attitude Control Subsystem of a Satellite," World Automatic Congress, PP. 1-6, July 2006.

[129] C. Zhao-hui, W. Jiao-long, R. Jiang, and L. Xiong, "Real-time Fault Diagnosis of Satellite Attitude Control System Based on Sliding-Window Wavelet and DRNN," Control and Decision Conference (CCDC), 2010 Chinese, vol., no., pp.1218-1222, 26-28 May 2010.

[130] N. Meskin, “Fault Detection and Isolation in a Networked Multi-Vehicle Unmanned System,” PHD Thesis, Department of Electrical and computer Engineering, Concordia University, October 2008.

[131] N. Meskin, and K. Khorasani, “Fault Detection and Isolation of Actuator Faults in Spacecraft Formation Flight”, pp. 1159-1164, December 2006.

[132] A. Barua, and K. Khorasani, "Hierarchical Fault Diagnosis and Fuzzy Rule-Based Reasoning for Satellites Formation Flight," Aerospace and Electronic Systems, IEEE Transactions on , vol.47, no.4, pp.2435-2456, October 2011.

[133] A. Barua, and K. Khorasani, "Hierarchical Fault Diagnosis and Health Monitoring in Satellites Formation Flight," Systems, Man, and Cybernetics, Part C: Applications and Reviews, IEEE Transactions on , vol.41, no.2, pp.223-239, March 2011.

[134] A. Barua, and K. Khorasani, "Verification and Validation of Hierarchical Fault Diagnosis in Satellites Formation Flight," Systems, Man, and Cybernetics, Part C: Applications and Reviews, IEEE Transactions on , vol.42, no.6, pp.1384-1399, Nov. 2012.

[135] S. M. Azizi, “Cooperative Fault Estimation and Accommodation in Formation Flight of Unmanned Vehicles”, PHD Thesis, Department of Electrical and Computer Engineering, Concordia University, December 2010.

[136] S. M. Azizi, and K. Khorasani, “A Hierarchical Architecture for Cooperative Actuator Fault Estimation and Accommodation of Formation Flying Satellites in Deep Space”, vol. 48, pp. 1428-1450, April 2012.

[137] Meng Guo; Dimarogonas, D.V.; Johansson, K.H., "Distributed real-time fault detection and isolation for cooperative multi-agent systems," American Control Conference (ACC), 2012 , vol., no., pp.5270,5275, 27-29 June 2012.

[138] Iman Shames, André M.H. Teixeira, Henrik Sandberg, Karl H. Johansson, "Distributed fault detection for interconnected second-order systems," Automatica, Volume 47, Issue 12, December 2011, Pages 2757-2764.

[139] Mendes, Mário JGC, and J. da Costa. "A multi-agent approach to a networked fault detection system." Control and Fault-Tolerant Systems (SysTol), 2010 Conference on. IEEE, 2010.

[140] Tousi, M.M.; Aghdam, A.G.; Khorasani, K., "A hybrid fault diagnosis and recovery for a team of unmanned vehicles," System of Systems Engineering, 2008. SoSE '08. IEEE International Conference on , vol., no., pp.1,6, 2-4 June 2008

[141] V. A. Chobotov, "Spacecraft Attitude Dynamics and Control," Malaber, FL: Krieger, 1991.

[142] P. C. Hughes, "Spacecraft Attitude Dynamics," New York: J. Wiley & Sons Inc., 1986.

[143] O. Montenbruck, and E. Gill, "Satellite Orbits: Models, Methods, and Applications," Springer-Verlag, 2000.

[144] D. A. Vallado, "Fundamentals of Astrodynamics and Applications," Microcosm Press and Kluwer Academic Publishers, 2001.

[145] M. J. Sidi, "Spacecraft Dynamics & Control: A Practical Engineering Approach," Cambridge University Press, 2002.

[146] L. King, G. Parker, S. Deshmukh, and J. H. Chong, "A study of Interspacecraft Coulomb Forces and Implications for Formation Flying," AIAA Guidance, Navigation and Control Conference, 2002.

[147] E. Wnuk, and J. Golebiewska, "Geopotential and Luni-solar Perturbations in the Satellite Constellation and Formation Flying Dynamics," AAS/AIAA Spaceflight Mechanics Meering, 2003.

[148] C. D. Brown, "Elements of Spacecraft Design," AIAA Education Series, 2002.

[149] J. R. Wertz, "Spacecraft Attitude Determination and Control," D. Reidel Publishing Company Inc., 1978.

[150] Paul Mather, Brandt Tso, “Classification Methods for Remotely Sensed Data”, second edition.